Aerodynamic Model Identification of the Flying V using Wind Tunnel Data

Alberto Ruiz García

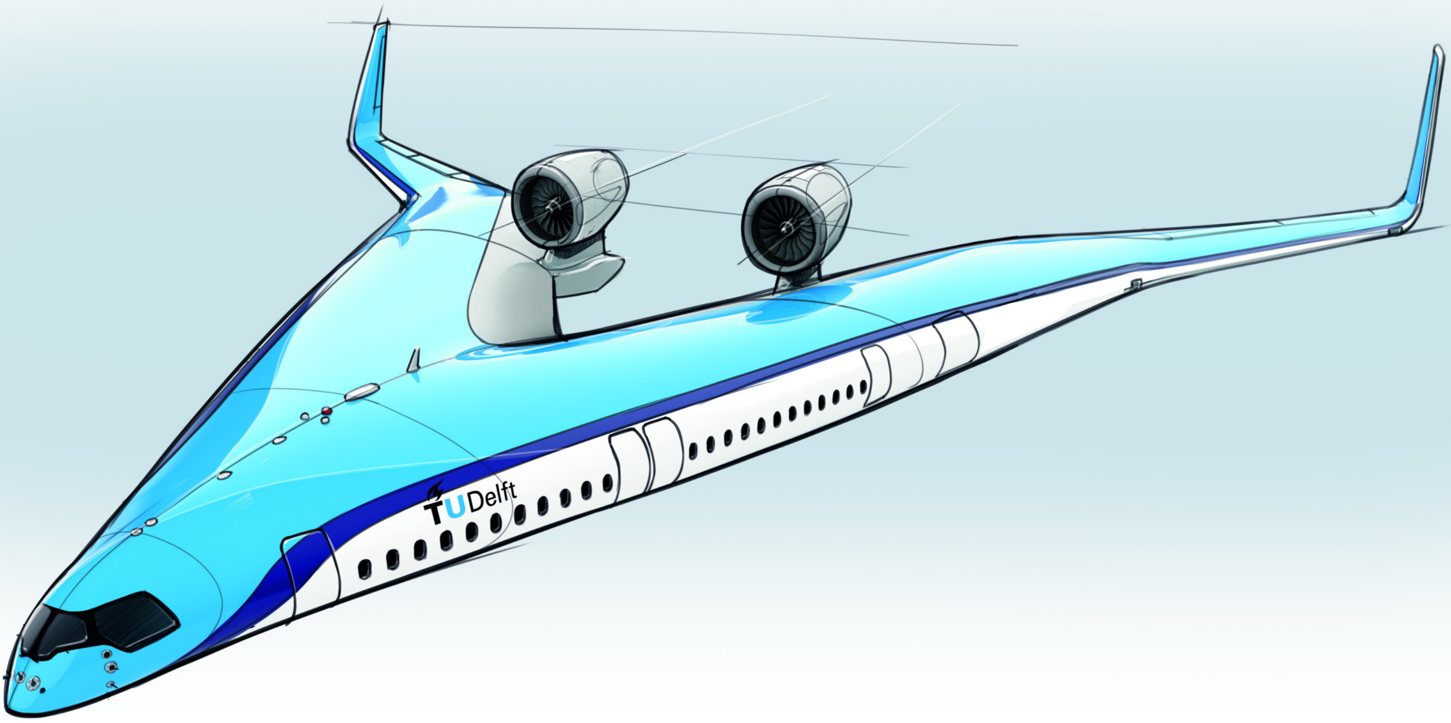

TU Delft Delft University of Technology

Front cover image source: ***Studio OSO***

Aerodynamic Model Identification of the Flying V from Wind Tunnel Data

Master Thesis Report

by

Alberto Ruiz García

to obtain the degree of
Master of Science in Aerospace Engineering

at
Delft University of Technology,

to be defended publicly on
Thursday July 4, 2019 at 10:00 AM.

Student number:	4616014	
Project duration:	April 1, 2018 – July 4, 2019	
Thesis committee:	Dr. ir. R. Vos,	TU Delft, supervisor
	Prof. dr. ir. P. Colonna di Paliano,	TU Delft
	Dr. ir. C.C. de Visser,	TU Delft

An electronic version of this thesis is available at `http://repository.tudelft.nl/`.

Abstract

The Flying V is a tailless flying wing with a V-shaped planform, where the passenger cabin has been integrated inside the main lifting surface. The main goal of this project is the aerodynamic model identification of this novel aircraft configuration, using wind tunnel data from a 4.6% scaled model. Models using Multivariate Orthogonal Functions and splines were postulated for the aerodynamic forces and moments, in order to construct a global input/output model to estimate the aerodynamic response of the Flying V. The aerodynamic model structure was unknown *a priori*, and was determined from the measured data using a modified stepwise regression technique, which achieved parsimonious models with tight confidence bounds. The models were validated against a partition of the data, showing good prediction capabilities and reasonably random, uncorrelated residuals, especially in the case of the spline models.

The resulting models are analytical functions in the state and control variables, which can be used to determine the aerodynamic forces and moments of the Flying V at any given flight condition inside the region of validity of the model. Using the estimated models, a trim routine was programmed to calculate the thrust and control settings required for trimmed flight at different airspeeds and flight path angles. Bounds for the center of gravity regarding controllability and stability were calculated using the estimated models, and a feasible center of gravity location for the Flying V was identified. In addition, a safe flight envelope for the flight test can be defined from the results of the trim routine.

Some discrepancies are expected with respect to flight test results, specially arising from wind tunnel wall interference and because of the half model used for the tests, whose effects are very difficult to estimate at this stage of the project.

Models for the actuators dynamics were estimated using a nonlinear regression technique and ARMAX models, which achieved accurate predictions of the delay and transient response and led to suitable models to be used in the design of a flight control system.

The results of the aerodynamic estimation indicate that once flight-test data is available, a dynamic model could also be estimated using the technique described here using either a polynomial model or a spline model. The aerodynamic model resulting from this work consists in the first step in the System Identification field for the Flying V, and it will allow for detailed studies in the area of flight control design, dynamic simulations, or stall characterization, among others.

Acknowledgements

First and foremost, I would like to thank all the people without whom this thesis would not have been possible.

First, I would like to thank my supervisor Roelof Vos for his trust, support, and advice during the whole project, and for giving me the opportunity to work in the amazing project this has become.

I would also like to thank Coen de Visser for his help and guidance throughout the project, which always helped steer the thesis towards the right direction. His door was always open, and his directions have immensely improved the quality of my work. Thank you!

A great thanks also goes to all the technicians that helped us building the wind tunnel model, and to my colleagues Marco and Rob. A big mention should go to Malcom, it was great working with you. Your knowledge and dedication, our discussions, and the necessary coffee breaks were key to make this project work.

I would also like to thank my family and friends, who have always been there when I needed them; and to my uncle Mariano, whose advice and expertise in electronics avoided me all kinds of unimaginable pain.

Special mention goes to Irina, who no matter how busy I was, always found the way to visit me and cheer me up.

And last but not least, I would like to thank my parents, without whom I would never have achieved any of this. Gracias.

Alberto Ruiz García
Delft, June 2019

Contents

Abstract i

List of Figures vii

List of Tables ix

Nomenclature xii

1 Introduction 1
- 1.1 Project background and objective 2
- 1.2 Thesis outline 3

2 Aerodynamic Model Identification 5
- 2.1 Classification of identification problems 5
- 2.2 Parameter Estimation 6
  - 2.2.1 Model postulation 9
  - 2.2.2 Definitions 11
  - 2.2.3 Ordinary Least Squares (OLS) 11
- 2.3 Analysis of the OLS estimator 12
  - 2.3.1 Main characteristics 12
  - 2.3.2 Confidence bounds 13
  - 2.3.3 Data collinearity 14
  - 2.3.4 Residual analysis 16
- 2.4 Model structure determination 16
  - 2.4.1 Modified Stepwise Regression 17
  - 2.4.2 Regressors orthogonalization 18
  - 2.4.3 Metrics and variables for model selection 19
- 2.5 Chosen approach and motivation 19
- 2.6 Actuators identification 20
  - 2.6.1 First-order lag with dead time (step response) 20
  - 2.6.2 First-order lag with dead time (nonlinear regression) 21
  - 2.6.3 ARMAX models 21

3 Experiment Description 23
- 3.1 Wind tunnel model and scaling effects 23
- 3.2 Wind tunnel setup description 25
- 3.3 Control and measurement of the control surfaces 27
- 3.4 Instrumentation 29

4 Data preprocessing 31
- 4.1 Wind tunnel corrections 31
  - 4.1.1 Lift interference corrections 31
  - 4.1.2 Blockage corrections 36
  - 4.1.3 Expected discrepancies 37

4.2 Translation to body axes 38
4.3 Uncertainty analysis 39
4.4 Control surfaces kinematics 40
4.5 Data coverage 42

5 Results and Discussion 45
5.1 Polynomial models 45
5.1.1 Model structure determination 45
5.1.2 Parameter estimation 47
5.1.3 Model validation 50
5.1.4 Sensitivity analysis 51
5.2 Spline models 51
5.2.1 Model structure determination 52
5.2.2 Parameter estimation 54
5.2.3 Model validation 56
5.2.4 Sensitivity analysis 57
5.3 Global model inspection and discussion 57
5.4 Application example: longitudinal stability and control 61
5.4.1 Center of gravity location 62
5.4.2 Trim at different airspeeds and flight path angles 63
5.4.3 Longitudinal trim results 67
5.4.4 Pitch damping and dynamic stability 69

6 Conclusions 73

Bibliography 77

Appendices 81

A Controller and DAQ design 83

B Frames of Reference 87

C Wind tunnel test matrix 91

D Aerodynamic Model Identification Results 93
Polynomial models 93
Forward force coefficient 93
Vertical force coefficient 95
Rolling moment coefficient 96
Pitching moment coefficient 98
Yawing moment coefficient 101
Spline models 103
Forward force coefficient 103
Vertical force coefficient 105
Rolling moment coefficient 107
Pitching moment coefficient 109
Yawing moment coefficient 116

E Actuators identification results 119

List of Figures

1.1 Timeline of the *Flying V* project 3

2.1 Schematics of output-error and filter-error methods 6
2.2 Scheme of the Two-Step Method for Aerodynamic Model Identification 7
2.3 Nonlinear regression scheme 21

3.1 Pictures of the wind tunnel model 24
3.2 Schematic of the OJF wind tunnel 26
3.3 Isometric view of the wind tunnel setup used for the tests 26
3.4 Rear view and side view of the wind tunnel setup used for the tests 27
3.5 Electronic calibration results 29

4.1 Lift spanwise distribution (CFD simulations) 32
4.2 Drawings of the reflected setup on the reflection plane 33
4.3 Lift interference parameter for elliptic loading in elliptic test sections 34
4.4 Lift interference correction for the stream direction 35
4.5 Plots of τ_2 for streamline curvature corrections 36
4.6 Plots of T_R for solid blockage corrections 37
4.7 Blockage corrections 38
4.8 3-σ confidence values for clean configuration data 40
4.9 Lift coefficient and pitching moment (detail) 41
4.10 Schematic of the control surfaces kinematics 41
4.11 Control surfaces deflections versus servo angle 41
4.12 Measured aerodynamic forces and moment coefficients during the tests 42
4.13 Convex hull of the estimation dataset ($\alpha - V$ and $\alpha - \delta_1$ cuts) 43

5.1 Stepwise regression results for the polynomial model for C_m 46
5.2 Sensitivity of RMS to changes in the polynomial model parameters 52
5.3 Stepwise regression results for the spline model for C_m 53
5.4 Sensitivity of RMS to changes in the spline model parameters 57
5.5 Overall fit comparison of estimated models 58
5.6 Local spatial quality of the models 59
5.7 Example of estimation and validation residuals for an overfitted model 60
5.8 Aft center of gravity limits estimation 62
5.9 Forward center of gravity limits estimation 63
5.10 Pitching moment for clean configuration and control authority ($x_{cg} = 1.36$ m) 64
5.11 Forces during flight in a vertical plane 64
5.12 Required thrust-to-weight ratio for horizontal flight (untrimmed) 66
5.13 Trim results for horizontal flight for different center of gravity locations) 67
5.14 Trim results for flight at different flight path angles ($x_{cg} = 1.36$ m) 68
5.15 Thrust-to-weight ratio for different flight path angles and rates of climb ($x_{cg} = 1.36$ m) . 68
5.16 Pitch damping schematic 69
5.17 Center of pressure longitudinal position for $\alpha - V$ 70

A.1 Schematic of the controller and DAQ for the control surfaces 84
A.2 Buffer circuit details 85
A.3 Flowchart with the logic for the communication PC-Controller-DAQ 86

B.1 Earth and body reference frames 88
B.2 Orientation between wind and body reference frames 88
B.3 Center of gravity and balance reference location 89

D.1 Stepwise regression results (C_X polynomial model) 93
D.2 Residual analysis (C_X polynomial model) 94
D.3 Model cuts with confidence bounds (C_X polynomial model) 94
D.4 Stepwise regression results (C_Z polynomial model) 95
D.5 Residual analysis (C_Z polynomial model) 95
D.6 Model cuts with confidence bounds (C_Z polynomial model) 96
D.7 Stepwise regression results (C_l polynomial model) 96
D.8 Residual analysis (C_l polynomial model) 97
D.9 Model cuts with confidence bounds (C_l polynomial model) 97
D.10 Stepwise regression results (C_m polynomial model) 98
D.11 Residual analysis (C_m, polynomial model) 99
D.12 Model cuts with confidence bounds (C_m polynomial model) 100
D.13 Stepwise regression results (C_n polynomial model) 101
D.14 Residual analysis (C_n polynomial model) 101
D.15 Model cuts with confidence bounds (C_n polynomial model) 102
D.16 Stepwise regression results (C_X spline model) 103
D.17 Residual analysis (C_X spline model) 103
D.18 Model cuts with confidence bounds (C_X spline model) 104
D.19 Collinearity indicators (C_X spline model) 104
D.20 Stepwise regression results (C_Z spline model) 105
D.21 Residual analysis (C_Z spline model) 105
D.22 Model cuts with confidence bounds (C_Z spline model) 106
D.23 Collinearity indicators (C_Z spline model) 106
D.24 Stepwise regression results (C_l spline model) 107
D.25 Residual analysis (C_l spline model) 107
D.26 Model cuts with confidence bounds (C_l spline model) 108
D.27 Collinearity indicators (C_n spline model) 108
D.28 Stepwise regression results (C_m spline model) 109
D.29 Residual analysis evolution (C_m spline model) 110
D.30 Model cuts with confidence bounds (C_m spline model) 112
D.31 Collinearity indicators evolution (C_m spline model) 114
D.32 Collinearity indicators (C_m spline model) 115
D.33 Stepwise regression results (C_n spline model) 116
D.34 Residual analysis (C_n spline model) 116
D.35 Model cuts with confidence bounds (C_n spline model) 117
D.36 Collinearity indicators (C_n spline model) 117

E.1 ARMAX and 1st order lag model for the actuator from CS#2 (estimation) 120
E.2 ARMAX and 1st order lag model for the actuator from CS#2 (validation) 120

List of Tables

3.1 List of components for the control surfaces control and measurements 28
3.2 Available instrumentation for the wind tunnel tests 30

5.1 Parameter variances for the candidates of the C_m polynomial model 47
5.2 Model fit comparison for the C_m polynomial model candidates 47
5.3 Coefficients of the polynomial model for C_X 48
5.4 Coefficients of the polynomial model for C_Z 49
5.5 Coefficients of the polynomial model for C_l 49
5.6 Coefficients of the polynomial model for C_m 49
5.7 Coefficients of the polynomial model for C_n 50
5.8 Model characteristics (polynomial models) 50
5.9 Maximum absolute relative residuals of the polynomial models 50
5.10 Parameter variances for the candidates of the C_m spline model 53
5.11 Model fit comparison for the C_m spline model candidates 54
5.12 Coefficients of the spline model for C_X 54
5.13 Coefficients of the spline model for C_Z 55
5.14 Coefficients of the spline model for C_l 55
5.15 Coefficients of the spline model for C_m 55
5.16 Coefficients of the spline model for C_n 56
5.17 Model characteristics (spline models) 56
5.18 Maximum absolute relative residuals of the spline models 57

C.1 Wind tunnel test matrix 92

Nomenclature

Acronyms and abbreviations

Acronym	Description
ADC	Analog-to-Digital Converter
ARMAX	AutoRegressive Moving Average model with eXogeneous inputs
BLUE	Best Linear Unbiased Estimator
CFD	Computational Fluid Dynamics
DAQ	Data Acquisition System
FCS	Flight Control System
MSE	Mean Square Error
OJF	Open Jet Facility
OLS	Ordinary Least Squares
PSE	Predicted Square Error
RLI	Resin Liquid Infusion
RMS	Root Mean Square Error

Greek Symbols

Symbol	Description	Units
α	Angle of attack	[rad, °]
β	Sideslip angle	[rad, °]
δ_i	Deflection of the ith control surface, $i = 1, 2, 3$	[rad, °]
δ_{corr}	Boundary correction factor	[−]
ϵ	Blockage factor	[−]
φ	Servo angle	[rad, °]
ψ	Coupler angle	[rad, °]
ρ	Density	[kg/m^3]
τ_2	Streamwise correction factor	[−]
$\boldsymbol{\theta}$	Parameter vector	[−]
$\boldsymbol{\xi}_j$	Orthogonal regressors, $j = 1, 2, ..., n$	[−]

Roman Symbols

Symbol	Description	Units
b	Wing span of the model	[m]
$\bar{c}$	Reference chord	[m]
C_D	Drag coefficient	[−]
C_L	Lift coefficient	[−]
C_l	Rolling moment coefficient	[−]
C_m	Pitching moment coefficient	[−]
C_n	Yaw moment coefficient	[−]
C_X	Forward force coefficient	[−]
C_Y	Lateral force coefficient	[−]
C_Z	Vertical force coefficient	[−]
$\mathbf{F}_{bal}$	Forces at the balance	[N]
G	Orthogonalization matrix	[−]
J	OLS cost function	[−]
L	Rolling moment	[N·m]
M	Pitching moment	[N·m]
$\mathbf{M}_{bal}$	Moments at the balance	[N·m]
N	Number of samples	[−]
N	Yaw moment	[N·m]
n	Number of regressors in model	[−]
$\mathbf{p}_j$	Model regressors, $j = 1, 2, ..., n$	[−]
q_∞	Dynamic pressure	$[\mathrm{kg} \cdot \mathrm{m}^{-1}\mathrm{s}^{-2}]$
Re	Reynolds Number	[−]
S	Wing area	$[\mathrm{m}^2]$
$\mathbf{v}$	Residual vector	[−]
V	Wind speed	[m/s]
$\hat{V}$	Dimensionless wind speed	[−]
$\mathbf{x}$	State vector	[−]
X	Regression matrix	[−]
X	Forward force	[N]
$\mathbf{y}$	Output vector	[−]
Y	Lateral force	[N]
$\mathbf{z}$	Measurement vector	[−]
Z	Vertical force	[N]

Chapter 1

Introduction

An important task in the development of a new aircraft is the creation of an aerodynamic model to evaluate its performance and handling qualities. To do so, different theoretical approaches are possible[1]: low fidelity techniques such as panel methods and strip theory; complex Computational Fluid Dynamics (CFD) simulations, where the partial differential equations are solved; or a variety of methods developed from the experience acquired throughout the years (e.g. U.S. Air Force DATCOM), among others. Nevertheless, even with the increasingly computational power available nowadays, wind tunnel tests and flight tests are still the most reliable source of aerodynamic data. There are some conditions where aerodynamic simulations can offer good results, such as for low angles of attack or for low rotational rates, but typically the accuracy worsens when non-linearities occur.

Input/output data is gathered during the tests (control inputs, aircraft states, forces in a wind tunnel...), and can be used to derive a model that explains the observed behavior. The field of System Identification deals with the creation of such a mathematical model, which describes a system based on observations (measurements) of its input/output behavior. The ability to capture an aerodynamic model allows to predict the response of the aircraft at conditions that might have not been tested, providing at the same time with a better understanding of the aerodynamics, without the need of a detailed knowledge of all possible aerodynamic effects.

Global models offer certain advantages with respect to local models[2]. Local models spanning just a small region of the flight envelope may be accurate but they are not suitable for control design, where smooth gradients of the aerodynamic coefficients are required. In addition, they do not provide as much information about the nonlinear regimes as a differentiable global model that is able to capture these nonlinearities.

The identification of an aerodynamic model is considered a required step in the design of an aircraft[1]; it is used, among others, to:

1. Verify and calibrate the developed theoretical models and CFD (Computational Fluid Dynamics) simulations.
2. Verify wind tunnel test results.
3. Obtain proper mathematical models of the aircraft dynamics to perform simulations and for the design of the Automatic Flight Control System.
4. Develop flight simulators, which should be able to accurately reproduce all the necessary flight conditions for a proper pilot training.
5. Expand the flight envelope for new aircraft, investigating highly non-linear regimes, such as post-stall or spin recovery[3].
6. Investigate how to recover controllability from damaged configurations using real-time system identification[4] (Fault tolerant control).

In the most general case, one may distinguish among three types of models, depending on the amount of known information about them[5]:

- *White-box models*: the equations are known and the model is completely deterministic.
- *Black-box models*: input/output models, based only on the data they receive. The parameters of the model may have little or no physical meaning.
- *Grey-box models*: in between both extremes, combining prior physical knowledge with information from the measured data. The physical knowledge is used to build the model, and the data is used to estimate the values of the proposed parameters.

A white-box model is usually not possible in the aerospace field since the necessary *a priori* knowledge to build the model is not available. An example of a white-box model is Einstein's Field Equations [6], which explains the behavior of the Universe from a completely deterministic perspective. On the other hand, black-box models such as neural networks can be used in some aircraft-related applications,[7, 8], but they are not that common since they do not provide any physical insight of the model[9], they require a large amount of training data, and it is difficult to assess their quality[10].

In addition, a basic rule in estimation is to use any knowledge available to define the model structure[5]. Under certain assumptions, the equations that govern the dynamics of the aircraft can be derived and used to build a grey-box model, along with a certain postulated aerodynamic model structure. The already existing knowledge helps to choose an appropriate model structure, which offers a better physical insight than a completely black-box model.

A study of the existing scientific literature was done in order to understand how this problem has been tackled historically, and what the state of the art is in the aerodynamic identification field.

1.1 Project background and objective

The present work focuses on the *Flying V*, a recent design of a passenger aircraft in an unconventional flying wing configuration where the passenger cabin is integrated into the main lifting surface. A timeline of the project is shown in Figure 1.1.

This aircraft was first devised by Benad[11], who showed how his preliminary design could theoretically outperform the Airbus A350, improving by 10% its aerodynamic efficiency and having a slightly lower empty weight. This preliminary design was improved by Faggiano in [12], who optimized the planform geometry and aerodynamic surfaces to further increase the aerodynamic efficiency of the aircraft, which is expected to translate into substantial fuel savings. An oval fuselage cross section was also designed by Vos et al.[13], and a concept of the structure was analysed by van der Schaft[14]. More recently, Palermo[15] and Viet[16] studied the low speed characteristics of the Flying V from wind tunnel data.

The availability of sub-scale wind tunnel data provides a very useful insight in the aerodynamics of the Flying V, which are not well known yet because of the very recent nature of the project. Following the lines of reasoning from the introduction, the identification of an aerodynamic model from experimental data seems a natural next step in the development of the Flying V, and will allow to open several important fields of research, such as control design and flight dynamics simulations. The model structure (unknown *a priori*) needs to be postulated, and the parameters that define the model estimated. In order to do so, a 4.6% scaled wind tunnel model of the Flying V was built by a team which the author was part of, which was instrumented and tested in the Open Jet Facility of the Faculty of Aerospace Engineering at TU Delft. A secondary goal will be the identification of the actuators dynamics for the control surfaces, which is required in order to develop a Flight Control System and will be used in the future.

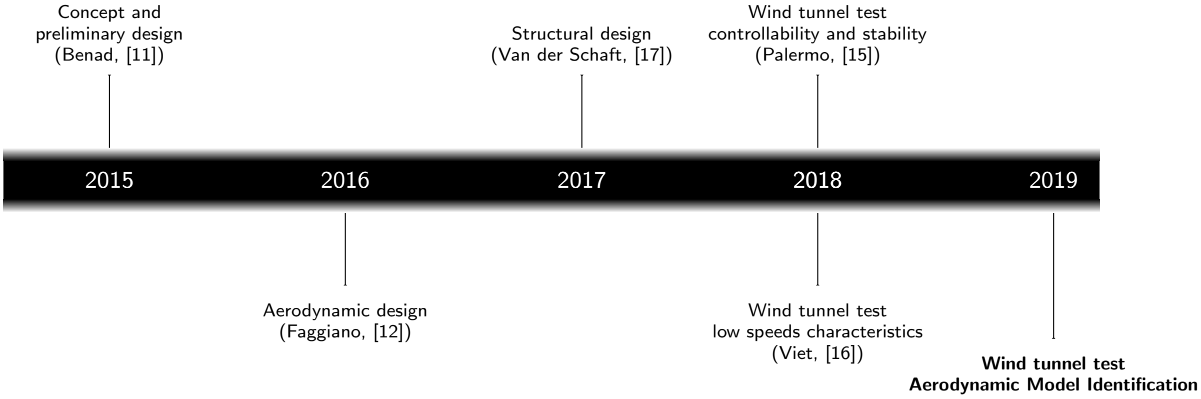
Concept and preliminary design (Benad, [11])
Structural design (Van der Schaft, [17])
Wind tunnel test controllability and stability (Palermo, [15])
2015
2016
2017
2018
2019
Aerodynamic design (Faggiano, [12])
Wind tunnel test low speeds characteristics (Viet, [16])
Wind tunnel test Aerodynamic Model Identification

Figure 1.1: Timeline of the *Flying V* project

A main research objective can be formulated for the present thesis:

Determine an input/output model to estimate the aerodynamic response of the Flying V from sub-scale wind tunnel data, using an adequate model structure determination technique.

This objective can be broken down into three subquestions:

Research question #1: *What is the most convenient framework for the estimation of an aerodynamic model of the Flying V from experimental data?*

Research question #2: *What is an adequate aerodynamic model structure and how can it be determined?*

Research question #3: *What are the main expected discrepancies between the sub-scale results and the full-scale characteristics?*

1.2 Thesis outline

This report is structured into several parts: in Chapter 2 the background required for the aerodynamic model identification of the Flying V is presented, along with the chosen methodology, which includes the parameter estimation, model structure determination, and model validation. In Chapter 3 the conducted experiment is described, including the wind tunnel setup, scaling effects to expect and the instrumentation. Chapter 4 explains the required preprocessing to the data before the system identification can begin. In Chapter 5 the results of the Aerodynamic Model Identification are presented and discussed for two different approaches, and their performance is compared. An application of the estimated aerodynamic model to calculate a longitudinal trim routine is also presented. Finally, in Chapter 6 the conclusions are summarized and the future work is discussed.

Additional information is available in the appendices:

- Appendix A presents the electronic design for the controller and Data Acquisition System of the control surfaces.
- Appendix B presents the reference frames used in the thesis.
- Appendix C includes the test matrix used for the wind tunnel experiments.
- Appendix D includes all Aerodynamic Identification results referenced in Chapter 5, to keep the report compact and readable.
- Appendix E briefly presents the results of the actuator identification.

Chapter 2

Aerodynamic Model Identification

2.1 Classification of identification problems

Laban distinguishes in [18] three main types of identification problems:

1. *General system identification problem*: black-box problem, not only the states and parameters are unknown, but also the system and observation equations need to be estimated from the measured data.
2. *Joint state-parameter estimation problem*: this is the usual case for aircraft system identification. The system and observation equations are assumed to be known, but the state variables and the system parameters remain unknown and must be estimated together.
3. *Parameter estimation problem*: if the state variables are known, only the system parameters need to be estimated, reducing the complexity of the estimation problem.

Given that both the dependent variables (aerodynamic forces and moments) and independent variables (angle of attack, wind speed and control surface deflections) can be measured directly, the problem to be solved for the present thesis is a parameter estimation problem. In a flight test, however, the problem to be solved is a joint state-parameter estimation problem, since the dependent variable to model (aerodynamic forces and moments) needs to be calculated from noisy measurements of the states.

Estimation methods can be divided intro three broad categories[9]: equation-error,output-error, and filter-error methods.

The equation-error method consists on a linear estimation problem, which allows to use classical regression techniques. Because of its simplicity, it is the first option to use if an adequate accuracy can be achieved with this method. If the dependent variables (aerodynamic forces and moments) can be written as a linear combination of a vector of constant parameters and the independent variables (angular rates, airspeed, flow angles, control inputs), a least squares regression method can be used, finding the best estimate in one shot for a fixed model structure.

The output-error method and the filter-error method involve nonlinear optimization problems which can account for noise. The output-error method only accounts for measurement noise, whereas the filter-error method can account for both process and measurement noise. Fig. 2.1 shows a scheme of the system identification procedure for the output-error and the filter-error methods.

Equation-error, output-error, and filter-error methods are all maximum likelihood estimators, they just differ on the noise characteristics that are assumed. Output-error methods have probably been the most widely procedure used for aircraft system identification, where the absence of process noise is a reasonable assumption if the atmosphere is calm[19, 20, 9]. For the most general case, the filter-error method seems to be the most convenient framework to work with, and has been used successfully for aircraft system identification in a turbulent atmosphere[21].

These methods are complex though, and may suffer from convergence problems when a large number of unknown parameters are involved[3]. Mulder proposed in [22] a simplification of the joint

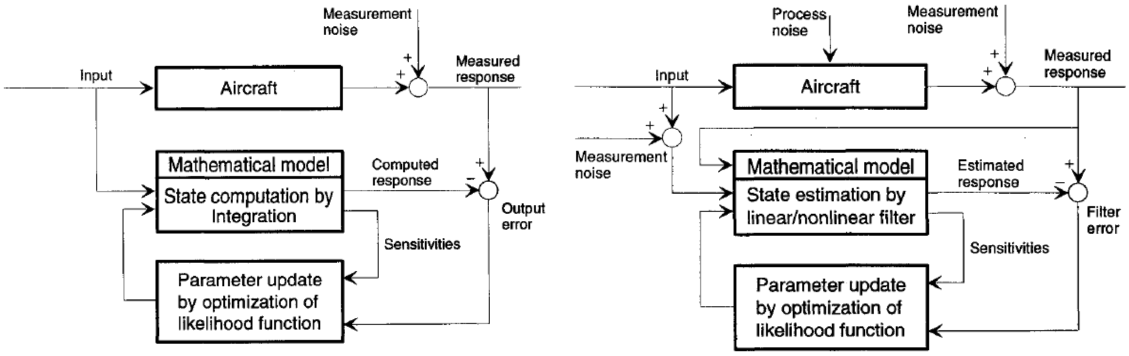
Measurement noise
Input
Aircraft
Measured response
Mathematical model
State computation by Integration
Computed response
Output error
Sensitivities
Parameter update by optimization of likelihood function
Process noise
Measurement noise
Input
Aircraft
Measured response
Measurement noise
Mathematical model
State estimation by linear/nonlinear filter
Estimated response
Filter error
Sensitivities
Parameter update by optimization of likelihood function

(a) Output-error method (b) Filter-error method

Figure 2.1: Schematics of output-error and filter-error methods (adapted from Ref. [9])

state-parameter estimation problem for aircraft called the *Two-Step method.* If certain conditions are met (regarding measurement accuracy and the type of variables that are measured), the estimation problem can be decomposed into two separate estimation problems. An analytical and numerical comparison was done in Ref. [23] between the Two-Step method and a one-step Maximum Likelihood based on an output-error method. The outcome was that the accuracy of the state of the art flight test measurement systems is enough to neglect measurement noise, proving the Two-Step Method as a convenient way of dealing with the aircraft system identification problem. Indeed, the Two-Step method has been used extensively in Delft University of Technology ([10], [18],[22], [24]) achieving very good results.

The main feature of the Two-Step method is the decomposition of the joint state-parameter estimation problem into two simpler ones: a state estimation problem (flight path reconstruction) and a parameter estimation problem (aerodynamic estimation). The schematic of the procedure is shown in Fig. 2.2. The core of the flight path reconstruction procedure is the Kalman filter block, which will depend on the formulation of the problem: if the nonlinear equations of motion are used, a nonlinear Kalman filter will be needed. Examples can be found using an Extended Kalman Filter (EKF)[22], an Iterative Extended Kalman Filter (IEKF)[10], or an Unscented Kalman Filter (UKF)[24].

Even though only wind tunnel data is available at the moment, flight test data will be available in the near future, so the methodology used for this thesis should also be able to identify a dynamic model from real flight data. In this sense, the "modular" approach of the Two-Step method makes it very suitable for this purpose, since the aerodynamic parameter estimation module can be built, tested, and validated using wind tunnel data before it is used with dynamic data, reducing future uncertainties. This thesis will focus then on the construction of the aerodynamic identification module from Figure 2.2. This module has two main tasks:

- To determine an appropriate model structure to represent the aerodynamic response of the Flying V, since the lack of previous information about this aircraft makes it difficult to postulate an adequate model to represent its aerodynamic response.
- To perform a valid parameter estimation once the model structure has been fixed, and to provide with enough information about the model in order to validate (or disprove) it by means of different tools (e.g. residual characteristics, collinearity, sensitivity analysis...)

This last objective (parameter estimation) will be explained first, since the model structure determination is based on performing a number of estimations with different variable combinations until an adequate structure is found.

2.2 Parameter Estimation

The first goal of parameter estimation is to find the values of a certain set of parameters θ that best describe the behavior of the system of interest. As stated in [25], this field of study deals with the

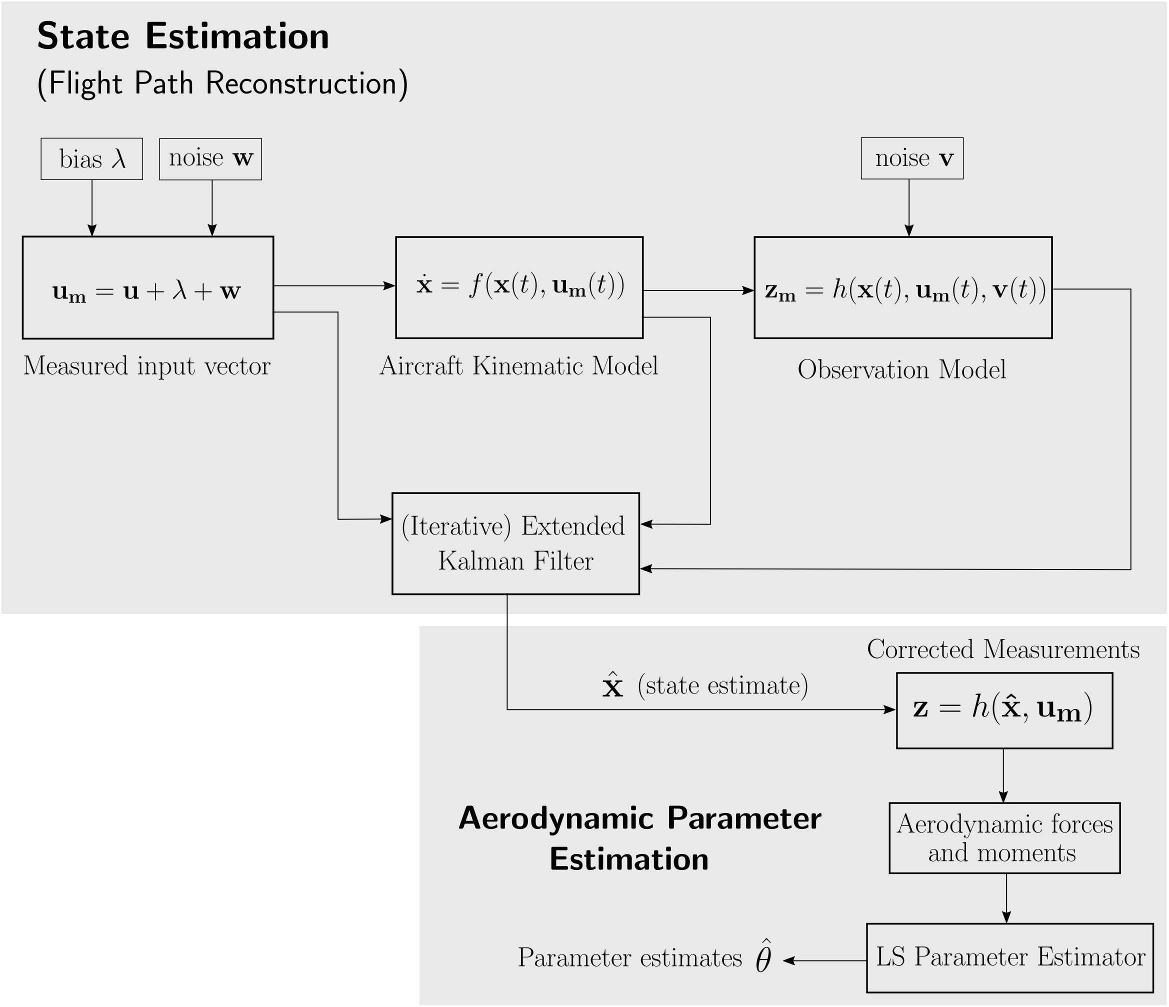
State Estimation
(Flight Path Reconstruction)
bias λ
noise $\mathbf{w}$
noise $\mathbf{v}$
$\mathbf{u_m} = \mathbf{u} + \lambda + \mathbf{w}$
Measured input vector
$\dot{\mathbf{x}} = f(\mathbf{x}(t), \mathbf{u_m}(t))$
Aircraft Kinematic Model
$\mathbf{z_m} = h(\mathbf{x}(t), \mathbf{u_m}(t), \mathbf{v}(t))$
Observation Model
(Iterative) Extended Kalman Filter
$\hat{\mathbf{x}}$ (state estimate)
Corrected Measurements
$\mathbf{z} = h(\hat{\mathbf{x}}, \mathbf{u_m})$
Aerodynamic Parameter Estimation
Aerodynamic forces and moments
LS Parameter Estimator
Parameter estimates $\hat{\theta}$

Figure 2.2: Scheme of the Two-Step Method for Aerodynamic Model Identification

problem of extracting information from non-reliable measurements, since the observations are always contaminated with noise. Thus, the accuracy of the model also needs to be quantified, to know until what extent it is possible to trust the identified model.

To start with the parameter estimation procedure, measurements of the dependent and the independent variables should be available, and a model structure should be postulated. The model structure determination will be studied in detail in Section 2.4, and for the purpose of this chapter, it will be assumed that the model structure has already been determined.

Since both the dependent and independent variables can be measured directly, in this thesis there is no need to apply a state estimation routine (contrary to a flight test, where the forces need to be calculated afterwards). An equation-error method will be used, which assumes that the measurements of the dependent variable (the aerodynamic forces and moments) are corrupted with noise, and that the independent variables (airspeed, angle of attack, and control surface deflections) are known without error. Each observation can be described by the measurement equation:

$$\mathbf{z}(i) = \mathbf{y}(i) + \mathbf{v}(i); \qquad i = 1, 2, ..., N \tag{2.1}$$

where:

$$\mathbf{z} = \text{measurement vector, } [N \times 1] \tag{2.2}$$

$$\mathbf{y} = \text{output vector, } [N \times 1] \tag{2.3}$$

$$\mathbf{v} = \text{vector of measurement errors, } [N \times 1] \tag{2.4}$$

where N is the number of samples. In the specific case of aerodynamic parameter estimation, the measured values can be different states of the aircraft depending on the test, such as airspeed, angles of attack and sideslip, forces and moments in a wind tunnel, or accelerations in a flight test.

An estimator is a function that finds the values of the parameter vector $\hat{\theta}$ that best describe the observed model behavior, that is, the fitting of the model output to the measured data when the same inputs are applied. The estimator to construct is limited by the available information about the parameters and noise statistics. Uncertainties models can be classified into three different categories according to Schweppe[26]: Bayesian, Fisher, and Least Squares.

Both the Bayesian and Fisher models require some information about the probability density of θ and $\mathbf{v}$. If this information is available, a more detailed study can be done[27]. In general, the probability density of the parameters and the noise is unknown for aircraft system identification purposes, and so the model must be formulated according to Least-squares assumptions: θ is considered to be a vector of unknown constant parameters, and $\mathbf{v}$ is considered to be a random vector of measurement noise.

Linear-in-the-parameters models are normally used, where the parameters are considered constant with time. That does not mean that the model is linear, but that its dependence on the parameters is linear. An example is shown in Eq. (2.5).

$$y = \theta_0 + \theta_1 x_1 + \theta_2 x_1 x_2 + \theta_3 x_2^2 + ... + \theta_n x_n. \tag{2.5}$$

As it can be seen, the variable to model y (e.g. pitching moment coefficient), can be written in a way that depends linearly on the parameters θ_i but nonlinearly on the independent variables (e.g. angle of attack, angle of sideslip, pitch rate,...). Unsteady aerodynamic coefficients are not usually taken into account, since they are much more difficult to identify (sometimes impossible), and they generally lead to small differences in the model results[28].

The dependent variables to be estimated are the dimensionless aerodynamic coefficients of forces and moments in body axes. The forces and moments (and thus their dimensionless coefficients) are assumed to depend on a state vector which includes the independent variables that were varied during the tests.

$$\begin{aligned} C_X(\mathbf{x}) &= \frac{X(\mathbf{x})}{qS} & C_l(\mathbf{x}) &= \frac{L(\mathbf{x})}{qSb} \\ C_Y(\mathbf{x}) &= \frac{Y(\mathbf{x})}{qS} & C_m(\mathbf{x}) &= \frac{M(\mathbf{x})}{qS\bar{c}} \\ C_Z(\mathbf{x}) &= \frac{Z(\mathbf{x})}{qS} & C_n(\mathbf{x}) &= \frac{N(\mathbf{x})}{qSb} \end{aligned} \tag{2.6}$$

The state vector is given by: $\mathbf{x} = [\alpha, \hat{V}, \delta_1, \delta_2, \delta_3]$, where $\hat{V}$ is the wind speed normalized with a reference speed in order to avoid large differences in the magnitudes of the regressors. Of course, in a more general case, (e.g. flight test), the dependencies will include more variables, such as thrust or angular rates.

Only the coefficients related to the longitudinal motion of the aircraft (C_X, C_Z, C_m) share the same values in the half model and the complete aircraft. This is because the left and right wing contributions to these coefficients has the same sign. Regarding the lateral coefficients, the contribution of each wing have opposite sign; for instance, a positive elevon deflection of the left wing will produce a positive rolling moment, while the same deflection on the right wing will produce a negative one. From the symmetry of the aircraft is follows that the total rolling and yawing moments will be zero when no control surfaces are deflected and no sideslip is present.

Whereas the identification of the lateral-directional coefficients of a half model is not as useful as the longitudinal ones because of the absence of the sideslip term, it is possible to derive the contributions of the control surfaces, and create a model of the whole aircraft for $\beta = 0$ which has useful applications such as a calculation of the lateral-directional control powers, or to assess if the elevons could be used for yawing by differential drag, which could be used to reduce the size of the rudders at the winglets.

A complete aerodynamic identification of the half model is needed, taking into account all contributions as it was done for the longitudinal coefficients, in order to extract the useful information about the control surfaces we seek for. The rolling and yawing moment coefficients of the complete aircraft can be calculated as:

$$(C_l)_{A/C} = (C_l)_L(\alpha, \hat{V}, \delta_i^L) + (C_l)_R(\alpha, \hat{V}, \delta_i^R) \tag{2.7}$$

$$(C_n)_{A/C} = (C_n)_L(\alpha, \hat{V}, \delta_i^L) + (C_n)_R(\alpha, \hat{V}, \delta_i^R), \tag{2.8}$$

where the subscripts L, R are used to label the coefficients and control surfaces deflections of the left and right wing respectively. The rolling and yawing moments of the right wing will be same as for the left wing but in opposite sign. Since $\alpha, \hat{V}$ are equal for both wings, the only contributions that will remain are those from the control surfaces, so the expressions above can be simplified as:

$$(C_l)_{A/C} = (C_l)_L(\delta_i^L) - (C_l)_L(\delta_i^R) \tag{2.9}$$

$$(C_n)_{A/C} = (C_n)_L(\delta_i^L) - (C_n)_L(\delta_i^R) \tag{2.10}$$

which will allow to find expressions for the rolling and yawing moments for different control surfaces deflection of both wings from the estimated model from the left wing used in the wind tunnel experiments.

2.2.1 Model postulation

The model structure determination will not be treated yet, but some assumptions in the model form need to be done to start with the least squares regression. Recalling the measurement equation introduced in last section:

$$\mathbf{z}(i) = \mathbf{y}(t_i) + \mathbf{v}(i). \tag{2.11}$$

It will be assumed that N samples of the dependent variable y and the independent variables $x_1, x_2, ...x_m$ are available. If y can be written as a linear-in-the-parameters model:

$$\mathbf{y} = \theta_0 + \sum_{j=1}^{n} \theta_j \mathbf{x}_j, \tag{2.12}$$

The forces and moments coefficients will be then approximated by polynomials in the state and control variables, which may not be homogeneous, and can be of any degree. This formulation allows for the estimation of both the forces and moments in stationary and non-stationary conditions, and is valid for larger deviations from nominal conditions than its linear counterpart[22], which makes it also suitable for a more complete aerodynamic identification once dynamic data is made available from a flight test.

Eq. (2.12) can be rewritten as:

$$\mathbf{y} = X \cdot \theta; \quad X = [1, \mathbf{x_1}, \mathbf{x_2}, ..., \mathbf{x_m}], \tag{2.13}$$

where:

$$\begin{aligned} \mathbf{y} &= \text{dependent variable, } [N \times 1] \\ \theta &= \text{parameter vector, } [n \times 1] \\ X &= \text{regression matrix, } [N \times n] \\ \mathbf{x}_j &= \text{independent variables } (j = 1, 2, ..., m), \ [N \times 1] \\ \mathbf{v} &= \text{model residual vector, } [N \times 1] \end{aligned} \tag{2.14}$$

If $n < N$, the parameter vector can be estimated using least squares regression.

Polynomial models

One may change the independent variables by functions of the independent variables, allowing for nonlinear terms ($x_i \cdot x_j$, x_i^n,...), keeping a linear-in-the-parameters model, as shown before.

The dependent variable will then depend on a linear combination of functions in the state and control variables. Calling these functions (regressors) $p_j = p_j(X)$:

$$\mathbf{y} = \theta_0 + \sum_{j=1}^{n} \theta_j \mathbf{p}_j(X), \tag{2.15}$$

The new regression matrix is given by:

$$X = [1, \mathbf{p_1}, \mathbf{p_2}, ..., \mathbf{p_n}], \tag{2.16}$$

The dependent variable can be written as:

$$\mathbf{y} = \theta_0 + \sum_{j=1}^{n} \theta_j \mathbf{p}_j, \tag{2.17}$$

or:

$$\mathbf{y} = X \cdot \boldsymbol{\theta}; \qquad X = [1, \mathbf{p}_1, \mathbf{p}_2, ..., \mathbf{p}_n], \tag{2.18}$$

where $\mathbf{p}_j$ are functions of the independent variables (also called regressors), and X is the regression matrix.

As a remark, an underlying assumption with this approach is that the aerodynamic forces and moments can be approximated arbitrarily closely by a multivariate Taylor series in the independent variables. Because of this, they become inaccurate far from zero, specially for high angles of attack, as it was confirmed experimentally.

Spline models

Because of the shortcomings of polynomial models explained above, spline models were developed so that larger regions of the flight envelope could be covered with a single global model. This approach was considered after discovering model deficiencies with polynomial models when they were used for the complete range of angle of attack. The simple "+" basis function was used for the current spline implementation because its simplicity and its past good results ([29, 30, 31]. Each aerodynamic coefficient $C_a = C_X, C_Z, ...$ is modeled as follows:

$$\begin{aligned}
&C_a = C_{a0} + C_{a\alpha}(\alpha) \cdot \alpha + C_{a\delta_1}(\alpha, \delta_1) \cdot \delta_1 + C_{a\delta_2}(\alpha, \delta_2) \cdot \delta_2 + C_{a\delta_3}(\alpha, \delta_3) \cdot \delta_3 + C_{a\hat{V}}(\alpha, \hat{V}) \cdot \hat{V} \\
&C_{a\alpha}(\alpha) = \sum_{n=0}^{n_\alpha} C_{\alpha^n} \cdot \alpha^n + \sum_{l=1}^{k} C_{\alpha_l}^{d} (\alpha - \alpha_l)_+^d; \\
&C_{a\delta_i}(\alpha) = \sum_{n=0}^{n_{\delta_i}} C_{\delta_i^n} \cdot \delta_i^n + \sum_{l=1}^{k} C_{\delta_i \alpha_l} (\alpha - \alpha_l)_+^0; \quad i = 1, 2, 3 \\
&C_{a\hat{V}}(\alpha) = \sum_{n=0}^{n_V} C_{\hat{V}^n} \cdot \hat{V}^n + \sum_{l=1}^{k} C_{\hat{V}\alpha_l} (\alpha - \alpha_l)_+^0.
\end{aligned} \tag{2.19}$$

where $n_\bullet$ is the maximum degree considered of each of the regressors, k is the number of knots, and $(\alpha - \alpha_l)_+^d$ is defined as:

$$(\alpha - \alpha_l)_+^d = \begin{cases} 0 & \alpha < \alpha_l \\ (\alpha - \alpha_l)^d & \alpha > \alpha_l \end{cases} \tag{2.20}$$

A knot of degree d has C^{d-1} continuity; that is, the model has $d-1$ continuous derivatives at that knot location. The knots were placed every 3 degrees in the angle of attack to be able to model local nonlinearities where the polynomial models failed and became unstable. In order to implement the spline model, each knot is modeled as a different regressor, and such it will have its own associated estimated coefficient ($\hat{\theta}_j$).

2.2.2 Definitions

Some definitions are presented here, as they appear in [1], which will be useful later on for the discussion:

Definition 2.1 *An estimator is linear if the parameter estimates* $\hat{\theta}$ *are given by a linear function of the measurements. If* $\hat{\theta}$ *is given by a nonlinear function, the estimator will be nonlinear.*

Definition 2.2 *An estimator is said to be unbiased if its expected value is equal to the expected value of* θ *(the true value of the parameters, which is unknown). If it is not, the estimator is said to be biased.*

$$bias = \mathrm{E}[\hat{\theta}] - \mathrm{E}[\theta] \tag{2.21}$$

Definition 2.3 *An minimum square error estimator is such that minimizes the mean square error (MSE), defined by:*

$$MSE = E\left[(\hat{\theta} - \theta)^T(\hat{\theta} - \theta)\right] \tag{2.22}$$

The MSE can be divided in two different terms: a variance error (which is random), and a squared bias error (which is systematic). This topic will be studied in more detail in Section 2.4, where it will be explained how these two terms can be used to define an adequate model structure through the coefficient of determination.

Definition 2.4 *A consistent estimator is such that it converges to the true value* θ *when the number of samples* N *tends to infinity.*

$$\lim_{N\to\infty} \hat{\theta}(N) = \theta \tag{2.23}$$

Definition 2.5 *BLUE: Best Linear Unbiased Estimator. The estimator with minimum MSE within the family of linear unbiased estimators.*

It is reasonable to expect that if enough samples of a measurement are taken, they will be centered around the true value[32]. Because of this an unbiased estimator (BLUE) is usually desired.

Definition 2.6 *Cramér-Rao lower bound: minimum covariance an unbiased estimator can achieve for a certain model and dataset.*

$$\mathrm{Cov}(\hat{\theta}) = E\left[(\hat{\theta} - \theta)(\hat{\theta} - \theta)^T\right] \geq M^{-1}, \tag{2.24}$$

where M *is the so-called Fisher matrix*[33].

This bound is very useful since it provides a measure of the maximum achievable accuracy for the parameters[34]: the closer the covariance gets to the Cramér-Rao lower bound, the more “efficient” the estimator will be.

2.2.3 Ordinary Least Squares (OLS)

The least squares method was derived independently by Gauss and Legendre[33]. It is an equation-error method that minimizes a cost function that measures the deviation of the model from the data. The cost function value only depends on input-output data, so the complexity of the model does not affect the regression results[35], which makes it a suitable method for aerodynamic parameter estimation.

The Ordinary Least Squares estimator is the simplest form of Least Squares regression. Some assumptions need to be done regarding noise characteristics which may not be completely true, but as it was mentioned above, good results have been obtained in the past[19, 2, 34], and the required information to use a more complex estimator is not readily available. The following assumptions are made to derive the OLS:

- The independent variables $[x_1, x_2, ..., x_n]$ are not contaminated with noise (X is deterministic).
- The dependent variables $y(t_i)$ are contaminated with uniformly distributed noise (white noise).
- The residuals are uncorrelated with X.

If the assumptions to apply a least squares regression method are held, it can be shown that the OLS is indeed the BLUE (Best Linear Unbiased Estimator)[36], where "best" implies minimum variance (Gauss-Markov Theorem). It can also be shown that the estimates are consistent and efficient[37].

On the other hand, if these assumptions are not true, the estimates might be inaccurate, so they need to be tested to guarantee that OLS is indeed a valid estimation method. If errors are present in the independent variables the estimator will be biased[38] and the covariance of the estimates will be affected by this noise.

More general least squares methods can be derived if some information about the noise is known, such as the Weighted Least Squares (WLS) estimation or the Generalized Least Squares (GLS) estimation. No information is readily available regarding noise statistics, and it is difficult to infer it from the measured data, since no validated wind tunnel data was available to cross-check. The estimation of the noise statistics does not guarantee better results than OLS if the assumptions are only slightly violated, so it is decided to keep the model as simple as possible to better understand the results of the estimation. The assumptions will be tested after the model estimation in order to validate the regression and find model deficiencies, as it will be discussed in Section 2.3.4.

Thus, no assumptions on the probability density of $\boldsymbol{\theta}$ or $\mathbf{v}$ are done. The errors (residuals) are assumed to be zero-mean and to have a constant covariance.

$$\mathrm{E}[\mathbf{v}] = 0, \quad \mathrm{E}[\mathbf{v}\mathbf{v}^T] = \sigma^2 I \tag{2.25}$$

As a remark, the Cramér-Rao lower bound is not necessary since the OLS is the best unbiased linear estimator if these assumptions are valid (besides, it cannot be calculated because of lack of information about the probability densities). The well-known cost function for OLS and the parameter vector estimate that minimizes it are:

$$J = \frac{1}{2}[\mathbf{z} - X\boldsymbol{\theta}]^T[\mathbf{z} - X\boldsymbol{\theta}] = \frac{1}{2}[\mathbf{v}^T\mathbf{v}], \qquad \hat{\boldsymbol{\theta}} = (X^TX)^{-1}X^T\mathbf{z} \tag{2.26}$$

2.3 Analysis of the OLS estimator

An analysis of the OLS estimator will be done in order to determine its main characteristics (parameter variances and covariances, measurement error variance, correlation among regressors), along with confidence bounds for the parameters and model output.

A data collinearity review and a residual analysis are also presented here. They will be used as validation tools to assess whether the assumptions done regarding the noise, residuals, and confidence bounds are actually true. When the estimated model strongly violates the assumptions, it should be discarded since the OLS estimator is not the BLUE anymore, and their estimates will be biased, inconsistent, and inefficient.

2.3.1 Main characteristics

The covariance of the estimates is given by:

$$\mathrm{Cov}(\hat{\boldsymbol{\theta}}) = E\left[(\hat{\boldsymbol{\theta}} - \boldsymbol{\theta})^T(\hat{\boldsymbol{\theta}} - \boldsymbol{\theta})\right], \tag{2.27}$$

where the true value of the estimates is:

$$\boldsymbol{\theta} = (X^TX)^{-1}X^T\mathbf{y}, \tag{2.28}$$

since $\mathbf{y}$ is defined as the real value of the variable to model. The covariance of the estimates can be regarded as a measure of the sensitivities of the parameters to the noise. Introducing the values of $\boldsymbol{\theta}$,

$\hat{\boldsymbol{\theta}}$, and the noise statistics in Eq (2.27) and rearranging terms, the final expression for the covariance is:

$$\mathrm{Cov}(\hat{\boldsymbol{\theta}}) = (X^T X)^{-1} X^T E\left[\mathbf{v}\mathbf{v}^T\right] X (X^T X)^{-1} \underset{\underset{E\left[\mathbf{v}\mathbf{v}^T\right] = \sigma^2 I}{\uparrow}}{=} \sigma^2 (X^T X)^{-1}. \tag{2.29}$$

The measurement error variance σ^2 is unknown and needs to be estimated from the measured data. An unbiased but model dependent estimate for σ^2 can be found based on the residuals:

$$\hat{\sigma}^2 = \frac{\sum\limits_{i=1}^{N} [z(i) - \hat{\mathbf{y}}(i)]^2}{N - n} = s^2, \tag{2.30}$$

which will only give adequate results if the model structure is adequate[38].

A matrix D may be defined which helps to rewrite the expressions for parameter variances and covariances:

$$\begin{aligned} &D = (X^T X)^{-1} = [d_{jk}], \quad j, k = 1, 2, ..., n \\ &\mathrm{Var}(\hat{\theta}_j) = \sigma^2 d_{jj}, \qquad \mathrm{Cov}(\hat{\theta}_j, \hat{\theta}_k) = \sigma^2 d_{jk}. \end{aligned} \tag{2.31}$$

Now it is possible to define the correlation coefficient r_{jk}, which measures the pairwise correlation between $\hat{\theta}_j$ and $\hat{\theta}_k$:

$$r_{jk} = \frac{\mathrm{Cov}(\hat{\theta}_j, \hat{\theta}_k)}{\mathrm{Var}(\hat{\theta}_j)\mathrm{Var}(\hat{\theta}_k)} = \frac{d_{jk}}{\sqrt{d_{jj} d_{kk}}} \tag{2.32}$$

A value of $|r_{jk}|$ close to 1 means that a linear relation exists between both parameters $\hat{\theta}_j, \hat{\theta}_k$ or between their associated regressors $\mathbf{p}_j, \mathbf{p}_k$.

The so-called prediction matrix K maps the measured outputs to the estimated outputs and will be useful to define the output confidence bounds:

$$\hat{\mathbf{y}} = X\hat{\boldsymbol{\theta}} = K\mathbf{z}; \quad K = X(X^T X)^{-1} X^T, \tag{2.33}$$

2.3.2 Confidence bounds

Additionally, the noise can be assumed to follow a Gaussian (normal) distribution:

$$\mathbf{v} = \mathcal{N}\left[0, \sigma^2 I\right] \tag{2.34}$$

Since a linear function of a Gaussian variable will also be Gaussian, it follows that the parameters and the output will also be given by a Gaussian distribution:

$$\hat{\boldsymbol{\theta}} = \mathcal{N}\left[\theta, \sigma^2 (X^T X)^{-1}\right], \qquad \hat{\mathbf{y}} = \mathcal{N}\left[\mathbf{y}, \sigma^2 K\right]. \tag{2.35}$$

Confidence bounds for the parameters and the output can be derived based on the normality of the residuals, which needs to be tested in order to trust the derived bounds. In addition, by making this assumption the OLS also becomes the maximum-likelihood estimator[38].

Parameters confidence bounds

To define a confidence interval one needs to use the statistics:

$$t = \frac{\hat{\theta}_j - \theta_j}{\sqrt{\sigma^2 d_{jj}}}, \tag{2.36}$$

which is a t-distribution with $N - n$ degrees of freedom. It is possible to define a $100(1 - \alpha)$ percent confidence interval for each estimate $\hat{\theta}_j$. A 95% confidence level is a typical value and is given by $\alpha = 0.05$.

$$\hat{\theta}_j - t(\alpha/2, N - n)\sqrt{(\sigma^2 d_{jj})} \leq \theta \leq \hat{\theta}_j + t(\alpha/2, N - n)\sqrt{(\sigma^2 d_{jj})} \tag{2.37}$$

Output confidence bounds

The estimated output at each data point is given by:

$$\hat{y}(i) = \mathbf{x}^T(i)\hat{\boldsymbol{\theta}}, \tag{2.38}$$

where $\mathbf{x}^T(i)$ is the ith row of the regression matrix X. It contains the values of the regressors $\mathbf{p}_j(i)$, which depend directly on the independent variables. The variance of the estimated output can be calculated:

$$\mathrm{Var}\left[\hat{y}(i)\right] = \mathrm{E}\left[(\hat{y}(i) - y(i))(\hat{y}(i) - y(i))^T\right] = \sigma^2 \mathbf{x}^T(i)(X^T X)^{-1}\mathbf{x}(i). \tag{2.39}$$

Since the values of the independent variables are known for each data point, the confidence interval for the estimated output of the model $\hat{\mathbf{y}}$ can also be calculated at each data point. The $100(1-\alpha)$ confidence for the output is:

$$\hat{y}(i) - t(\alpha/2, N-n)\sqrt{\mathrm{Var}\left[\hat{y}(i)\right]} \leq y(i) \leq \hat{y}(i) + t(\alpha/2, N-n)\sqrt{\mathrm{Var}\left[\hat{y}(i)\right]} \tag{2.40}$$

Predicted output confidence bounds

The model may also be used as a predictor, to estimate the model output for a certain set of values of the independent variables. One must take into account that the predicted values may not be accurate if the values of the independent variables are outside the so called *convex data hull.* This region is the region of validity of the model, where interpolation is allowed[38]. Extrapolation must be done with caution, since the real system might change radically its behavior outside of the estimation dataset, and this behavior will not be captured, leading to large innacuracies.

Assume that a new measurement is done $z(i)$ with $\mathbf{x}(i)$ the values of the independent variables for that data point. The prediction error variance is:

$$\mathrm{Var}\left[z(i) - \hat{y}(i)\right] = \mathrm{E}\left[(z(i) - \hat{y}(i))(z(i) - \hat{y}(i))\right] = \sigma^2\left[1 + \mathbf{x}^T(i)(X^T X)^{-1}\mathbf{x}(i)\right], \tag{2.41}$$

which is a combination of the variance of the estimated output plus the measurement error variance σ^2. With this value it is possible to define again a $100(1-\alpha)$ confidence interval for the predicted output:

$$\hat{y}(i) - t(\alpha/2, N-n)\sqrt{\mathrm{Var}\left[z(i) - \hat{y}(i)\right]} \leq y(i) \leq \hat{y}(i) + t(\alpha/2, N-n)\sqrt{\mathrm{Var}\left[z(i) - \hat{y}(i)\right]} \tag{2.42}$$

2.3.3 Data collinearity

From Eq. (2.26), it can be seen that the matrix $X^T X$ needs to be inverted to calculate the parameter estimates. If this columns of X are linearly dependent, $X^T X$ will not be full rank and the inverse will not exist. In practice, this extreme situation is not that common; instead, the columns of X may exhibit *near linear dependence.* This translates into the matrix $X^T X$ being ill-conditioned, and numerical innacuracies can occur when calculating its inverse: the most important effects are larger absolute values of the parameters and larger parameter variances and covariances[38].

The main sources of collinearity in aircraft system identification are according to Klein[19]: 1) the *experiment design*, when it only covers a small region of the design space, 2) *constraints in the data*: when the independent variables affect each other (e.g. with an Automatic Flight Control System), and 3) an *inadequate model structure*, when regressors are near linearly dependent.

The first two sources of collinearity were avoided by exploring the largest possible range of the independent variables in an independent manner and randomizing the test conditions, and the last one will be addressed in Section 5.2.1.

Three collinearity indicators were used in this work: correlation indices, Variance Inflation Factors (VIF), and the SVD decomposition of the regression matrix.

The off-diagonal terms in the correlation matrix r_{jk} indicate whether $\mathbf{p}_j$ and $\mathbf{p}_k$ are linearly related. If $|r_{jk}| = 1$, there is an exact linear dependency between them. 0 indicates that the regressors are linearly independent, or *orthogonal.* Note that the inspection of this quantities only gives information about the pair-wise collinearity, which may not invalidate completely a model.

The Variance Inflation Factors (VIF) are given by the diagonal elements of $D = (X^T X)^{-1}$, d_{jj}, which measure the multicollinearity of the jth regressor $\mathbf{p}_j$ with the $n-1$ remaining regressors.

$$\mathrm{VIF}(\hat{\theta}_j) = d_{jj}, \quad j = 1, 2, ..., n \tag{2.43}$$

The VIFs also serve as a measure of how bigger the confidence interval for the parameters is because of multicollinearity[38]:

$$\frac{L_j}{L^*} = \sqrt{d_{jj}}, \quad j = 1, 2, ..., n \tag{2.44}$$

where L_j is the length of the confidence interval for the *jth* estimate and L^* is the length of the corresponding interval if an orthogonal reference design is chosen.

Finally, the SVD decomposition of X is also suggested to detect collinearity[39]:

$$X = U \Sigma V^T, \tag{2.45}$$

where U is a $[N \times n]$ unitary matrix and V is a $[n \times n]$ matrix, also unitary ($UU^T = VV^T = I$). When this specific decomposition is done, the matrix Σ is a $[n \times n]$ matrix with the so-called *singular values of* X in the main diagonal.

$$\mu_j = \Sigma_{jj}, \quad j = 1, 2, ..., n \tag{2.46}$$

The singular values μ_j are the square roots of the eigenvalues of $X^T X$. One can define a *condition index* for each of the parameters:

$$\eta_j = \frac{\mu_{max}}{\mu_j}. \tag{2.47}$$

The largest value for η_j is the condition number of $X^T X$. Klein suggests in [19] that condition indices from 30 to 100 indicate moderate to severe multicollinearity.

It is worth noting that the collinearity analysis is usually done with standardized regressors so that the magnitudes of the different regressors do not influence the results. Standardization removes the mean of the regressors and the dependent variable and scales them to unit length. This also removes the bias from the regressors, since the mean of the standardized dependent variable becomes zero.

In the present work it was decided not to work with standardized regressors for the estimation since they were already of the same order of magnitude (~ 1), and only the scaling to unit length was done to assess collinearity in order to keep the bias term in the model.

Biased estimation techniques

A remark should be done here to biased estimation techniques. In certain situations (for instance, when data collinearity is present) a biased estimator might offer a better result than the OLS estimator. Gauss-Markov Theorem states that the least squares regression will find the best unbiased linear estimator (BLUE) if the necessary conditions for least squares are held, as it was already explained. However, that does not mean that there cannot be a better *biased* estimator (with a smaller variance). Similarly, the Cramér-Rao lower bound previously defined only applies to unbiased estimators. That is, a biased estimator might achieve a lower variance than the Cramér-Rao lower bound.

A technique called Principal Components Regression (PCR) is considered in the present thesis, which has been used previously in the past[40], achieving good results. It transforms the estimation problem to the space of orthogonal regressors, where the eigenvalues that are close to zero, which are responsible for the ill-conditioning of the matrix $X^T X$ can be detected. Another estimation in the new orthogonal space will be done, removing the eigenvalues below a certain threshold. This removes some information from the model, but also avoids collinearity problem and leads to better parameter variances. For this reason, PCR was applied to some of the estimated spline models after some collinearity problems were found, and the results will be discussed in Chapter 5.

2.3.4 Residual analysis

The residual vector, given by the difference between the measured variable and the model output, can be considered as a vector with samples of the measurement errors $v(i)$. For the derivation of the OLS, it was assumed that the errors contaminating the measurements are zero mean, with constant covariance, and uncorrelated with X, so the residuals should behave the same way if the model is adequate.

With a careful analysis of the residuals, violations of these assumptions can be spotted, and also corrected. The zero mean assumption follows from the expansion of $\mathrm{E}\left[\mathbf{v}\right]$ and does not need further attention[1]. The residual vector is given by:

$$\mathbf{v} = \mathbf{z} - \hat{\mathbf{y}} = \mathbf{z} - X\hat{\boldsymbol{\theta}}, \quad i = 1, 2, ..., N \tag{2.48}$$

A plot may be done to detect model deficiencies: the residuals plotted against the estimated output $\hat{\mathbf{y}}$, which should form a random pattern, without showing any *deterministic content*. If deterministic content is present, it might be a signal of an unmodeled effect, or in other words a modeling error, as follows from the previous equation.

On the other hand, the normality assumption of the residuals was needed to establish the confidence bounds. A common test is to plot the sorted residuals against the Inverse Cumulative Probability Distribution Function[38] (ICDF). This plot should resemble a straight line if the residuals are normally distributed as it was assumed, although small deviations are often accepted since their effects are not so critical. The central part is more important that both ends: deviations from the straight line can also indicate the presence of outliers in the data and should not completely invalidate the estimation.

The probabilities $P(i)$ at which one should calculate the inverse cumulative probability distribution are given by:

$$P(i) = \frac{1}{N}\left(i - 1/2\right), \quad i = 1, 2, ..., N \tag{2.49}$$

The Anderson-Darling and Kolmogorov-Smirnov statistical tests were also used as a double check for the normality assumption of the residuals.

2.4 Model structure determination

Up to this point, it was assumed that the model structure, that is, the functions (regressors) $\mathbf{p}_j$ that define the regression matrix, was known. However, they also need to be determined since the result of the estimation differs greatly from one model structure to another. An adequate model structure, according to Murphy[34], is such that 1) sufficiently fits the data, 2) allows for a successful parameter estimation, and 3) has good prediction capabilities.

The Stone-Weierstrass approximation theorem states that every continuous function defined in a closed interval can be uniformly approximated by a polynomial[41], so one could think that the continuous addition of regressors is a solution to get an arbitrarily close fit to the measured data. Nevertheless, certain choices of regressors are more convenient than others (for example, to avoid data collinearity problems).

The number of parameters should be kept as small as possible because large numbers of regressors lead to overparameterization issues; the residual between the model and the measurements always decreases with the addition of regressors, so the model fit to the data always improves. However, noise and outliers will eventually enter the model, which is obviously not desired, since it degrades the prediction capabilities of the model. Usually, the *principle of parsimony* is applied to determine a good model structure: “given a model with equal residual variances, choose the model with fewer parameters”[34].

A remark should be done here: this work deals with the creation of a *phenomenological model*, that is, a model that explains the observed phenomena (measurements of the forces and moments) in terms of the measured independent variables. Some of the terms might not have a direct physical meaning, but just predict the measured variables in a satisfactory way.

2.4.1 Modified Stepwise Regression

Stepwise regression is a well known iterative statistical technique used to determine an adequate model structure given a dependent variable an a predefined pool of regressors[38], which has been successfully used in the field of aerodynamic model identification[30, 29, 42, 43].

The core of the model structure determination routine is the Modified Stepwise Regression (MSR) as it is presented by Klein et al.[3]. Usual stepwise regression relies only in statistical metrics to select the regressors to enter and leave the model, but experience shows that this leads to a large number of terms in the model, which increases overfitting and worsens the prediction capabilities. A user-guided selection will be done, and priority will be given to regressors that carry some useful meaning (e.g. $C_{m\alpha}$) and to regressors of lower degrees (that is, α^2 before α^7). For the spline models, the Modified Stepwise Regression identifies the most statistically significant knots and polynomial terms.

The model selection process starts by including the bias in the model, and then steps 1-4 are repeated at every iteration:

1) Forward selection step

The correlations of each of the regressors with the dependent variable are calculated:

$$r_{jz} = \frac{(\mathbf{p}_j - \bar{\mathbf{p}}_j)^T(\mathbf{z} - \bar{\mathbf{z}})}{\sqrt{S_{jj}S_{zz}}}, \tag{2.50}$$

where $S_{jj} = (\mathbf{p}_j - \bar{\mathbf{p}}_j)^T \cdot (\mathbf{p}_j - \bar{\mathbf{p}}_j)$ and $S_{zz} = (\mathbf{z} - \bar{\mathbf{z}})^T \cdot (\mathbf{z} - \bar{\mathbf{z}})$. The partial F-statistic of each of the regressors is also calculated: all regressors are added individually to the model from the previous iteration (the initial model includes just the bias term), and a separate regression is performed for each model. The partial F-statistic (F_p) for each regressor $\mathbf{p}_j$ is given by:

$$(F_p)_j = \frac{\theta_j^2}{\text{Var}\left[\theta_j\right]}, \quad j = 1, 2, ..., n \tag{2.51}$$

A high value of the correlation index (in absolute value) and of the partial F-statistic indicate that the addition of the regressor is statistically significant to the model and that the variance will be reasonably small compared to its value (and so the confidence bounds), so these two factors were used to decide whether a regressor should enter the model at a certain iteration. As a remark, in an orthogonal framework both criteria will point to the same regressor at each iteration.

2) Backward elimination step

All regressors are evaluated in terms of their partial F-statistic (with the new regressor already included in the model). If the F_p of the least significant regressor is below a certain threshold, it can be removed to keep the model as simple as possible.

3) Definition of new variables

Finally, the residuals from this model are found, and a new dependent variable is constructed subtracting the output of the model to the original dependent variable:

$$\mathbf{z}^* = \mathbf{z} - X_k\hat{\boldsymbol{\theta}}_k, \tag{2.52}$$

where X_k and $\hat{\boldsymbol{\theta}}_k$ are the regression matrix and the parameter vector of the model at the kth iteration. The next correlations will be calculated with this new dependent variable, in order to focus on the characteristics that have not been modeled yet (represented by the residuals at each iteration).

In addition, if the original regressors were not orthogonal, new regressors $\mathbf{p}_j^*$ can be constructed by finding the residuals of $\mathbf{p}_j$ $(j = 2, 3, ..., n)$ after regressing them on X_k. This step orthogonalizes the remaining regressors in the pool with respect to the regressors already in the model, which reduces collinearity.

4) Model analysis

At the end of each iteration, a complete model analysis (covariances, correlations, collinearity, residuals) is done in order to evaluate each model's performance later on and select the best one.

The stepwise regression routine stops when no more regressors are available or when the remaining regressors are not significant enough to be included.

2.4.2 Regressors orthogonalization

Since only 5 independent variables can be used to construct the regressors (wind speed, angle of attack, and the deflections of the 3 control surfaces), the pool of regressors needs to be defined with combinations of these regressors up to different degrees, such as $\alpha^p, V^p, \alpha^p \cdot \delta_i^q, ...$. It is easy to see that with such a model, collinearity problems will arise soon during the model structure determination routine, leading to the ill-conditioning of $(X^T X)^{-1}$, which will worsen the accuracy of the estimation.

For this reason, it was decided to use an orthogonal framework for the estimation to completely remove any collinearity problems: if the columns of X (the regressors) are orthogonal, $X^T X$ will be a diagonal matrix and its inverse will not suffer from ill-conditioning.

Two different approaches were considered: the iterative orthogonalization of the regressors during the stepwise regression (already mentioned in the previous section), and the definition of an orthogonal pool of regressors beforehand. The iterative orthogonalization consists on 1) perform a regression on X_k of the regressors that are not in the model, and 2) subtract the component of each regressor that is in the direction of the regressors in the model. Thus, the orthogonal regressors $\boldsymbol{\xi}_j$ are given by:

$$\boldsymbol{\xi}_j = \mathbf{p}_j - X_k \cdot \hat{\boldsymbol{\beta}}, \qquad \hat{\boldsymbol{\beta}} = (X_k^T \cdot X_k)^{-1} X_k^T \cdot \mathbf{p}_j \tag{2.53}$$

This technique, although simple to implement, presents some difficulties to de-orthogonalize in order to recover the dependencies in terms of the original regressors, which have physical meaning. For this reason, the creation of an orthogonal pool of regressors proposed by Morelli and DeLoach[44] was used, which is based on a Gram-Schmidt orthogonalization procedure and allows for an easy de-orthogonalization. Starting from the bias term ($\mathbf{p}_0 = \boldsymbol{\xi}_0 = \mathbf{1}$), all regressors are successively orthogonalized with respect to the previous ones. The jth orthogonal function is given by:

$$\boldsymbol{\xi}_j = \mathbf{p}_j - \sum_{k=0}^{j-1} \gamma_{kj} \boldsymbol{\xi}_k; \quad \gamma_{kj} = \frac{\boldsymbol{\xi}_k^T \mathbf{p}_j}{\boldsymbol{\xi}_k^T \boldsymbol{\xi}_k}, \qquad j = 1, 2, ..., n \tag{2.54}$$

Arranging the indices γ_{kj} in an upper-triangular matrix G as follows:

$$G = \begin{bmatrix} 1 & \gamma_{01} & \gamma_{02} & \cdots & \gamma_{0n} \\ 0 & 1 & \gamma_{12} & \cdots & \gamma_{1n} \\ 0 & 0 & 1 & \cdots & \gamma_{2n} \\ \vdots & \vdots & \vdots & \ddots & \vdots \\ 0 & 0 & 0 & \cdots & 1 \end{bmatrix}, \tag{2.55}$$

one can express the orthogonal regressors (now the columns of the regression matrix X, to keep the same notation) in terms of the original regressors (columns of X_0) as:

$$X = X_0 \cdot G^{-1}; \qquad X = [\boldsymbol{\xi}_0, \boldsymbol{\xi}_1, ..., \boldsymbol{\xi}_n], \quad X_0 = [\mathbf{p}_0, \mathbf{p}_1, ..., \mathbf{p}_n] \tag{2.56}$$

The use of orthogonal regressors certainly offers several advantages besides the disappearance of collinearity, as it is shown by Morelli[2]: since the regressors are orthogonal, the regression equations are decoupled, and the parameter estimate for the jth regressor only depends on itself and the dependent variable:

$$\hat{\theta}_j = \frac{\boldsymbol{\xi}_j^T \mathbf{z}}{\boldsymbol{\xi}_j^T \boldsymbol{\xi}_j} \tag{2.57}$$

In addition, the reduction of the cost function (defined in Eq. (2.26)) due to each regressor can be calculated separately and will be used as an additional variable to select the regressors to enter the model:

$$J_j = -\frac{1}{2}\, \theta_j^2 (\boldsymbol{\xi}_j^T \boldsymbol{\xi}_j); \qquad j = 1, 2, ..., n \tag{2.58}$$

2.4.3 Metrics and variables for model selection

In some references where Multivariate Orthogonal Functions were used[2, 45, 46] an automatic model selection process was used, based on a single metric, the so-called Predicted Square Error (PSE), and including regressors in order of greatest to smallest reduction of the cost function (Eq. (2.58)). Nevertheless, in the present work it was decided to keep a user-guided selection and to base the model selection decision on more metrics, since it was found experimentally that the mentioned procedure did not always lead to the best model, and some of the terms that provided the greatest reductions of the cost function were high degree terms which 1) stopped some regressors which carried physical meaning from entering the model 2) had higher variances which worsened the estimation compared to different choices of regressors. The overall fit to the data was assessed with the relative Root Mean Square error (RMS$_{rel}$), normalized with the difference between the maximum and minimum values of the variable being estimated. A value of 1 indicates that the error is of the order of magnitude of the range of the dependent variable.

$$\mathrm{RMS}_{rel}(\mathbf{v}) = \frac{\sqrt{\frac{1}{N}\sum_{i=1}^{N}\mathbf{v}(i)^2}}{|\max(\mathbf{z}) - \min(\mathbf{z})|}. \tag{2.59}$$

Morelli suggests in [2] to use the Predicted Square Error as an useful metric for model selection, based on the work of Barron[47]. It measures the model fit through the Mean Square Error (the square of the RMS), and includes an overfit penalty which increases linearly with the number of regressors in the model n:

$$PSE = \underbrace{\frac{1}{N}\sum_{i=1}^{N}\mathbf{v}(i)^2}_{\text{Mean Square Error}} + \underbrace{\hat{\sigma}^2_{max}\frac{n}{N}}_{\text{Overfit penalty}} \tag{2.60}$$

The value of $\hat{\sigma}_{max}$ needs to be estimated from the data. Barron proposes in the same reference an estimate which is independent of the model structure:

$$\sigma^2_{max} = \frac{1}{N}\sum_{i=1}^{N}(\mathbf{z}(i) - \bar{z})^2 \tag{2.61}$$

The well-known coefficient of determination R^2 is also used, which measures the proportion of the variation explained by the terms other than the bias[48] :

$$R^2 = 1 - \frac{\sum_{i=1}^{N}\mathbf{v}(i)^2}{\sum_{i=1}^{N}(\mathbf{z}(i) - \bar{z})^2} \tag{2.62}$$

Finally, the overall statistical significance of the regression is measured with the F-statistic:

$$F = \frac{N-n}{n-1}\cdot\frac{R^2}{1-R^2} \tag{2.63}$$

High values of both the F-statistic and the coefficient of determination are indicators of good model quality. In addition, a residual analysis for each model is done to guarantee that the assumptions made for the OLS estimation are consistent.

2.5 Chosen approach and motivation

The approach presented here was chosen because it combines the benefits from different model structure determination techniques to find an adequate model of the Flying V. Stepwise regression finds the strongest correlations between the regressors and the dependent variable, leading to parsimonious models with good prediction capabilities. In addition, it allows for the use of both polynomial and splines, which is a good starting point, since before the identification there was little information about the complexity of the aerodynamics and the approximation power it would require. On the other hand, the generation of Multivariate Orthogonal Functions leads to smaller variances and tighter confidence bounds for the parameters and the model output by removing the collinearity from the regressors, which allows models with a large number of regressors to keep small parameter variances and good prediction capabilities.

Since there are no previous models or simulations to which it can be compared, the validation needs to be performed statistically, by means of residual analysis, model fit, metrics for model quality, and analysis of the parameters variances and sensitivities. A global model inspection of the model from the flight mechanics point of view will be done afterwards, in order to ensure the control and stability derivatives are as it is expected from conventional aircraft typical values, or to report any significant change with respect to them.

2.6 Actuators identification

The actuators are considered to be Linear-Time-Invariant systems, or LTIs. This allows for the application of many powerful available methods to estimate their response. 3 approaches were considered: a linear and a nonlinear regression considering the actuator a first-order lag model with dead time; and ARMAX (AutoRegressive Moving Average with eXternal model inputs) models included in the System Identification Toolbox from MATLAB, which are higher order models. Two kind of input commands were used, doublets and “3211” inputs: the doublets formed the estimation dataset, and the 3211 inputs the validation one.

2.6.1 First-order lag with dead time (step response)

The first-order model with dead time is based on the following equation:

$$\tau\frac{\mathrm{d}y(t)}{\mathrm{d}t} = y(t) + K \cdot u(t - t_d), \tag{2.64}$$

where:

$$\begin{aligned} u &= \text{input command} \\ y &= \text{output} \\ t_d &= \text{dead time} \\ \tau &= \text{time constant} \\ K &= \text{gain} \end{aligned}$$

If the control step is applied at $t = t_c$ (known):

$$y(t,\theta) = y_0 + K\left(1 - \exp\left(\frac{-(t - t_c - t_d)}{\tau}\right)\right), \quad t \geq t_c + t_d \tag{2.65}$$

$$y(t,\theta) = y_0, \qquad t \leq t_c + t_d \tag{2.66}$$

where θ is again the parameter vector to estimate: $\theta = [y_0, K, \tau, t_d]^T$.
If τ and t_d can be calculated, one can isolate their influence:

$$y_1(t, t_c, t_d, \tau) = 1 - \exp\left(\frac{-(t - t_c - t_d)}{\tau}\right), \quad t \geq t_c + t_d$$

$$y_1(t, t_c, t_d, \tau), = 0, \qquad t \leq t_c + t_d$$

Linear regression can now be applied: defining: $\theta = [y_0, K]$, $\Phi = [1, y_1]$,

$$y(t,\theta) = y_0 + K \cdot y_1(t, t_c, t_d, \tau) \longrightarrow y(t,\theta) = \Phi \cdot \theta, \tag{2.67}$$

and the best estimate is given by: $\hat{\theta} = (\Phi^T \Phi)^{-1} \Phi^T z$, where z is the measured output.

To calculate τ and t_d, we can define a loss function $V = \sum_{i=1}^{N} \left[z(t_i) - \hat{y}(t, \tau, t_d)\right]^2$ to be evaluated for different values of τ and t_d, since their estimated ranges will be known. This process can be summed up as:

1) Guess τ and t_d
2) Calculate y_1
3) Calculate regression model ($\hat{\theta} = (\Phi^T \Phi)^{-1} \Phi^T z, \quad \hat{y} = \Phi \cdot \hat{\theta}$)
4) Calculate loss function
5) Iterate until a minimum of the loss function is found

2.6.2 First-order lag with dead time (nonlinear regression)

For the linear regression to work, one needs to focus just on the step response (either step up or down), or define multiple linear regression problems for each ramp up and ramp down in the estimation and validation dataset. However, if the differential equation that describes the first order model can be solved numerically, an optimization routine can be define to find a minimum of the loss function, which allows to fit any kind of input/output data, not just the step response (Figure 2.3). The parameter vector for the optimization would still be given by: (y_0, K, τ, t_d).

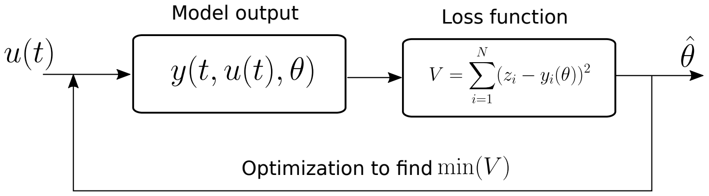
Model output
Loss function
$u(t)$
$y(t, u(t), \theta)$
$V = \sum_{i=1}^{N} (z_i - y_i(\theta))^2$
$\hat{\theta}$
Optimization to find $\min(V)$

Figure 2.3: Nonlinear regression scheme

2.6.3 ARMAX models

One technique that seems specially suitable for the case when the model structure is unknown is the estimation of an ARMAX model structure, which postulates that the output will depend on the input, on its own lagged value, and on a certain noise corrupting the measurements[25]. It postulates a model given by the following equation:

$$\begin{aligned} A(q)y(t) &= B(q) \cdot u(t - \tau_d) + C(q)v(t), \\ A(q) &= 1 + a_1 \cdot q^{-1} + a_2 \cdot q^{-2} + ... + a_{n_a} \cdot q^{-n_a}, \\ B(q) &= b_1 \cdot q^{-1} + b_2 \cdot q^{-2} + ... + b_{n_b} \cdot q^{-n_b+1}, \\ C(q) &= 1 + c_1 \cdot q^{-1} + c_2 \cdot q^{-2} + ... + c_{n_c} \cdot q^{-n_c}, \end{aligned} \tag{2.68}$$

where y is the output, u is the input, v is the measurement error, q is the delay operator, and a_i, b_j, c_k the parameters to be estimated, which define the matrices A, B, and C. τ_d is the dead time, a delay between the input and the start of the response. n_a is the number of poles, n_b is equal to the number of zeros plus one, n_c is the number of coefficients of the matrix C, and n_k the dead time in number of samples before the input affects the response.

Kraus et al.[49] propose a model order of 4 for the ARMAX model for DC servos according to its physical description (the response, and thus, the model structure will depend on the internal wiring of the servo and on the internal controller). Different model orders were tried for the estimation, and it was indeed confirmed that the model order of 4 ($n_a = n_b = n_c = 4$) offered the best results.

MATLAB command *armax* was used for the estimation, which finds the parameter estimates by minimizing a prediction error criterion using an iterative search algorithm.

Chapter 3

Experiment Description

The data for the present work come from a series of wind tunnel tests done in January 2019. A 4.6%-scaled half model of the Flying V was used during these tests, built by a small team which the author was part of. The wind tunnel test campaign was split in two: 1) static tests where the main focus was on the static aerodynamic forces and moments for the aerodynamic model identification, and 2) tests for a system identification of the actuators.

The limited availability of the wind tunnel conditioned the test to a large extent: it was not possible to implement the engine and winglet, and due to the time constraints of the MSc. thesis they had to be left out of the study. Nevertheless, the methodology for the aerodynamic identification used herein does not depend on the aircraft configuration, and can be used again once these components are assembled to estimate their contributions.

A description of the wind tunnel model and the scaling effects is given in Section 3.1, a description of the model setup is presented in Section 3.2, the steps taken to design the controller and Data Acquisition System (DAQ) for the control surfaces are explained in Section 3.3, and the instrumentation is briefly discussed in Section 3.4.

3.1 Wind tunnel model and scaling effects

A 4.6% scaled glass fiber model was built from scratch using Resin Liquid Infusion (RLI) with epoxy resin as the main manufacturing technique. The skin was infused using negative moulds of the outer shape of the aircraft, with 165 g/m^2 glass fiber and including foam panels (Airex C70.75) between ribs and spars to increase the bending stiffness. Ribs and spars were waterjet cut from a previously infused large sandwich panel using Depron foam and 300 g/m^2 glass fiber. The final assembly of all parts was done with different epoxy glues, using the moulds and the CAD model for reference. Once properly glued, the outer skin for the control surfaces was cut from the aircraft skin and the control surfaces were manually manufactured using sandwich panel spars and balsa wood ribs. A control and measurement system for the control surfaces also had to be developed, and will be presented in detail in Section 3.3. A picture of the wind tunnel model manufacturing is shown in Figure 3.1(a), and the final model assembled to the balance connection is shown in Figure 3.1(b), where the inspection holes have been left open to show the electronics inside.

The effects of scaling can be studied through dimensional analysis. Wolowicz et al.[50] show that neglecting elastic deformations the aerodynamics depend on six dimensionless numbers: Froude, Reynolds, Mach, Strouhal, the relative density factor and the relative moment of inertia. It is common to neglect elastic deformations for wind tunnel models because of their usual higher stiffness, and in certain regimes some other dimensionless numbers can be neglected because of their small effects.

Mach number effects can be neglected since this work focuses on the low speed characteristics of the Flying V: the maximum speed in the tests was 30 m/s, so compressibility effects are assumed to be small. Strouhal number effects will also be neglected, since no oscillatory perturbations are expected during the tests.

Regarding Reynolds number, when small scaling factors are chosen it is difficult (usually impossible) to match the very large full-scale Reynolds number. Cryogenic facilities are required to decrease the viscous forces and achieve the required Reynolds number for total similarity[50]. It follows that

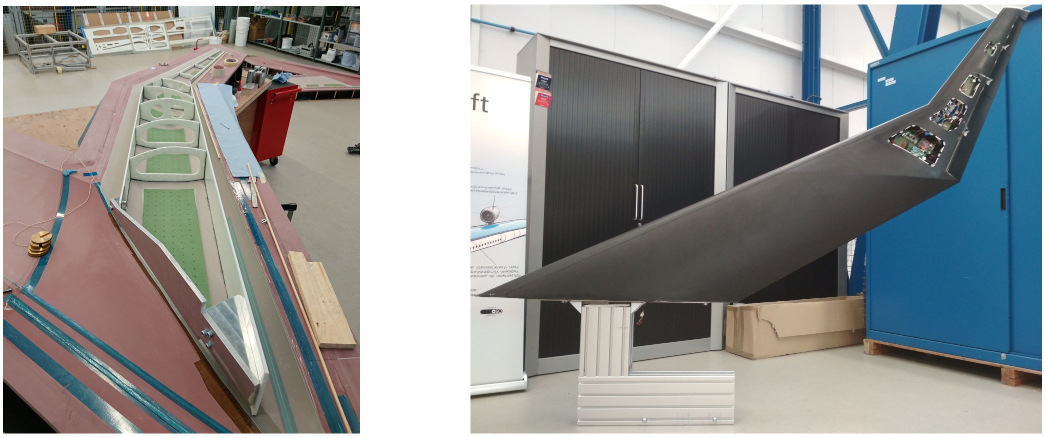

(a) Wind tunnel model manufacturing (b) Wind tunnel model with balance connection

Figure 3.1: Pictures of the wind tunnel model

Reynolds number effects are unavoidable for sub-scale flight testing and for the present wind tunnel test.

Froude number governs inertial and gravitational effects, and it is the required scaling law for sub-scale dynamic testing. If the relative density factor and the relative moment of inertia are the same as in the full-scale aircraft, a Froude scaled model can be used to predict the full-scale rigid-body modes. Since Reynolds number cannot be matched for the sub-scale test, discrepancies are expected with respect to the full-scale characteristics.

A thorough description and classification of the aerodynamic scale effects to be expected can be found in Haines[51], and is briefly summarized here:

- **Differences in geometry**: model fidelity and aeroelasticity effects are not direct Reynolds number effects, but they cause an appreciable effect in the results when the differences in Reynolds number are large.
- **Pseudo-Reynolds number effects**: effects that could be mistakenly identified as Reynolds number effects but in fact have other different sources. Some examples are: wind tunnel calibration, wall interference effects, transition location, surface finish, or model accuracy.
- **Reynolds number effects**: these are those effects which are directly caused by the different Reynolds number used in the test, that is, changes in the boundary layer, the wake, and the pressure distribution.

Other additional discrepancies will exist, such as the effects of the different response speed of the sub-scale actuators with respect to the full-scale ones, but they are not treated here since only the static aerodynamics were studied in the conducted wind tunnel test.

A first attempt to minimize the aforementioned effects was done by building a half wind tunnel model and choosing the largest scaling factor according to the wind tunnel size. The already mentioned scaling factor $n_s = 4.6\%$ was chosen in order to get a 25 kg model given by the Froude scaling law:

$$m_{model} = m_{fullscale} \cdot n_s^3 \cdot \frac{\rho_{model}}{\rho_{fullscale}} \tag{3.1}$$

Since the full-scale aircraft will always fly at higher altitudes than the sub-scale model, the minimum value for $\rho_{model}/\rho_{fullscale}$ happens when both altitudes (and air densities) are equal, which will give the maximum possible scaling factor for a given model mass.

Assuming that the Flying V will have a take-off weight 2% less than the Airbus A350-900[11], the selected scaling factor for $\rho_{model}/\rho_{fullscale} = 1$ yields a model mass of 25 kg, which is the maximum permitted weight by the current drone regulation in the Netherlands, country where this study was done. Since for the Froude scaling it was assumed that both altitudes were equal, the study will focus on the low altitude characteristics of the Flying V because of the model limitations and regulations.

Another important factor to minimize the discrepancies between the sub-scale and full-scale characteristics is to have the same nature of the boundary layer, which for the full-scale aircraft will be fully turbulent. Trip strips were placed in both the upper and lower surface of the wing, to fix the transition point around the expected location for transition in the full-scale wing.

The geometric differences such as model fidelity, or aeroelasticity effects cannot be studied properly at this moment of the project, since no full-scale Flying V has ever been built and very little has been studied so far. Because of this, according to Haines[51] it is very difficult to determine Reynolds number effects with any confidence because of the many effects involved at once,

Wind tunnel wall interference is an example of a pseudo-Reynolds number effect: since the flow in a wind tunnel has boundaries which do not exist in a flight test, discrepancies will be present, but they do not arise from the Reynolds number difference. This topic is presented in more detail in Section 4.1.

The fact that a half model was used will also introduce differences in the flow and uncertainties in the prediction of the full-scale characteristics, which are again unfortunately difficult to predict at the current stage of the project. Model manufacturing accuracy can also introduce discrepancies: for instance, surface roughness is usually translated into an increase of the drag because of the increase of the boundary layer thickness.

Only once the previous scale effects have been identified, the Reynolds number effects can be determined. According to Barlow et al.[52], the main discrepancies to be expected are an underestimation of the maximum lift coefficient and an overestimation of the drag. However, most of the existing knowledge about the correlation between flight test and wind tunnel results is kept inside the aircraft companies because of its strategic value and the very high cost required to acquire it.

Because of the gathered experience throughout the years, guidelines and correlations from different aircraft are available in the open literature, which can be sometimes used with confidence when studying a similar and well understood configuration. Nevertheless, even in this case, experience has shown that they are extremely difficult to estimate, and some examples of contradictory results are reported by [51].

If, as in the present study, the aircraft is not well known and the flow is not properly understood, making predictions of the scale effects becomes even more uncertain[52, 53], and the full-scale test at the actual Reynolds number will eventually be required for a proper assessment[51].

3.2 Wind tunnel setup description

The wind tunnel used for the tests was the Open Jet Facility (OJF) from the Faculty of Aerospace Engineering of Delft University of Technology (Figure 3.2. Its cross section is a 285x285 cm octagon, and its maximum speed is around 30 m/s. The velocity deviations in the vertical plane (two meters from the outlet) are smaller than 0.5%, and the longitudinal turbulence intensity level is smaller than 0.24%[54].

CAD drawings of the wind tunnel setup used for the tests with the basic dimensions can be seen in Figures 3.3 and 3.4.

The different components of the setup can be distinguished in the mentioned figures. The model is risen from the bottom wall of the wind tunnel in order to avoid interactions with the wind tunnel wall boundary layer. A reflection plane is placed in order to isolate the wing from the interaction with the connection to the balance, including elliptical-shaped edges in order to avoid vortex shedding which would influence the airflow at the wing[56]. The connection between wing and balance was shielded from the airstream as well with an aerodynamic cover, which is connected to both the splitter and the reflection planes and prevents the air to influence the balance measurements.

A turntable was used to place the wing at different angles of attack. The balance is mounted on top of the turntable and fixed to it so that they move together. The position of the wing with respect to the balance had to be carefully set in order to stay within the balance load limits.

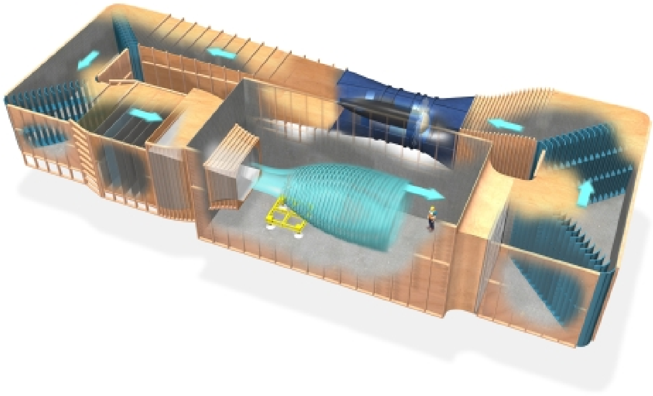

Figure 3.2: Schematic of the OJF wind tunnel (adapted from [55]

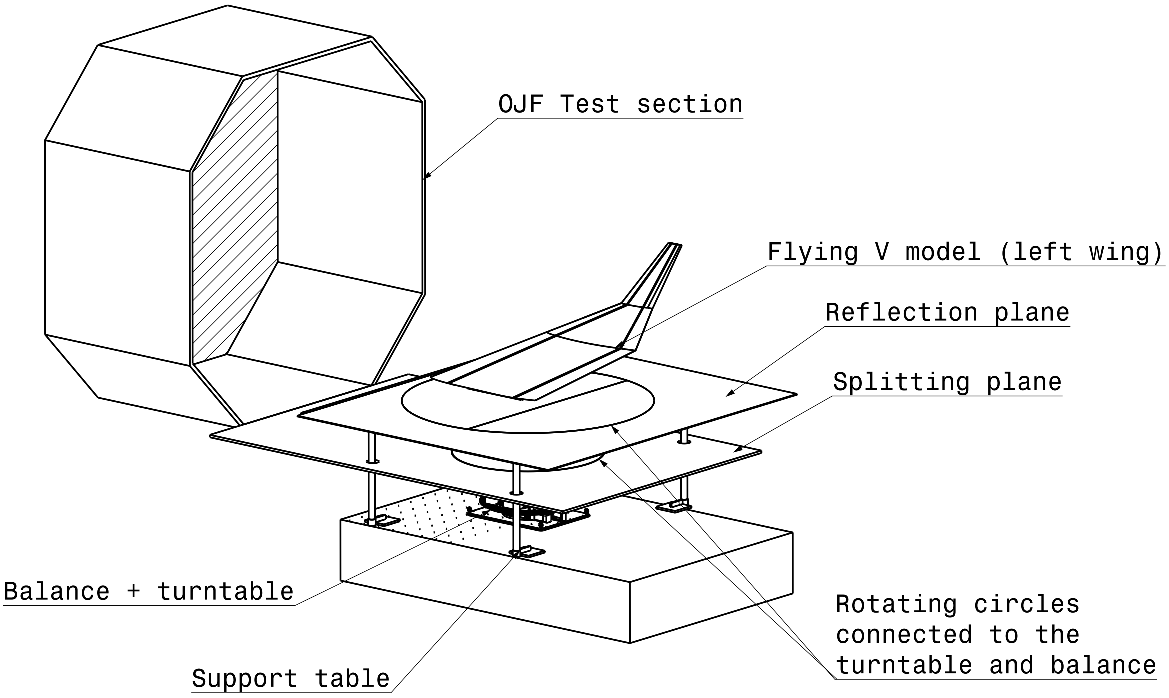
OJF Test section
Flying V model (left wing)
Reflection plane
Splitting plane
Balance + turntable
Support table
Rotating circles connected to the turntable and balance

Figure 3.3: Isometric view of the wind tunnel setup used for the tests

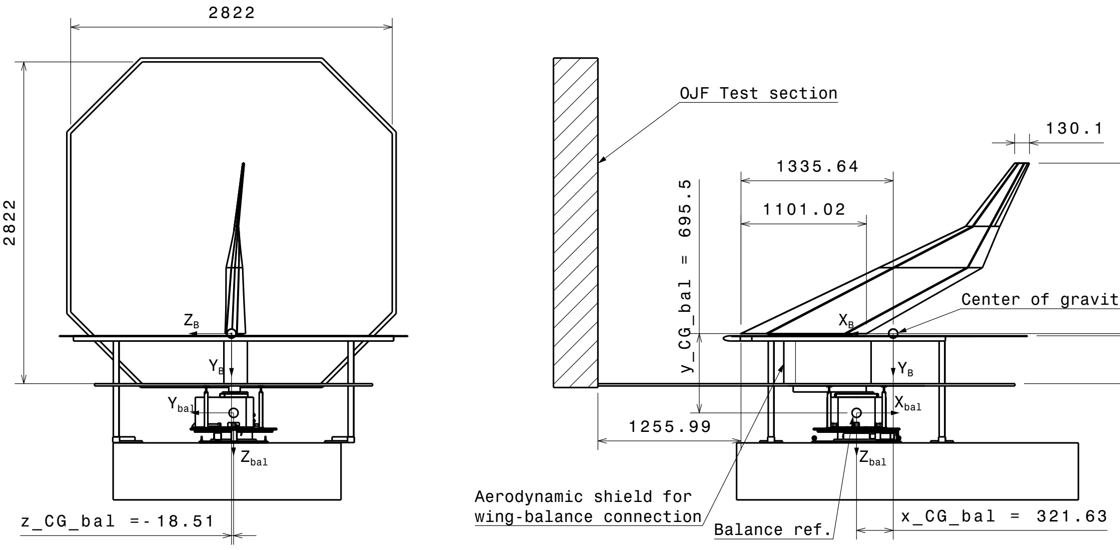

Figure 3.4: Rear view and side view of the wind tunnel setup used for the tests

3.3 Control and measurement of the control surfaces

Since the wind tunnel model was done from scratch, both the control system and a measurement system for the control surfaces had to be implemented as well: two Arduino UNOs were chosen as the microcontroller boards to perform both tasks. The most demanding task (a fast sampling rate for the actuator identification) could be achieved with the Arduinos, and its low price, the large amount of components available and ease of programming made it a suitable platform to use for this first model. In addition, since Arduino is programmed in C/C++, the code could be partially recycled afterwards if a more sophisticated board had to be used.

The control surfaces were actuated by servos which were controlled by one of the boards connected to a computer through a USB cable; from the computer the deflections were set for the static tests, and time-dependent inputs were commanded for the actuator identification. The servos are controlled using a form of Pulse Width Modulation (PWM): the position to which the servo will move depends on the length of the pulse sent, which had to be calibrated (the exact values vary from one servo to another), and this position is tracked by an internal potentiometer. It was decided to measure the deflections of the control surfaces using an external potentiometer in order to identify the servos dynamic response, which can be critical when designing an Automatic Flight Control System.

To do so, potentiometers were connected to the output shaft of the servo, and their voltage was measured by an Analog-to-Digital Converter (ADC) connected to a second Arduino UNO. The reduced space inside the wing forced the choice of potentiometers to measure the deflections since there was not enough space for any kind of digital sensors (such as encoders). Analog measurements however come with several difficulties: 1) a very stable voltage reference is needed so that there is no voltage drift with time, since it would look as an angle variation, 2) measurements are sensitive to electrical noise and electromagnetic interferences (EMI), 3) the length of the wires can have an effect due to voltage drops along the line, and 4) the internal impedance of the analog to digital converter should be taken into account when a voltage is measured. These problems were solved as follows:

1. *Voltage reference drift*: a 5V voltage reference was purchased and tested to ensure that there was no voltage drift over long periods of time. The output voltage from the voltage reference was measured every 10 seconds for 3 hours while realistic and varying loads coming from 4 potentiometers were applied. The results are shown in Figure 3.5, where a moving average every 6 samples (1 minute) was done to remove noise. The drift over three hours was less than 0.02 mV which can be neglected regarding measurement accuracy.

2. *Electrical noise and electromagnetic interference*: differential connections were used for every potentiometer, which effectively reduces the noise. The signal wires for analog measurements and the wires to power the servos were as far away as possible from each other to avoid inter-

ference. This setup was tested and it was concluded that there was no need for electromagnetic shielding.

3. *Wire length*: cables of adequate section were chosen and all systems were placed as close as possible.

4. *Internal impedance of the ADC*: an ADC with programmable gain amplifier was used, which adjusts the internal impedance (and thus the resolution) using the value of the last measured sample. The internal impedance of the chosen ADC was sufficiently large for all resolutions, so the effect on the measurements was negligible. A buffer circuit was also included to decrease the output impedance from the potentiometers, which isolates the part of the circuit containing the analog measurements electrically from the rest of the circuit.

The components that were used to build such a circuit are listed in Table 3.1.

Table 3.1: List of components for the control surfaces control and measurements

Component	Description
2 x Arduino UNO	Microcontroller boards (Controller/Master and DAQ)
Hitec D954SW	Servo for the control surface #1
Hitec D89MW	Servo for the control surface #2
Hitec 5070MH HV	Servo for the control surface #3
Hitec D89MW	Servo for the control surface #4 (winglet, not included)
2 x Voltage regulator	Step-down voltage regulators to power the servos from the battery
Adafruit ADS1015	Analog-to-digital converter with Programmable Gain Amplifier
Adafruit ADA254	MicroSD breakout board
3 x Vishay Spectrol 148	10 kΩ potentiometers to measure control surface deflections
Battery	11.1 V battery to power servos and electronics
KKmoon AD584-M	5V voltage reference to provide a stable reference for analog measurements
2 x LM358	Operational amplifiers for a buffer circuit to boost the impedance of the analog signals from the potentiometers

Two C/C++ programs were written to control the Arduinos. The most critical parts of the code were: 1) the communication and syncing between both Arduinos, which was implemented using an I^2C bus and hardware-based interrupts through digital inputs and outputs; and 2) the fast sampling and logging required to capture the unsteady response of the actuator, which required modifications to the provided libraries for the ADC to increase the sampling rate up to 100 samples per second.

For the actuator identification tasks, both Arduinos had to be carefully synced so that the DAQ would start measuring and logging at the exact same time that the controller started the dynamic input. The delay due to our software is of the order of microseconds, and the internal delay of the servo due to software/hardware is of the order of milliseconds, so the software delay was considered negligible. For the static tests there were no time-critical tasks: the commanded deflection was set, measurements were taken and averaged, and they were logged into the SD card.

The potentiometers were calibrated using an angle reference, and their standard deviation was calculated from linear calibration curves. The calibration curve of one of the potentiometers is shown in Figure 3.5 as an example, along with the test to confirm the stability of the voltage reference.

Some additional information can be found in Appendix A, where a schematic of the electronic design is shown (Figure A.1), some details about the calculations of the buffer circuit are given (Figure A.2), and a flowchart to explain the logic of the programs used to control the actuators, measure the deflections, and sync both boards is presented (Figure A.3).

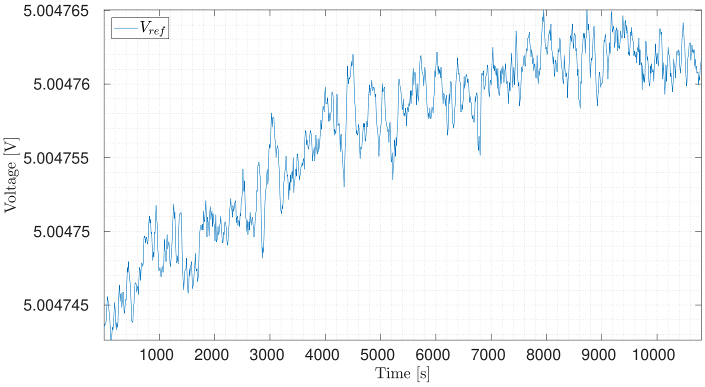

(a) Voltage reference test

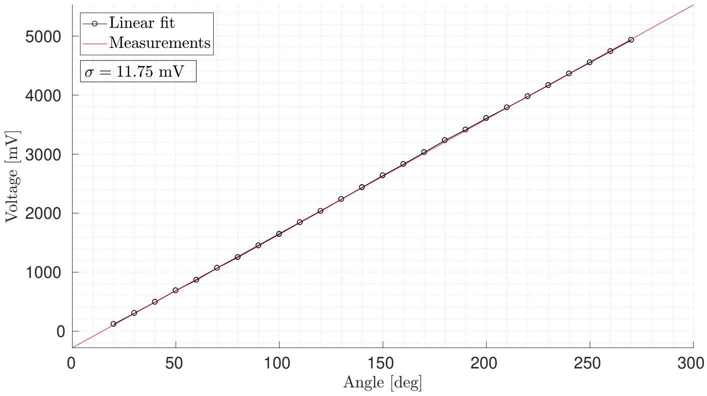

(b) Potentiometer calibration curve

Figure 3.5: Electronic calibration results

3.4 Instrumentation

The aerodynamic forces and moments were measured using the balance from the OJF wind tunnel, the wind speed was automatically controlled by the wind tunnel through the fan rotational speed, and the control surfaces deflections were logged using an Arduino-UNO and potentiometers connected to the actuators' shafts. The angle of attack was set by a turntable connected to the wing, and no other angle of attack measurements were available, so the commanded position will be used for the identification.

During the static tests measurements were taken at a fast sampling rate, and the average over 10 seconds was computed for every datapoint to improve the accuracy of the measurement. On the other hand, during the tests for the actuators identification, the raw output of the potentiometers was directly logged into the SD card, since a high sampling rate was required to capture the unsteady response of the actuators. No unsteady forces or moments were measured during the actuator identification tests, and the angle of attack and the wind speed were kept constant for each of these runs.

A summary of the instrumentation used for the test and its basic characteristics are shown in Table 3.2, where the values for the standard deviation of the measurements come from the calibration of the balance and the potentiometers. No calibration data was found for the wind speed measurements or the angle of attack from the turntable.

Table 3.2: Available instrumentation for the wind tunnel tests

Measurement	Sample rate	Std. deviation	Remarks
Force (balance X-axis) F_{Xb} [N]	2 kHz	0.02	Average over 10 s.
Force (balance Y-axis) F_{Yb} [N]	2 kHz	0.05	Average over 10 s.
Force (balance Z-axis) F_{Zb} [N]	2 kHz	0.05	Average over 10 s.
Moment (balance X-axis) M_{Xb} [N·m]	2 kHz	0.01	Average over 10 s.
Moment (balance Y-axis) M_{Yb} [N·m]	2 kHz	0.01	Average over 10 s.
Moment (balance Z-axis) M_{Zb} [N·m]	2 kHz	0.07	Average over 10 s.
Wind speed V [m/s]	2 kHz	-	Average over 10 s.
Angle of attack α [deg]	-	-	Set by the turntable
Control surface deflections δ_i [deg]	100 Hz	0.5	Average (static tests), Raw output (actuator id. tests)

Chapter 4

Data preprocessing

Before the measured data can be used to feed the aerodynamic identification routine some preprocessing is required. In the present chapter, the wind tunnel corrections are estimated for the proposed wind tunnel setup, although they were finally not applied because of the uncertainties that their derivation entail (Section 4.1). The measured forces and moments need to be translated into body axes and made dimensionless as it is customary (Section 4.2), a simple analysis is done to estimate the expected uncertainty (Section 4.3), and the kinematics of the control surfaces are explained in order to calculate the control surfaces deflections from the measured angles of the servos (Section 4.4).

Finally, an analysis of the data coverage of the test and the convex hull of the dataset, which determines the region of validity of the model, is presented in Section 4.5.

4.1 Wind tunnel corrections

During flight, the flow past an aircraft is virtually unconstrained, with infinite boundaries in all directions, whereas in a wind tunnel the flow is confined by the its walls. The different boundary conditions due to the solid walls cause differences in the flow around the body, and will lead to discrepancies between wind tunnel and flight test results if no corrections are applied to the measured data. No other interference effects will be studied, such as those arising from wind tunnel walls boundary layers or irregularities of the airstream (e.g. non-uniformity).

Wind tunnel corrections depend on the size of the model, among others. In the simplest case, where the model is assumed to be small, the free stream will be corrected in direction and speed. For moderate lengths, average values can be used, and for even larger models, the corrections include streamline curvature and longitudinal pressure gradient corrections, which would affect pitching moment and drag[57]. These corrections can be divided in: *lift interference*, which includes the streamline curvature and the stream direction, and *blockage interference*, which involves the corrections to the longitudinal velocity. They are considered to be independent of each other in most applications and can be calculated separately.

Nevertheless, it is difficult to determine whether the data is actually correctable; the derivation of the corrections require a series of simplifying assumptions which may or may not be completely true, so the accuracy of the corrected measurements depends directly on their validity. Furthermore, examples can be found in the open literature which report that wind corrections are suspected to be the main source of scatter in measured data for tests at different sizes[51].

4.1.1 Lift interference corrections

Two corrections are required to account for the change in upwash at the model location. The change in the effective stream direction can be taken into account by means of corrections to the angle of attack and drag; assuming that the corrected angle is small $|\Delta\alpha| \ll 1$ and $C_D \ll C_L$:

$$\begin{aligned} C_{L_{corr}} &= C_{L_{raw}} \cdot \cos\Delta\alpha - C_{D_{raw}} \cdot \sin\Delta\alpha \cong C_{L_{raw}} \\ C_{D_{corr}} &= C_{D_{raw}} \cdot \cos\Delta\alpha + C_{L_{raw}} \cdot \sin\Delta\alpha \cong C_{D_{raw}} + C_{L_{raw}} \cdot \Delta\alpha \\ \Delta\alpha &= \delta_{corr} \frac{S}{S_{wt}} C_{L_{raw}} \end{aligned} \tag{4.1}$$

where the subscript “raw” indicates uncorrected data, “corr” indicates corrected values, S is the wing area, S_{wt} is the area of the test section, and δ_{corr} is the so-called boundary correction factor.

The streamline curvature correction is done in order to account for the decreasing upwash (in an open tunnel) along the stream, which can be regarded as an effective decrease in camber compared to an unbounded flow[52]. The corrections are:

$$\begin{aligned} \Delta\alpha_{sc} &= \tau_2 \cdot \Delta\alpha; \quad \Delta\alpha_{total} = \Delta\alpha \cdot (1+\tau_2) \\ \Delta C_{m_{sc}} &= \frac{1}{8}\Delta\alpha_{sc}\frac{\partial C_L}{\partial \alpha} \end{aligned} \tag{4.2}$$

τ_2 is a parameter used for streamwise corrections, which represents the increase of boundary-induced upwash at a point behind the wing half chord, referred to the value at the half chord.

The values of δ_{corr} and τ_2 usually come from analytical corrections derived for different wind tunnel test sections, walls, and models. Each of them requires different assumptions, such as a small model or the postulation of a certain lift spanwise distribution. In this sense, the characteristics of the wind tunnel setup that was used for the test complicated the search for wind tunnel corrections. First of all, the derivation of wind tunnel corrections for open jets is more complex than closed jets[57], and there is less information available in the literature. Also, as it was explained above, the connection between the balance and the wing lies in the stream, shielded by an aerodynamic cover. A reflection plane is placed to isolate the wing from the aerodynamic effects of the shield, but the new boundary layer that will develop on the reflection plane will affect the aerodynamics at the root of the wing, with effects which are difficult to take into account.

For models of appreciable span, as the model being studied, the spanwise lift distribution is required as an input to calculate the lift interference; so far, only CFD simulations have been done for the full-scale aircraft at $M = 0.85$[12] and for the scaled half-model[15] at low speeds, which can be seen in Figure 4.1.

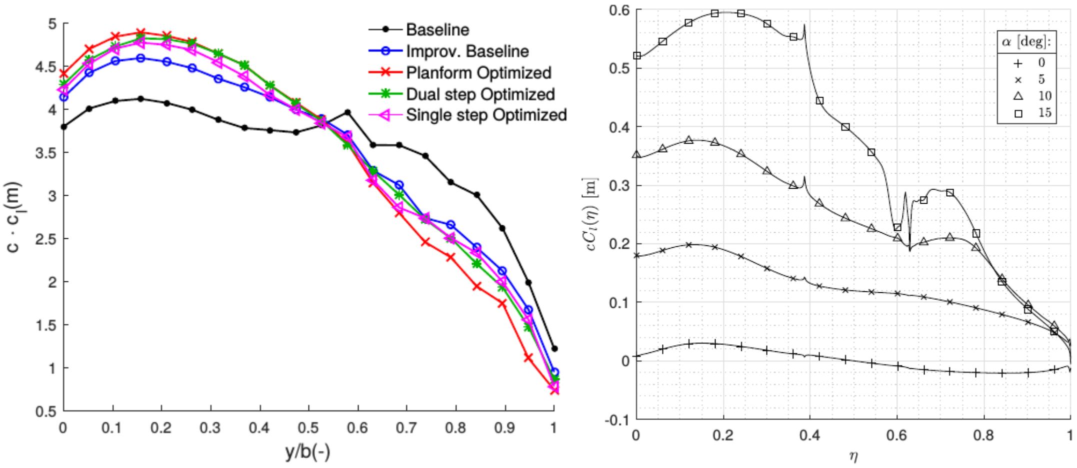

(a) Lift distribution ($M = 0.85$, $C_L = 0.26$)[12]

(b) Lift distribution ($\alpha \in (0, 15)$ deg, $\eta = 2y/b$) [15]

Figure 4.1: Lift spanwise distribution (CFD simulations)

It can be seen that the spanwise lift distribution resembles an elliptical distribution, specially for the full-scale aircraft at its design point, as it was intended in the design. These estimations have not been validated yet, since this aircraft is still in a preliminary design phase, so they can only be trusted up to a certain extent. However, the estimation of the corrections assuming the wing has an elliptic loading is possible by reflecting the wing and the wind tunnel section on the reflection plane, which will give an idea of the order of magnitude of the discrepancies that can be expected. It should be noted that the reflection cannot be used in tests with aileron deflections, since the mirror image would be deflected oppositely. This invalidates this method to calculate the corrections for all datapoints, since the most part of the dataset include nonzero elevon deflections.

Since the entire dataset cannot be corrected, it is decided then to not apply lift interference corrections before the aerodynamic identification, but only use the corrections on some clean polars to estimate the discrepancies to expect between the wind tunnel and flight test results. Other alternatives exist to estimate the lift interference, such as CFD simulations[58, 59] of both the constrained and unbounded flow, but are beyond the scope of this work and will not be discussed here.

In addition, flight test data from a full model of the same scaling factor (4.6 %) will be available in just a few months, and will allow to investigate which corrections lead to the best results.

Reflected setup

Neglecting the part of the stream that flows below the reflection plane, the reflected setup is shown in Figure 4.2. Two variables are defined to characterize the test section and the model:

$$\lambda = h/B; \quad k = b/B, \tag{4.3}$$

where h is the height of the test section, B is the width of the test section, and b is the model span, all including their reflected image, as it is shown in the figure. Introducing the values of h, B, and b, the height-to-width ratio of the reflected test section yields $\lambda = 0.59$, and the span-to-width ratio $k = 0.627$.

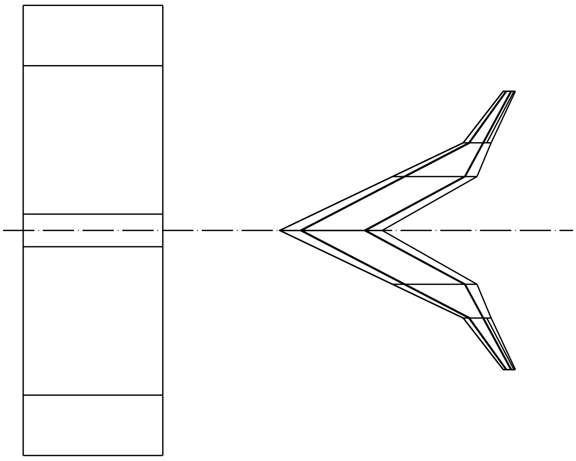

(a) Top view of the reflected setup

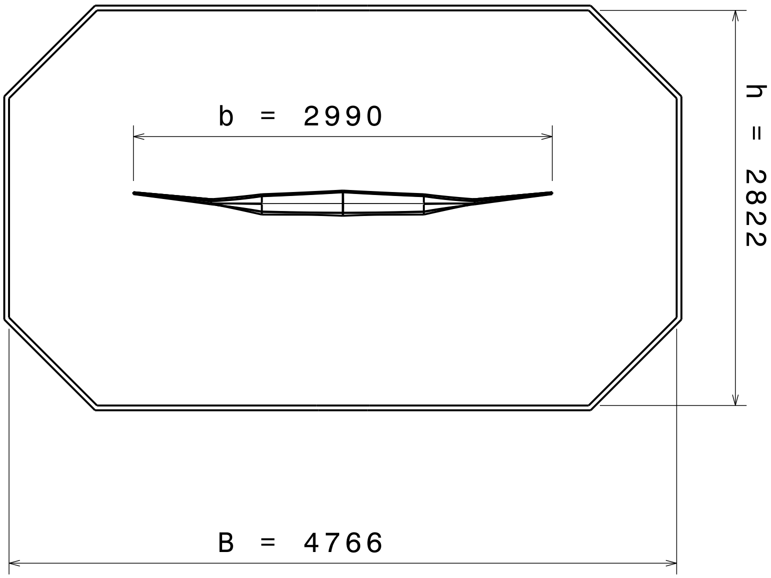

(b) Front view of the reflected setup

Figure 4.2: Drawings of the reflected setup on the reflection plane

If the fillets at the center of the setup are neglected (which only account for 0.39% of the total area), the reflected test section is again an octagon, which historically has not been studied as thoroughly as elliptical or rectangular test sections in the field of wall interference. However, according to Ref. [52], the corrections for an octagonal jet are virtually the same as those of an elliptical jet with the same height-width ratio. These corrections can be found in the same reference, and are recommended in Ref. [60], which is considered by many engineers the standard reference for subsonic wall corrections.

Changes in flow direction

The lift interference parameter for a wing with an elliptical spanwise lift distribution is shown in Figure 4.3 for an open jet elliptical wind tunnel for different aspect ratios of the test section. The value of $\lambda = 0.59$ required for the reflected setup is far from the available curves in the graph, so it is extrapolated using a surrogate model with the digitized data from the figure to predict the value of δ_{corr} at that value of λ. This is only acceptable because of the qualitative character of this calculation, since there is no guarantee about the accuracy of the result. However, as it can be seen in Figure 4.3(b), it seems to follow the same trends as the other curves and it is preferred against a random guess between the two closest curves. The predicted value for the lift interference parameter is:

$$\delta_{corr} = -0.162 \tag{4.4}$$

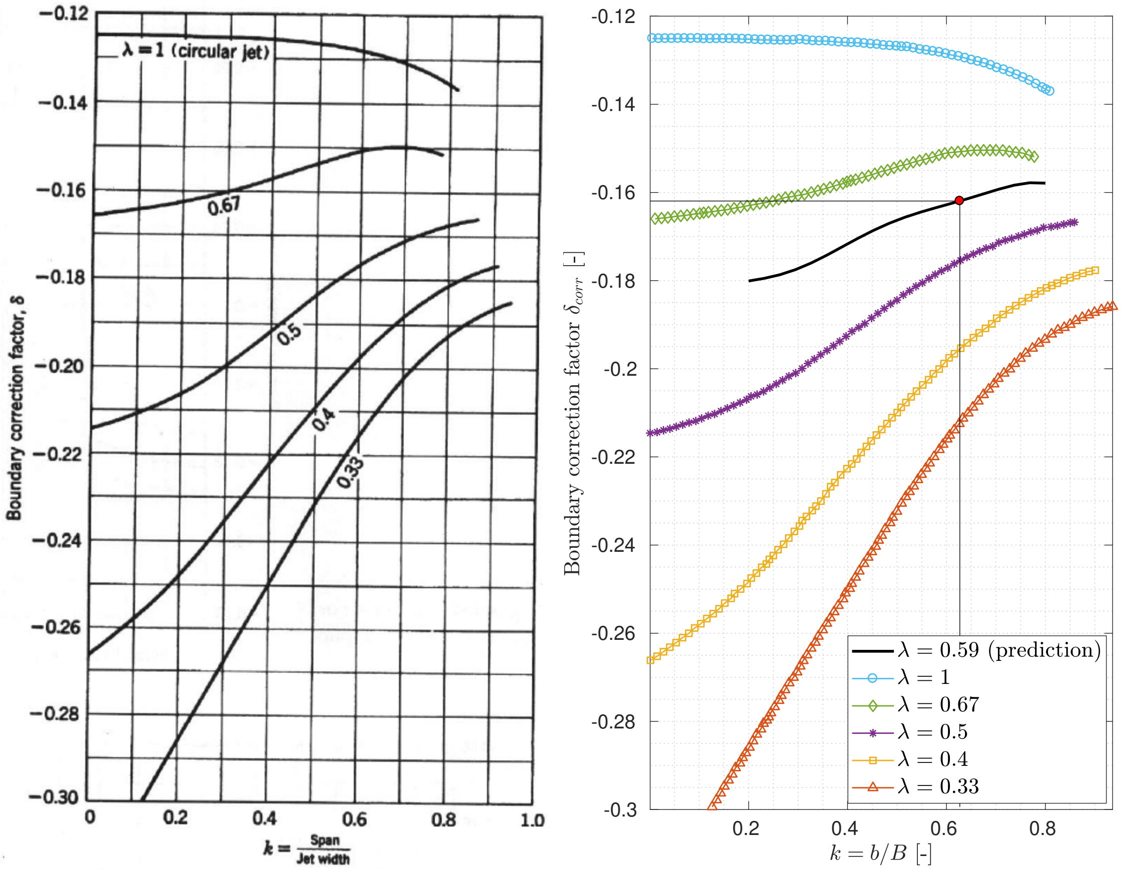

(a) Analytical lift interference parameter, extracted from Ref. [52]

(b) Digitized values of δ_{corr} and its prediction for $\lambda = 0.59$ using a surrogate model

Figure 4.3: Lift interference parameter for elliptic loading in elliptic test sections

The corrections are calculated using the total wing area S_t, including the image, and the original test section area S_0, without its image.

$$\Delta\alpha = \delta_{corr}\frac{S_t}{S_0}C_L \tag{4.5}$$

$$\Delta C_D = \delta_{corr}\frac{S_t}{S_0}C_L^2 \tag{4.6}$$

Substituting the values of C_L, δ_{corr}, and the areas of the wing and test section, the angle of attack and drag corrections can be calculated; the corrected and uncorrected values for two clean polars at $V = 20$ m/s are shown in Figure 4.4. It should be noted that these corrections are made assuming linear aerodynamics, so the maximum lift coefficient at which these corrections should be applied should be limited to $C_L \cong 0.8$.

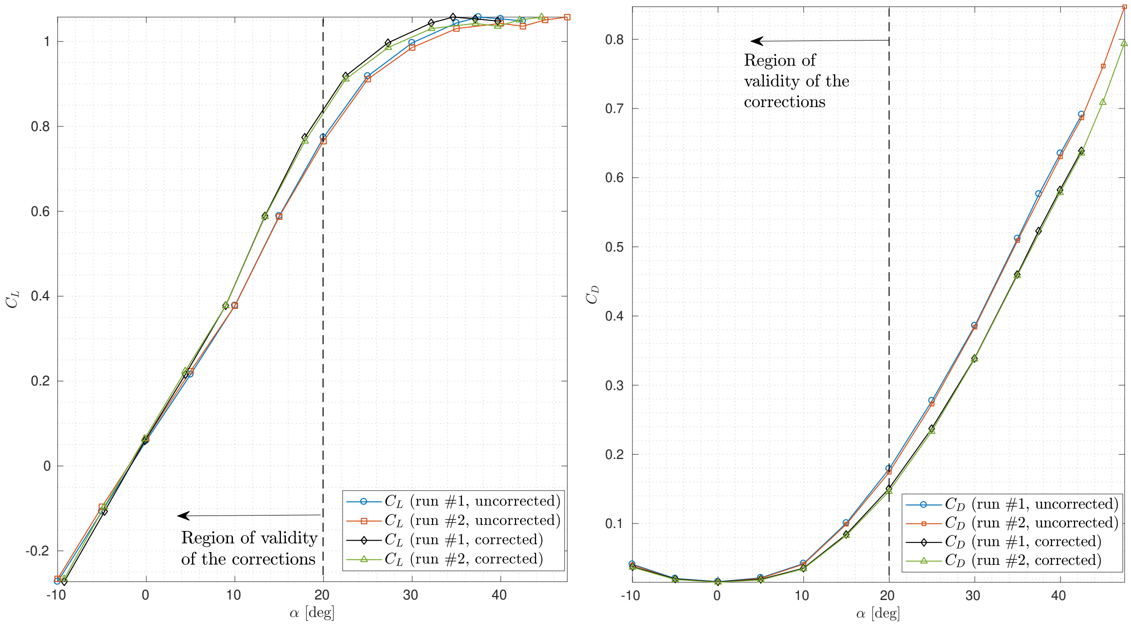

(a) Corrected lift coefficient (lift interference) (b) Corrected drag coefficient (lift interference)

Figure 4.4: Lift interference correction for the stream direction

The maximum correction in absolute value would occur at $C_L = 0.8$, which corresponds to:

$$(\Delta\alpha)_{max} = -2.31^\circ \quad (\Delta C_D)_{max} = -0.03$$

From the corrected curves and the value of maximum correction, it can be seen that the lift interference corrections do not appear to be negligible, and might have an appreciable effect in the aerodynamics of the vehicle.

Streamline curvature corrections

The value of τ_2 is found from graphs as well. The original graph and the digitized version are shown in Figure 4.5.

τ_2 is given as a function of the “tail length” because it is also used for corrections of the flow at the tail. Since this aircraft does not have a tail, only the streamline curvature correction for the wing be applied, which is calculated using a “tail length” of $\bar{c}/2$. From the graph:

$$\tau_2 = 0.165 \tag{4.7}$$

Introducing the values of τ_2 and $(\Delta\alpha)_{max}$ in Eq.(4.2), the streamline curvature corrections are:

$$(\Delta\alpha_{sc})_{max} = 0.36^\circ, \quad (\Delta C_m)_{max} = 0.0013, \tag{4.8}$$

which are considerably lower than the corrections for the stream direction.

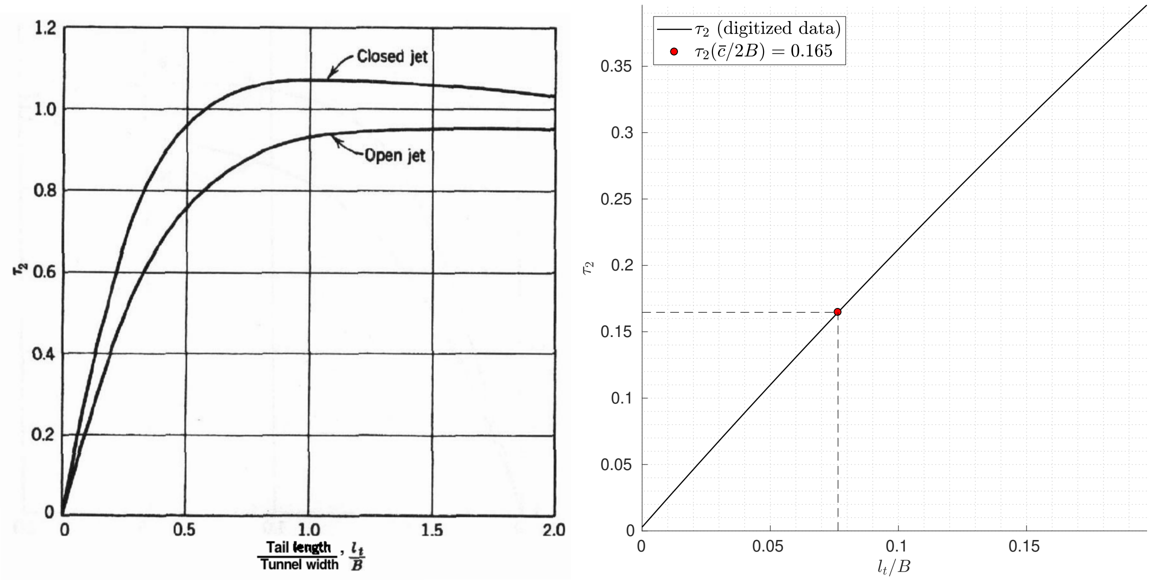

(a) τ_2 for open and closed jets[52]

(b) Digitized values for the region of interest

Figure 4.5: Plots of τ_2 for streamline curvature corrections

4.1.2 Blockage corrections

Apart from the lift interference corrections, blockage corrections are required for the correspondence with the solution for an unbounded stream to account for the volume that the model and its wake occupy within the finite stream of the wind tunnel. This effect can be taken into account by a blockage factor ϵ that corrects the longitudinal component of the flow (V). This is only true if the model is mounted in the center of the tunnel, so the reflected setup derived for lift interference corrections will be used again. The overall blockage factor can be split in two independent terms, the solid blockage ϵ_s and the wake blockage ϵ_w, which depend on the relation between the sizes and cross sections of the model and the wind tunnel[57].

$$\epsilon = \epsilon_s + \epsilon_w; \quad \epsilon = \frac{\Delta V}{V} \tag{4.9}$$

The underlying assumptions of this division are that the model is small compared to the test section and that the lift is not too large. For open jet tunnels, the wake is usually supposed to have enough space to expand behind the model, and in most cases it is considered to be negligible ($\epsilon_w \cong 0$)[60], so only solid blockage will be calculated. Blockage corrections are smaller in open jets than in closed wind tunnels, and of opposite sign. The blockage factor affects the following flow quantities: velocity, Mach number, dynamic pressure, static pressure, temperature, density, and Reynolds number; only the corrections to the velocity, dynamic pressure, and Reynolds number will be calculated, since the rest of the quantities are not used in the aerodynamic identification.

$$\begin{aligned}
\Delta V &= V_{raw} \cdot \epsilon \\
\Delta q &= q_{raw} \left(2 - (\text{Mach})^2_{raw}\right) \cdot \epsilon \\
\Delta \text{Re} &= \text{Re}_{raw} \left(1 - \frac{\gamma}{2} (\text{Mach})^2_{raw}\right) \cdot \epsilon
\end{aligned} \tag{4.10}$$

The solid blockage factor for an elliptical open jet will be used, which can be found in Ref. [57]:

$$\epsilon \cong \epsilon_s = (T_R + 0.029) \cdot \left(\frac{1}{S_{wt}}\right)^{3/2} \cdot \frac{V_{model}}{\beta_c^3} \tag{4.11}$$

where T_R is a parameter that depends on the cross section, and $\beta_c = \sqrt{1-(\text{Mach})^2}$ to account for compressibility effects, which will be almost negligible (maximum Mach number during the test was ~ 0.09). T_R is taken from graphs for rectangular open jets of the same width-to-height ratio (Ref. [57]). The extracted graph and the digitized curve is shown in Figure 4.6 (the different sign of the slope is because of the inverted vertical axis of the original graph).

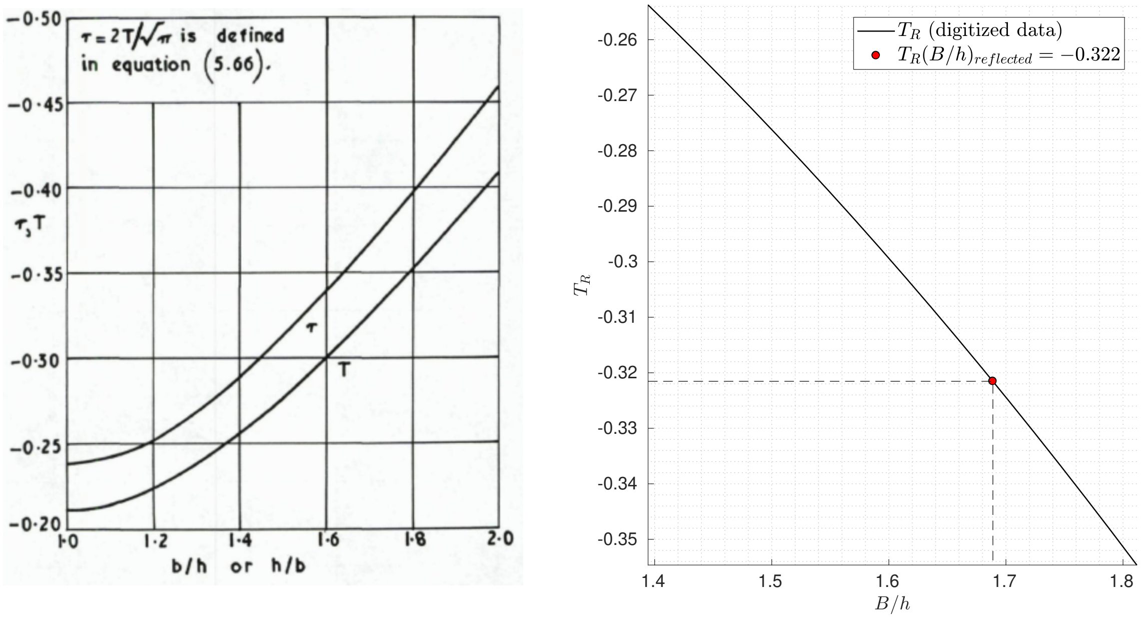

(a) T_R for rectangular open jets[52]

(b) Digitized values for the region of interest

Figure 4.6: Plots of T_R for solid blockage corrections

T_R is retrieved from the graph using the width-to-height ratio of the reflected setup, and introducing the values of the model volume, Mach number, and test sections dimensions in Eq.(4.11), the blockage factor yields:

$$T_R = -0.322 \quad \epsilon \cong \epsilon_s = 5.65 \cdot 10^{-4} \tag{4.12}$$

The maximum corrections for the velocity, dynamic pressure, and Reynolds number would occur at $V = V_{max} = 30$ m/s:

$$(\Delta V)_{max} = -0.017 \text{ m/s}, \quad (\Delta q)_{max} = -0.61 \text{ kgm}^{-1}\text{s}^{-2}, \quad (\Delta \text{Re})_{max} = -1.05 \cdot 10^3 \tag{4.13}$$

which imply maximum differences of -0.05% for the wind speed, -0.11% for the dynamic pressure, and -0.05% for the Reynolds number. The effect in the aerodynamic coefficients of the correction to the dynamic pressure is considered to be negligible, as the uncorrected and corrected curves are basically overlapping. In Figure 4.7, where the uncorrected and corrected lift and drag coefficients are shown for the same two clean polars considered above, it can be seen that the differences between the two runs are larger than the corrections, so the blockage corrections will not have an appreciable effect in the results.

4.1.3 Expected discrepancies

As it was explained, the wind tunnel corrections derived here were finally not applied to the measured data because of several reasons. The assumptions required to derive the corrections (elliptical lift distribution, small model, neglect the airflow below the reflection plane...) are not guaranteed to hold, and no information about the accuracy of the angle of attack measurements is available since it was directly set by the turntable and no calibration data was found. In addition, not all the data was

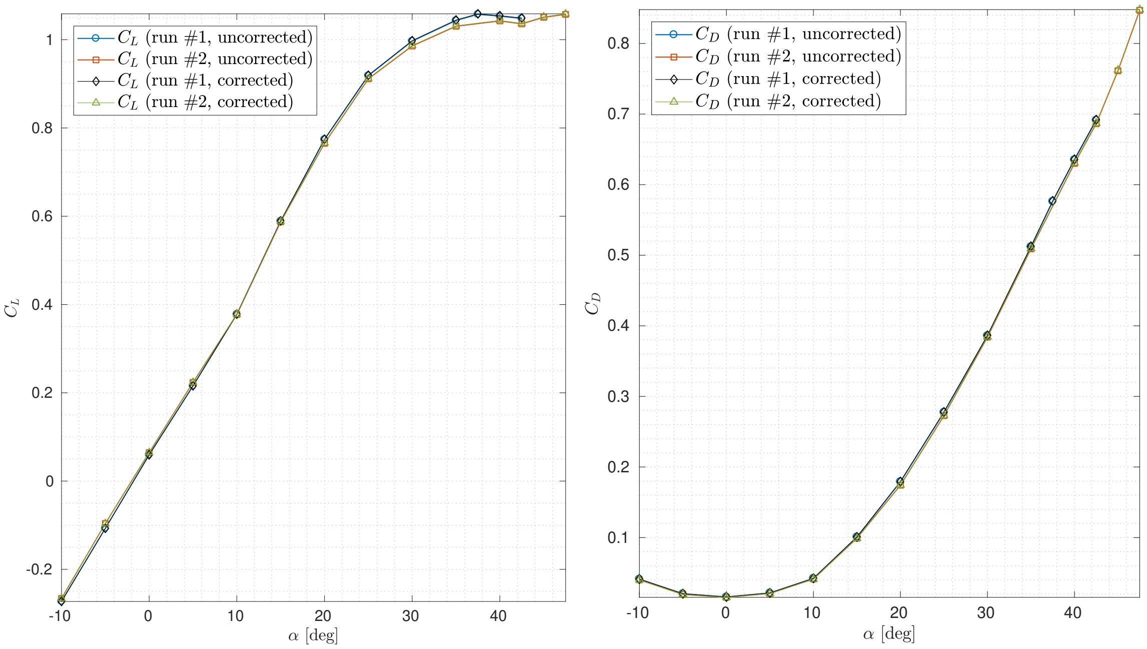

(a) Corrected lift coefficient (blockage)

(b) Corrected drag coefficient (blockage)

Figure 4.7: Blockage corrections

correctable, since the derived corrections are only valid for linear aerodynamics, and for zero elevon deflections (symmetrical conditions at both wings).

Because of the associated uncertainties and since the estimated effects of the corrections are not expected to change the aerodynamic model structure drastically, it was finally decided to not apply any wind tunnel corrections to the data.

In practice, test data from different model sizes, flight tests, etc. is normally used in order to adjust the correlation between wind tunnel and flight test results[60]. Once flight data is available from a sub-scale flight test, it will be possible to assess the accuracy of these corrections factors, and to modify them as required for an adequate wind tunnel-flight test correlation. This is regarded as a more efficient way of dealing with this problem with less involved speculation and unknowns.

4.2 Translation to body axes

The forces and moments are measured with respect to the balance reference point, which is provided in the manual. They will be translated to body axes, which are normally used for aircraft system identification. The reason behind this is that the tensor of inertia in body axes remains almost constant during a flight test (except for the effect of the fuel consumption). This avoids computing the derivatives of the tensor of inertia with time to solve the equations of motion (even though this is of course not an issue for the present wind tunnel test).

The balance measurements were unbiased twice: first, the initial forces and moments from the weight of the model and setup were removed (tare), and second, measurements before and after each run were taken with zero wind speed, in order to check the drift of the balance readings throughout the run. It was assumed that this drift evolved linearly with time, and the corresponding quantity was subtracted from each measurement using a linear interpolation.

The position and orientation of the balance reference frame with respect to the body axes are shown in Appendix B (Figure B.3). The rotation matrix from balance to body axes is:

$$[R_{bB}] = \begin{bmatrix} -1 & 0 & 0 \\ 0 & 0 & 1 \\ 0 & 1 & 0 \end{bmatrix} \tag{4.14}$$

so the forces and moments in body axes can be calculated as:

$$\begin{aligned}\mathbf{F}_B &= [R_{bB}]\mathbf{F}_{bal} \\ \mathbf{M}_B &= [R_{bB}]\mathbf{M}_{bal} + r_{cg,bal} \times [R_{bB}]\mathbf{F}_{bal}\end{aligned} \tag{4.15}$$

Once they are expressed in body axes, they are made dimensionless using the dynamic pressure, the planform area, the mean aerodynamic chord, and the span:

$$\begin{aligned} C_X &= \frac{X}{qS} \qquad & C_l &= \frac{L}{qSb} \\ C_Y &= \frac{Y}{qS} \qquad & C_m &= \frac{M}{qS\bar{c}} \\ C_Z &= \frac{Z}{qS} \qquad & C_n &= \frac{N}{qSb} \end{aligned} \tag{4.16}$$

4.3 Uncertainty analysis

During the tests some vibrations were observed at high angles of attack, which directly affect the accuracy of the balance measurements. Since no previous, validated data if available at the moment of the tests, the true value of the coefficients is unknown. For this reason, 4 of the runs with no control surfaces inputs (two for $V = 18$ m/s and two for $V = 20$ m/s) were used as follows: for each wind speed, a "true" coefficient was found by averaging the measurements taken at the same angles of attack (several for each run), and the standard deviation of the original values to this "true" coefficient was used as a measure of the uncertainty.

The results are shown in Figure 4.8, with the 3-σ values for each angle of attack. If the error is assumed to follow a normal distribution (which is customary and it is a reasonable assumption as it will be shown later on) the 99.73% of the data is expected to fall within the bounds. It should be noted that this result should be regarded more as qualitative than quantitative, since the amount of samples to calculate the standard deviation at each data point were only a few, and it assumes that the true values of the coefficients are given by the average of just two runs.

Nevertheless, this qualitative result is useful to determine a region where the measurements are considered to be accurate enough, which would span the region from $\alpha = -10°$ to $\alpha = 30°$. In addition, it is also clear that the lateral force (Fig. 4.8, upper right plot) shows a much larger uncertainty than the rest of the coefficients. It is hypothesized that the aforementioned vibrations that occurred during the test are the cause of the larger errors in this coefficient since they are exactly in the direction of the body Y-axis. Since the lateral-directional coefficients cannot be fully studied because of using a half-model (no sideslip angle can be applied), it was decided to leave the lateral force out of the study. The roll and yaw coefficients were studied partially: even though sideslip contributions could not be calculated, the effects of the control surfaces on the moments can be used in the future for the controller design, so a model for zero sideslip angle was estimated.

It is also worth mentioning here an observed aerodynamic effect which affects the accuracy of the pitching moment coefficient: different values values of the lift coefficient were observed depending on the previous angle of attack at which the model was sitting. When the angle of attack was decreasing, the lift coefficient tended to be lower than when it was increasing, specially around the region between 5 and 10°.

In this region, an aerodynamic effect called *vortex lift*[61, 62] is expected, which consists on the formation of a vortex over the wing which increases the lift coefficient. This increase of the lift slope is clear in Figure 4.7(a), which was also studied by Viet [16] using oil flow techniques, and by Palermo[15] through CFD simulations.

It is hypothesized that the different values of the lift coefficient could be related to the vortex formation: a similar effect has been reported in Ref. [63], where RANS simulations were done in order to predict the effect of the wind tunnel walls in the formation of vortices over delta wings. The outcome of this study was a prediction of a delay of the reformation of vortices when coming from high angles of attack because of the presence of the wind tunnel walls. Since the presence of the vortices contribute positively to the lift, this delay would translate in a decrease of the lift coefficient for the same angle of attack.

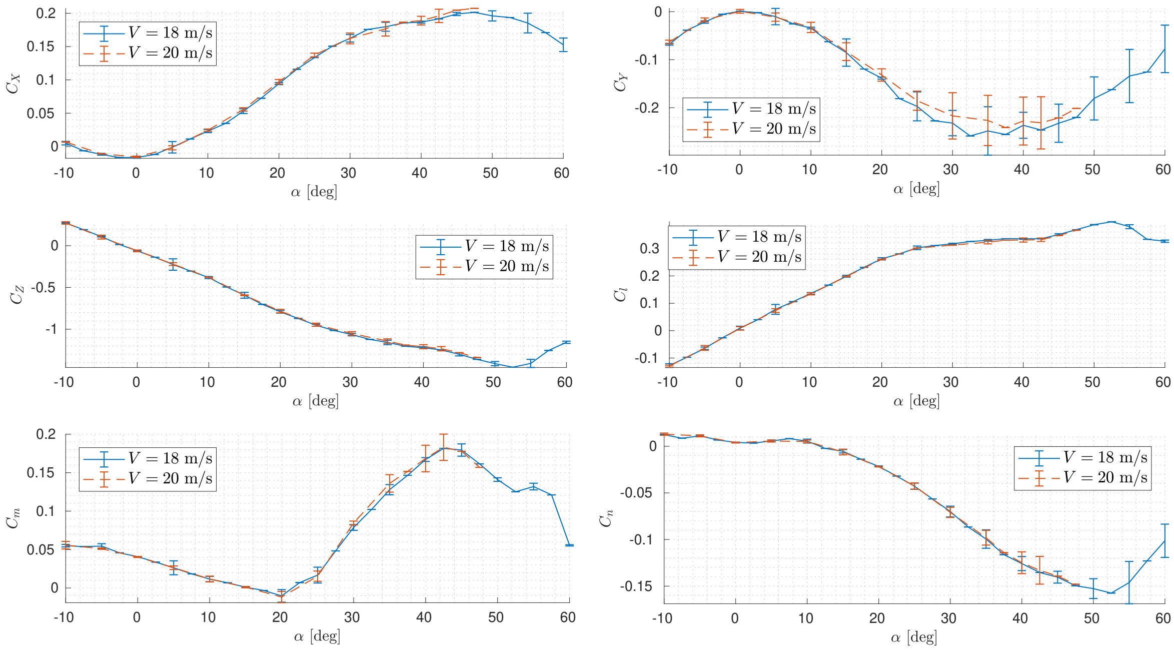

Figure 4.8: 3-σ confidence values for the six aerodynamic coefficients for wind tunnel data with clean configuration ($\delta_i = 0$)

The agreement of the trends with the presented experimental results makes this a plausible explanation, which is also in accordance with the vortex patterns of the Flying V studied experimentally by Viet [16]. It can be seen in Figure 4.9 how very small changes in the lift coefficient lead to large variations of the pitching moment, which contributes to the higher uncertainty of the measurements and will degrade the model quality for C_m. It is also reasonable to think that the pitching moment characteristics of the full model will be different than those of the half model because of the different strength and location of the generated vortices. This result was found experimentally in Ref [64] for subsonic speeds and a turbulent boundary layer using a half-delta wing with 68° sweep angle (the Flying V is 63°).

4.4 Control surfaces kinematics

The control surfaces deflections could not be measured directly; instead, they had to be derived from the measured angles of the servos and the geometry, which was known from the CAD model and direct measurements from the actual wind tunnel model. The mechanism to move the control surfaces is known as a 4-bar linkage, which is shown in Figure 4.10. The closure equations of the mechanism kinematics can be derived by starting from one of the joints (e.g. the actuator shaft) and following the linkages until the starting point is reached. They are given by:

$$l_{0x} = -l_1 \sin(\varphi - \varphi_0) + l_2 \cos\psi - l_3 \cos(\delta + \delta_0) \tag{4.17}$$

$$l_{0y} = -l_1 \cos(\varphi - \varphi_0) - l_2 \sin\psi + l_3 \sin(\delta + \delta_0), \tag{4.18}$$

The closure equations are solved for δ, and the results are presented in Figure 4.11 for the three control surfaces, where the control surface deflections are given as functions of the servo angles.

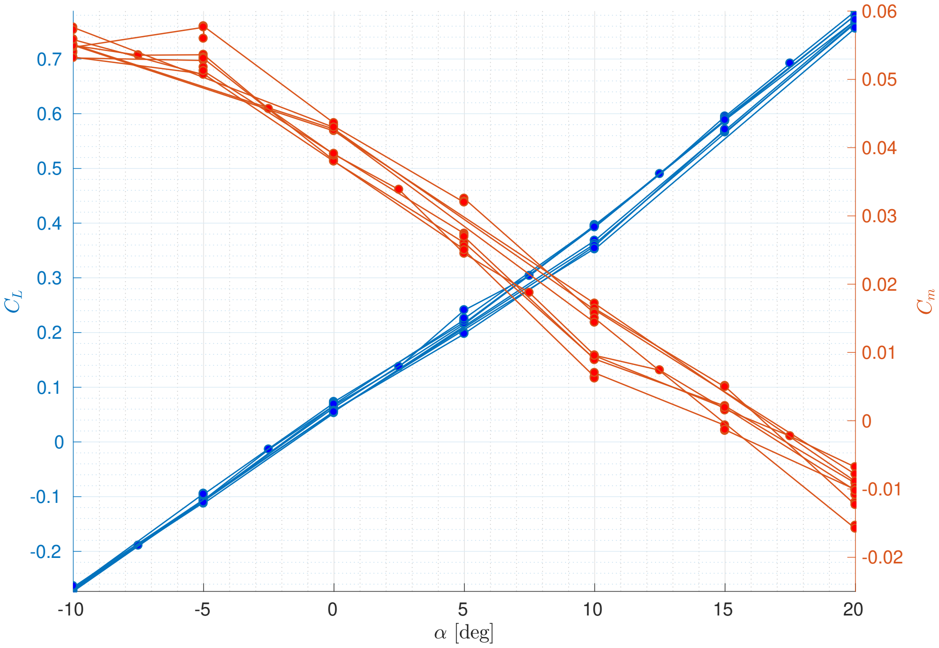

Figure 4.9: Lift coefficient and pitching moment (detail)

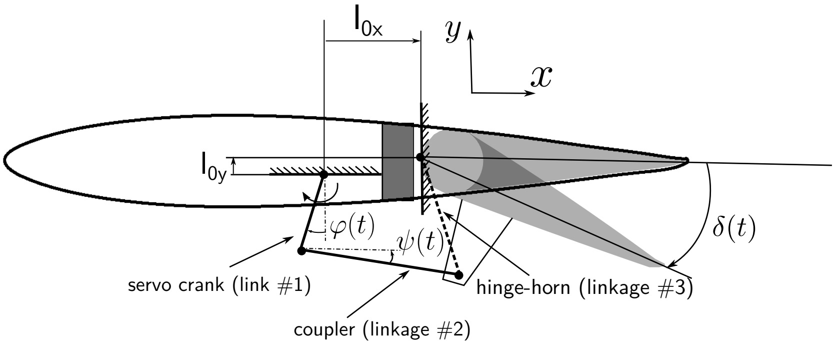
l_{0x}
y
x
l_{0y}
$\varphi(t)$
$\psi(t)$
$\delta(t)$
servo crank (link #1)
hinge-horn (linkage #3)
coupler (linkage #2)

Figure 4.10: Schematic of the control surfaces kinematics

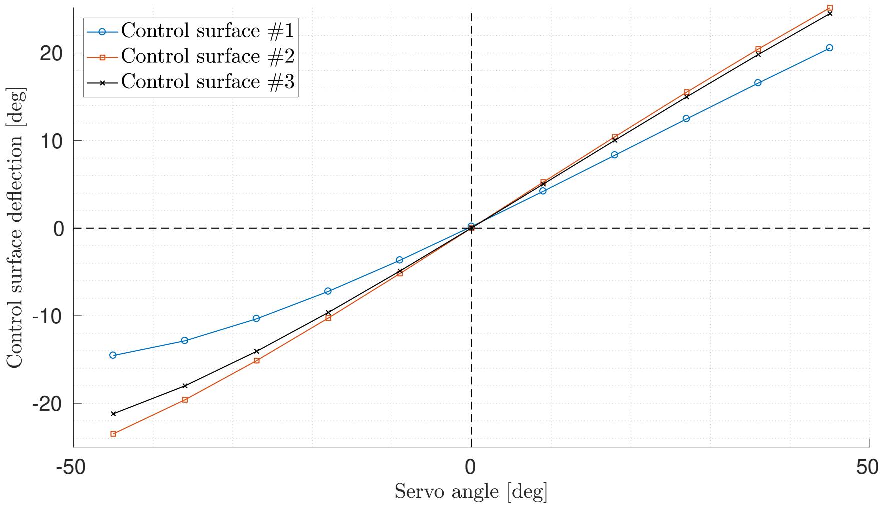

Figure 4.11: Control surfaces deflections versus servo angle

4.5 Data coverage

The designed test matrix attempts to cover the majority of low speed flight conditions which the Flying V sub-scale model could encounter during the flight test, so that it can be done with a higher level of confidence. Measurements were also taken at high angles of attack until the stall was reached in order to check the repeatability with respect to previous wind tunnel experiments. In addition, in a large number of runs the test conditions were randomized, as it is recommended in Ref. [65] in order to minimize the effect of systematic bias errors. A fine coverage in the $\alpha - \delta_i$ planes was achieved, and a coarser one for the airspeed which was limited by the available test time. The test matrix is presented in Appendix C.

All measured values for the six aerodynamic coefficients are plotted against the angle of attack in Figure 4.12 (up to $\alpha = 30°$). The vertical displacement of the points at the same angles of attack is due to the different control surfaces deflections and wind speeds. It can be seen that the pitching moment is the most affected by the control surfaces as it was expected, followed by the rolling moment and the vertical force.

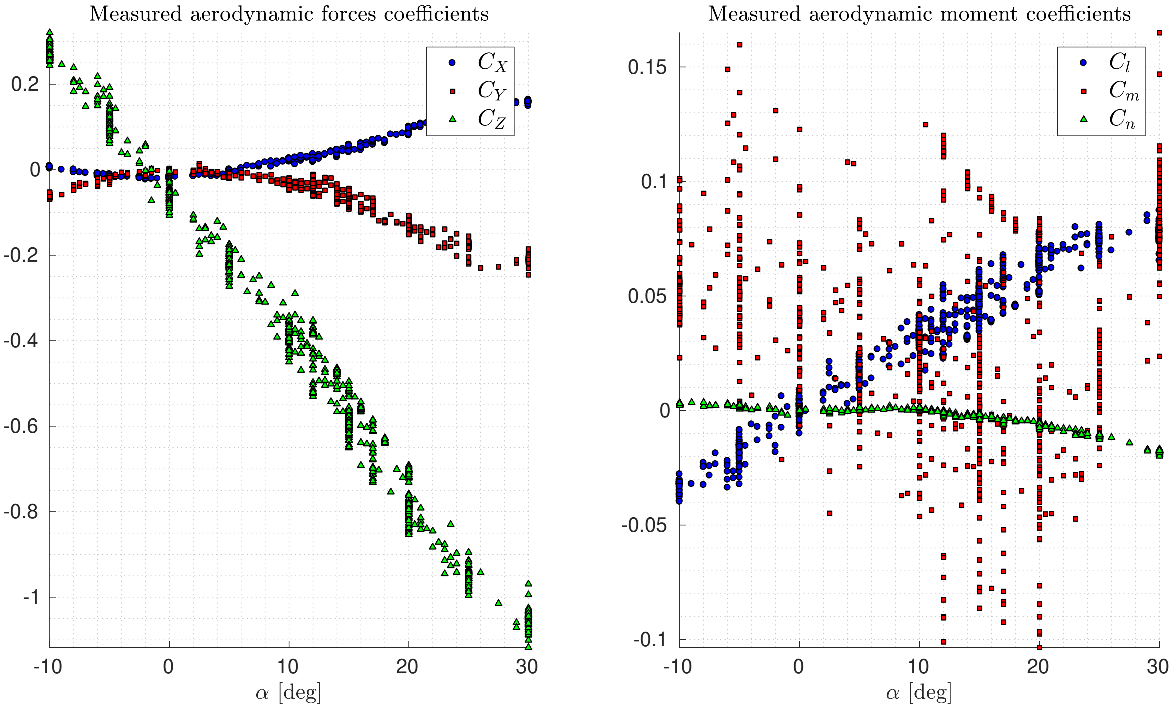

Figure 4.12: Measured aerodynamic forces and moment coefficients during the tests

To define the region of validity of the models the concept of convex hull needs to be introduced. Defined as the smallest convex set that contains the data, it is an polyhedral subspace of the n-dimensional space (with n the number of measured variables) where: 1) any point inside the convex hull can be interpolated with a polynomial of at least degree one, and 2) any point outside of the convex hull must be extrapolated[10]. Outside this hull, no measurements are taken, so one should not extrapolate outside it, since new, unmodeled effects might occur, so it is considered as the region of validity for any estimated model.

Figure 4.13 shows two cuts of the convex hull for the estimation dataset, where it can be seen that all validation points are contained in it, so the model can be evaluated in them since they are all inside its region of validity.

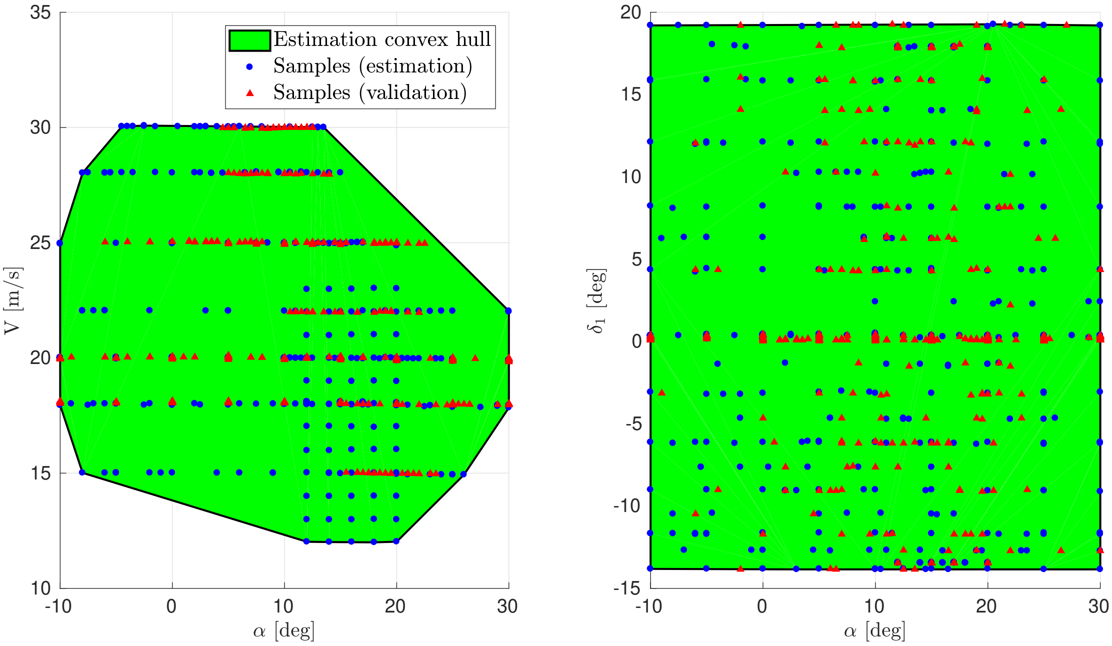

Figure 4.13: Convex hull of the estimation dataset ($\alpha - V$ and $\alpha - \delta_1$ cuts)

Chapter 5

Results and Discussion

In this chapter, the results for the model structure determination and parameter estimation for the measured dataset will be shown. The derived models will be discussed according to the metrics and measures of quality explained in the previous chapter in order to find the best possible models, which will be validated by testing the assumptions made to derive the OLS estimator and the confidence bounds. In the spline models, data collinearity indicators will also be used to validate the estimation, since no orthogonalization to the regressors was done.

The chapter is divided into several sections: first, an analysis of the results for polynomial models (Section 5.1) and spline models (Section 5.2) will be done, which includes the model structure determination, parameter estimation, model validation, and sensitivity analysis. A global inspection through model cuts for different combinations of the independent variables and an overall discussion of the results will be presented in Section 5.3. Finally, a flight mechanics analysis is done to identify a feasible center of gravity location, and a trimming routine for flight at different airspeeds and flight path angles is presented in Section 5.4, as an example of the applications that the estimated models may have.

Because of the large amount of figures required to describe the model structure determination process and to show all results discussed in the text, most figures from the aerodynamic identification were placed in Appendix D in order to keep the report compact and readable. In the same sense, in order not to eclipse the main aerodynamic identification results, the results of the actuators identification are shown in Appendix E, since they are actuator-dependent and so they do not share the same importance.

5.1 Polynomial models

5.1.1 Model structure determination

The results from the stepwise regression for the polynomial models are presented, along with the final model structure. The model selection was done according to the metrics explained previously, except in the case where the different metrics differ; in those cases, the best models according to all metrics were compared in terms of model fit, residual characteristics, and parameter variances, and finally the best one was chosen.

Different pools of regressors were used for the different coefficients, and the order of the regressors for the orthogonalization was carefully chosen for each of them, by applying a previous stepwise regression to the data without orthogonalizing the regressors. The most correlated regressors found with the stepwise regression routine were good candidates to be the first ones to be orthogonalized to keep the model as compact as possible.

The maximum order of the regressors to be used was driven by the value of the parameter variances, which increased with higher order regressors: variances and covariances can be regarded as a measure of the sensitivity of the estimates to the noise, so they should be kept as small as possible. Several regressions using pools of regressors up to different orders were tried beforehand in order to determine which regressors cause large increases of the variances in order to avoid them in the generation of the final pool of regressors.

As an example, the model structure determination procedure will be shown in detail for the pitching moment coefficient, which proved the most difficult model to estimate because of the much larger nonlinearities with respect to the rest of the coefficient, as it was shown in Figure 4.12. In this example, the two best candidates will be compared and discussed in order to choose the best model structure. Similar criteria was used to derive models for the rest of the aerodynamic coefficients, whose results from the model structure determination are shown in Appendix D.

In Figure 5.1 the results of the stepwise regression for the pitching moment coefficient are shown. It can be seen that two main candidates can be selected: number 8 and 14. They show a local and a global maximum of the F-statistic, they cause the two biggest steps in decreasing the RMS, both for the estimation and validation data (after them, the RMS almost “stagnates”), and they show a low value of the PSE, which can be regarded as a measure of how compact models are. Although the validation residual actually keeps decreasing with the addition of regressors, the changes are so small that the F-statistic decreases from iteration 14 on because of the addition of non-significant regressors.

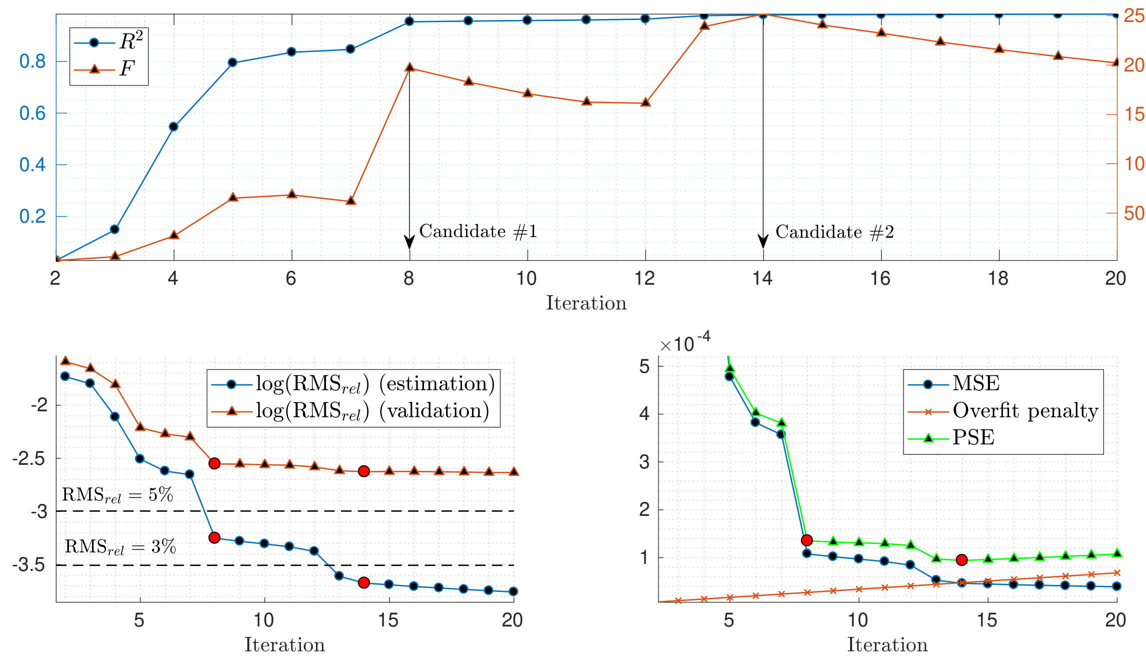

Figure 5.1: Stepwise regression results for the polynomial model for C_m

A residual analysis for both of them is shown in Figure D.11 in order to test the whiteness (upper plots) and the normality assumptions (lower plots) for the estimation and validation datasets. The model output against the model residual is plotted to find model deficiencies, as it was explained before. Both models seem to have random estimation and validation residuals, which validates the whiteness assumption, and from the lower plots it can be seen that the normality assumption seems to hold as well, since the majority of the points of the ICDF are condensed in the center of the interval, forming a straight line.

The positive outcome of the residual analysis suggests that the assumptions to apply the OLS estimation and derive the confidence bounds are reasonably true. On the other hand, the variances of the estimated parameters are shown in Figure 5.1. It can be seen that the model at iteration #14 has a considerably high value of the variance of one of the regressors ($\hat{\theta}_{13}$), which will be translated into the parameter confidence bounds. However, the rest of the parameter estimates feature a smaller variance than their corresponding parameters at iteration #8 (the first 8 regressors are the same in both models).

Another comparison that may be done is through some model cuts, which helps to see how the model fits the data in a visual manner and to spot unmodeled characteristics. Model cuts for $\alpha - V$ and $\alpha - \delta_i$ for both candidates are shown in Figure D.12. Finally, the model fit can be compared using Table 5.2

Table 5.1: Parameter variances for the candidates of the C_m polynomial model

Parameter	$\mathrm{Var}(\hat{\theta}_j)$ (model #11)	$\mathrm{Var}(\hat{\theta}_j)$ (model #14)
$\hat{\theta}_1$	$1.607 \cdot 10^{-7}$	$6.959 \cdot 10^{-8}$
$\hat{\theta}_2$	$4.223 \cdot 10^{-6}$	$1.829 \cdot 10^{-6}$
$\hat{\theta}_3$	$9.912 \cdot 10^{-5}$	$4.293 \cdot 10^{-5}$
$\hat{\theta}_4$	$6.014 \cdot 10^{-6}$	$2.605 \cdot 10^{-6}$
$\hat{\theta}_5$	$3.055 \cdot 10^{-6}$	$1.323 \cdot 10^{-6}$
$\hat{\theta}_6$	$5.529 \cdot 10^{-6}$	$2.395 \cdot 10^{-6}$
$\hat{\theta}_7$	$6.258 \cdot 10^{-6}$	$2.710 \cdot 10^{-6}$
$\hat{\theta}_8$	$2.943 \cdot 10^{-3}$	$1.275 \cdot 10^{-3}$
$\hat{\theta}_9$	–	$2.398 \cdot 10^{-3}$
$\hat{\theta}_{10}$	–	$5.106 \cdot 10^{-4}$
$\hat{\theta}_{11}$	–	$8.250 \cdot 10^{-4}$
$\hat{\theta}_{12}$	–	$3.049 \cdot 10^{-4}$
$\hat{\theta}_{13}$	–	$3.759 \cdot 10^{-2}$
$\hat{\theta}_{14}$	–	$4.056 \cdot 10^{-5}$

Table 5.2: Model fit comparison for the C_m polynomial model candidates

	RMS_{rel} (est.)	RMS_{rel} (val.)	$\hat{\sigma}^2$	$\max(\lvert\mathbf{v}_{rel}\rvert)$ (est.)	$\max(\lvert\mathbf{v}_{rel}\rvert)$ (val.)
Iteration #8	3.873 %	7.78 %	$1.095 \cdot 10^{-4}$	14.85 %	20.92 %
Iteration #14	2.54 %	7.23 %	$4.73 \cdot 10^{-5}$	9.51 %	17.6 %

It can be seen that although the relative validation RMS does not decrease much from the 8th iteration till the 14th, the maximum relative residual shows an appreciable decrease, which is related to the nonlinear terms present in the last model, as it can be seen in the presented model cuts (Figure D.12). It can be seen how the model deficiencies at the edges of the cuts for the control surfaces disappear, or how the model at the 8th iteration misses a large part of the phenomena related to the angle of attack variation. The model at the 14th iteration does a better work to explain the dataset, and fits the data much better, having as only drawback a single coefficient with a considerably higher variance ($\hat{\theta}_{13}$) . However, this variance is still considered to be small, and it does not affect dramatically the output confidence bounds, which indeed, are much tighter than for the model at the 8th iteration. For these reasons, the higher complexity of this model is accepted for the sake of a more accurate model, and considered to be the best candidate for the polynomial model structure for the Flying V pitching moment coefficient.

As it can be seen, the model structure determination is usually a back and forth, trial and error process, until the right combination of regressors which has small variances, normal residuals, good fit, etc. is found, including the preliminary step of finding a proper pool of regressors for each coefficient and its order for the orthogonalization.

5.1.2 Parameter estimation

Once the model structure is determined and fixed for each coefficient, the de-orthogonalization of the regressors takes place, in order to recover the dependencies in terms of the original independent variables. The final aerodynamic model structure for the 5 estimated coefficients after the de-orthogonalization is shown below in the form of equations to show their dependencies, and the values of the parameters including their confidence bounds (confidence level $\alpha = 0.05 \longrightarrow 95\%$) are presented in Tables 5.3-5.7.

It should be noted that the confidence bounds for the original regressors could not be calculated in the way described in Section 2.3.2. This method was used to calculate the confidence bounds for the orthogonal regressors used during for the estimation. The confidence bounds for the original regressors were calculated then by de-orthogonalizing two models: one for $\boldsymbol{\theta} = \hat{\boldsymbol{\theta}}$ and another one for $\boldsymbol{\theta} = \hat{\boldsymbol{\theta}} + \Delta\hat{\boldsymbol{\theta}}$, and subtracting the difference in the model coefficients.

$$\begin{aligned} C_X = C_{X0} + C_{X\alpha} \cdot \alpha + C_{X\alpha^2} \cdot \alpha^2 + C_{X\alpha^3} \cdot \alpha^3 + C_{X\alpha^4} \cdot \alpha^4 + C_{X\delta_1} \cdot \delta_1 + C_{X\delta_2} \cdot \delta_2 + \\ + C_{X\delta_3} \cdot \delta_3 + C_{X\delta_1^2} \cdot \delta_1^2 + C_{X\delta_2^2} \cdot \delta_2^2 + C_{X\hat{V}} \cdot \hat{V} + C_{X\hat{V}^2} \cdot \hat{V}^2 \end{aligned} \tag{5.1}$$

$$C_Z = C_{Z0} + C_{Z\alpha} \cdot \alpha + C_{Z\alpha^2} \cdot \alpha^2 + C_{Z\alpha^3} \cdot \alpha^3 + C_{Z\delta_1} \cdot \delta_1 + C_{Z\delta_2} \cdot \delta_2 + C_{Z\delta_3} \cdot \delta_3 + C_{Z\hat{V}} \cdot \hat{V} \tag{5.2}$$

$$C_l = C_{l0} + C_{l\alpha} \cdot \alpha + C_{l\alpha^2} \cdot \alpha^2 + C_{l\alpha^3} \cdot \alpha^3 + C_{l\alpha^4} \cdot \alpha^4 + C_{l\delta_1} \cdot \delta_1 + C_{l\delta_2} \cdot \delta_2 + C_{l\delta_3} \cdot \delta_3 + C_{l\hat{V}} \cdot \hat{V} \tag{5.3}$$

$$\begin{aligned} C_m = C_{m0} + C_{m\alpha} \cdot \alpha + C_{m\alpha^2} \cdot \alpha^2 + C_{m\alpha^3} \cdot \alpha^3 + C_{m\alpha^4} \cdot \alpha^4 + C_{m\delta_1} \cdot \delta_1 + C_{m\delta_2} \cdot \delta_2 + \\ + C_{m\delta_3} \cdot \delta_3 + C_{m\delta_1^2} \cdot \delta_1^2 + C_{m\delta_2^2} \cdot \delta_2^2 + C_{m\delta_1\delta_2} \cdot (\delta_1 \cdot \delta_2) + C_{m\alpha\delta_1^2} \cdot (\alpha \cdot \delta_1^2) + C_{m\alpha\delta_2^2} \cdot (\alpha \cdot \delta_2^2) + \\ + C_{m\alpha^2\delta_1} \cdot (\alpha^2 \cdot \delta_1) + C_{m\alpha^2 \cdot \delta_2} \cdot (\alpha^2 \delta_2) + C_{m\hat{V}} \cdot \hat{V} + C_{m\hat{V}\delta_1} \cdot (\hat{V} \cdot \delta_1) \end{aligned} \tag{5.4}$$

$$C_n = C_{n0} + C_{\alpha} \cdot \alpha + C_{\alpha^2} \cdot \alpha^2 + C_{\alpha^3} \cdot \alpha^3 + C_{\alpha^4} \cdot \alpha^4 + C_{\delta_1} \cdot \delta_1 + C_{\delta_2} \cdot \delta_2 + C_{\delta_1^2} \cdot \delta_1^2 + C_{\delta_2^2} \cdot \delta_2^2 + C_{\hat{V}} \cdot \hat{V} \tag{5.5}$$

In these equations, $\alpha, \delta_1, \delta_2, \delta_3$ are in radians, and the dimensionless wind speed is defined as $\hat{V} = V/V_{ref}$, with the wind speed in meters per second and $V_{ref} = 20$ m/s for the subscale model. The equivalent reference airspeed for the full-scale aircraft would be $(V_{ref})_{fs} = (V_{ref})_{ss}/\sqrt{n} \sim 335$ km/h[50].

Table 5.3: Coefficients of the polynomial model for C_X

Parameter	Value ± confidence bounds
C_{X0}	$-2.029 \cdot 10^{-2} \pm (8.556 \cdot 10^{-4})$
$C_{X\alpha}$	$4.288 \cdot 10^{-2} \pm (2.662 \cdot 10^{-3})$
$C_{X\alpha^2}$	$9.792 \cdot 10^{-1} \pm (2.227 \cdot 10^{-3})$
$C_{X\alpha^3}$	$-1.617 \cdot 10^{-2} \pm (7.731 \cdot 10^{-2})$
$C_{X\alpha^4}$	$-1.519 \pm (1.639 \cdot 10^{-1})$
$C_{X\delta_1}$	$1.060 \cdot 10^{-2} \pm (6.473 \cdot 10^{-4})$
$C_{X\delta_2}$	$7.162 \cdot 10^{-3} \pm (1.193 \cdot 10^{-3})$
$C_{X\delta_3}$	$6.893 \cdot 10^{-4} \pm (1.294 \cdot 10^{-4})$
$C_{X\delta_1^2}$	$-3.928 \cdot 10^{-2} \pm (2.945 \cdot 10^{-3})$
$C_{X\delta_2^2}$	$-2.047 \cdot 10^{-2} \pm (4.027 \cdot 10^{-3})$
$C_{X\hat{V}}$	$8.727 \cdot 10^{-3} \pm (3.708 \cdot 10^{-4})$
$C_{X\hat{V}^2}$	$-3.075 \cdot 10^{-3} \pm (3.318 \cdot 10^{-4})$

Table 5.4: Coefficients of the polynomial model for C_Z

Parameter	Value ± confidence bounds
C_{Z0}	$-7.583 \cdot 10^{-2} \pm (5.310 \cdot 10^{-3})$
$C_{Z\alpha}$	$-1.943 \pm (1.564 \cdot 10^{-2})$
$C_{Z\alpha^2}$	$-1.026 \pm (1.288 \cdot 10^{-1})$
$C_{Z\alpha^3}$	$1.866 \pm (2.343 \cdot 10^{-1})$
$C_{Z\delta_1}$	$-1.353 \cdot 10^{-1} \pm (5.239 \cdot 10^{-3})$
$C_{Z\delta_2}$	$-8.462 \cdot 10^{-2} \pm (6.915 \cdot 10^{-3})$
$C_{Z\delta_3}$	$-5.012 \cdot 10^{-3} \pm (7.192 \cdot 10^{-4})$
$C_{Z\hat{V}}$	$3.747 \cdot 10^{-2} \pm (7.564 \cdot 10^{-3})$

Table 5.5: Coefficients of the polynomial model for C_l

Parameter	Value ± confidence bounds
C_{l0}	$3.584 \cdot 10^{-3} \pm (4.866 \cdot 10^{-4})$
$C_{l\alpha}$	$1.842 \cdot 10^{-1} \pm (1.895 \cdot 10^{-3})$
$C_{l\alpha^2}$	$-1.543 \cdot 10^{-2} \pm (4.737 \cdot 10^{-4})$
$C_{l\alpha^3}$	$3.215 \cdot 10^{-1} \pm (4.315 \cdot 10^{-2})$
$C_{l\alpha^4}$	$-8.141 \cdot 10^{-1} \pm (8.337 \cdot 10^{-2})$
$C_{l\delta_1}$	$1.842 \cdot 10^{-2} \pm (2.649 \cdot 10^{-4})$
$C_{l\delta_2}$	$1.450 \cdot 10^{-2} \pm (3.125 \cdot 10^{-4})$
$C_{l\delta_3}$	$9.893 \cdot 10^{-3} \pm (5.844 \cdot 10^{-4})$
$C_{l\hat{V}}$	$-3.036 \cdot 10^{-3} \pm (5.311 \cdot 10^{-4})$

Table 5.6: Coefficients of the polynomial model for C_m

Parameter	Value ± confidence bounds
C_{m0}	$3.361 \cdot 10^{-2} \pm (2.788 \cdot 10^{-3})$
$C_{m\alpha}$	$-1.069 \cdot 10^{-1} \pm (5.938 \cdot 10^{-3})$
$C_{m\alpha^2}$	$-2.883 \cdot 10^{-1} \pm (6.506 \cdot 10^{-3})$
$C_{m\alpha^3}$	$-8.492 \cdot 10^{-1} \pm (1.839 \cdot 10^{-1})$
$C_{m\alpha^4}$	$4.088 \pm (3.731 \cdot 10^{-1})$
$C_{m\delta_1}$	$-1.482 \cdot 10^{-1} \pm (2.139 \cdot 10^{-3})$
$C_{m\delta_2}$	$-1.092 \cdot 10^{-1} \pm (1.433 \cdot 10^{-3})$
$C_{m\delta_3}$	$-6.377 \cdot 10^{-2} \pm (3.673 \cdot 10^{-3})$
$C_{m\delta_1^2}$	$1.039 \cdot 10^{-1} \pm (1.608 \cdot 10^{-2})$
$C_{m\delta_2^2}$	$3.400 \cdot 10^{-2} \pm (1.127 \cdot 10^{-2})$
$C_{m\delta_1\delta_2}$	$6.120 \cdot 10^{-2} \pm (1.248 \cdot 10^{-2})$
$C_{m\alpha\delta_1^2}$	$-5.459 \cdot 10^{-1} \pm (5.529 \cdot 10^{-2})$
$C_{m\alpha\delta_2^2}$	$-2.125 \cdot 10^{-1} \pm (4.211 \cdot 10^{-2})$
$C_{m\alpha^2\delta_1}$	$1.729 \cdot 10^{-1} \pm (4.450 \cdot 10^{-2})$
$C_{m\alpha^2\delta_2}$	$1.775 \cdot 10^{-1} \pm (3.443 \cdot 10^{-2})$
$C_{m\hat{V}}$	$8.071 \cdot 10^{-3} \pm (3.664 \cdot 10^{-3})$
$C_{m\hat{V}\delta_1}$	$2.203 \cdot 10^{-3} \pm (4.492 \cdot 10^{-4})$

Table 5.7: Coefficients of the polynomial model for C_n

Parameter	Value ± confidence bounds
C_{n0}	$2.636 \cdot 10^{-3} \pm (2.609 \cdot 10^{-4})$
$C_{n\alpha}$	$5.085 \cdot 10^{-5} \pm (4.599 \cdot 10^{-4})$
$C_{n\alpha^2}$	$9.565 \cdot 10^{-3} \pm (5.479 \cdot 10^{-4})$
$C_{n\alpha^3}$	$-2.732 \cdot 10^{-1} \pm (1.304 \cdot 10^{-2})$
$C_{n\alpha^4}$	$2.324 \cdot 10^{-1} \pm (2.823 \cdot 10^{-2})$
$C_{n\delta_1}$	$-1.097 \cdot 10^{-3} \pm (1.224 \cdot 10^{-4})$
$C_{n\delta_2}$	$-1.311 \cdot 10^{-3} \pm (2.030 \cdot 10^{-4})$
$C_{n\delta_1^2}$	$-6.060 \cdot 10^{-3} \pm (8.422 \cdot 10^{-4})$
$C_{n\delta_2^2}$	$-5.544 \cdot 10^{-3} \pm (6.520 \cdot 10^{-4})$
$C_{n\hat{V}}$	$-1.075 \cdot 10^{-3} \pm (2.293 \cdot 10^{-4})$

5.1.3 Model validation

The models characteristics are summarized in Table 5.8, where the metrics used for the selection are presented.

Table 5.8: Model characteristics (polynomial models)

	RMS_{rel} (est.)	RMS_{rel} (val.)	F-statistic	R^2	PSE	$\hat{\sigma}^2$
C_X model	1.42 %	2.42 %	$2.452 \cdot 10^4$	99.74 %	$5.422 \cdot 10^{-5}$	$7.193 \cdot 10^{-6}$
C_Z model	1.42 %	2.38 %	$3.870 \cdot 10^4$	99.70 %	$1.881 \cdot 10^{-3}$	$4.236 \cdot 10^{-4}$
C_m model	2.54 %	7.24 %	$2.516 \cdot 10^3$	98.00 %	$9.416 \cdot 10^{-5}$	$4.732 \cdot 10^{-5}$
C_l model	1.18 %	4.59 %	$4.264 \cdot 10^4$	99.80 %	$1.747 \cdot 10^{-5}$	$2.287 \cdot 10^{-6}$
C_n model	2.25 %	2.74 %	$8.286 \cdot 10^3$	99.11 %	$7.394 \cdot 10^{-7}$	$2.830 \cdot 10^{-7}$

All models are considered adequate in terms of model fit, and their high values of the F-statistic and the coefficient of determination are indicators of a good model. The maximum absolute relative residuals for the models are presented in Table 5.9, where it can be seen that the pitching moment coefficient has relatively large values for the maximum residuals (specially in the validation dataset), which could indicate model deficiencies, or the presence of outliers in the data due to measurement errors as it was anticipated in Section 4.3. The coefficient for the yawing moment also shows higher maximum relative residuals, which come from the inability to model some nonlinearities around $\alpha = 0°$, which can be seen in Figure D.15.

Table 5.9: Maximum absolute relative residuals of the polynomial models

	$\max(\lvert\mathbf{v}_{rel}\rvert)$ (est.)	$\max(\lvert\mathbf{v}_{rel}\rvert)$ (val.)
C_X model	4.96 %	6.52 %
C_Z model	3.99 %	6.20 %
C_m model	9.51 %	17.60 %
C_l model	3.96 %	8.05 %
C_n model	9.67 %	9.65 %

A residual analysis to test the whiteness and normality assumptions was done for each model and the results are shown in Figures D.2, D.5, D.8, D.11, D.14, for C_X, C_Z, C_l, C_m, C_n respectively. It can be seen that there seems to be a deterministic trend in the residuals of the models for C_X and C_Z, while residuals from C_l, C_m, C_n look more random. Some "blank areas" can be seen in the residual from C_n, but they are solely because of the lack of datapoints in those regions.

These unmodeled characteristics in C_X and C_Z have their origin in a change of the lift slope at $\alpha \cong 10°$, which can be clearly seen in Figure 4.4 from Chapter 4. This will be further discussed and compared with the spline model in Section 5.3.

The mean of all the validation residuals is distinct from zero, which is one of the assumptions required to derive the OLS estimator, but it is not expected to affect the estimation greatly expect in the case of the rolling moment coefficient, where the mean of the residual is considerably far from zero, given the absolute value of the residuals.

In the case where the residuals cannot be considered white (C_X, C_Z, C_l), the estimates are expected to be biased. As it was mentioned before, these models are Taylor approximations of the aerodynamic coefficient, and so are intrinsically inaccurate far from the center of the series. Because of the large range that this model aims to approximate ($\alpha \in [-10, 30]^\circ$), these polynomial models fail to explain all the nonlinearities present in the data.

This problem can easily be solved by partitioning the data: the dataset is split in smaller ones which span only a limited range of the independent variables, and a different model is estimated for each partition, which leads to a piecewise continuous model. This technique has been used with good results in the past [19, 43], and can be used to fix the polynomial models. However, a single spline model to cover the whole range of angles of attack could also be estimated with the current framework, which has a higher approximation power and is preferred in order to keep a continuous model over the complete dataset.

Regarding the normality assumption, they all seem to hold for the most part of the points (note the density of points at the center of the interval), so the confidence bounds derived from it are assumed to be reasonably accurate, and indeed most datapoints seem to fall within the prediction confidence bounds (Figures D.3, D.6, D.9, D.12, D.15).

Even though model deficiencies are present, the low value of the RMS and the rest of satisfactory characteristics of the estimation suggests that if only the flyable region of the flight envelope is estimated, polynomial models will perform better, and in the author's opinion they should still be considered as a first model to be tried because of their higher simplicity, and because the results also give an idea of how nonlinear the observed data is.

5.1.4 Sensitivity analysis

A sensitivity analysis was done in order to assess whether changes in the parameter estimates would lead to large changes in the model errors in the estimation and validation datasets. Each parameter was perturbed individually with its 95% confidence bounds ($(100(1-\alpha),\ \alpha = 0.05)$, and the change in relative RMS was calculated for each case. The results are shown in Figure 5.2.

It can be seen that both the positive and negative perturbation lead to the same increase of the error in the estimation dataset for every regressor due to the normalization done during the orthogonalization process. In the validation dataset, the perturbation of the first regressors leads to a higher increase of the error because of their higher relevance. The same sign of the error in the estimation dataset comes from the fact that OLS minimizes the square error, so deviations from the estimated parameters will always increase it; in the validation dataset, the sign depends on the specific data used (which should be independent from the estimation dataset), and so it does not follow a pattern.

The sensitivity of the error to changes of the parameters is remarkably small, leading to a maximum error increase of $\sim 5 \cdot 10^{-3}\%$ in the estimation dataset and $\sim 0.15\%$, so the parameter estimates from the Stepwise Regression + Multivariate Orthogonal Functions seem to be robust against perturbations, and even though the estimates will be biased as it was discussed above, they lead to reasonably accurate models.

5.2 Spline models

Models using splines in the angle of attack were used to cope with the inability of the polynomial models to identify the complete measured range of angles of attack. If each of the terms that form the splines are used as independent regressors, stepwise regression will find the most significant knot locations and its degree, using the framework described above.

The orthogonalization method presented above could be applied to splines too, but it was decided not to since it led to models in which the first regressors orthogonalized were always the most significant to the model. This behavior is due to the high similarity among the regressors: the contribution of each regressor is removed from the next regressors in the orthogonalization, so if two regressors have a similar contribution, such as $(\alpha - \alpha_m)^d$ for $d = 1, 2, ...$; the first regressor to be orthogonalized

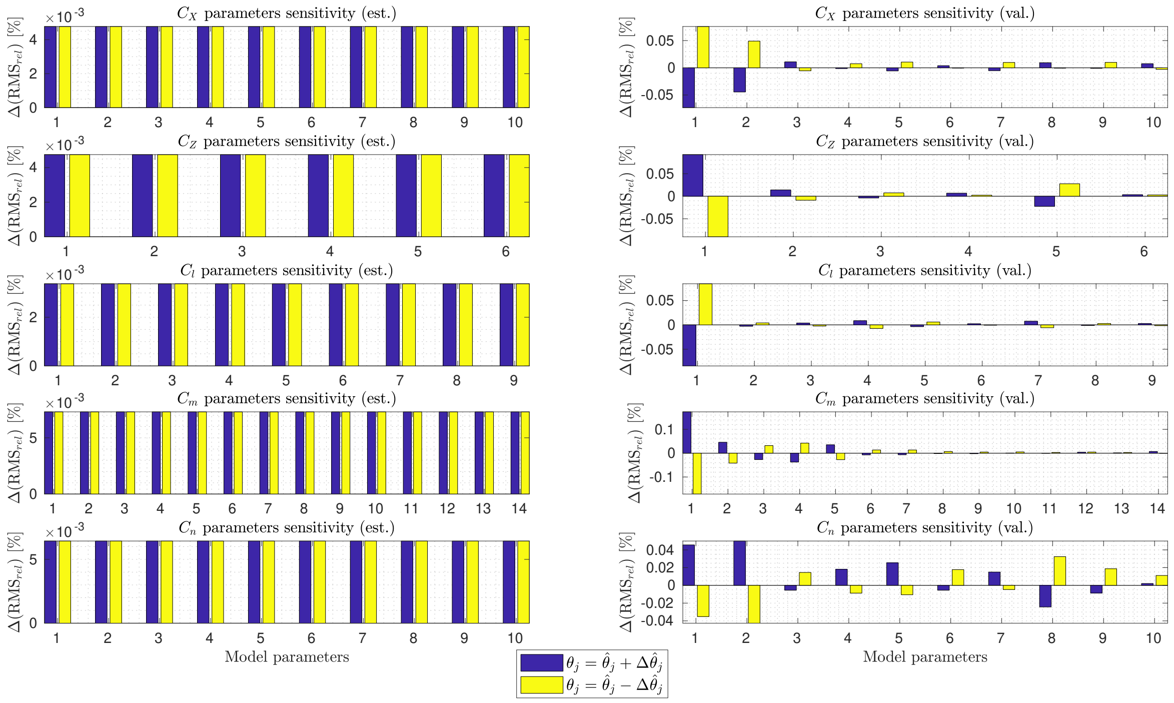

Figure 5.2: Sensitivity of the estimation and validation relative RMS to changes in the polynomial model parameters equal to their confidence bounds

will remove most of the significant information of the next ones. Collinearity among the regressors needs to be addressed then to validate the estimation.

It should be noted that once the stepwise regression (without orthogonalization) was completed, Multivariate Orthogonal Functions were introduced using the already estimated model structure to sort the regressors in order of significance. Although the orthogonal spline models were also good and they led to models with smaller variances and no collinearity, the non-orthogonal models showed a closer similarity between the estimation and validation dataset (fit, whiteness, and normality) keeping the variances sufficiently small, so they were accepted as better models and are the only ones shown here.

From Eq. 2.19, substituting $n_\alpha = n_{\delta_i} = n_{\hat{V}} = 0$ gives a linear spline model in the angle of attack, which in principle should be able to perfectly reproduce the aerodynamics by the successive addition of knots. However, because of the already mentioned collinearity of the knots, the variances become increasingly higher with the number of knots in the model, so polynomial coupling terms such as $(\alpha \cdot \delta_i)$ are also allowed in the model in order to improve the fitting without such a large penalty in the variances.

5.2.1 Model structure determination

Analogically to the previous section, the model structure determination process is presented for the pitching moment coefficient. The results from the rest of the models are presented in Appendix D. Figure 5.3 shows the results of the stepwise regression, where the best three candidates are selected because of their maximum values of the F-statistic (local and global), the low values of PSE (the three of them are in a plateau), and because after that point the relative RMS stagnates and the small decreases of the errors are not worth the increase of the variances.

The residual analysis (Figures D.29) showed a very good agreement with the whiteness and normality assumptions for the three models, for both the estimation and validation datasets, so all three models are considered valid in this sense.

The parameter variances are shown in Table 5.10, and the model fit evolution in Table 5.11. The model cuts (Figure D.30) show that the model at iteration #8 fails to capture most of the present nonlinearities in the dataset, while the greatest difference between iteration #14 and 17 is the tighter

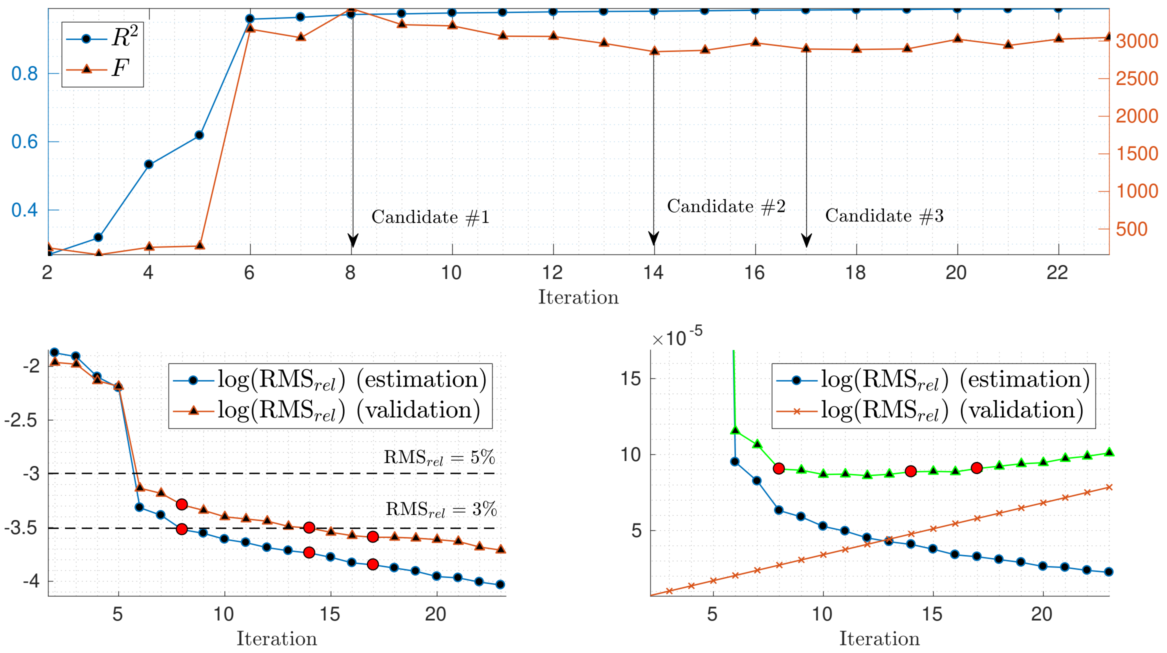

Figure 5.3: Stepwise regression results for the spline model for C_m

confidence bounds regarding $\hat{V}$ and δ_3, which is patent by visually comparing the figures. Model #8 has the smallest variances, but it is discarded because of its larger errors. Between model #14 and #17 the increase of the variances is not so great since the most conflicting parameter is $\hat{\theta}_{10}$, which is present in both models. A study of the collinearity (Figure D.32) suggests that the increase of the collinearity due to the extra three regressors of the last model is not problematic, so it is decided as the best one because of its better capture of the aerodynamic response.

Table 5.10: Parameter variances for the candidates of the C_m spline model

Parameter	Var($\hat{\theta}_j$) (model #8)	Var($\hat{\theta}_j$) (model #14)	Var($\hat{\theta}_j$) (model #17)
$\hat{\theta}_1$	$4.106 \cdot 10^{-6}$	$1.692 \cdot 10^{-5}$	$1.386 \cdot 10^{-5}$
$\hat{\theta}_2$	$4.083 \cdot 10^{-6}$	$2.819 \cdot 10^{-5}$	$2.273 \cdot 10^{-5}$
$\hat{\theta}_3$	$3.785 \cdot 10^{-6}$	$2.799 \cdot 10^{-6}$	$3.023 \cdot 10^{-6}$
$\hat{\theta}_4$	$2.248 \cdot 10^{-3}$	$1.966 \cdot 10^{-2}$	$1.624 \cdot 10^{-2}$
$\hat{\theta}_5$	$3.261 \cdot 10^{-6}$	$2.404 \cdot 10^{-6}$	$6.131 \cdot 10^{-6}$
$\hat{\theta}_6$	$3.646 \cdot 10^{-6}$	$2.527 \cdot 10^{-6}$	$2.061 \cdot 10^{-6}$
$\hat{\theta}_7$	$6.828 \cdot 10^{-6}$	$4.767 \cdot 10^{-6}$	$3.893 \cdot 10^{-6}$
$\hat{\theta}_8$	$4.195 \cdot 10^{-6}$	$2.919 \cdot 10^{-6}$	$2.377 \cdot 10^{-6}$
$\hat{\theta}_9$	–	$3.788 \cdot 10^{-5}$	$3.196 \cdot 10^{-5}$
$\hat{\theta}_{10}$	–	$7.014 \cdot 10^{-1}$	$5.728 \cdot 10^{-1}$
$\hat{\theta}_{11}$	–	$2.016 \cdot 10^{-5}$	$1.661 \cdot 10^{-5}$
$\hat{\theta}_{12}$	–	$3.208 \cdot 10^{-5}$	$2.595 \cdot 10^{-5}$
$\hat{\theta}_{13}$	–	$3.147 \cdot 10^{-5}$	$2.537 \cdot 10^{-5}$
$\hat{\theta}_{14}$	–	$3.497 \cdot 10^{-5}$	$3.035 \cdot 10^{-5}$
$\hat{\theta}_{15}$	–	–	$3.653 \cdot 10^{-4}$
$\hat{\theta}_{16}$	–	–	$2.885 \cdot 10^{-5}$
$\hat{\theta}_{17}$	–	–	$8.540 \cdot 10^{-6}$

Table 5.11: Model fit comparison for the C_m spline model candidates

	RMS_{rel} (est.)	RMS_{rel} (val.)	$\hat{\sigma}^2$	$\max(\lvert\mathbf{v}_{rel}\rvert)$ (est.)	$\max(\lvert\mathbf{v}_{rel}\rvert)$ (val.)
Iteration #8	2.96 %	3.73 %	$6.393 \cdot 10^{-5}$	10.18 %	12.14 %
Iteration #14	2.38 %	3.00 %	$4.174 \cdot 10^{-5}$	12.10 %	9.50 %
Iteration #17	2.13 %	2.76 %	$3.362 \cdot 10^{-5}$	9.32 %	10.62 %

5.2.2 Parameter estimation

The equations for the spline models are shown below, and the parameter estimates, confidence bounds, parameter variances and VIFs are presented in Tables 5.12-5.16.

$$\begin{aligned} C_X = {} & C_{X\alpha} \cdot \alpha + C_{X\alpha^2} \cdot \alpha^2 + C_{X\delta_1} \cdot \delta_1 + C_{X\delta_2} \cdot \delta_2 + C_{X\delta_3} \cdot \delta_3 + \\ & + C_{X\hat{V}} \cdot \hat{V} + C_{X\hat{V}^2} \cdot \hat{V}^2 + C_{X\alpha_{20}^2} \cdot (\alpha - \alpha_{20^\circ})_+^2 \end{aligned} \tag{5.6}$$

$$\begin{aligned} C_Z = {} & C_{Z0} + C_{Z\alpha} \cdot \alpha + C_{Z\delta_1} \cdot \delta_1 + C_{Z\delta_2} \cdot \delta_2 + C_{Z\delta_3} \cdot \delta_3 + C_{Z\hat{V}} \cdot \hat{V} + \\ & + C_{Z\alpha_{11}^1} \cdot (\alpha - \alpha_{11^\circ})_+ + C_{Z\alpha_{17}^2} \cdot (\alpha - \alpha_{17^\circ})_+^2 \end{aligned} \tag{5.7}$$

$$\begin{aligned} C_l = {} & C_{l\alpha} \cdot \alpha + C_{l\delta_1} \cdot \delta_1 + C_{l\delta_2} \cdot \delta_2 + C_{l\delta_3} \cdot \delta_3 + C_{l\alpha_2^1} \cdot (\alpha - \alpha_{2^\circ})_+ + \\ & + C_{l\alpha_{20}^2} \cdot (\alpha - \alpha_{20^\circ})_+^2 + C_{l\delta_2\alpha_{14}} \cdot \delta_2 \cdot (\alpha - \alpha_{14^\circ})_+^0 + C_{l\delta_1\alpha_{23}} \cdot \delta_1 \cdot (\alpha - \alpha_{23^\circ})_+^0 \end{aligned} \tag{5.8}$$

$$\begin{aligned} C_m = {} & C_{m0} + C_{m\alpha} \cdot \alpha + C_{m\delta_1} \cdot \delta_1 + C_{m\delta_2} \cdot \delta_2 + C_{m\delta_3} \cdot \delta_3 + C_{m\hat{V}} \cdot \hat{V} + \\ & + C_{m\delta_1\delta_2} \cdot \delta_1\delta_2 + C_{m\delta_2\delta_3} \cdot \delta_2 \cdot \delta_3 + C_{m\delta_2^2} \cdot \delta_2^2 + C_{m\alpha\delta_2^2} \cdot \alpha \cdot \delta_2^2 + \\ & + C_{m\alpha_{20}^2} \cdot (\alpha - \alpha_{20^\circ})_+^2 + C_{m\alpha_{26}^2} \cdot (\alpha - \alpha_{26^\circ})_+^2 + \\ & + C_{m\delta_1\alpha_2} \cdot \delta_1 \cdot (\alpha - \alpha_{2^\circ})_+^0 + C_{m\delta_1\alpha_{23}} \cdot \delta_1 \cdot (\alpha - \alpha_{23^\circ})_+^0 + \\ & + C_{m\delta_2\alpha_{-7}} \cdot \delta_2 \cdot (\alpha - \alpha_{-7^\circ})_+^0 + C_{m\delta_2\alpha_{14}} \cdot \delta_2 \cdot (\alpha - \alpha_{14^\circ})_+^0 + \\ & + C_{m\delta_3\alpha_8} \cdot \delta_3 \cdot (\alpha - \alpha_{8^\circ})_+ \end{aligned} \tag{5.9}$$

$$\begin{aligned} C_n = {} & C_{n0} + C_{n\alpha} \cdot \alpha + C_{n\alpha^2} \cdot \alpha^2 + C_{n\delta_1} \cdot \delta_1 + C_{n\delta_2} \cdot \delta_2 + C_{n\delta_2^2} \cdot \delta_2^2 + \\ & + C_{n\hat{V}} \cdot \hat{V} + C_{n\alpha_8^1} \cdot (\alpha - \alpha_{8^\circ})_+ + C_{n\alpha_5^2} \cdot (\alpha - \alpha_{5^\circ})_+^2 \end{aligned} \tag{5.10}$$

Table 5.12: Coefficients of the spline model for C_X

Parameter	Value ± confidence bounds	Variance	VIF
$C_{X\alpha}$	$4.590 \cdot 10^{-2} \pm (3.49 \cdot 10^{-3})$	$9.003 \cdot 10^{-7}$	1.169
$C_{X\alpha_2}$	$7.484 \cdot 10^{-1} \pm (1.29 \cdot 10^{-2})$	$1.072 \cdot 10^{-6}$	46.946
$C_{X\delta_1}$	$8.103 \cdot 10^{-3} \pm (1.86 \cdot 10^{-3})$	$5.851 \cdot 10^{-7}$	1.331
$C_{X\delta_2}$	$6.727 \cdot 10^{-3} \pm (1.50 \cdot 10^{-3})$	$7.476 \cdot 10^{-7}$	1.419
$C_{X\delta_3}$	$7.246 \cdot 10^{-3} \pm (1.69 \cdot 10^{-3})$	$7.144 \cdot 10^{-7}$	38.009
$C_{X\hat{V}}$	$-2.276 \cdot 10^{-2} \pm (2.03 \cdot 10^{-3})$	$3.166 \cdot 10^{-6}$	9.810
$C_{X\hat{V}^2}$	$1.011 \cdot 10^{-2} \pm (1.66 \cdot 10^{-3})$	$4.334 \cdot 10^{-5}$	19.783
$C_{X\alpha_{20}^2}$	$-1.921 \pm (7.88 \cdot 10^{-2})$	$1.616 \cdot 10^{-3}$	4.127

where all angles are in radians, and α_* is the angle of attack (in radians) where the knots are located (labeled in degrees for a better readability).

Table 5.13: Coefficients of the spline model for C_Z

Parameter	Value ± confidence bounds	Variance	VIF
C_{Z0}	$-8.554 \cdot 10^{-2} \pm (5.53 \cdot 10^{-3})$	$6.866 \cdot 10^{-6}$	42.245
$C_{Z\alpha}$	$-1.869 \pm (8.62 \cdot 10^{-3})$	$7.966 \cdot 10^{-6}$	46.476
$C_{Z\delta_1}$	$-1.284 \cdot 10^{-1} \pm (5.31 \cdot 10^{-3})$	$5.932 \cdot 10^{-6}$	1.363
$C_{Z\delta_2}$	$-7.395 \cdot 10^{-2} \pm (3.70 \cdot 10^{-3})$	$3.878 \cdot 10^{-3}$	4.860
$C_{Z\delta_3}$	$-4.303 \cdot 10^{-2} \pm (4.77 \cdot 10^{-3})$	$1.550 \cdot 10^{-4}$	15.576
$C_{Z\hat{V}}$	$3.126 \cdot 10^{-2} \pm (5.14 \cdot 10^{-3})$	$1.933 \cdot 10^{-5}$	8.590
$C_{Z\alpha^1_{11}}$	$-5.559 \cdot 10^{-1} \pm (2.44 \cdot 10^{-2})$	$7.350 \cdot 10^{-6}$	1.156
$C_{Z\alpha^2_{17}}$	$3.176 \pm (1.22 \cdot 10^{-1})$	$3.572 \cdot 10^{-6}$	1.247

Table 5.14: Coefficients of the spline model for C_l

Parameter	Value ± confidence bounds	Variance	VIF
$C_{l\alpha}$	$1.959 \cdot 10^{-1} \pm (2.21 \cdot 10^{-3})$	$1.269 \cdot 10^{-6}$	27.538
$C_{l\delta_1}$	$1.891 \cdot 10^{-2} \pm (7.38 \cdot 10^{-4})$	$1.072 \cdot 10^{-7}$	1.425
$C_{l\delta_2}$	$1.690 \cdot 10^{-2} \pm (8.42 \cdot 10^{-4})$	$9.441 \cdot 10^{-5}$	1.689
$C_{l\delta_3}$	$9.542 \cdot 10^{-3} \pm (6.42 \cdot 10^{-4})$	$2.832 \cdot 10^{-7}$	2.897
$C_{l\alpha^1_2}$	$-1.077 \cdot 10^{-2} \pm (2.60 \cdot 10^{-3})$	$1.416 \cdot 10^{-7}$	1.288
$C_{l\alpha^2_{20}}$	$-6.556 \cdot 10^{-1} \pm (1.90 \cdot 10^{-2})$	$1.847 \cdot 10^{-7}$	2.944
$C_{l\delta_2\alpha_{14}}$	$-4.619 \cdot 10^{-3} \pm (1.04 \cdot 10^{-3})$	$1.755 \cdot 10^{-6}$	29.548
$C_{l\delta_1\alpha_{23}}$	$-4.795 \cdot 10^{-3} \pm (2.37 \cdot 10^{-3})$	$1.468 \cdot 10^{-6}$	1.104

Table 5.15: Coefficients of the spline model for C_m

Parameter	Value ± confidence bounds	Variance	VIF
C_{m0}	$2.440 \cdot 10^{-2} \pm (3.02 \cdot 10^{-3})$	$3.653 \cdot 10^{-4}$	4.960
$C_{m\alpha}$	$-1.461 \cdot 10^{-1} \pm (3.41 \cdot 10^{-3})$	$2.061 \cdot 10^{-6}$	43.964
$C_{m\delta_1}$	$-9.921 \cdot 10^{-2} \pm (7.30 \cdot 10^{-3})$	$5.728 \cdot 10^{-1}$	18.881
$C_{m\delta_2}$	$-8.065 \cdot 10^{-2} \pm (9.34 \cdot 10^{-3})$	$1.661 \cdot 10^{-5}$	7.801
$C_{m\delta_3}$	$-7.077 \cdot 10^{-2} \pm (4.85 \cdot 10^{-3})$	$2.595 \cdot 10^{-5}$	1.171
$C_{m\hat{V}}$	$1.383 \cdot 10^{-2} \pm (2.81 \cdot 10^{-3})$	$1.624 \cdot 10^{-2}$	22.655
$C_{m\delta_2^2}$	$4.729 \cdot 10^{-2} \pm (1.05 \cdot 10^{-2})$	$2.273 \cdot 10^{-5}$	27.494
$C_{m\alpha\delta_2^2}$	$-2.243 \cdot 10^{-1} \pm (3.75 \cdot 10^{-2})$	$6.131 \cdot 10^{-6}$	4.885
$C_{m\delta_1\delta_2}$	$4.165 \cdot 10^{-2} \pm (1.11 \cdot 10^{-2})$	$2.885 \cdot 10^{-5}$	5.039
$C_{m\delta_2\delta_3}$	$3.312 \cdot 10^{-2} \pm (1.08 \cdot 10^{-2})$	$8.540 \cdot 10^{-6}$	5.357
$C_{m\alpha^2_{20}}$	$5.545 \pm (2.50 \cdot 10^{-1})$	$2.537 \cdot 10^{-5}$	29.542
$C_{m\alpha^2_{26}}$	$-8.353 \pm (1.48 \cdot 10^{0})$	$3.035 \cdot 10^{-5}$	2.330
$C_{m\delta_1\alpha_2}$	$-4.691 \cdot 10^{-2} \pm (7.99 \cdot 10^{-3})$	$1.386 \cdot 10^{-5}$	7.560
$C_{m\delta_1\alpha_{23}}$	$5.040 \cdot 10^{-2} \pm (9.99 \cdot 10^{-3})$	$3.893 \cdot 10^{-6}$	2.823
$C_{m\delta_2\alpha_{-7}}$	$-3.080 \cdot 10^{-2} \pm (9.87 \cdot 10^{-3})$	$3.196 \cdot 10^{-5}$	1.602
$C_{m\delta_2\alpha_{14}}$	$3.383 \cdot 10^{-2} \pm (3.87 \cdot 10^{-3})$	$2.377 \cdot 10^{-6}$	48.083
$C_{m\delta_3\alpha_8}$	$1.476 \cdot 10^{-2} \pm (5.73 \cdot 10^{-3})$	$3.023 \cdot 10^{-6}$	4.656

Table 5.16: Coefficients of the spline model for C_n

Parameter	Value ± confidence bounds	Variance	VIF
C_{n0}	$2.200 \cdot 10^{-3} \pm (2.68 \cdot 10^{-4})$	$7.940 \cdot 10^{-8}$	2.026
$C_{n\hat{V}}$	$-1.039 \cdot 10^{-3} \pm (2.31 \cdot 10^{-4})$	$7.877 \cdot 10^{-8}$	17.719
$C_{n\alpha}$	$-3.013 \cdot 10^{-3} \pm (5.50 \cdot 10^{-4})$	$1.863 \cdot 10^{-8}$	55.031
$C_{n\alpha^2}$	$5.844 \cdot 10^{-2} \pm (6.15 \cdot 10^{-3})$	$6.684 \cdot 10^{-9}$	1.181
$C_{n\delta_1}$	$-1.535 \cdot 10^{-3} \pm (2.33 \cdot 10^{-4})$	$1.417 \cdot 10^{-8}$	1.129
$C_{n\delta_2}$	$-1.251 \cdot 10^{-3} \pm (1.60 \cdot 10^{-4})$	$2.115 \cdot 10^{-6}$	171.828
$C_{n\delta_2^2}$	$-6.453 \cdot 10^{-3} \pm (5.52 \cdot 10^{-4})$	$1.391 \cdot 10^{-8}$	43.349
$C_{n\alpha_8^1}$	$-1.423 \cdot 10^{-2} \pm (2.85 \cdot 10^{-3})$	$9.836 \cdot 10^{-6}$	337.844
$C_{n\alpha_5^2}$	$-1.453 \cdot 10^{-1} \pm (5.90 \cdot 10^{-3})$	$9.054 \cdot 10^{-6}$	123.659

5.2.3 Model validation

The residual characteristics (Figures D.17, D.21, D.25, D.29, D.34) proved to be very good, achieving better fitting than polynomial models ($\text{RMS}_{rel} < 3\%$ for all models), random residuals in both estimation and validation datasets, small variances and tighter confidence bounds. Some unmodeled characteristics are still present in the models for C_X and C_Z, but they are of much smaller absolute value than in polynomial models. The mean of the validation residuals is also much closer to zero, which shows the higher approximation power of simple spline models with a few number of knots with respect to polynomial models, which may be adequate for smaller ranges of the independent variables.

A collinearity analysis was also done, where the condition indices from the SVD decomposition of X, the variance inflation factors (VIF) and the correlation indices among the regressors were calculated. The results are shown in Figures D.19, D.23, D.27, D.32, and D.36. It can be seen that except the model for C_n, the collinearity is not severe and the estimated models can be trusted. The "moderate" and "severe" limits for the condition indices are suggested by Klein in [19].

For C_n, it was not possible to find a model with adequate characteristics that did not show collinearity because of several nonlinearities close to $\alpha = 0$, which made the problem worse because for small absolute values of α most regressors and knots that include the angle of attack will be very similar, so the estimator might fail to find the most significant regressor. Because of this collinearity problems, two other models were done for C_n:

1. A model using Multivariate Orthogonal Functions as it was explained before to orthogonalize the regressors in the order they were selected during the stepwise regression
2. A model using Principal Components Regression as it was explained in Section 2.3.3, which removes the eigenvalues associated with high levels of collinearity.

It was found that the model with Multivariate Orthogonal Functions performed better than the non-orthogonal spline model and the Principal Components Regression, which was able to remove collinearity but had a much worse performance in all aspects. This shows that the orthogonalization may also lead to better results for spline models, and should still be considered a possibility when collinearity problems arise in non-orthogonal models. As it was said before, the results from orthogonal spline models are not shown here in order not to make this report too lengthy and because in general they led to slightly worse models than the non-orthogonal framework.

Table 5.17: Model characteristics (spline models)

	RMS_{rel} (est.)	RMS_{rel} (val.)	F-statistic	R^2 (est.)	PSE	$\hat{\sigma}^2$
C_X model	1.99%	1.97%	$1.602 \cdot 10^4$	99.49%	$5.164 \cdot 10^{-5}$	$1.411 \cdot 10^{-5}$
C_Z model	0.75%	0.96%	$1.249 \cdot 10^5$	99.92%	$1.9 \cdot 10^{-3}$	$1.165 \cdot 10^{-4}$
C_l model	1.11%	1.25%	$4.472 \cdot 10^4$	99.82%	$1.697 \cdot 10^{-5}$	$2.015 \cdot 10^{-6}$
C_m model	2.13 %	2.75 %	$2.894 \cdot 10^3$	98.58%	$9.084 \cdot 10^{-5}$	$3.362 \cdot 10^{-5}$
C_n model	2.03%	2.28%	$1.148 \cdot 10^4$	99.27%	$6.416 \cdot 10^{-7}$	$2.3 \cdot 10^{-7}$

Table 5.18: Maximum absolute relative residuals of the spline models

	$\max(\lvert\mathbf{v}_{est}\rvert)$	$\max(\lvert\mathbf{v}_{val}\rvert)$
C_X model	7.11 %	6.57 %
C_Z model	2.35 %	2.92 %
C_l model	4.68 %	5.1 %
C_m model	9.32 %	10.62 %
C_n model	9.31 %	7.96 %

5.2.4 Sensitivity analysis

For the spline models, the sensitivity analysis is even more important than for the polynomial ones because of the collinearity among the estimates. If they are poorly estimated, the prediction capabilities might degrade with small changes in the parameters, so again, they are perturbed individually with their 95% confidence bounds and the effect in the relative RMS increase was calculated (Figure 5.4).

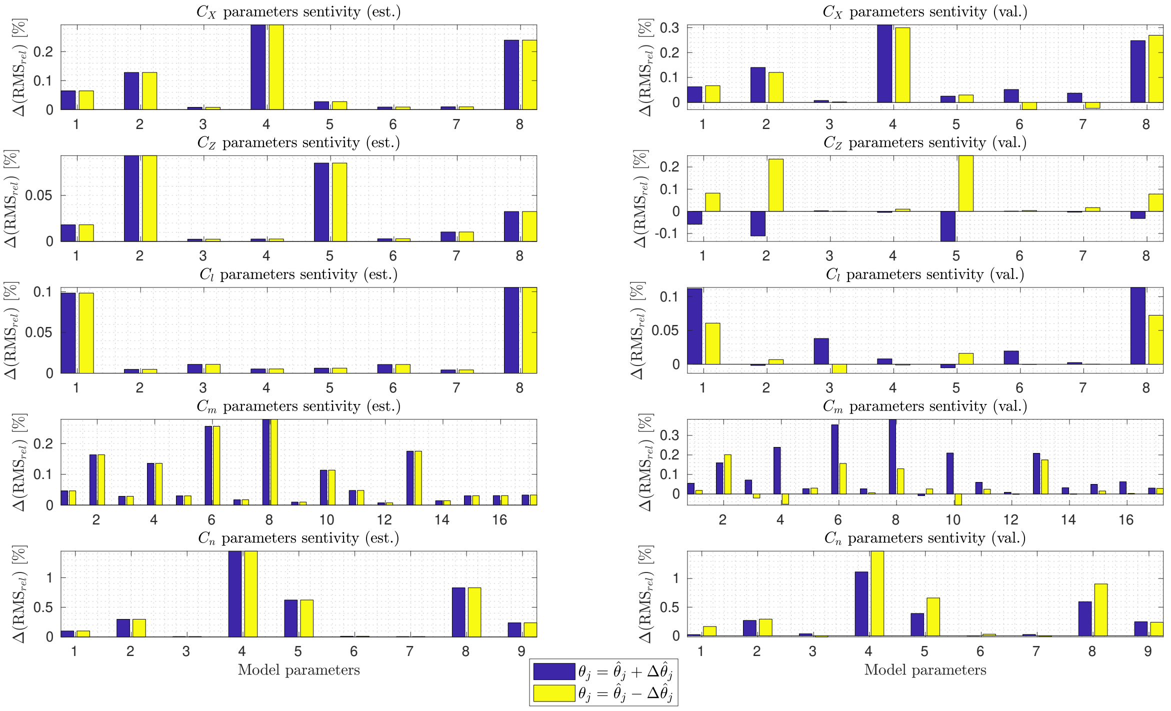

Figure 5.4: Sensitivity of the estimation and validation relative RMS to changes in the spline model parameters equal to their confidence bounds

The lack of normalization is patent in the different error increases that each parameter causes, contrary to the polynomial models shown before. It can also be seen how the error increase is higher in general but the behavior of the estimation and validation residuals is much similar than for polynomial models, including signs and magnitudes of most parameters, which is again a sign of the better approximation that splines achieve.

It is clear that the collinearity does not present a problem in the sense of parameter sensitivity, since the maximum increase in the validation RMS is of ∼1% for the “problematic” C_n model and below 0.3% for the rest of the models.

5.3 Global model inspection and discussion

A general inspection of the models through the residual characteristics and the model cuts will be done as a final comparison of spline and polynomial models. First they will be compared in terms of model fit and then the main terms of the model equations will be discussed.

Model fit

With regard to the model fit, as it was anticipated in previous sections, the splines models achieved in general a better fitting than the polynomial ones, which is clearly reflected in Figure 5.5, where the relative RMS and the maximum validation residual have been plotted for all iterations of the stepwise regression for polynomials and splines and shows that spline models outperform polynomial ones for most cases.

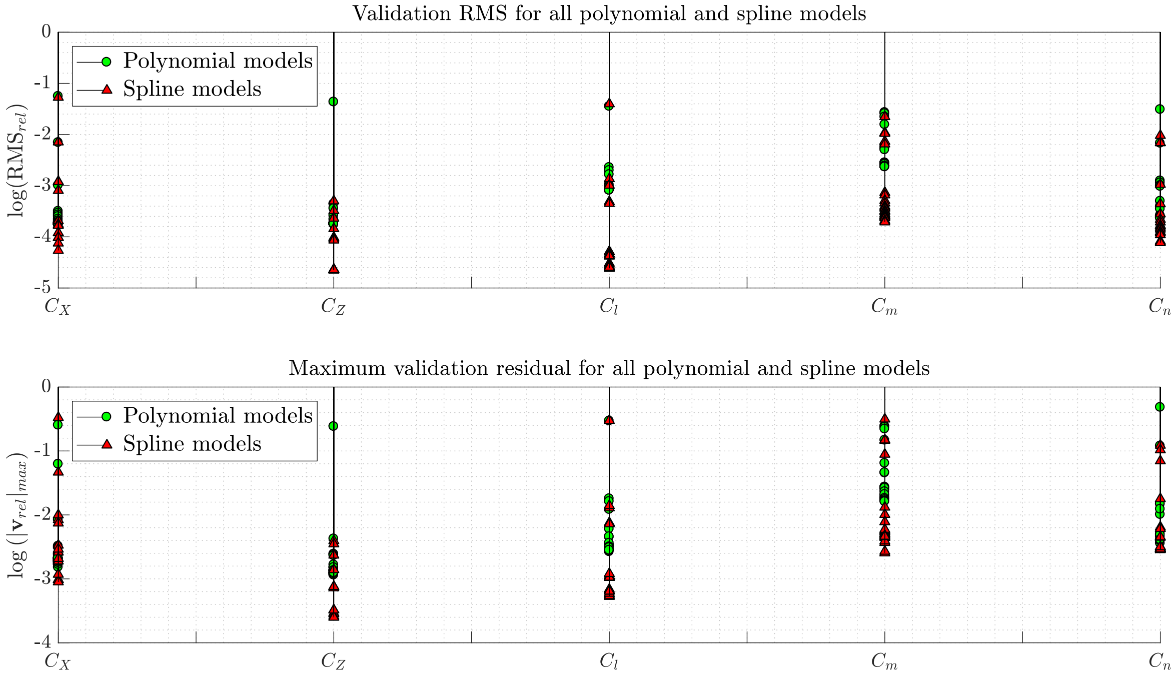

Figure 5.5: Overall fit comparison of all estimated models during the stepwise regression for polynomial and splines

It also is interesting to compare the "local model quality" of the spline models with respect to the polynomial models, that is, how the model quality changes for the different values of the independent variables. In this case the angle of attack was the variable of choice since it is the most significant one. In order to do so, the validation residuals were split according to their value of the angle of attack in segments of 5 degrees, and the relative RMS was calculated for each of these segments. The results are shown in Figure 5.6, where it can be seen that the overall local quality of spline models is better, and has a smaller spatial variability than in the polynomial models, specially at the edges as it was anticipated. It can be seen how for polynomials, the assumption that the residuals are uncorrelated with the independent variables does not always hold (in this case, it is correlated with the angle of attack).

A remark should be done here: all the previous discussion is based on the assumption that the measured data is free of systematic errors, but in case this was not true, the estimates would be biased. The same holds for errors in the independent variables. With the available equipment at the moment of the test, no measurements of the angle of attack could be taken, and the setting for the turntable was used as the "measured" angle of attack. In case the control of the turntable fails to deliver the correct angle, the estimates will also be biased as it was discussed in Section 2.3. The calculated wind tunnel corrections, which were not applied because of the lack of previous flight test data to properly adjust them, could be regarded as errors in the measured coefficients (which will not affect the estimation greatly because of their very small value), and in the angle of attack, which would again introduce a bias in the estimates.

All this information can only be known by performing additional wind tunnel tests or, as it is planned at the moment, a sub-scale flight test. If the results actually show the presence of errors in this wind tunnel dataset, a state estimation routine to get reliable estimates of the states or an output error method, which takes errors of the independent variables into account would be needed. However, note that a better understanding of the noise statistics are required in order to derive any

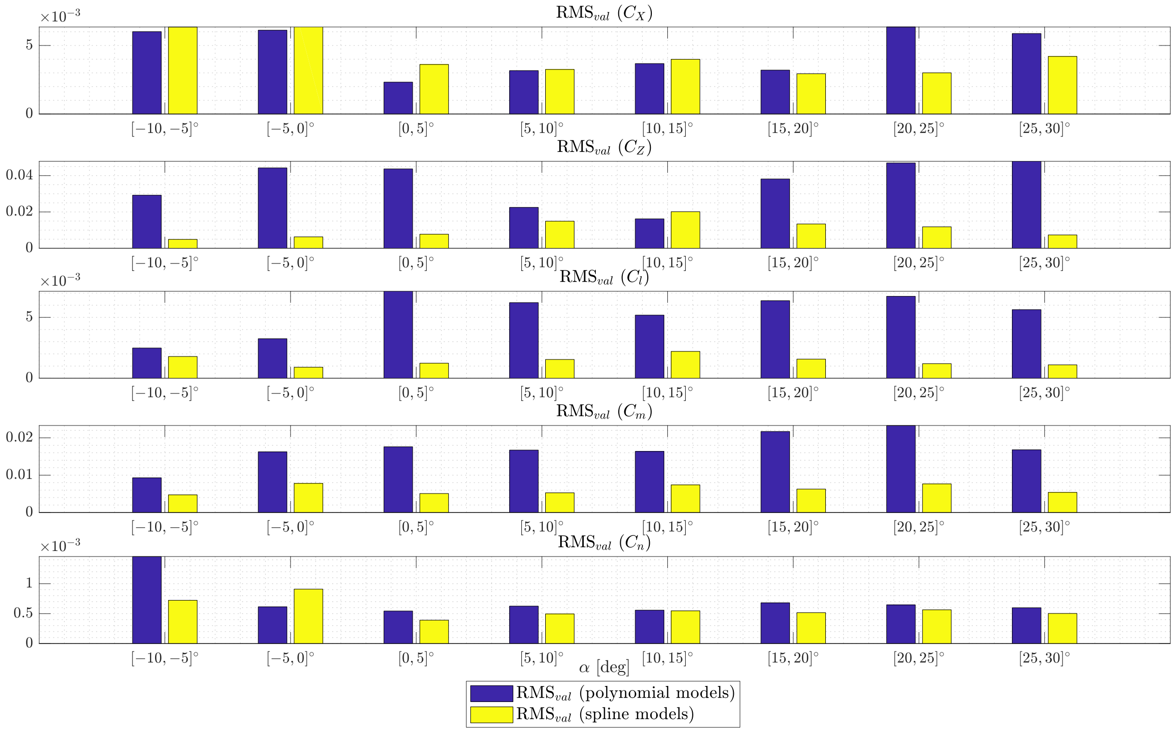

Figure 5.6: RMS of 5 degrees segments in the angle of attack (local spatial quality)

of this methods, and that its unavailability was one of the reasons of the chosen identification method in the first place.

From the results and the previous discussion, Modified Stepwise Regression with Multivariate Orthogonal Functions and splines seem adequate methods to determine a good model structure to estimate the aerodynamic response of the Flying V. It is believed that no overfitting is present in the models because of the good behavior of the validation residual with the addition of terms. In the polynomial models, the orthogonalization effectively removes the collinear content so each new regressor contains less information than the previous one and a large number of iterations are needed for overfitting to appear. For the spline models, the Modified Stepwise Regression was able to select the most significant knots even without the orthogonalization of the regressors, mainly because the Modified Stepwise Regression does include an orthogonalization of the model output with respect to the regressors in the model at each iteration, which is key to determine a parsimonious model.

To show an example of an overfitted model, an automatic selection process was implemented for the polynomial models as it is presented in Ref. [2] selecting the regressors in order of decrease of the cost function; and another automatic selection was implemented based in Ref. [3], which was modified by removing the backward selection step. This step removes the least significant regressor in the model, and had to be skipped to allow more regressors in the model than it usually would. This is equivalent to set the F-statistic value required to leave the model to infinity.

The model for C_m was used again as a example because of its higher complexity. Two models with a large number of regressors were used, including terms of very high degree in the polynomial models, and knots up to 4th order in the angle of attack for the spline models. The results of the estimation and validation RMS evolution are shown in Figure 5.7, which actually represents a very good example of the differences between both models. It can be seen that the splines achieve a much higher approximation at every iteration, and that the estimation residual keeps decreasing steadily. On the other hand, the polynomial estimation residual stagnates because of the performed orthogonalization. The point at which the validation residuals “explode” in the presented figures cannot be compared, since they depend on the included regressors in the pool (polynomial and spline models up to 200 terms were found which did not show any overfitting).

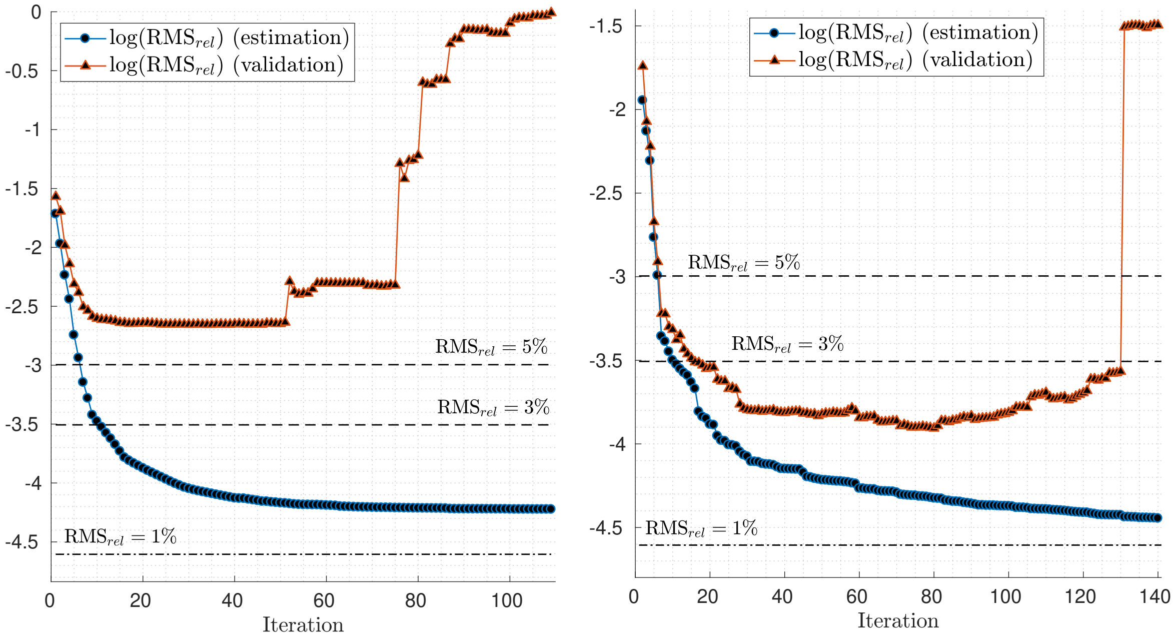

Figure 5.7: Example of estimation and validation residuals for an overfitted model.

Model parameters

Some of the model parameters are known as the control and stability derivatives and have known signs for conventional aircraft, so their comparison will be useful to see if any unexpected change in this new configuration.

An inspection of the model parameters for C_X for both the spline and polynomial models shows a good agreement with the expected control and stability derivatives for this coefficient. $C_{X\alpha} > 0$ and $C_{X\delta_i} > 0$ for the linear part of the aerodynamics: higher angles of attack and control surfaces deflection create a higher lift, which in turn translates to a higher forward force due to the tilting of the lift. For the polynomial model, $C_{X\delta_1^2}$ and $C_{X\delta_2^2}$ appear with a negative sign, which could come from the drag tendency to increase with the square of the lift coefficient: positive control surfaces deflections increase the lift coefficient by $\sim C_{L\delta_i} \cdot \Delta\delta_i$, which would affect the drag as: $\sim k(C_{L\delta_i} \cdot \Delta\delta_i)^2$, decreasing the forward force. On the other hand, the spline model achieves a similar accuracy than the polynomial model with less terms thanks to a knot in $\alpha = 20°$. In both models $C_{X\hat{V}}$ is negative, which according to Ref. [66], helps mitigate unstable tuck (which from the results of this test, the Flying V appears not to have). Model cuts of the models are presented in Figures D.3 and D.18.

The vertical force coefficient should have been an easy one to estimate because of its higher linearity, but the already mentioned change in the lift slope around $\alpha = 10°$ made it difficult for the polynomial model. The reported unmodeled deficiencies can be mostly solved with the spline model, which included a knot in $\alpha = 11°$. The effect of this knot with respect to the polynomial model is clear when comparing Figures D.6 and D.22: the negative value of $C_{Z\alpha_{11}^1}$ decreases the slope of the vertical force to match the measured values for higher α. This increase of the lift slope was already mentioned in Section 4.1 as a possible effect of the so-called *vortex lift*.

The estimated models for the pitching moment coefficient show that $C_{m\alpha} < 0$ (statically stable aircraft) until a certain angle of attack where the pitch break occurs, and $C_{m\alpha}$ becomes positive making the Flying V unstable. This limits the flyable region of the flight envelope since if the angle of attack goes beyond this region, the pitching moment will rise fast, increasing the angle of attack until it reaches a point where it is impossible to trim the aircraft with the maximum deflections of the control surfaces.

All control derivatives $C_{m\delta_i},\ i = 1, 2, 3$ are negative because of their position behind the center of gravity, and multiple couplings among the control surfaces and the angle of attack can be seen. This is related to the location of the control surface on the main lifting surface instead of in a separate one (like a conventional tail): when the control surfaces are deflected, the camber of the wing changes, which changes the lift distribution, and thus the pitching moment coefficient.

The last derivative to discuss for C_m is the so-called "tuck-derivative" $C_{m\hat{V}} > 0$, which in conventional aircraft can be either positive, negative, or negligible depending on the aircraft and flight condition. Its positive sign suggests the Flying V will not suffer from pitch down instability, also denominated "tuck-under", and the estimated coefficient is within the usual range for conventional aircraft given by Roskam[67]. However, since its value usually varies with the flight condition it cannot be ensured that the full-scale Flying V will follow the same behavior. In addition, compressibility effects such as the transonic drag rise also affect the tuck characteristics of the aircraft, and Reynolds effects due to scaling have not been taken into account so it would be premature to confirm this prediction with the sub-scale data gathered so far.

Model cuts of the polynomial and spline models for C_m are shown in Figures D.12 and D.30, which shows the tighter confidence bounds of the spline model with respect to the polynomial one. It is also interesting to note the smaller confidence bounds for the control surfaces with respect to the airspeed, which is due to the worse coverage of the last one. Unfortunately this could not be avoided due to the limited ranges of wind speed deliverable by the wind tunnel and the small amount of available data (this wind tunnel dataset is the first one valid for identification purposes).

The only parameters worth talking from the rolling and yawing moment coefficients are the control derivatives, since for a full model the overall moments will be zero for the clean configuration in a symmetric aircraft. Positive deflections of the control surfaces lead to a positive rolling moment (which would lower the right wing), and a negative yawing moment which opposes to the desired turn in roll. This effect is known as adverse yaw, and it is caused for a difference in the drag of the left and right wing. An easy fix for this issue involves *differential aileron deflection*, which tries to balance the drag in both wings by using different deflections in the left and right wing to cancel the yawing moment[68].

A direct comparison of the values of the parameters with other estimated models is somehow difficult and impractical, so it is not presented here. The main reason is the large number of differences between the tests conditions (wind tunnel, flight test, Reynolds number, Mach number), which cause large changes in the parameter estimates. Moreover, even if a model from a similar experimental test is available, the different regressors in the model can change the value of the estimates greatly, or, in the case of the moment coefficients, a change in the center of gravity location (which is not fixed yet in the Flying V sub-scale model) will change all parameters.

5.4 Application example: longitudinal stability and control

Even though the identified model only represents the stationary behavior of the aircraft, there are different applications which it could be used for; the most immediate are listed below:

- Longitudinal stability and control
- Trim calculations
- Design of a preliminary flight controller (including the identified actuators dynamics)
- Study of take-off conditions and requirements

As an example, the first two applications were done, which involved: 1) a flight mechanics analysis to determine whether the assumed center of gravity location offers good static stability and controllability characteristics, and 2) build a program to trim the aircraft at different flight conditions.

The drag from nacelles, engines, landing gear and winglets was not taken into account since these contributions are unknown at the moment, so some extra thrust will be required for trimming. Only the longitudinal coefficients were included because of the absence of sideslip in the models, only stationary or quasi-stationary conditions can be considered. However, a simplified study was done to determine the sign of the pitch damping coefficient (C_{mq}), which will determine whether the dynamic stability and controllability limits are more or less restrictive than the static ones.

The most significant results of these calculations are:

- A center of gravity location is proposed because of the effects of thrust.

- Thrust and control surfaces settings are defined for horizontal flight at different speeds.
- Thrust and controls surfaces settings are defined for symmetrical flight at different speeds and rates of climb (RoC).
- Dynamic stability (in first approximation) is less restrictive than static stability for the most part of the flight envelope.

All these calculations were performed for the sub-scale model, since its results will improve the safety and control of the future flight test, and more importantly because it will allow to compare the results with actual flight data from the same model to try to correlate wind tunnel with flight test results.

5.4.1 Center of gravity location

So far, two center of gravity locations have been proposed, both from static controllability and stability studies:

$$x_{cg} = 1.336 \text{ m}, [15], \qquad x_{cg} = 1.365 \text{ m}, [16] \tag{5.11}$$

from the nose of the aircraft. Since thrust was not included in these calculations, and given that it will be at least as large as the drag, it was decided to determine a feasible center of gravity location including thrust effects. First the forward and aft limits for the center of gravity should be calculated taken the thrust into account, which provide a nose down effect.

The aft limit for the center of gravity is given by the neutral point, which is the position of the center of gravity where the pitching moment does not change with the angle of attack. The moment for different centers of gravity within achievable bounds given the model geometry and weight distribution were calculated for the clean configuration ($\delta_i = 0$), at a typical airspeed for cruise ($V = 20$ m/s), and are presented in Figure 5.8. Thrust will cause a constant stabilizing bias to the moment but will not affect the trends with the angle of attack (considering the same T/W for every α).

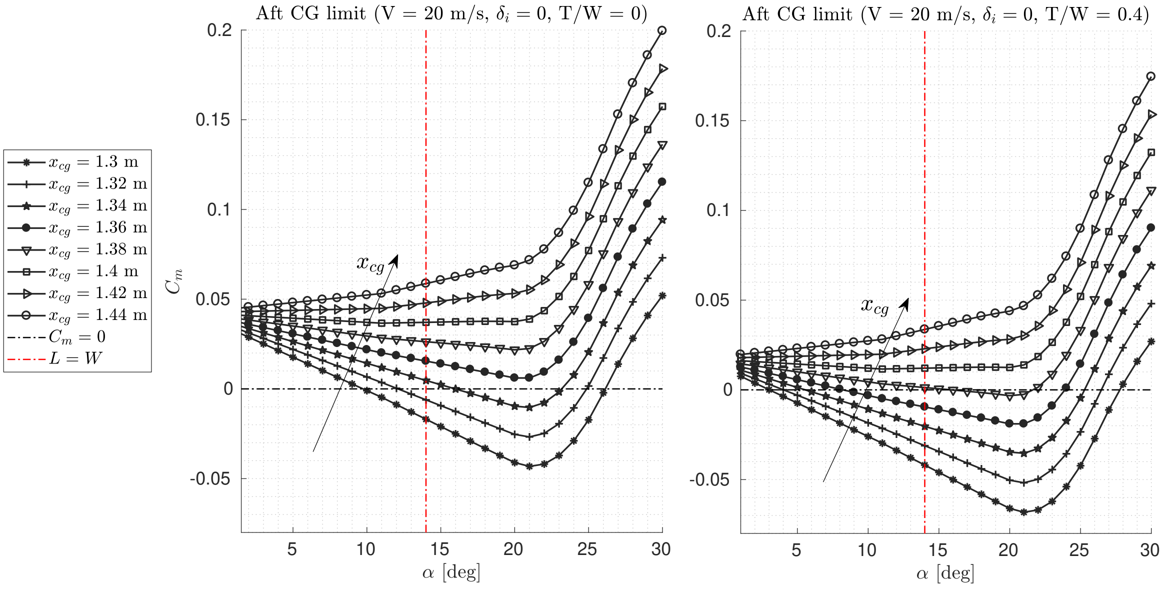

Figure 5.8: Aft center of gravity limits without thrust effects (left) and with thrust effects (right)

It can be seen $C_{m\alpha}$ becomes zero for $x_{cg} \cong 1.4$, so it is chosen as the aft limit of the center of gravity. Beyond that point, $C_{m\alpha}$ will be positive and the aircraft will become unstable for all angles of attack (all center of gravity locations become unstable after the pitch break).

The forward limit for the center of gravity is given by the point where the control surfaces location can just trim the aircraft at the maximum lift coefficient, using the maximum available deflections. The airspeed used for the forward limit calculation was $V = 17$ m/s, which is a more typical value for take off and the most limiting; and a thrust-to-weight ratio of 0.4 (10 kg) was used for the calculation, which is expected to be close to the thrust setting required for take-off. In addition, the pitch break was used as the practical condition for maximum lift coefficient since no stable flight is possible beyond it. The results are presented in Figure 5.9, where it can be seen that the thrust causes a more restrictive limit for the forward position. A value of $x_{cg} = 1.32$ m is chosen as forward center of gravity limit since it is the most forward position that allows to trim the Flying V (bring C_m to zero) in the more unfavourable situation, which is including thrust. Indeed, during the trim routine it was found that the aircraft could be trimmed just up to 1.31 m.

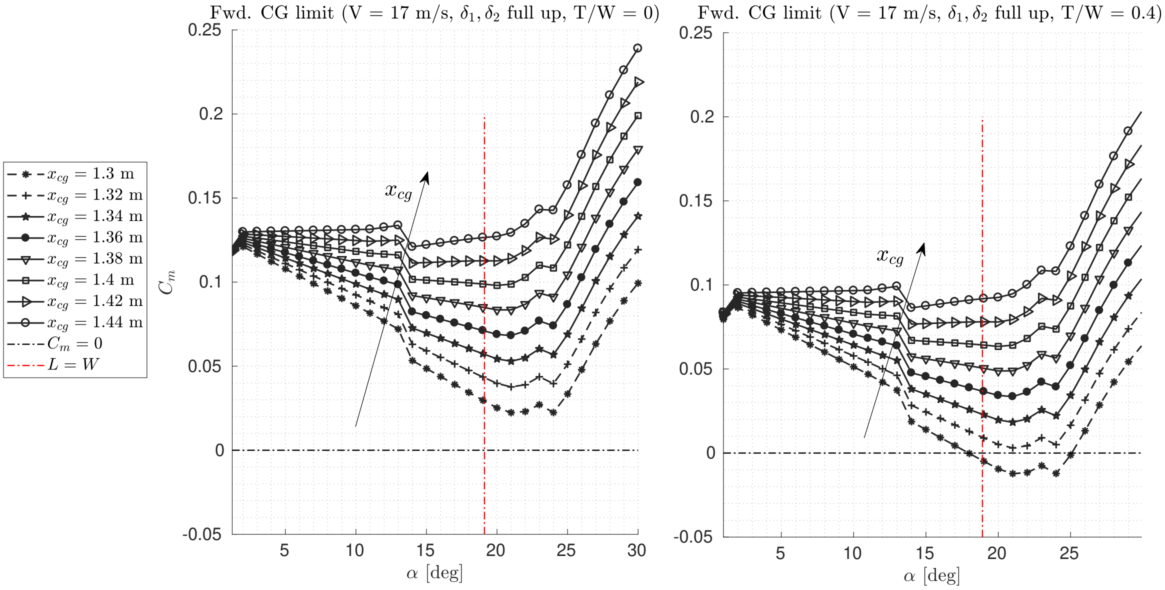

Figure 5.9: Forward center of gravity limits without thrust effects (left) and with thrust effects (right)

Finally, a center of gravity which is roughly in the middle between these two limits is chosen:

$$(x_{cg})_{new} = 1.36 \text{ m from the nose,} \tag{5.12}$$

and the pitching moment coefficient for clean configuration at typical cruise conditions ($V = 20$ m/s, $T/W = 0.2$) is shown in Figure 5.10, along with the control authority using the first and second control surfaces as a single elevon.

5.4.2 Trim at different airspeeds and flight path angles

Trimming consists in finding a point of equilibrium in the equations of motion where the vector sum of forces and moments is zero. To focus on stationary conditions, unsteady terms such as the horizontal acceleration or the pitch rate are neglected, and a schematic of the forces acting on the aircraft for flight in a vertical plane are shown in Figure 5.11.

The equations for the forces and moments are projected on the body frame of reference since our interest is to find γ:

$$\begin{aligned} T\cos(\alpha+\varepsilon_t) - D - W\cdot\sin\gamma &= 0 \\ T\sin(\alpha+\varepsilon_t) + L - W\cdot\cos\gamma &= 0 \\ M + T\sin(\varepsilon_t)\cdot x_t - T\cos(\varepsilon_t)\cdot z_t &= 0 \end{aligned} \tag{5.13}$$

The first two equations are made dimensionless so that they include the load factor $n = L/W$ and the thrust-to-weight ratio T/W. The pitching moment equation is made dimensionless using the

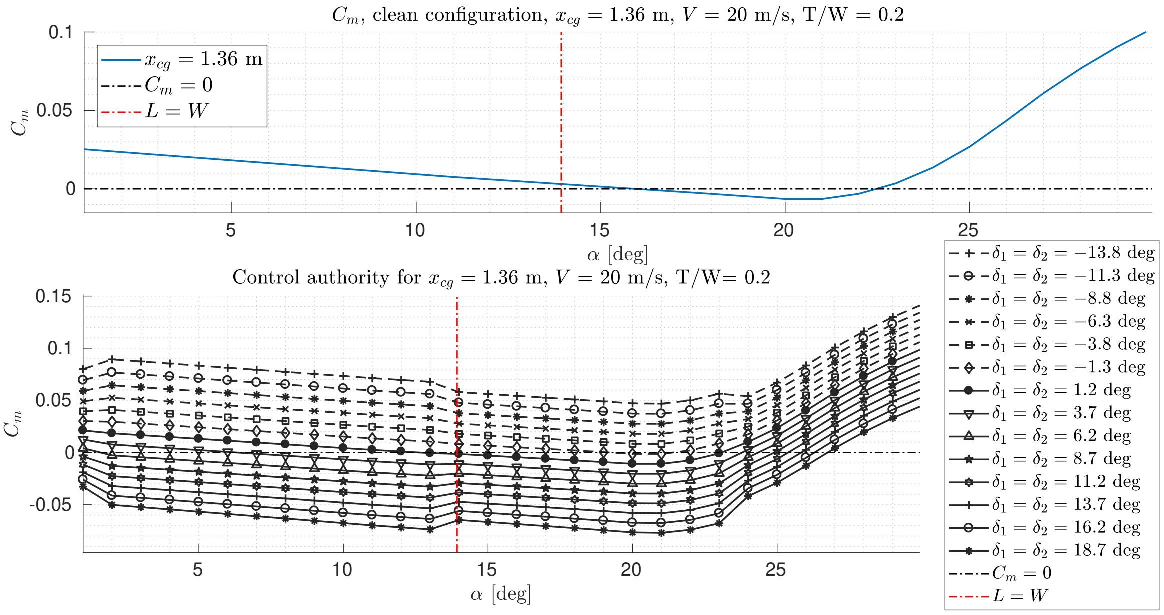

Figure 5.10: Pitching moment for clean configuration and control authority ($x_{cg} = 1.36$ m)

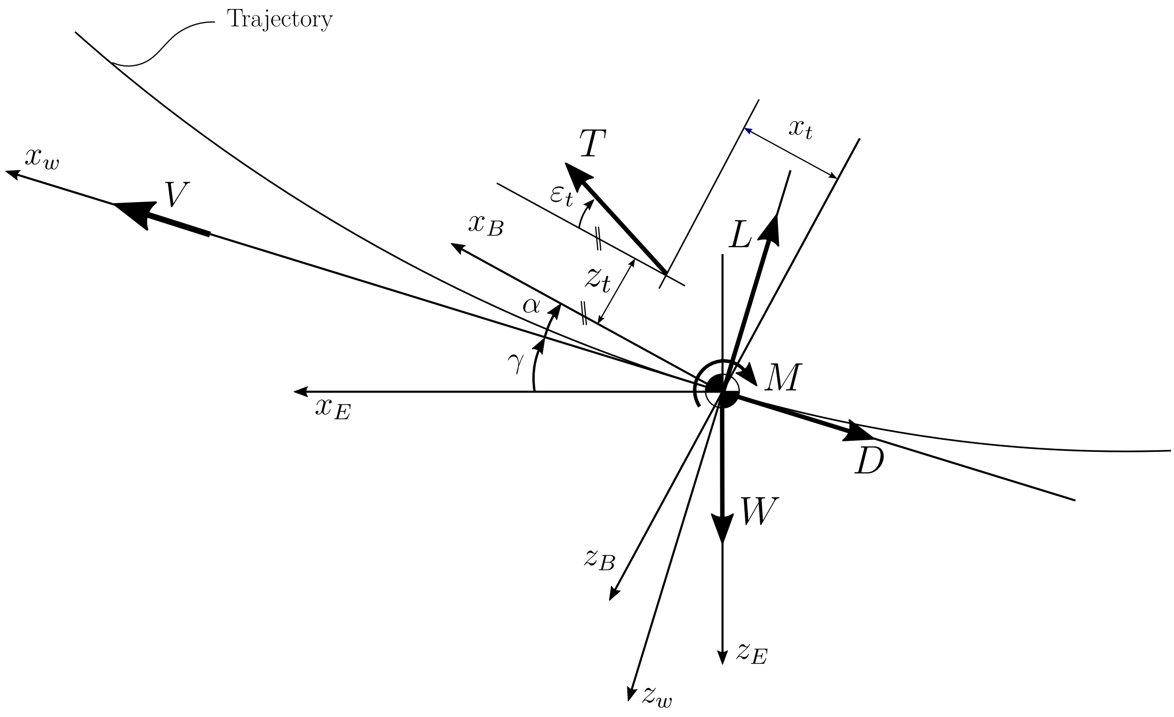
Trajectory
x_w
V
T
ε_t
x_t
x_B
z_t
α
L
γ
M
x_E
D
W
z_B
z_E
z_w

Figure 5.11: Forces during flight in a vertical plane

dynamic pressure, the planform area and the mean aerodynamic chord:

$$\begin{aligned} \frac{T}{W}\cos(\alpha+\varepsilon_t) - \frac{D}{W} - \sin\gamma = 0 \\ \frac{T}{W}\sin(\alpha+\varepsilon_t) + n - \cos\gamma = 0 \\ C_m + \hat{T}\sin(\varepsilon_t)\cdot\frac{x_t}{\bar{c}} - \hat{T}\cos(\varepsilon_t)\cdot\frac{z_t}{\bar{c}} = 0 \end{aligned} \tag{5.14}$$

where $\hat{T} = T/(q_\infty S)$ and the definition of C_m is the same as for the body axes (Eq. (2.6)) since $y_w \equiv y_B$ for no sideslip (See Appendix B, Figure B.2). In order to solve this system of equations, we introduce the identified model as:

$$L = q_\infty S (C_L)_{model}; \quad (C_L)_{model} = -C_X \cdot \sin\alpha - C_Z \cdot \cos\alpha = f(\alpha, \hat{V}, \delta_1, \delta_2, \delta_3) \tag{5.15}$$

$$D = q_\infty S (C_D)_{model}; \quad (C_D)_{model} = -C_X \cdot \cos\alpha - C_Z \cdot \sin\alpha = f(\alpha, \hat{V}, \delta_1, \delta_2, \delta_3) \tag{5.16}$$

Since there are more unknowns than equations, two relations among the control surfaces are included to serve as a control law:

$$\frac{\delta_2}{\delta_1} = K_{\delta_2} \tag{5.17}$$

$$\frac{\delta_3}{\delta_1} = K_{\delta_3} \tag{5.18}$$

Tuning the parameters K_{δ_2} and K_{δ_3} allows to have different control surfaces settings, such as having the first control surface as the elevator ($K_{\delta_2} = K_{\delta_3} = 0$), or joining the first and second control surfaces in a single elevator ($K_{\delta_2} = 1, K_{\delta_3} = 0$). This last configuration will be used in this analysis, but it should be noted that it does not fully exploit the limits of the control surfaces since the maximum deflections are different for each control surface. Some extra control power will be available in reality and the results are conservative in that sense.

The airspeed and flight path angle are the chosen degrees of freedom of the system and they will be used as inputs to the trimming routine. The system to be solved is formed by equations (5.14),(5.15),(5.16),(5.17), and (5.18). If the expressions from Eqs.(5.15),(5.16) are substituted into Eqs.(5.14), it can be seen that everything can be expressed in terms of five quantities $(T/W, \alpha, \delta_1, \delta_2, \delta_3)$. Solving the three equations for the equilibrium of forces and moments subject to the two chosen control laws will give the angle of attack and the thrust and control settings for trimmed flight at the desired airspeed and flight path angle.

The trimming routine was implemented in MATLAB using *fmincon*, a solver to find minima of constrained nonlinear functions. Equations (5.14) and (5.17), and (5.18) were implemented as nonlinear constraints, and updated every iteration with the calculated lift, drag, and pitching moment from the aerodynamic model. Since *a priori* it is difficult to know whether the aircraft will be trimmable at every point, the flight path angle was included as an additional parameter in the equations, and an objective function was introduced as:

$$J_{trim} = (\gamma - \gamma_{set})^2, \tag{5.19}$$

This improves the results for points where trim was not possible or difficult, since it is a less restrictive condition (when it is directly substituted into the equations, it is possible that the outcome is an unfeasible point). If there is no trim for that flight condition, the optimization will get as close as possible to the desired flight path angle without violating the constraints. The optimization problem to be solved is then:

$$[T/W, \alpha, \delta_1, \delta_2, \delta_3, \gamma] = \text{argmin}(J_{trim}), \quad \text{s.t.} \tag{5.20}$$

$$\frac{T}{W}\cos\left(\alpha+\varepsilon_t\right)-\frac{D}{W}-\sin\gamma=0 \tag{5.21}$$

$$\frac{T}{W}\sin\left(\alpha+\varepsilon_t\right)+n-\cos\gamma=0 \tag{5.22}$$

$$C_m+\hat{T}\sin\left(\varepsilon_t\right)\cdot\frac{x_t}{\bar{c}}-\hat{T}\cos\left(\varepsilon_t\right)\cdot\frac{z_t}{\bar{c}}=0 \tag{5.23}$$

$$\frac{\delta_2}{\delta_1}-K_{\delta_2}=0 \tag{5.24}$$

$$\frac{\delta_3}{\delta_1}-K_{\delta_3}=0 \tag{5.25}$$

$$\tag{5.26}$$

The horizontal and vertical velocities with respect to the Earth reference frame are determined by the equations below, where it can be seen that setting V and γ is equivalent to setting these velocities:

$$\dot{x}_E=V\cos\gamma \tag{5.27}$$

$$-\dot{z}_E=\mathrm{RoC}=\dot{h}=V\sin\gamma \tag{5.28}$$

Horizontal flight

A first check should be done to verify that horizontal level flight ($\gamma=0$) is possible with the available thrust from the engines. Any higher value of γ will require a higher thrust setting since some of the thrust will be used to climb. Substituting $\gamma=0$ in the trim equations shown above, the thrust-to-weight ratio required for horizontal flight can be calculated, and it is shown in Figure 5.12 as a function of the angle of attack and the flight speed.

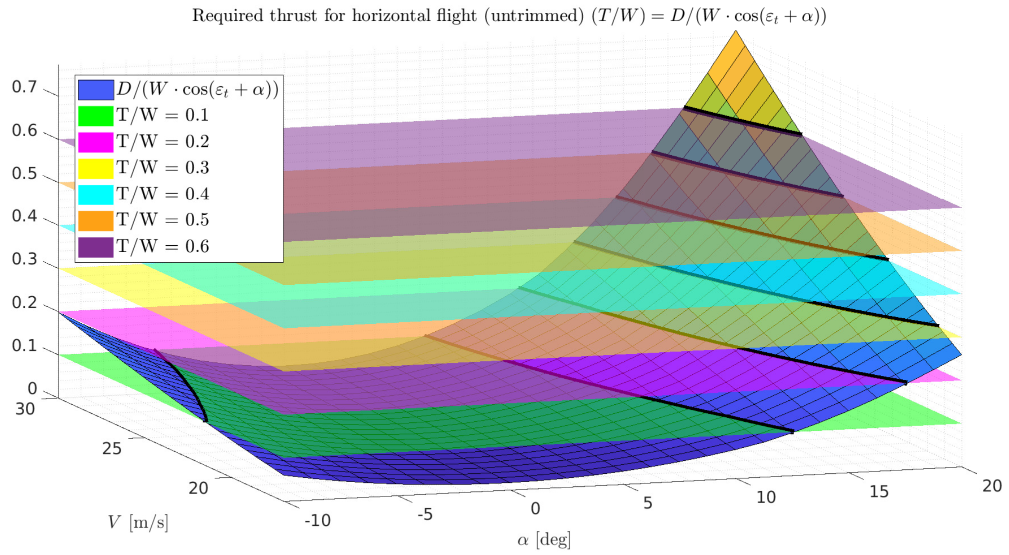

Figure 5.12: Required thrust-to-weight ratio for horizontal flight (untrimmed)

In addition, the lift should also be enough to overcome the weight (with the help from the vertical component of the thrust), which is largely determined by the velocity of the aircraft. The minimum speed to fly is the stall speed, which occurs at the maximum lift coefficient, but the flyable region of the flight envelope does not extend that far: once the pitch break occurs at around $\alpha=20°$, the aircraft becomes statically unstable, which is an undesired behavior for transport aircraft. The present study is then limited to $\alpha=20°$ in order to keep the aircraft in the "safe" region of the flight envelope, where perturbations in angle of attack (e.g. from a gust) will be dampened and not amplified.

The minimum speed to fly is then determined by the maximum lift coefficient from $\alpha \in [-10, 20]°$, which occurs at $\alpha = 20°$:

$$(V_{min})_{n=1} = \sqrt{\frac{2W}{\rho S (C_L)_{\alpha=20°}}} = 16.65 \text{ m/s} \tag{5.29}$$

These results for level horizontal flight give a lower limit for the airspeed and thrust the model will require to fly, but they are not trimmed, so they will not lead to equilibrium points (the pitching moment coefficient will not be zero in general). However, they were useful to set the limits for the trimming routine, to check that the results agreed with the expected trends with respect to horizontal flight, and as a first guess for the initial parameter vector in order to help the algorithm converge to a feasible point.

5.4.3 Longitudinal trim results

The trim routine was run in order to find equilibrium points for each position of the center of gravity within the bounds proposed in last section (Figure 5.13). It was found that the aircraft could be trimmed for all centers of gravity ($x_{cg} \in [1.3, 1.4]$) and airspeeds ($V \in [17, 30]$) using a reasonable thrust-to-weight ratio and control surfaces deflections. More forward centers of gravity could not be trimmed at all airspeeds, and more aft centers of gravity were not studied since they lead to an unstable aircraft.

The expected trends from the thrust-to-weight ratio, the trimmed angle of attack, and the control surfaces deflections match with those of conventional aircraft. The higher the airspeed, the less thrust-to-weight ratio is required for horizontal flight, the angle of attack for equilibrium lowers, and the control surfaces deflections become more positive in order to stabilize the aircraft (at higher angles of attack, trim requires negative deflections). Regarding the effect of the center of gravity, the more aft the center of gravity moves, the lower the angle of attack for equilibrium, which requires less thrust-to-weight ratio and higher control surfaces deflections. The maximum thrust-to-weight ratio available from the purchased engines is $(T/W)_{max} = 0.6$ (15 kg of thrust), and it can be seen that at any point that amount of force is required for horizontal flight, so the excess power can be used to climb at different flight path angles.

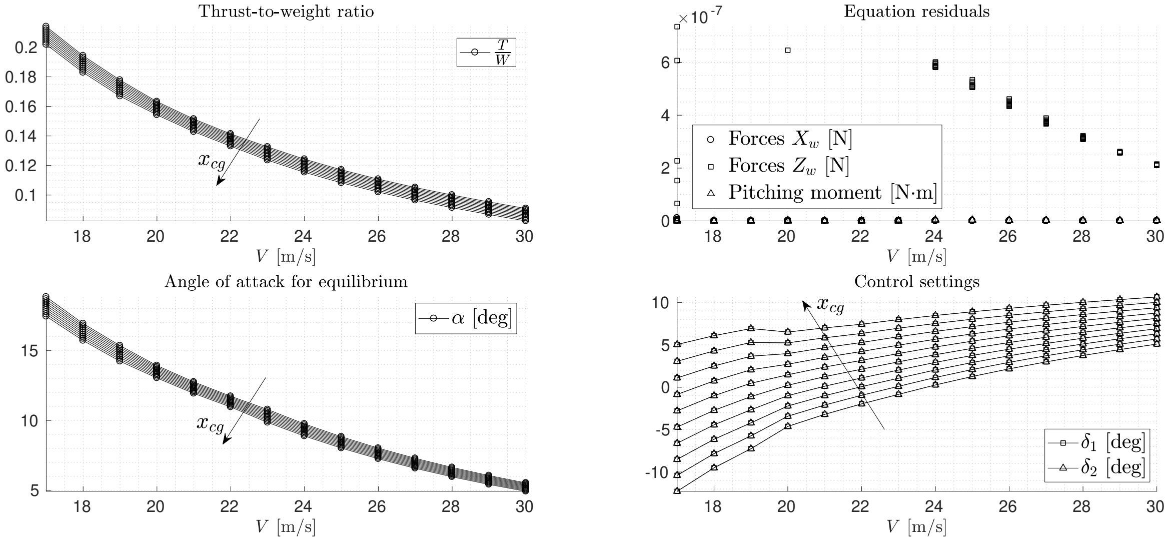

Figure 5.13: Trim results for horizontal flight for different center of gravity locations)

Using the proposed center of gravity location from last section, $x_{cg} = 1.36$ m from the nose, the trim routine is run to find the equilibrium points to climb at different airspeeds and flight path angles. The results are show in Figure 5.14, where again, all results match with the expected trends: the higher the flight path angle, the smaller the angle of attack for equilibrium (the velocity "aligns" with the trajectory), the higher thrust-to-weight ratio required (which provides the excess power), and the control surfaces become more negative to provide pitch-up moment.

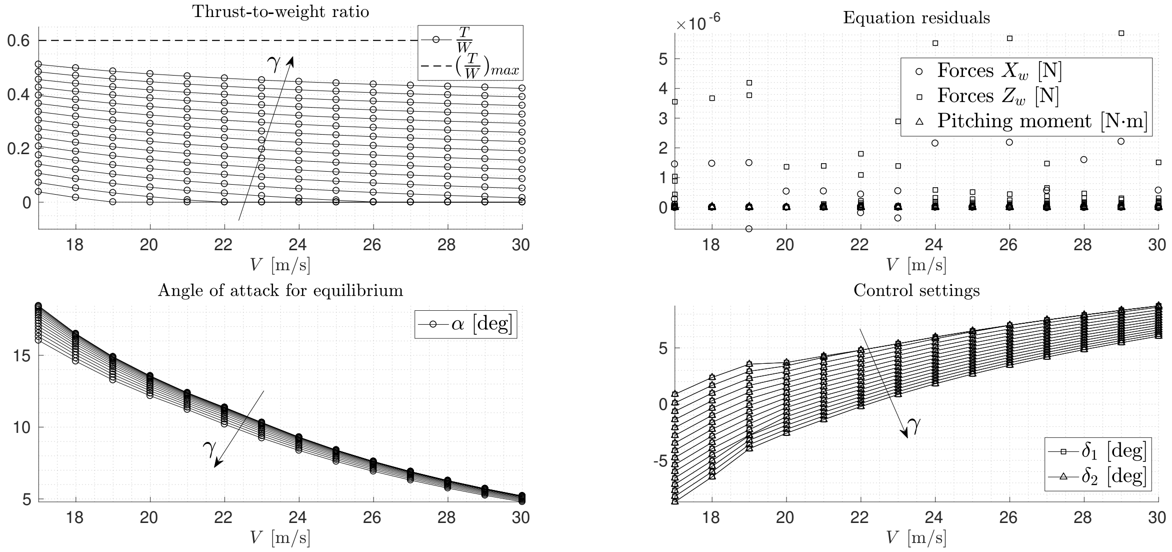

Figure 5.14: Trim results for flight at different flight path angles ($\gamma \in [-10, 20]°$), $x_{cg} = 1.36$ m from the nose

It is interesting to note that for the Flying V, positive control surfaces deflections are required (downward deflection) to trim the aircraft at low angles of attack, which is not the usual case for conventional transport aircraft.

Figure 5.15 shows the thrust-to-weight ratio required for trimmed flight at different airspeeds and flight path angles and the ascensional velocity or Rate of Climb it would entail. It can be seen that for some negative values of γ, no thrust is required for trimmed flight, which is again an expected result. The maximum thrust-to-weight ratio is not exceeded for any studied conditions, so the size of the engines seems appropriate for the model, since the extra power available provides a design margin for the extra thrust that the drag of engines, nacelles, landing gear and winglets will require.

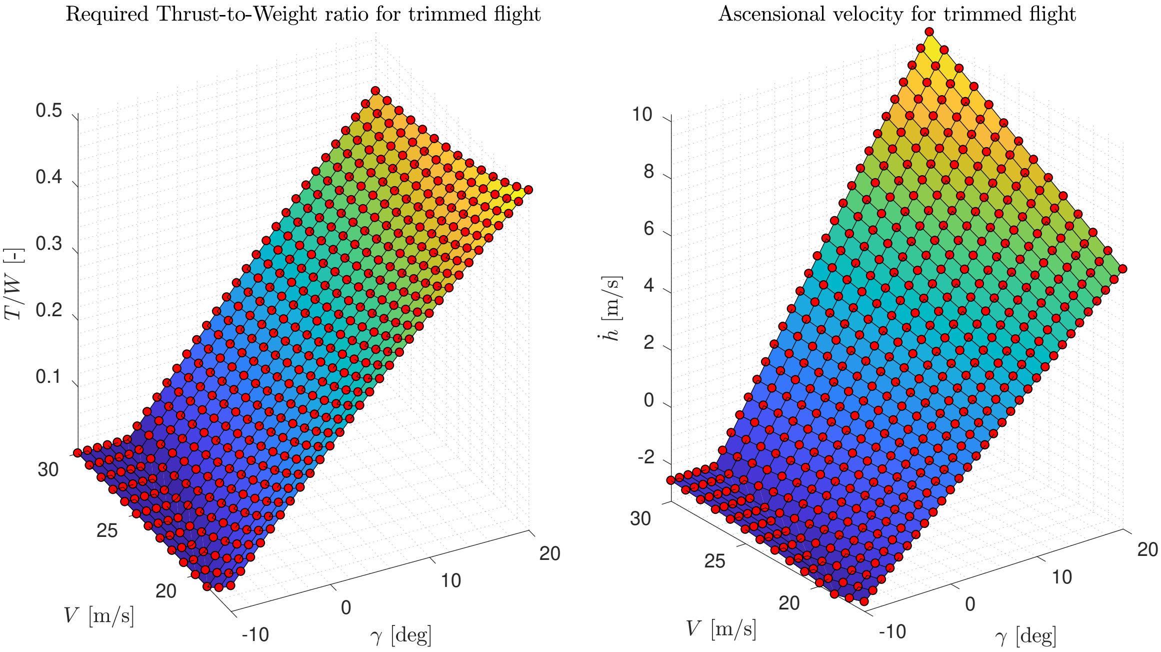

Figure 5.15: Thrust-to-weight ratio for different flight path angles and rates of climb ($x_{cg} = 1.36$ m)

5.4.4 Pitch damping and dynamic stability

The pitch rate affects the pitching moment coefficient since it induces a velocity in the center of pressure, which changes the effective angle of attack and creates a vertical force and consequently a moment about the center of gravity. A schematic is shown in Figure 5.16.

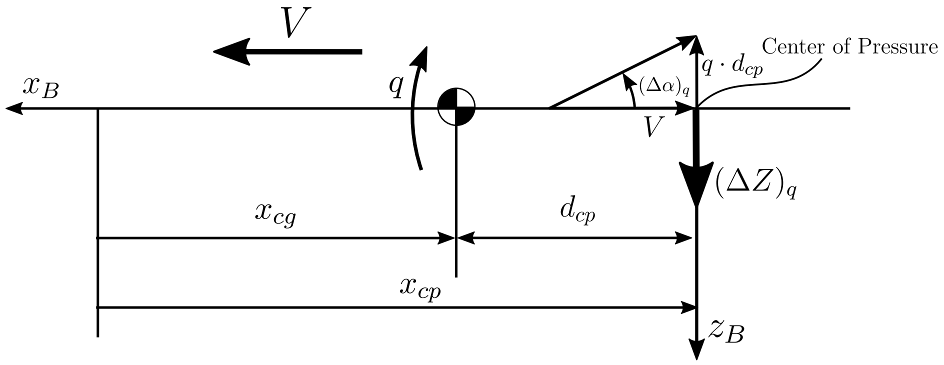

Figure 5.16: Pitch damping schematic

For small induced angles of attack ($q \cdot d_{cp} \ll V$):

$$\Delta\alpha_q \cong \frac{d_{cp} \cdot q}{V}, \quad |\Delta\alpha_q| \ll 1 \tag{5.30}$$

which will induce a moment about the center of gravity:

$$(\Delta M)_q = d_{cp} \cdot q_\infty \cdot S \cdot [C_Z(\alpha_0 + \Delta\alpha_q) - C_Z(\alpha_0)] \tag{5.31}$$

The equation is made dimensionless, and the spline model for the vertical force C_Z is used:

$$(\Delta C_m)_q = \frac{(\Delta M)_q}{q_\infty S} = d_{cp} \cdot [C_Z(\alpha_0 + \Delta\alpha_q) - C_Z(\alpha_0)] \tag{5.32}$$

$$\begin{aligned} C_Z(\alpha_0 + \Delta\alpha_q) &= C_{Z0} + C_{Z\alpha}(\alpha_0 + \Delta\alpha_q) + C_{Z\alpha^1_{11}}(\alpha_0 + \Delta\alpha_q - \alpha_{11^\circ})_+ + C_{Z\alpha^2_{17}}(\alpha_0 + \Delta\alpha_q - \alpha_{17^\circ})^2_+ \\ C_Z(\alpha_0) &= C_{Z0} + C_{Z\alpha}(\alpha_0) + C_{Z\alpha^1_{11}}(\alpha_0 - \alpha_{11^\circ})_+ + C_{Z\alpha^2_{17}}(\alpha_0 - \alpha_{17^\circ})^2_+ \end{aligned} \tag{5.33}$$

Until $\alpha = 17°$, the quadratic knot has a value of zero, so it is decided to skip it for this study since it will not make any difference for most part of the flight conditions the aircraft will encounter. Introducing the expressions for $C_Z(\alpha_0 + \Delta\alpha_q)$ and $C_Z(\alpha_0)$ in the equation for $(\Delta C_m)_q$, and substituting the value of $\Delta\alpha_q$ from Eq.(5.30) yields:

$$(\Delta C_m)_q = \frac{d^2_{cp}}{\bar{c}V} \cdot \left(C_{Z\alpha} + C_{Z\alpha^1_{11}}\right) \cdot q \tag{5.34}$$

The pitch damping derivative C_{mq} is given then by:

$$C_{mq} = \frac{\partial C_m}{\partial q} = \frac{d^2_{cp}}{\bar{c}V} \cdot \left(C_{Z\alpha} + C_{Z\alpha^1_{11}}\right) \tag{5.35}$$

which can also be written in terms of the dimensionless pitch rate $\hat{q} = \dfrac{q\bar{c}}{2V}$:

$$C_{m\hat{q}} = \frac{\partial C_m}{\partial \hat{q}} = \frac{\partial C_m}{\partial q}\frac{\partial q}{\partial \hat{q}} = \frac{2d^2_{cp}}{\bar{c}^2} \cdot \left(C_{Z\alpha} + C_{Z\alpha^1_{11}}\right) \tag{5.36}$$

From the parameter estimation results, $C_{Z\alpha} = 1.869 \pm (8.62 \cdot 10^{-3})$ and $C_{Z\alpha^1_{11}} = -5.559 \cdot 10^{-1} \pm (2.44 \cdot 10^{-2})$, which are both negative and such $(C_{Z\alpha} + C_{Z\alpha^1_{11}})$ will always be negative as well. It can be deduced from Eq.(5.35) or (5.36) that the pitch damping derivative will be negative as long as the center of pressure is behind the center of gravity. Otherwise, the induced moment will be of opposite sign and the pitch damping derivative will be positive.

It remains to find the position of the center of pressure for different flight conditions and see its sign. It is the point of application of the aerodynamic forces, so the aerodynamic moment is zero:

$$\mathbf{M}_{cp} = \mathbf{M}_{cg} + r_{cp,cg} \times \mathbf{F}_{cg} = 0, \tag{5.37}$$

The most important contribution is due to the longitudinal position of the center of pressure, which is the only one studied here. In dimensionless form:

$$\bar{c} \cdot C_m + C_Z(x_{cp} - x_{cg}) = 0; \tag{5.38}$$

which gives an expression for the distance from the center of pressure to the center of gravity:

$$d_{cp} = x_{cp} - x_{cg} = -\frac{\bar{c} \cdot C_m}{C_Z} \tag{5.39}$$

This distance is calculated for the same range of airspeeds and angles of attack used for the trim calculations. The results are shown in Figure 5.17. When the vertical coefficient changes its sign, the center of pressure tends to plus or minus infinity as it approaches $C_Z = 0$, and it can be seen that it is positive from $\alpha \sim -1°$ to the end of the region of validity of this model, which covers the most important region of the flight envelope. For that region, according to this first-approximation calculations, the aircraft will be more stable while maneuvering ($q \neq 0$) than in trimmed conditions ($q = 0$). This means that it is possible to design a controller for the model identified here, assuming $C_{mq} \cong 0$, which would present a worst-case scenario for the controller. From the findings presented here, it follows that the designed controller for the static model should be able to trim the aircraft in dynamic conditions inside the region delimited by $d_{cp} > 0$.

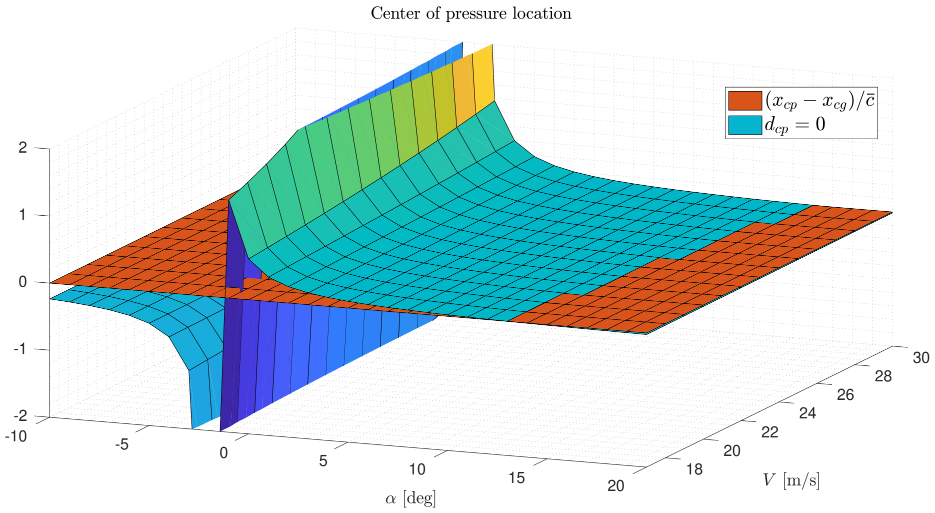

Figure 5.17: Center of pressure longitudinal position for $\alpha - V$

For high angles of attack, it can be seen that the center of pressure travels forward and d_{cp} eventually becomes negative, which would translate in a positive C_{mq}. However, this small distance of the center of pressure from the center of gravity suggests (again, within the limits of this approximation) that the pitch damping derivative will be small compared to other terms. If $d_{cp} \ll 1$, from the expression for $C_{m\hat{q}}$:

$$C_{m\hat{q}} \cong \underbrace{\frac{2d_{cp}^2}{\bar{c}^2}}_{\ll 1} \cdot \underbrace{\left(C_{Z\alpha} + C_{Z\alpha^1_{11}}\right)}_{\sim 1} \ll 1, \tag{5.40}$$

which of course is only representative of the region where the distance to the center of pressure is sufficiently small.

As a final check, the pitch damping derivative was calculated using AVL (Athena-Vortex-Lattice)[69], which is a common tool for preliminary aircraft design based in lifting line theory. A model of the sub-scale Flying V was used, which offered a value of $C_{m\hat{q}} \cong -2.4$, and even though its accuracy is highly questionable, it reinforces the hypothesis that $C_{m\hat{q}}$ is likely to be negative in the final dynamic model.

Chapter 6

Conclusions

The results from this thesis proves the Modified Stepwise Regression as an adequate technique for model structure determination to estimate the aerodynamics of the Flying V. It achieves compact models with appropriate prediction capabilities and tight confidence bounds. Global polynomial models attain good fitting and show good prediction capabilities for the most part of the dataset, but show some model deficiencies because of the large range of the measured angle of attack. Data partitioning is recommended to keep adequate polynomial models, which would lead to piecewise continuous models. Splines in the angle of attack were implemented as an alternative to data partitioning to keep continuous models, achieving better results than the polynomial models. Good model fit, small confidence bounds, and small parameter variances were achieved.

The models were validated against a partition of the data, showing good prediction capabilities and reasonably random, uncorrelated residuals, especially in the case of the spline models. Since no previous validated data from the Flying V is available, it is uncertain whether the dataset is free of systematic errors and errors in the independent variables, which would introduce bias in the estimates. Sub-scale tests, or further investigations in the wind tunnel are required in order to gain more confidence in the measured data, and to determine a proper correlation between flight test and and wind tunnel test results (including the adjustment of the wind tunnel corrections, and the effect of the wind tunnel walls on the vortex formation). The correlation with the full-scale results is difficult to assess because of the very early stage of the project and the much less knowledge available from this unconventional configuration.

The resulting models are analytical functions in the state and control variables, which can be used to determine the aerodynamic forces and moments of the Flying V at any given flight condition inside the convex hull of the estimation dataset. The availability of this model allowed to program an efficient trim routine which uses the aerodynamic models to calculate the thrust and control surfaces settings required for level flight at different airspeeds and flight angles. The results from this study include forward and aft limits for the center of gravity in order to ensure the controllability of the aircraft in most flight conditions, a feasible center of gravity location, and a definition of a safe flight envelope for the flight test. In addition, it was shown that in first approximation the dynamic stability of the aircraft is expected to be less restrictive than the static one.

Regarding the actuators identification, first order lag models using a nonlinear regression technique and *ARMAX* models seem to be adequate to estimate the actuator dynamics, leading to accurate predictions of the delay and the transient response, and are considered to be good enough to be used for control design in a future flight test.

The results indicate that once flight-test data is available, a dynamic model could also be estimated using the technique described here, by including the corresponding regressors in a (partitioned) polynomial model or a spline model.

Future work

A list of interesting ideas to be pursued are summarized here:

- **Aerodynamic Model Identification**
    - **Two-Step Method**: the estimation of a dynamic model can be done using the Two-Step Method[70], which will allow to perform dynamic simulations and to study the dynamic modes of the aircraft. A state estimation routine is the only additional required calculation, in order to get reliable estimates of the states before the aerodynamic model identification can begin.
    - **Estimation method**: a Generalized Least Squares and/or a Maximum Likelihood estimator are recommended in order to validate the OLS estimation. If the noise statistics can be estimated numerically from the measured data, the Crámer-Rao lower bound can be computed and compared with the variances and covariances of the OLS estimator derived here.
    - **Thrust effects**: the influence of the thrust in the aerodynamic coefficients should be studied, since their values will probably change for the engine-on tests. For example, the simple presence of the engine will increase the drag, affecting the value of C_{X0}. A thrust model in terms of the thrust setting, the angle of attack, sideslip and the airspeed is recommended to ensure that the engine is still capable to deliver the required thrust at high angles of attack.
    - **Online system identification**: used in topics such as Fault-Tolerant Control[4], is also regarded as a very interesting topic to follow because of its unconventional control configuration again: the six elevons available make possible to design a Fault-Tolerant control system, which would increase the safety of this configuration and advance further the design of this novel aircraft.
    - **Stall and post-stall characterization**: using the presented methodology, a model to predict the highly nonlinear regimes at very high angles of attack could be estimated if a more detailed coverage of high angles of attack is done, which could help understand the physical mechanisms of stall[3]. A similar framework to the one presented here has been used by van den Hoek et al.[24] to study post-stall characteristics.
- **Splines implementation**: it is clear that the spline models achieved better results than the polynomial ones, so increasingly complex spline models seem a natural next step to improve the estimation capabilities. Since the spline implementation presented here is rather limited, there is plenty of room for improvement in this regard.
    - **B-splines**: collinearity was clearly the limiting factor of the spline models, because of the "+" basis function used here. A more advantageous basis function can be used to take advantage of the splines higher approximation power. Examples are found in Ref. [31], where B-splines are used in a stepwise regression framework, and Ref. [71], where a straightforward implementation of a Maximum Likelihood estimator for a model based in B-splines is presented.
    - **Multivariate Simplex Splines**: in Ref. [10] some shortcomings of the tensor product splines implementations (all of the above) are described, and a framework for global system identification using multivariate simplex splines is presented. This approach is defined in a triangulation of the state space instead of the rectangular domain used in the tensor product splines, which allows to estimate models from scattered data. A much higher flexibility and approximation power is also achieved, as local nonlinearities can be modeled without affecting the global model structure.
- **Control design**: a model-based controller can be now designed with the available mathematical model of the aircraft, which allows to calculate smooth derivatives of the aerodynamic coefficients analytically (except in the few knots with C^0 continuity), which represents a big improvement with respect to the existing aerodynamic look-up tables.

- **Design of a preliminary flight controller**: if $C_{mq} < 0$ is assumed, a worst-case scenario for a controller is such that $C_{mq} = 0$, which corresponds to the static model estimated here. Thus, if a controller to stabilize the static model is designed, it should also be able control the aircraft for unsteady flight. Actuator dynamics could be included in order to get a more accurate controller.
- **Control allocation studies**: because of the unconventional control surfaces configuration of this aircraft, this is an interesting step in the field of control design. With a total of 6 elevons and 2 winglets with rudders, this redundancy can be exploited to define a safer and/or more efficient control system by a proper control allocation.

Bibliography

[1] V. Klein and E. A. Morelli, *Aircraft System Identification: Theory and Practice.* American Institute of Aeronautics and Astronautics, 2006.

[2] E. A. Morelli, “Global Nonlinear Aerodynamic Model Using Multivariate Orthogonal Functions,” *Journal of Aircraft*, vol. 32, no. 2, pp. 270–277, 1995.

[3] V. Klein, J. G. Batterson, and P. C. Murphy, “Airplane Model Structure Determination from Flight Data,” *Journal of Aircraft*, vol. 20, no. 5, pp. 469–474, 1983.

[4] T. Lombaerts, Q. Chu, J. Mulder, and D. Joosten, “Real Time Damaged Aircraft Model Identification for Reconfiguring Flight Control,” in *AIAA Atmospheric Flight Mechanics Conference and Exhibit*, aug 2007.

[5] L. Ljung, “Black-box Model from Input-output Measurements,” in *IEEE Instrumentation and Measurement Technology Conference*, vol. 2, IEEE, 2001.

[6] A. Einstein and H. Minkowski, *The Principle of Relativity.* University of Calcutta, 1920.

[7] T. Rajkumar, C. Aragon, J. Bardina, and R. Britten, “Prediction of aerodynamic coefficients for wind tunnel data using a generic algorithm optimized neural network,” in *FLAIRS*, American Association for Artificial Intelligence, 2002.

[8] M. Larson, P. D. Raedt, and M. Hedlund, “Aerodynamic identification using neural networks,” LiTH 154-1937, Linköping University, 1997.

[9] P. G. Hamel and R. V. Jategaonkar, “Evolution of Flight Vehicle System Identification,” *Journal of Aircraft*, vol. 33, no. 1, pp. 9–28, 1996.

[10] C. de Visser, J. Mulder, and Q. Chu, “A Multidimensional Spline Based Global Nonlinear Aerodynamic Model for the Cessna Citation II,” in *AIAA Atmospheric Flight Mechanics Conference*, American Institute of Aeronautics and Astronautics, aug 2010.

[11] J. Benad, “The Flying V - A new aircraft configuration for commercial passenger transport,” in *Deutscher Luft-und Raumfahrtkongress*, 2015.

[12] F. Faggiano, R. Vos, M. Baan, and R. van Dijk, “Aerodynamic Design of a Flying V Aircraft,” in *American Institute of Aeronautics and Astronautics*, no. 17, American Institute of Aeronautics and Astronautics, 2017.

[13] R. Vos, F. J. J. M. M. Geuskens, and M. F. M. Hoogreef, “A New Structural Design Concept for Blended Wing Body Cabins,” in *AIAA/ASME/ASCE/AHS/ASC Structures, Structural Dynamics and Materials Conference*, no. 53, American Institute of Aeronautics and Astronautics, 2012.

[14] L. van der Schaft, “Development, Model Generation and Analysis of a Flying V Structure Concept,” p. 119, 2017.

[15] M. Palermo, “The Longitudinal Static Stability and Control Characteristics of a Flying V Scaled Model,” Master’s thesis, Delft University of Technology, 2019.

[16] R. Viet, “Analysis of the flight characteristics of a highly swept cranked flying wing by means of an experimental test,” Master’s thesis, Delft University of Technology, 2019.

[17] L. van der Schaft, “Development, Model Generation and Analysis of a Flying V Structure Concept,” Master’s thesis, Delft University of Technology, 2017.

[18] M. Laban, *Online Aerodynamic Model Identification.* PhD thesis, Delft University of Technology, 1994.

[19] V. Klein, “Estimation of Aircraft Aerodynamic Paramters From Flight Data,” *Progress in Aerospace Sciences*, vol. 26, no. 1, pp. 1–77, 1989.

[20] K. W. Iliff, “Parameter Estimation for Flight Vehicles,” *Journal of Guidance*, vol. 12, no. 5, pp. 609–622, 1989.

[21] R. E. Maine and K. W. Iliff, “Formulation and implementation of a Practical Algorithm for Parameter Estimation with Process and Measurement Noise,” *SIAM Journal of Applied Mathematics*, vol. 41, no. 3, pp. 558–579, 1981.

[22] J. A. Mulder, *Design and evaluation of dynamic flight test manoeuvres.* PhD thesis, Delft University of Technology, 1986.

[23] Q. P. Chu, J. A. Mulder, and J. K. Sridhar, “Decomposition of Aircraft State and Parameter Estimation Problems,” in *Proceedings of the 10th IFAC Symposium on System Identification, Vol. 3, Danish Automation Society, Copenhagen, Denmark*, vol. 27, pp. 61–66, 1994.

[24] M. van den Hoek, C. de Visser, and D. Pool, “Identification of a Cessna Citation II Model Based on Flight Test Data,” in *CEAS Specialist Conference on Guidance, Navigation and Control*, no. 4, 2017.

[25] L. Ljung, *System Identification: Theory for the user.* Prentice Hall, 1999.

[26] F. C. Schweppe, *Uncertain Dynamic Systems.* Prentice Hall, 1973.

[27] E. Özger, “Aerodynamic Model Validation of Eurofighter Aircraft,” in *AIAA Atmospheric Flight Mechanics Conference and Exhibit*, aug 2007.

[28] V. Klein and K. D. Noderer, “Modeling of aircraft unsteady aerodynamic characteristics. Part 1: Postulated models,” NASA Technical Memorandum 109120, National Aeronautics and Space Administration, 1994.

[29] J. G. Klein, V.; Batterson, “Determination of Airplane Model Structure From Flight Data Using Splines and Stepwise Regression,” no. March, p. 52, 1983.

[30] V. Klein and J. G. Batterson, “Aerodynamic parameters estimated from flight and wind tunnel data,” *Journal of Aircraft*, vol. 23, no. 4, pp. 306–312, 1986.

[31] P. L. Smith, “Curve Fitting and Modeling with Splines using Statistical Variable Selection Techniques,” NASA Contractor Report (Old Dominion University Research Foundation) 166034, National Aeronautics and Space Administration, 1982.

[32] R. E. Maine and W. I. Kenneth, “Identification of Dynamic Systems,” NASA Reference Publication 1138, National Aeronautics and Space Administration, 1985.

[33] C. R. Rao, *Linear Statistical Interference and its Applications.* Wiley Series in Probability and Statistics, Wiley, second ed., 1973.

[34] P. C. Murphy, “A Methodology for Airplane Parameter Estimation and Confidence Interval Determination in Nonlinear Estimation Problems,” NASA Reference Publication 1153, National Aeronautics and Space Administration, apr 1986.

[35] R. V. Jategaonkar, “Flight Vehicle System Identification: A Time Domain Methodology,” *Progress in Aeronaunatics and Astronautics*, vol. 216, 2006.

[36] S. K. Mithra and C. R. Rao, “Conditions for Optimality and Validity of Simple Least Squares Theory,” *The Annals of Mathematical Statistics*, vol. 40, no. 5, pp. 1617–1624, 1969.

[37] T. C. Hsia, *System Identification.* Lexington Books, 1977.

[38] D. C. Montgomery, E. A. Peck, and G. G. Vining, *Introduction to Linear Regression Analysis.* Wiley Series in Probability and Statistics, Wiley, fifth ed., 2012.

[39] D. Belsley, E. Kuh, and R. Welsch, *Regression Diagnostics.* John Wiley & Sons, 1980.

[40] V. Klein, “Two biased estimation techniques in linear regression - application to aircraft,” NASA Technical Memorandum 100649, National Aeronautics and Space Administration, 1988.

[41] M. H. Stone, “Applications of the Theory of Boolean Rings to General Topology,” *Transactions of the American Mathematical Society*, vol. 41, no. 3, pp. 375–481, 1937.

[42] V. Klein, J. Batterson, and P. Smith, “On the Determination of Airplane Model Structure From Flight Data,” *IFAC Proceedings Volumes*, vol. 15, no. 4, pp. 1163–1168, 2017.

[43] G. Batterson, J. and V. Klein, “Partitioning of flight data for aerodynamic modeling of aircraft at high angles of attack,” *Journal of Aircraft*, vol. 26, no. 4, pp. 334–339, 1989.

[44] E. A. Morelli and R. Deloach, “Wind Tunnel Database Development using Modern Experiment Design and Multivariate Orthogonal Functions,” in *41st AIAA Aerospace Science Meeting and Exhibit*, (Reno), American Institute of Aeronautics and Astronautics, 2003.

[45] E. A. Morelli, “Global Nonlinear Parametric Modeling with Application To F-16 Aerodynamics,” in *Proceedings of the American Control Conference*, no. June, pp. 997–1001, 1998.

[46] J. A. Grauer and E. A. Morelli, “Generic Global Aerodynamic Model for Aircraft,” *Journal of Aircraft*, vol. 52, no. 1, pp. 13–20, 2015.

[47] A. Barron, “Predicted Squared Error: A Criterion for Automatic Model Selection,” in *Self-Organizing Methods in Modeling*, pp. 87–104, 1984.

[48] V. Klein, J. G. Batterson, and P. C. Murphy, “Determination of Airplane Model Structure From Flight Data by Using Stepwise Regression,” NASA Technical Paper 1916, National Aeronautics and Space Administration, 1981.

[49] F. Kraus, X. Qiu, and W. Schaufelberger, “Identification and Control of a Servo System,” *IFAC Proceedings Volumes*, vol. 30, no. 11, pp. 197–202, 2017.

[50] C. H. Wolowicz, J. S. Bowman-Jr, and W. P. Gilbert, “Similitude requirements and scaling relationships as applied to model testing,” NASA Technical Paper 1435, National Aeronautics and Space Administration, 1979.

[51] A. Haines, “Scale Effects on Aircraft and Weapon Aerodynamics,” AGARD Technical Report 323, Advisory Group for Aerospace Research and Development, 1994.

[52] J. B. Barlow, W. J. H. Rae, and A. Pope, *Low-Speed Wind Tunnel Testing.* Wiley, third ed., 1999.

[53] D. M. Bushnell, “Scaling: Wind tunnel to flight,” *Annual Rev. Fluid Mechanics*, vol. 38, pp. 111–128, 2006.

[54] W. Yu, V. Hong, C. Ferreira, and G. van Kuik, “Experimental analysis on the dynamic wake of an actuator disc undergoing transient loads,” *Experiments in Fluids*, vol. 58, 2017.

[55] “Open Jet Facility wind tunnel.” `https://www.tudelft.nl/lr/organisatie/afdelingen/aerodynamics-wind-energy-flight-performance-and-propulsion/facilities/low-speed-wind-tunnels/open-jet-facility/`. [Online; accessed 05-May-2019].

[56] Y. Nakamura, Y. Ohya, and H. Tsuruta, “Experiments on vortex shedding from flat plates with square leading and trailing edges,” *Journal of Fluid Mechanics*, vol. 222, pp. 437–447, 1991.

[57] W. Acum, H. Garner, E. Maskell, and E. Rogers, “Subsonic Wind Tunnel Wall Corrections,” AGARD Technical Report 109, Advisory Group for Aerospace Research and Development, 1986.

[58] J.-L. Hantrais-Gervois and J.-F. Piat, "A methodology to derive wind tunnel wall corrections from rans simulations," 10 2012.

[59] O. Fischer, *CFD Investigations of Wind Tunnel Interference Effects.* PhD thesis, University of Stuttgart, 2017.

[60] W. Acum, H. Garner, E. Maskell, and E. Rogers, "Subsonic Wind Tunnel Wall Corrections," AGARD Technical Report 109, Advisory Group for Aerospace Research and Development, 1986.

[61] E. C. Polhamus, "A concept of the vortex lift of sharp-edge delta wings based on a leading-edge-suction analogy," Nasa Technical Note D-3767, 1966.

[62] R. Vos and S. Farokhi, *Introduction to Transonic Aerodynamics.* Fluid Mechanics and Its Applications, Springer, 2015.

[63] M. Allan, K. Badcock, G. Barakos, and B. Richards, "Wind-tunnel interference effects on delta wing aerodynamics computational fluid dynamics investigation," *Journal of Aircraft*, vol. 42, 2005.

[64] R. D. Mehta and E. R. Cantwell, "Mean flow and turbulence measurements in a half-delta wing vortex," *Fluid Dynamics Research*, vol. 4, no. 2, pp. 123–137, 1988.

[65] D. C. Montgomery, *Design and Analysis of Experiments.* John Wiley & Sons, 7th ed., 2009.

[66] B. Stevens and F. Lewis, *Aircraft Control and Simulation.* Wiley, 2003.

[67] J. Roskam, *Airplane flight dynamics and automatic flight controls.* DARcorporation, 2003.

[68] M. A. Gómez-Tierno, M. Pérez-Cortés, and C. Puentes-Márquez, *Mecánica del Vuelo.* Garceta Grupo Editorial, second ed., 2012.

[69] "Athena Vortex Lattice (AVL)." `http://web.mit.edu/drela/Public/web/avl/`. [Online; accessed 15-May-2019].

[70] J. A. Mulder, Q. P. Chu, J. K. Sridhar, J. H. Breeman, and M. Laban, "Non-linear aircraft flight path reconstruction review and new advances," *Progress in Aerospace Sciences*, vol. 35, no. 7, pp. 673–726, 1999.

[71] P. D. Bruce and M. G. Kellett, "Modelling and identification of non-linear aerodynamic functions using b-splines," in *Proceedings of the Institution of Mechanical Engineers, Part G: Journal of Aerospace Engineering*, vol. 214, pp. 27–40, 2000.

[72] National Semiconductors, *LM158/LM258/LM358/LM2904 - Low Power Dual Operational Amplifiers Datasheet*, October 2005.

Appendices

Appendix A

Controller and DAQ design

Some details of the electronic design and programming logic of the controller and Data Acquisition System for the control surfaces are shown here:

- Electronic schematic of the controller and DAQ (Figure A.1)
- Details of the buffer calculations to electrically isolate the potentiometers and the rest of the circuit (Figure A.2)
- Simplified flowchart with the logic used to communicate between the PC and the two boards (Figure A.3)

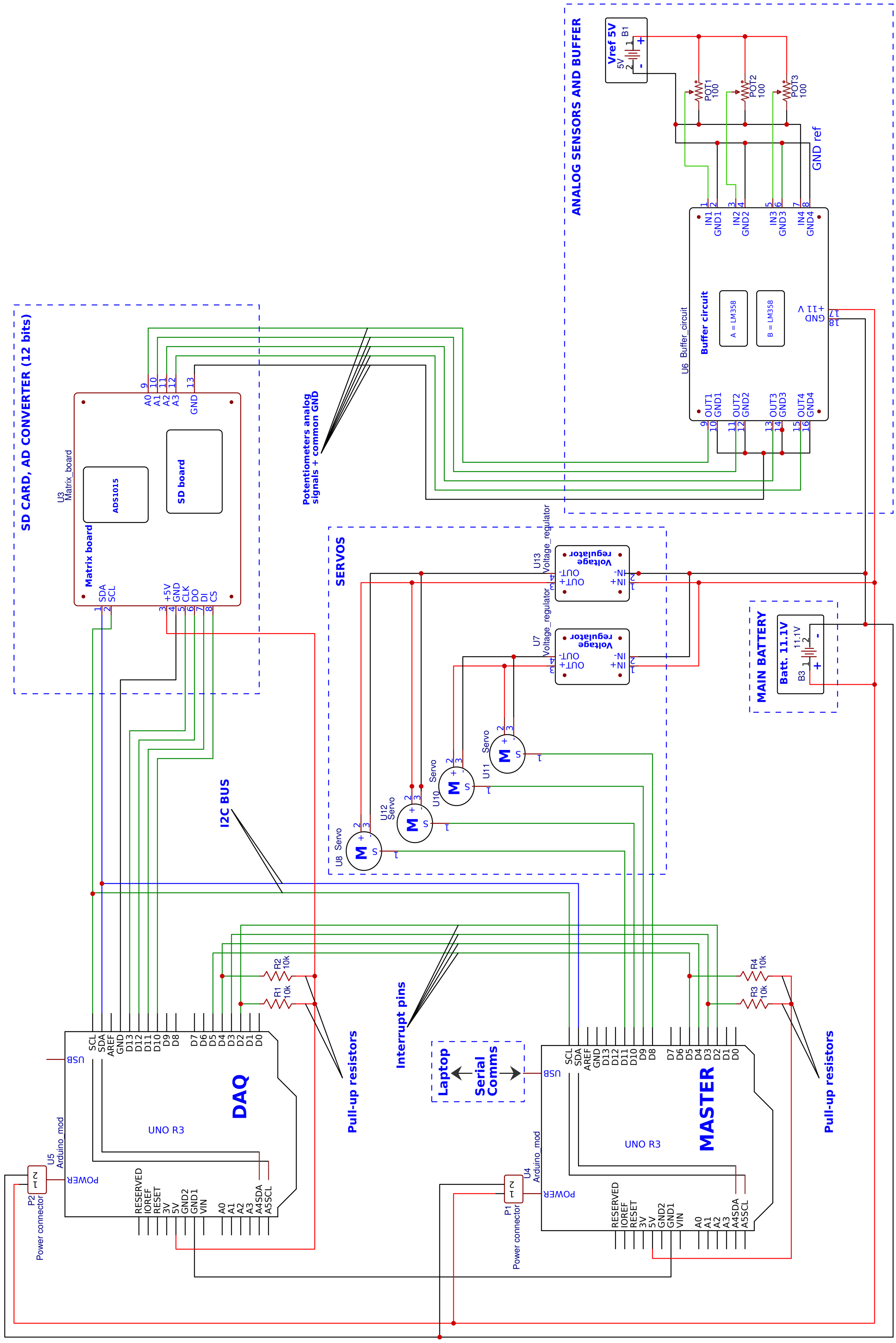
ANALOG SENSORS AND BUFFER
Vref 5V
5V
B1
POT1
100
POT2
100
POT3
100
GND ref
U6 Buffer_circuit
Buffer circuit
A = LM358
B = LM358
IN1
GND1
IN2
GND2
IN3
GND3
IN4
GND4
OUT1
GND1
OUT2
GND2
OUT3
GND3
OUT4
GND4
+11 V
GND
SD CARD, AD CONVERTER (12 bits)
U3
Matrix_board
Matrix board
ADS1015
SD board
A0
A1
A2
A3
GND
SDA
SCL
+5V
GND
CLK
DO
DI
CS
Potentiometers analog signals + common GND
SERVOS
U13
Voltage_regulator
U7
Voltage_regulator
Voltage regulator
IN+
IN-
OUT+
OUT-
U8 Servo
U12 Servo
U10 Servo
U11 Servo
M
MAIN BATTERY
Batt. 11.1V
B3
11,1V
I2C BUS
Interrupt pins
Pull-up resistors
R1 10k
R2 10k
R3 10k
R4 10k
DAQ
U5
Arduino_mod
UNO R3
P2
Power connector
MASTER
U4
Arduino_mod
P1
Power connector
USB
POWER
Laptop
Serial Comms
SCL
SDA
AREF
GND
D13
D12
D11
D10
D9
D8
D7
D6
D5
D4
D3
D2
D1
D0
RESERVED
IOREF
RESET
3V
5V
GND2
GND1
VIN
A0
A1
A2
A3
A4SDA
A5SCL

Figure A.1: Schematic of the controller and DAQ for the control surfaces

Buffer circuit details

It will be shown how a buffer circuit can be used to isolate the potentiometers electrically from the rest of the circuit. The diagram shown in Figure A.2 includes two LM358 (4 operational amplifiers) in closed loop. The closed loop input and output impedances ($Z_{c_{in}}, Z_{c_{out}}$) are given by:

$$Z_{c_{in}} = G \cdot Z_{o_{in}} \gg 1, \qquad Z_{c_{out}} = \frac{Z_{o_{out}}}{G} \ll 1, \tag{A.1}$$

where G is the gain and is equal to $G = 10^5$[72], and $Z_{o_{in}}, Z_{o_{out}}$ are the input and output impedances in open loop, which are not specified in the datasheet.

The operational amplifiers as they are connected here will keep the output voltage equal to the input voltage. Since the operational amplifier increases the input impedance and decreases the output impedance so that $Z_{c_{in}} \gg Z_{c_{out}}$, it effectively isolates both parts of the circuit. In this way, electric disturbances happening on the output side of the buffer will not affect the potentiometers reading, and besides, the much smaller output impedance means the signal will also be better shielded against electromagnetic interferences, since the induced currents will be much smaller.

Note also that the second input of the lower LM 358 (B) is reserved for the ground signal, which is measured at the same location where the potentiometers are and subtracted in the analog-to-digital converter to create differential connections for the signals, which are more robust against electrical noise than single-ended ones.

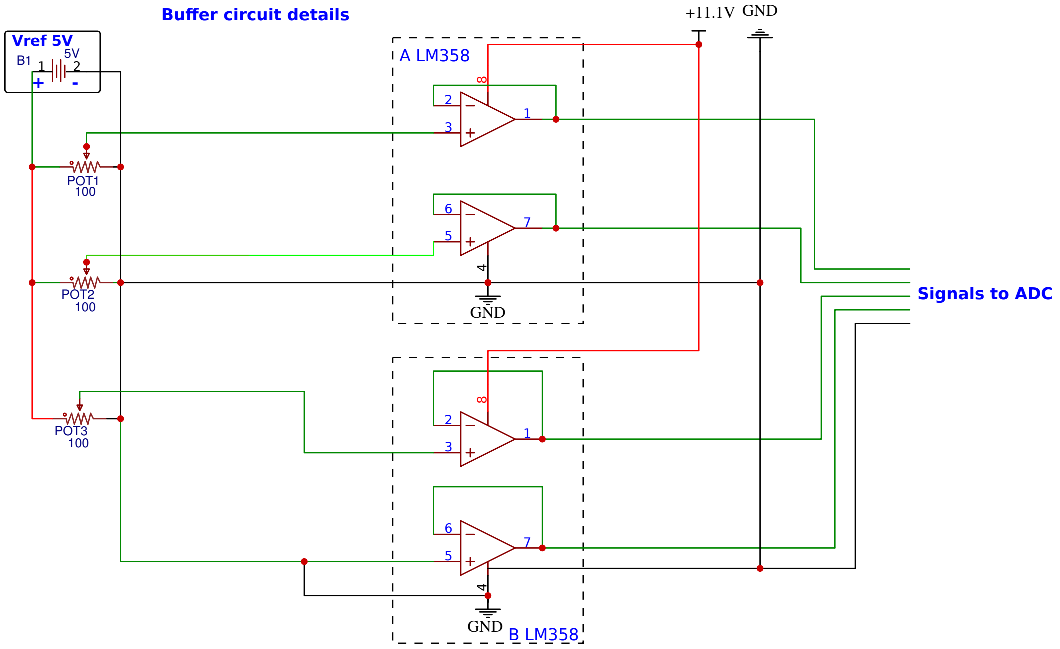

Figure A.2: Buffer circuit details

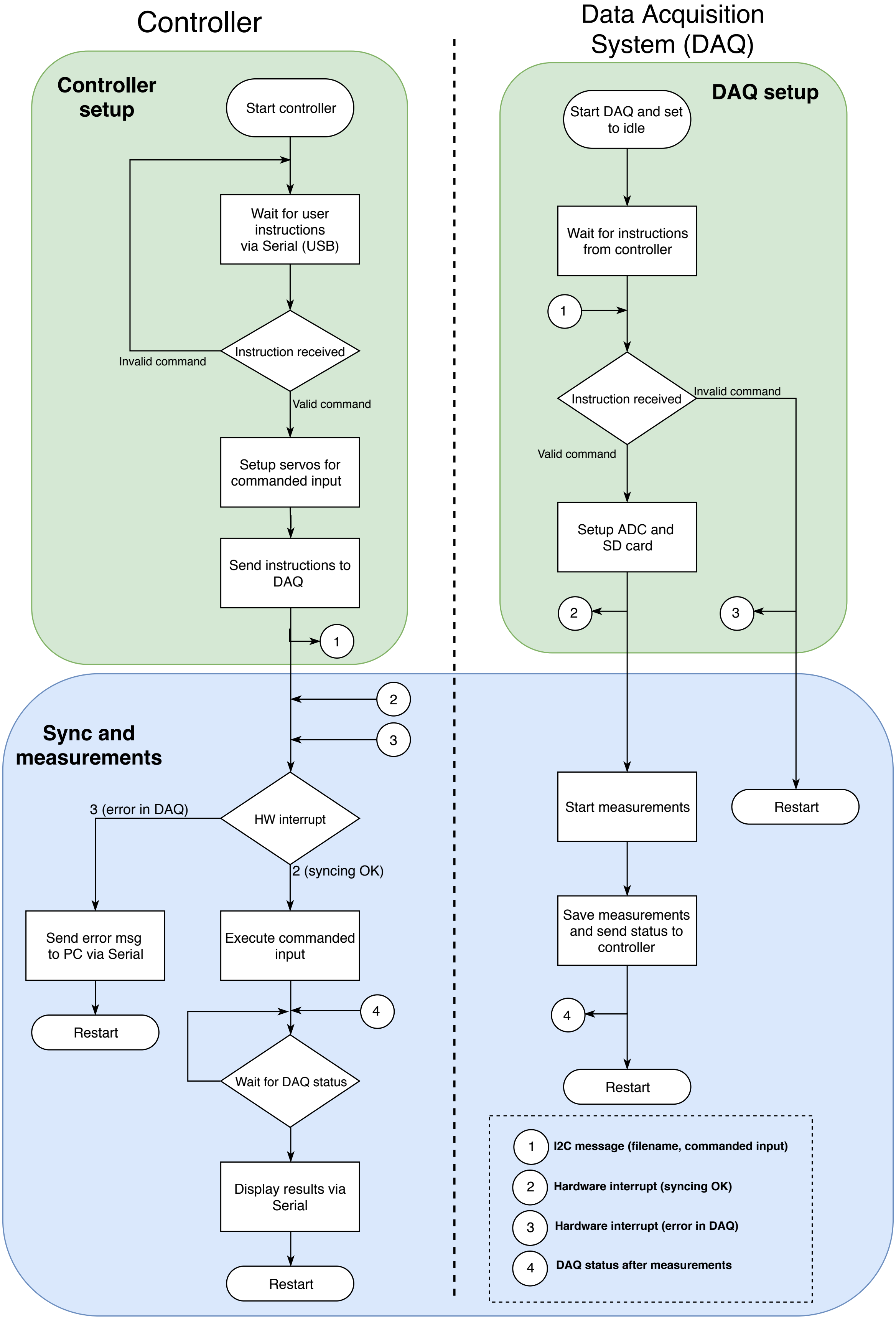
Controller
Data Acquisition System (DAQ)
Controller setup
Start controller
Wait for user instructions via Serial (USB)
Instruction received
Invalid command
Valid command
Setup servos for commanded input
Send instructions to DAQ
1
DAQ setup
Start DAQ and set to idle
Wait for instructions from controller
1
Instruction received
Invalid command
Valid command
Setup ADC and SD card
2
3
Sync and measurements
2
3
HW interrupt
3 (error in DAQ)
2 (syncing OK)
Send error msg to PC via Serial
Restart
Execute commanded input
4
Wait for DAQ status
Display results via Serial
Restart
Start measurements
Restart
Save measurements and send status to controller
4
Restart
1 I2C message (filename, commanded input)
2 Hardware interrupt (syncing OK)
3 Hardware interrupt (error in DAQ)
4 DAQ status after measurements

Figure A.3: Flowchart with the simplified logic used to communicate between the PC and the two boards

Appendix B

Frames of Reference

In this appendix the reference frames necessary to write the aircraft equations of motion are defined, along with the relations among them.

The conventions used for this definition are:

- F_X represents the reference frame X
- $\{\mathbf{F_X}\}$ represents the column of unit vectors in the directions of the reference frame X
- $[R_\bullet]$ represents a rotation matrix

The reference frames used in the present thesis are:

Earth reference frame F_E

The Earth reference frame is considered to be inertial, and used as a starting point for the rest of the reference frames. Its origin is located in an arbitrary point in the Earth's surface, its z-axis points to the center of the Earth, and the x-axis points to a reference direction (e.g. North). The y-axis will be defined so that the reference frame is right handed.

Body reference frame F_B

The body reference frame is attached to the aircraft. Its origin is defined in the aircraft center of mass, the x-axis points to the nose, the y-axis points to the right wing tip, and the z-axis defines a right-handed reference frame. It moves with $\mathbf{V} = (u, v, w)\{\mathbf{F_B}\}$ with respect to the Earth reference frame, and rotates with an angular velocity $\omega = (p, q, r)\{\mathbf{F_B}\}$.

Since the data used for this thesis comes from a static wind tunnel tunnel, the equations of motion to translate the results from Earth to Body axes are not needed.

Wind reference frame F_w

The wind axes has its origin fixed to the aircraft center of mass, and the x_w axis always pointing to the direction of the airspeed $\mathbf{V}$, such that:

$$\mathbf{V} = (u, v, w)\{\mathbf{F_B}\} = (V, 0, 0)\{\mathbf{F_w}\}. \tag{B.1}$$

The z_w axis is in the symmetry plane of the aircraft, perpendicular to x_w and pointing downwards for a normal flight attitude of the aircraft. The y_w axis is defined so that the frame is right-handed. It can be defined from the body axis just by two rotations (Fig. B.2):

- Angle of attack, α ($-\pi/2 < \alpha < \pi/2$). Angle between the projection of the airspeed onto the horizontal plane and x_B
- Sideslip angle, β ($-\pi < \beta < \pi$). Angle between the airspeed (x_w) and its projection onto the symmetry plane of the aircraft. Sideslip angle is usually considered to be positive when the velocity points to the right of the symmetry plane of the aircraft.

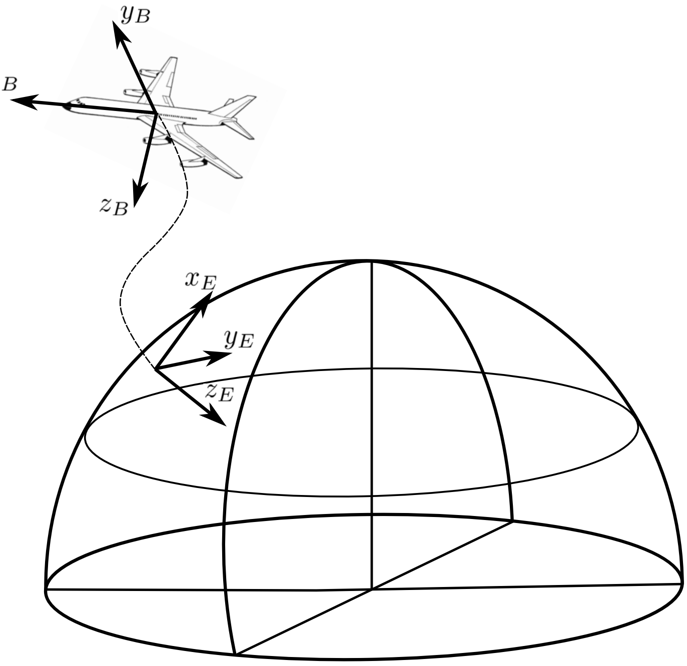
y_B
x_B
z_B
x_E
y_E
z_E

Figure B.1: Earth and body reference frames

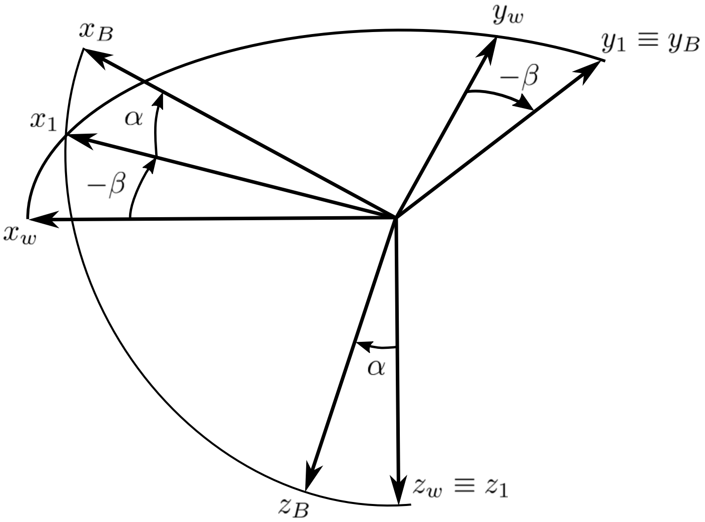
x_B
y_w
$y_1 \equiv y_B$
$-\beta$
x_1
α
$-\beta$
x_w
α
z_B
$z_w \equiv z_1$

Figure B.2: Orientation between wind and body reference frames

Balance reference frame

This reference frame is centered at the balance reference point for the measurements, which is given in the balance specifications manual, along with the definition of the balance reference frame. The location of the balance with respect to the center of gravity of the aircraft is shown in Figure B.3. The rotation matrix between the balance and the body reference frames is:

$$[R_{bB}] = \begin{bmatrix} -1 & 0 & 0 \\ 0 & 0 & 1 \\ 0 & 1 & 0 \end{bmatrix} \tag{B.2}$$

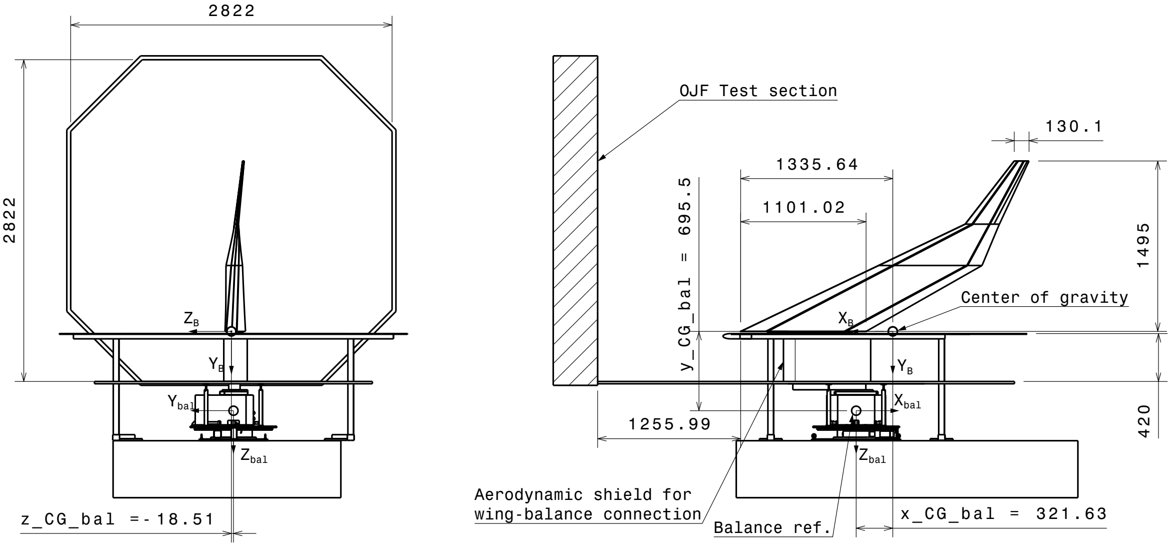
2822
2822
Z_B
Y_B
Y_{bal}
Z_{bal}
z_CG_bal =-18.51
OJF Test section
130.1
1335.64
1101.02
y_CG_bal = 695.5
1495
Center of gravity
X_B
Y_B
X_{bal}
420
1255.99
Z_{bal}
Aerodynamic shield for wing-balance connection
Balance ref.
x_CG_bal = 321.63

Figure B.3: Center of gravity and balance reference location

Appendix C

Wind tunnel test matrix

Test matrix in next page

Table C.1: Wind tunnel test matrix

Run id.	Description	Wind speed	Angle of attack	Control surfaces deflection
Run #1	Clean polar	15 m/s	[-10, 60]°	—
Run #2	Clean polar (detail stall)	15 m/s	[47.50, 60] °	—
Run #3	Clean polar	18 m/s	[-10, 60]°	—
Run #4	Clean polar	20 m/s	[-10, 42.50]°	—
Run #5	Clean polar	25 m/s	[-10, 20]°	—
Run #6	Clean polar ($\alpha = 10^\circ$ detail)	25 m/s	[5, 15] °	—
Run #7	Control surface #1 sweep	20 m/s	[-10, 35]°	Sweep
Run #8	Control surface #2 sweep	20 m/s	[-10, 35]°	Sweep
Run #9	Control surface #3 sweep	20 m/s	[-10, 35]°	Sweep
Run #10	Randomized conditions	15 m/s	[-8, 34] °	Random
Run #11	Randomized conditions	18 m/s	[-10, 35]°	Random
Run #12	Randomized conditions	20 m/s	[-9, 35] °	Random
Run #13	Randomized conditions	22 m/s	[-8, 30] °	Random
Run #14	Randomized conditions	25 m/s	[-6, 22] °	Random
Run #15	Randomized conditions	28 m/s	[-8, 15] °	Random
Run #16	Randomized conditions	30 m/s	[-4.50, 13.50] °	Random
Run #17	Randomized conditions	15 m/s	[15.50, 23.50] °	Random
Run #18	Randomized conditions	18 m/s	[15, 35] °	Random
Run #19	Randomized conditions	20 m/s	[10.50, 25] °	Random
Run #20	Randomized conditions	22 m/s	[10.50, 22] °	Random
Run #21	Randomized conditions	25 m/s	[7.50, 17] °	Random
Run #22	Randomized conditions	28 m/s	[5, 14] °	Random
Run #23	Randomized conditions	30 m/s	[4.50, 12.50] °	Random
Run #24	Clean polar	18 m/s	[-10, 60]°	—
Run #25	Clean polar	20 m/s	[-10, 47.50]°	—
Run #26	Randomized conditions	25 m/s	[0, 22.50] °	Random
Run #27	Control surfaces stall (CS2-CS3)	18 m/s	[40, 55] °	Sweep
Run #28	Control surfaces sweep (CS2-CS3)	18 m/s	[-10, 40]°	Random
Run #29	Control surfaces stall (CS2-CS3)	20 m/s	[40, 47.50] °	Sweep
Run #30	Control surfaces sweep (CS2-CS3)	20 m/s	[-10, 40]°	Sweep
Run #31	Control surfaces @stall ($CS1_{min}$, CS2-CS3)	18 m/s	[12, 50] °	Sweep
Run #32	Control surfaces @stall ($CS1_{min}$, CS2-CS3)	20 m/s	[12, 50] °	Sweep
Run #33	Control surfaces @stall ($CS1_{max}$, CS2-CS3)	18 m/s	[12, 50] °	Sweep
Run #34	Control surfaces @stall ($CS1_{max}$, CS2-CS3)	20 m/s	[12, 45] °	Sweep
Run #35	Minimum unstick speed	[12 - 23] m/s	[12, 20] °	Full-up
Run #36	Data filling	[17 - 22] m/s	[20, 60] °	Random

Appendix D

Aerodynamic Model Identification Results

Polynomial models

Forward force coefficient

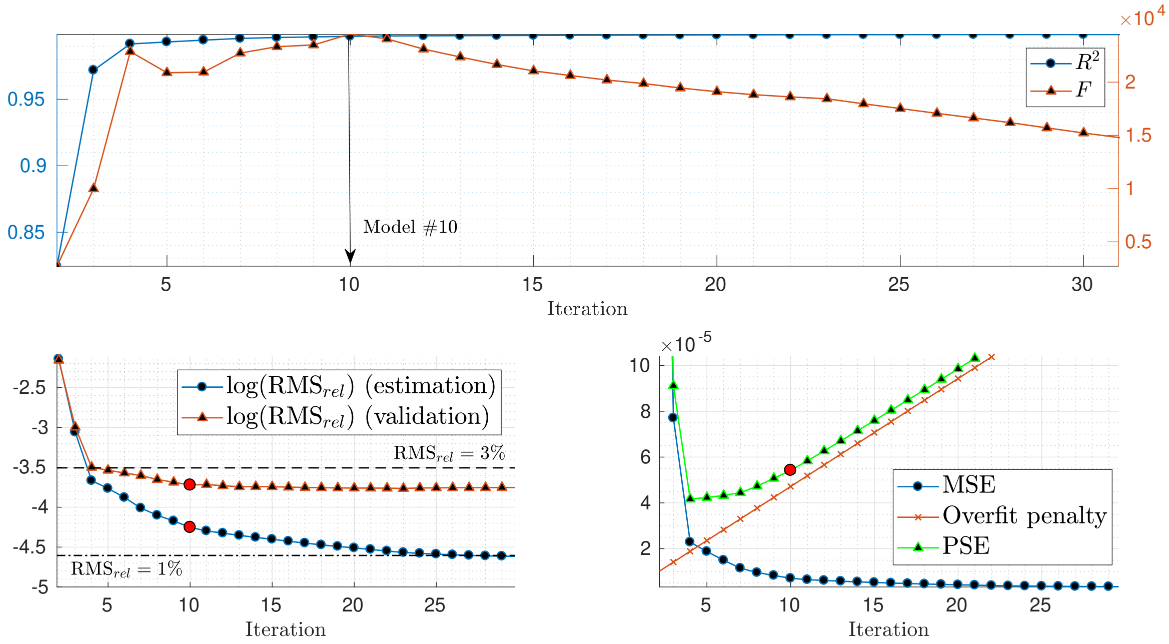

Figure D.1: Stepwise regression results (C_X polynomial model)

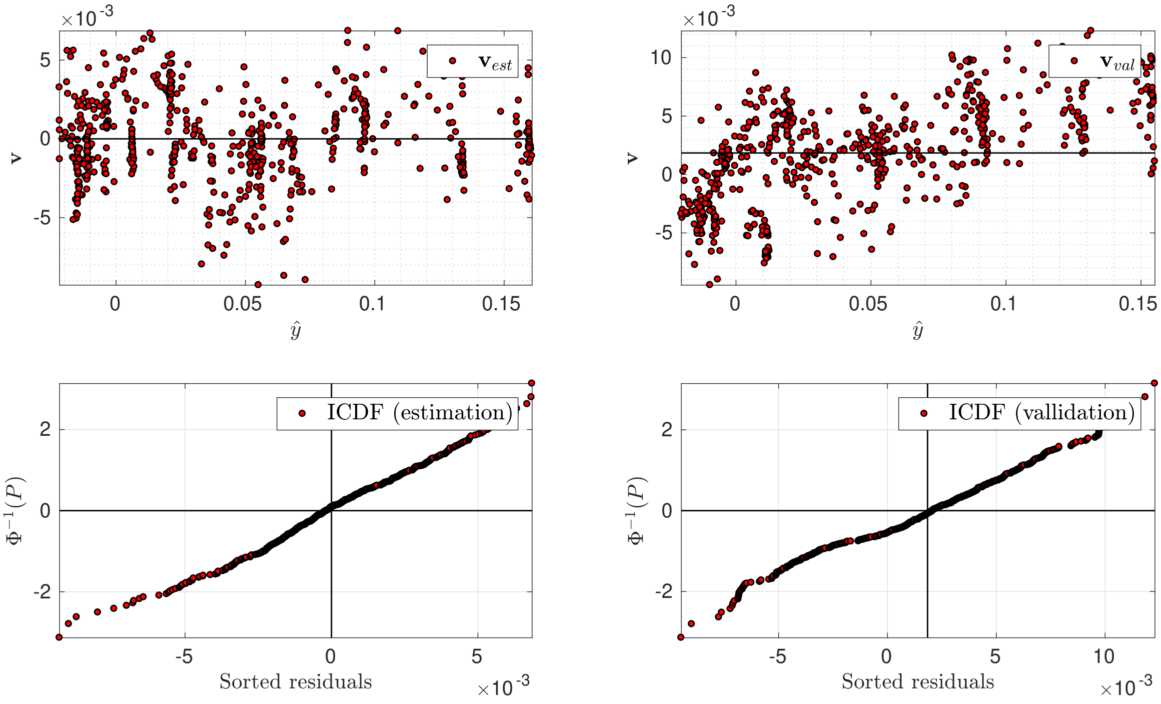

Figure D.2: Residual analysis (C_X polynomial model). Whiteness + normality assumptions.

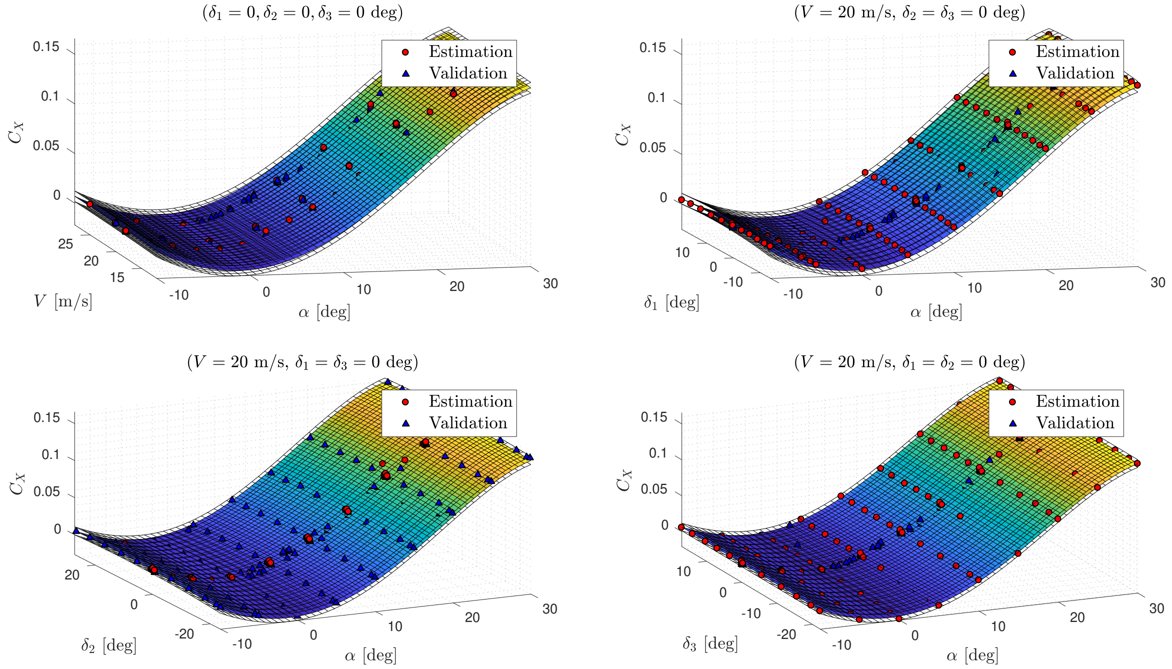

Figure D.3: Model cuts with prediction confidence bounds for $\alpha - V$ and $\alpha - \delta_i$ (C_X polynomial model)

Vertical force coefficient

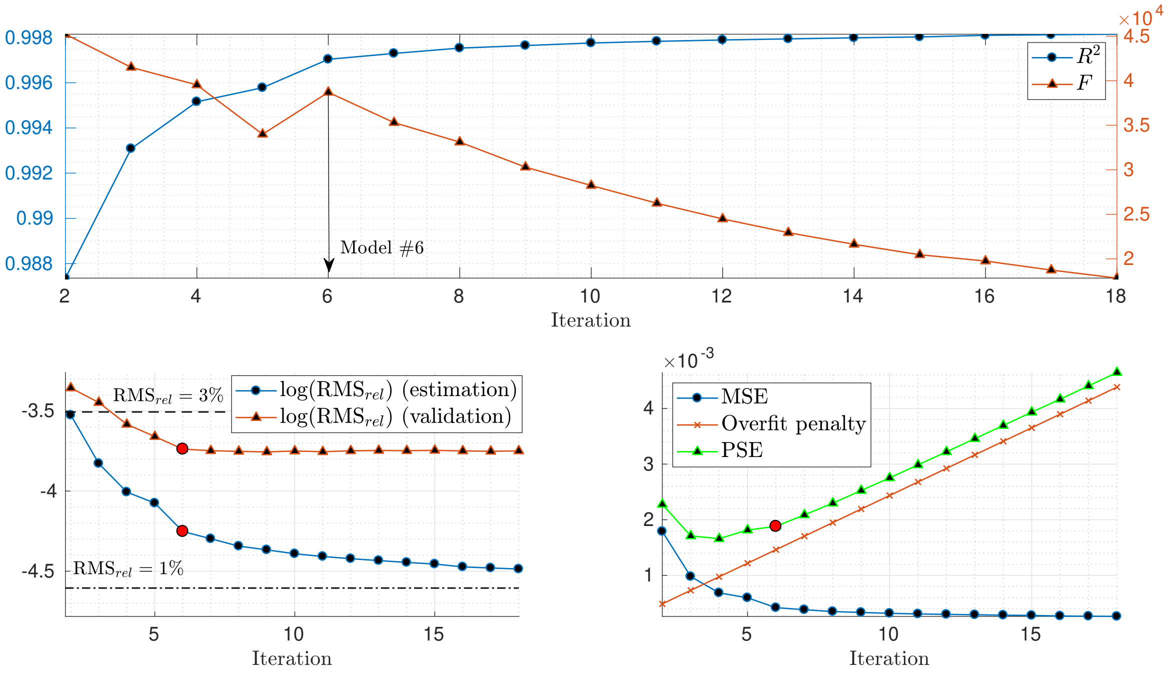

Figure D.4: Stepwise regression results (C_Z polynomial model)

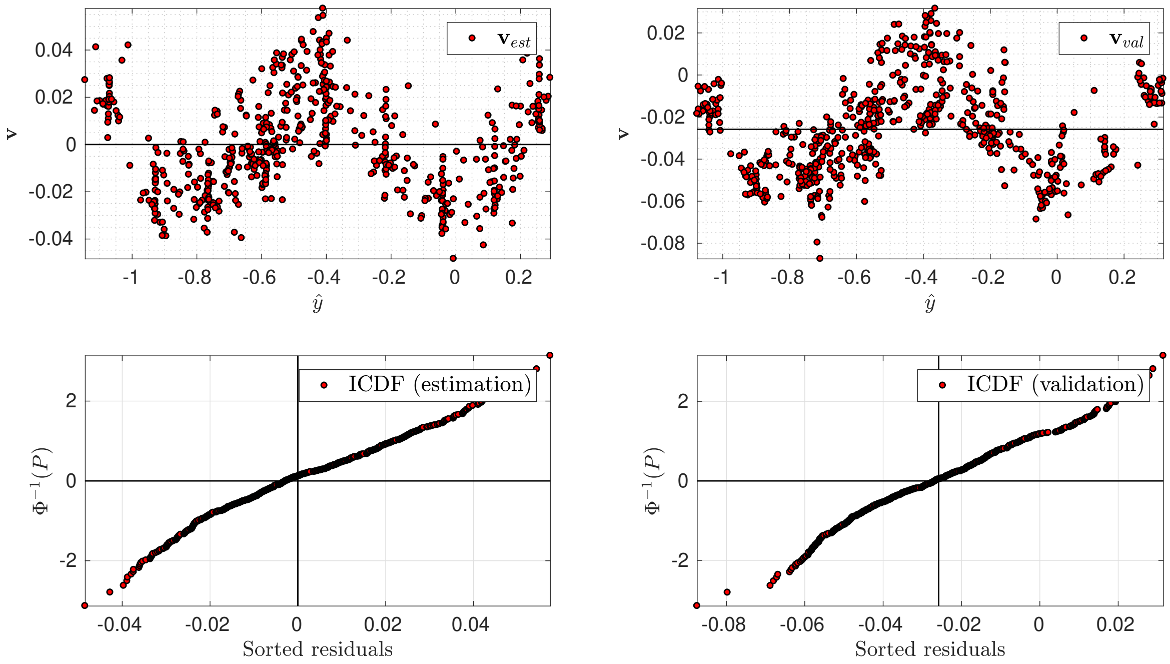

Figure D.5: Residual analysis (C_Z polynomial model). Whiteness + normality assumptions.

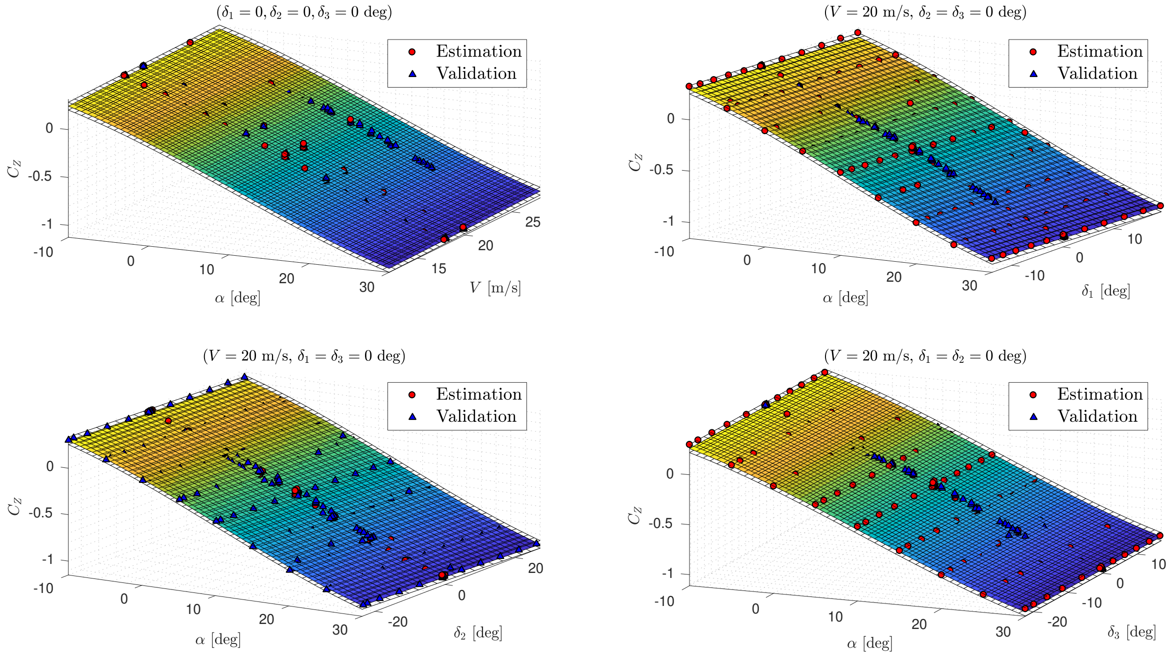

Figure D.6: Model cuts with prediction confidence bounds for $\alpha - V$ and $\alpha - \delta_i$ (C_Z polynomial model)

Rolling moment coefficient

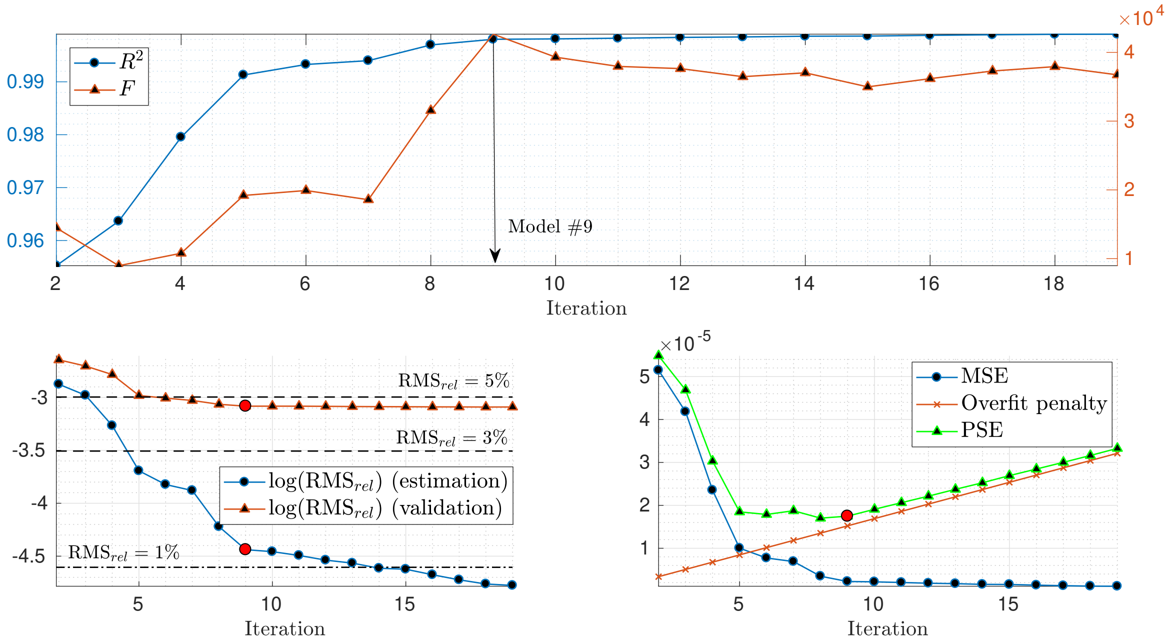

Figure D.7: Stepwise regression results (C_l polynomial model)

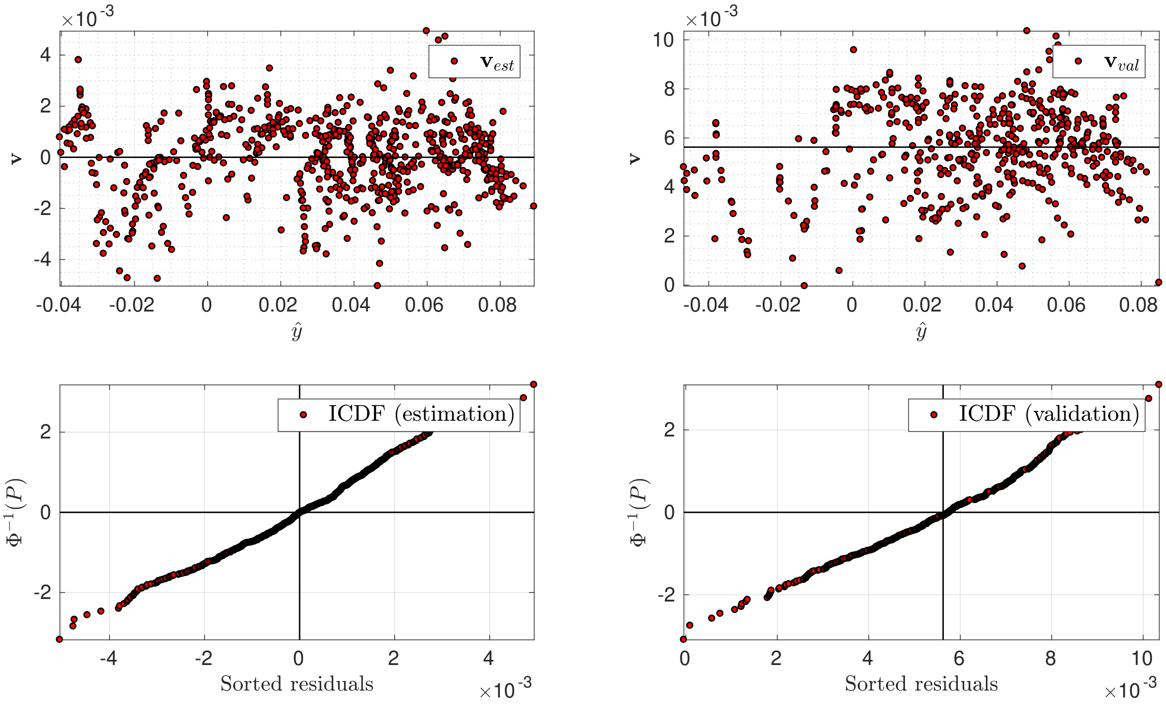

Figure D.8: Residual analysis (C_l polynomial model). Whiteness + normality assumptions.

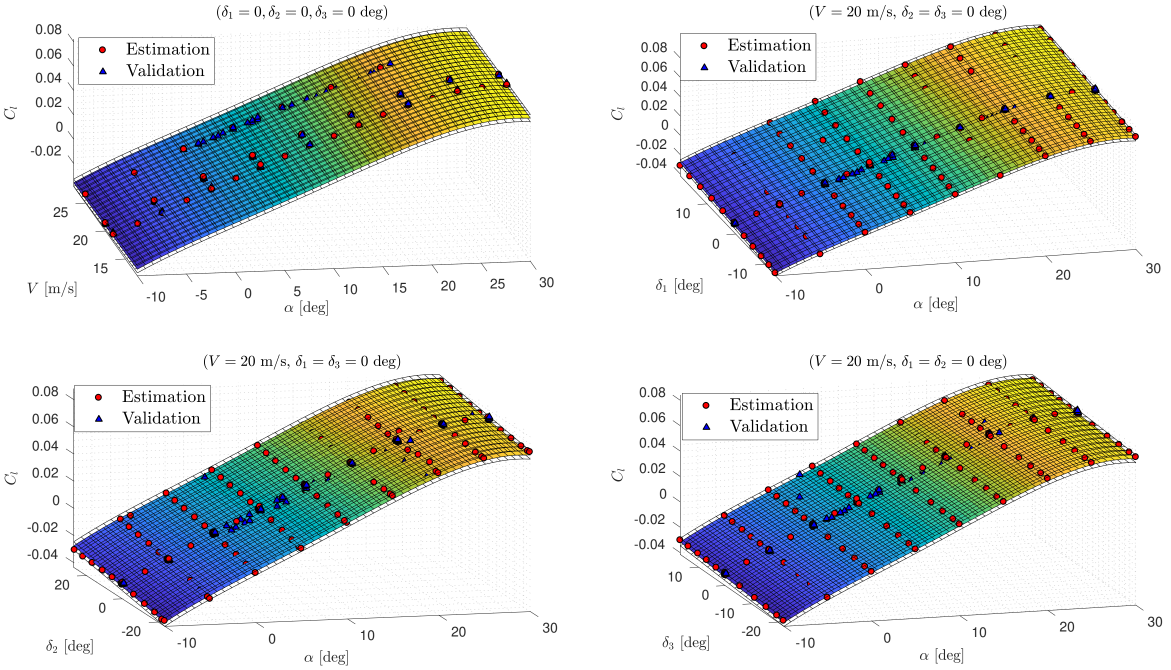

Figure D.9: Model cuts with prediction confidence bounds for $\alpha - V$ and $\alpha - \delta_i$ (C_l polynomial model)

Pitching moment coefficient

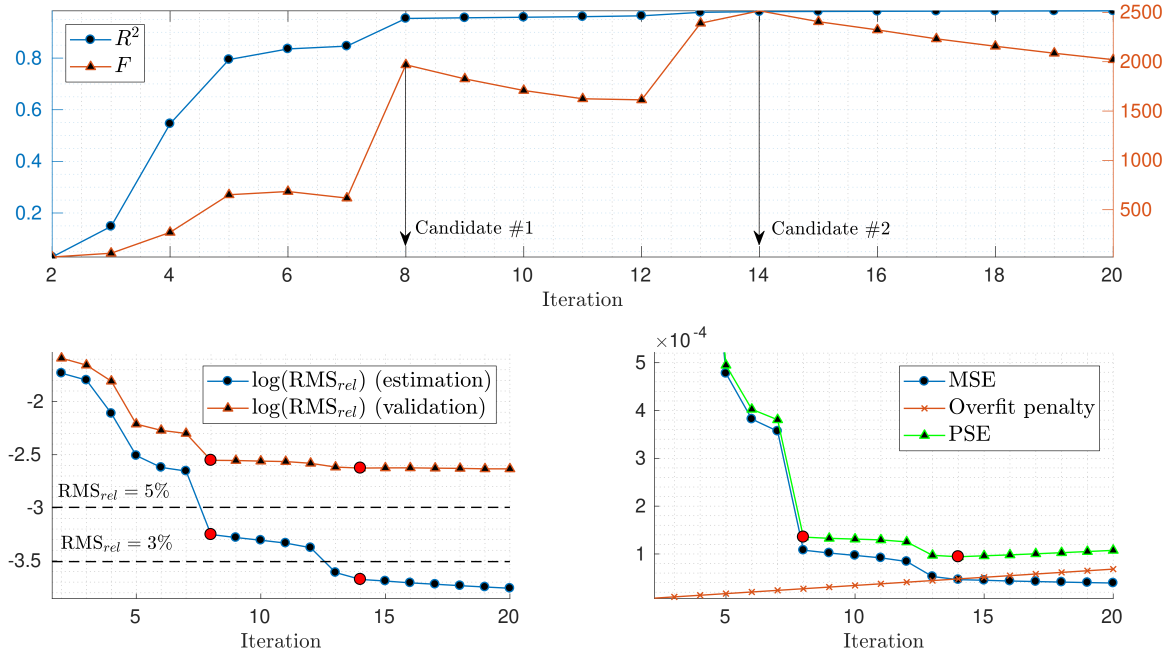

Figure D.10: Stepwise regression results (C_m polynomial model)

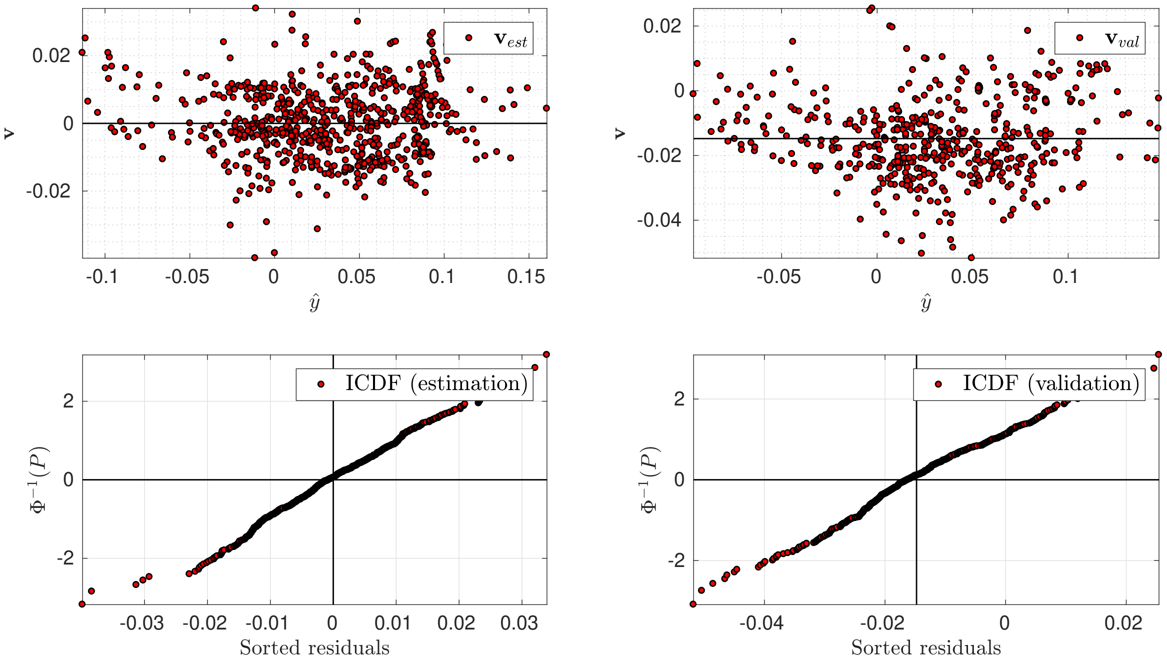

(a) Iteration #8

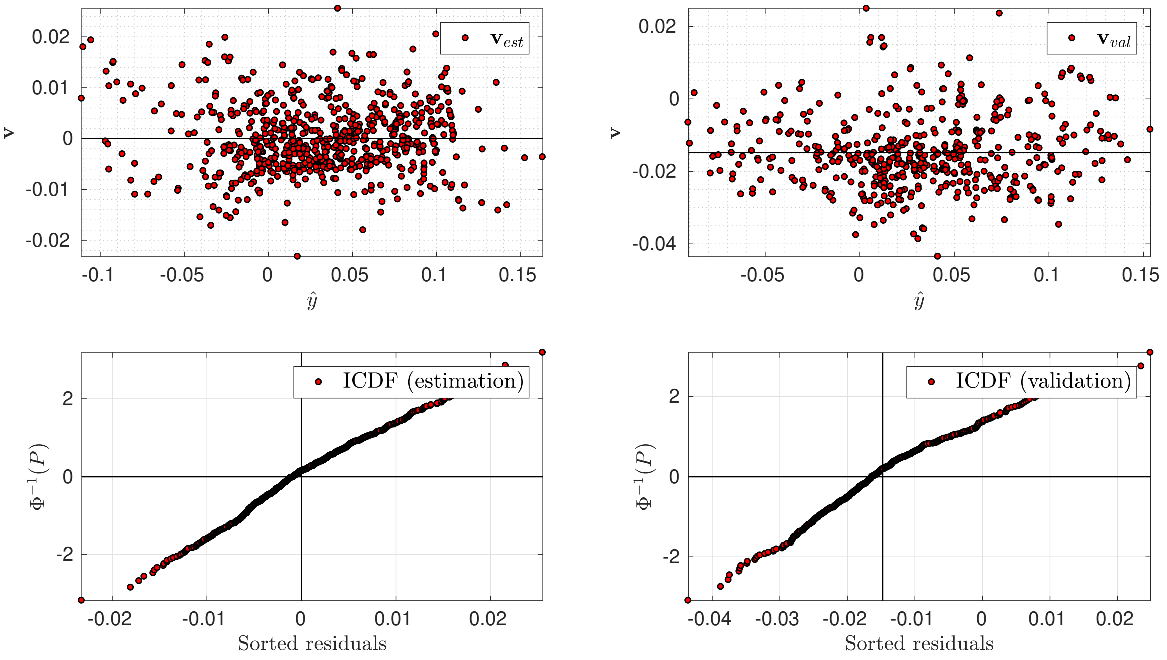

(b) Iteration #14

Figure D.11: Residual analysis at different iterations of the stepwise regression (C_m polynomial model) (whiteness + normality assumption)

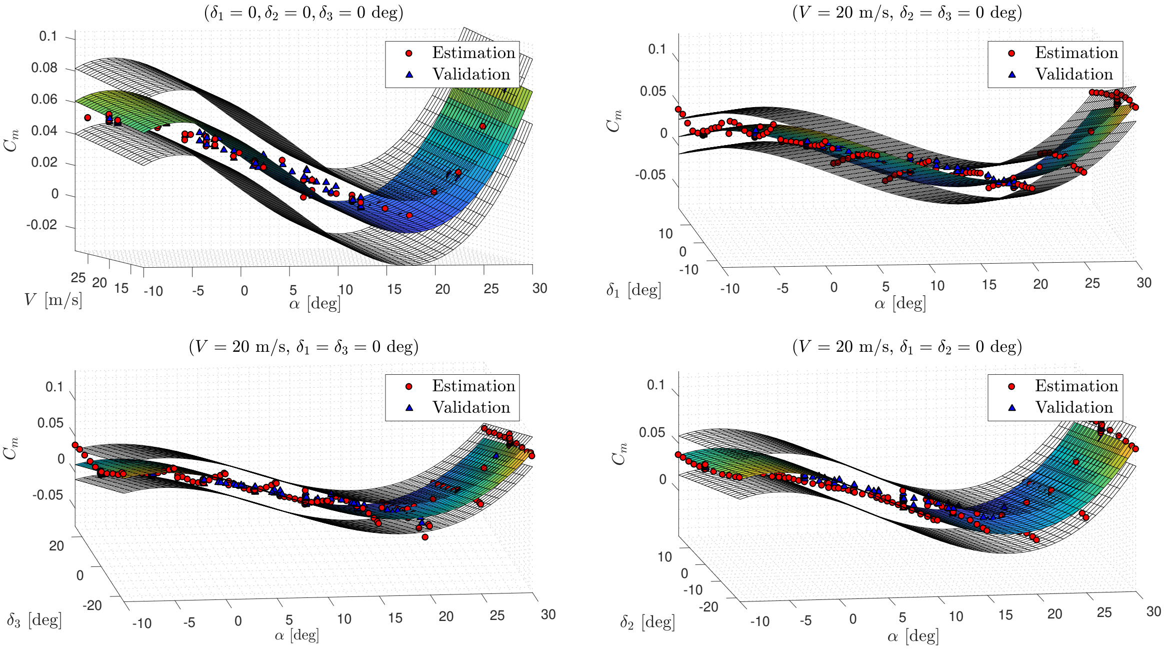

(a) Iteration #8

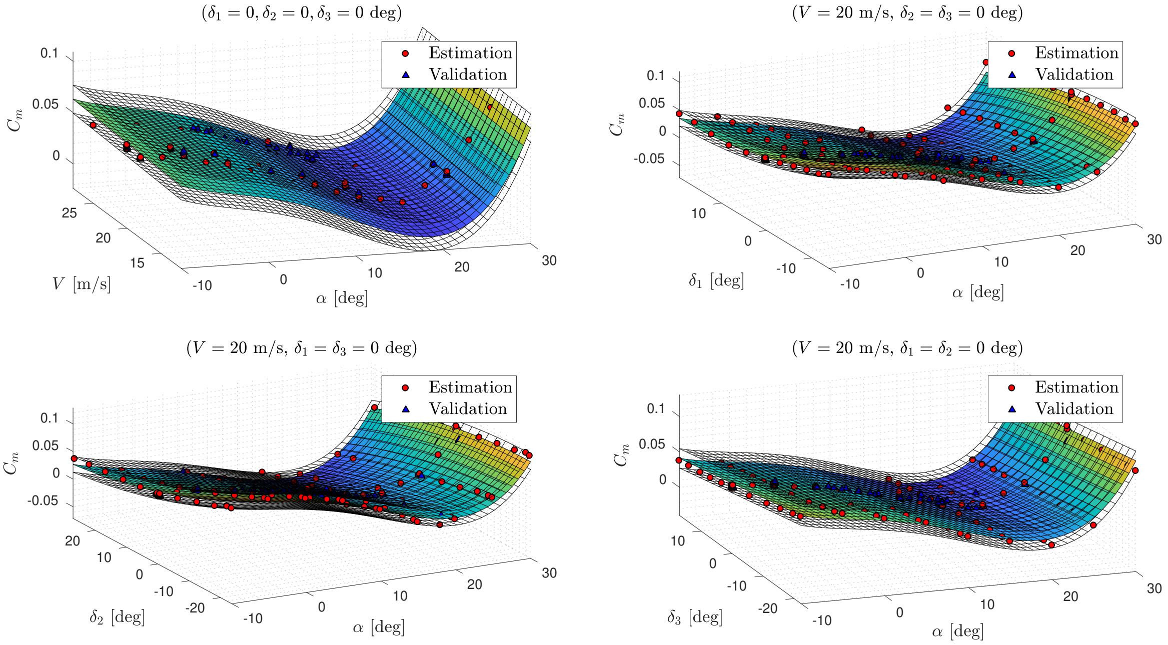

(b) Iteration #14

Figure D.12: Model cuts with prediction confidence bounds for $\alpha - V$ and $\alpha - \delta_i$ at different iterations of the stepwise regression (C_m polynomial model)

Yawing moment coefficient

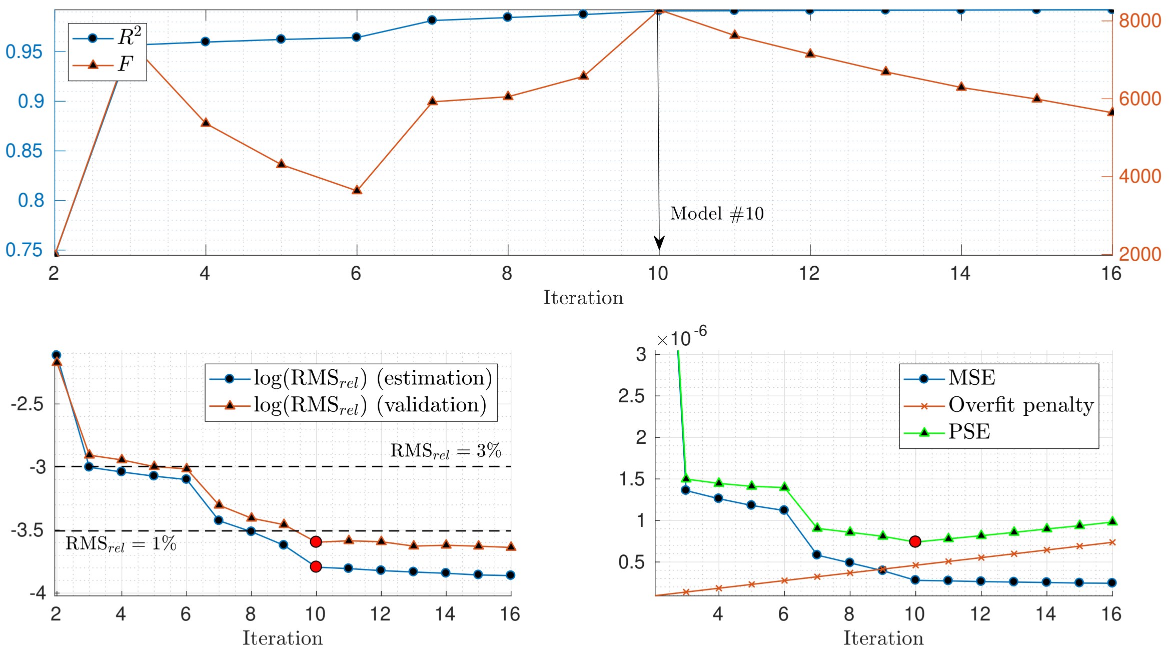

Figure D.13: Stepwise regression results (C_n polynomial model)

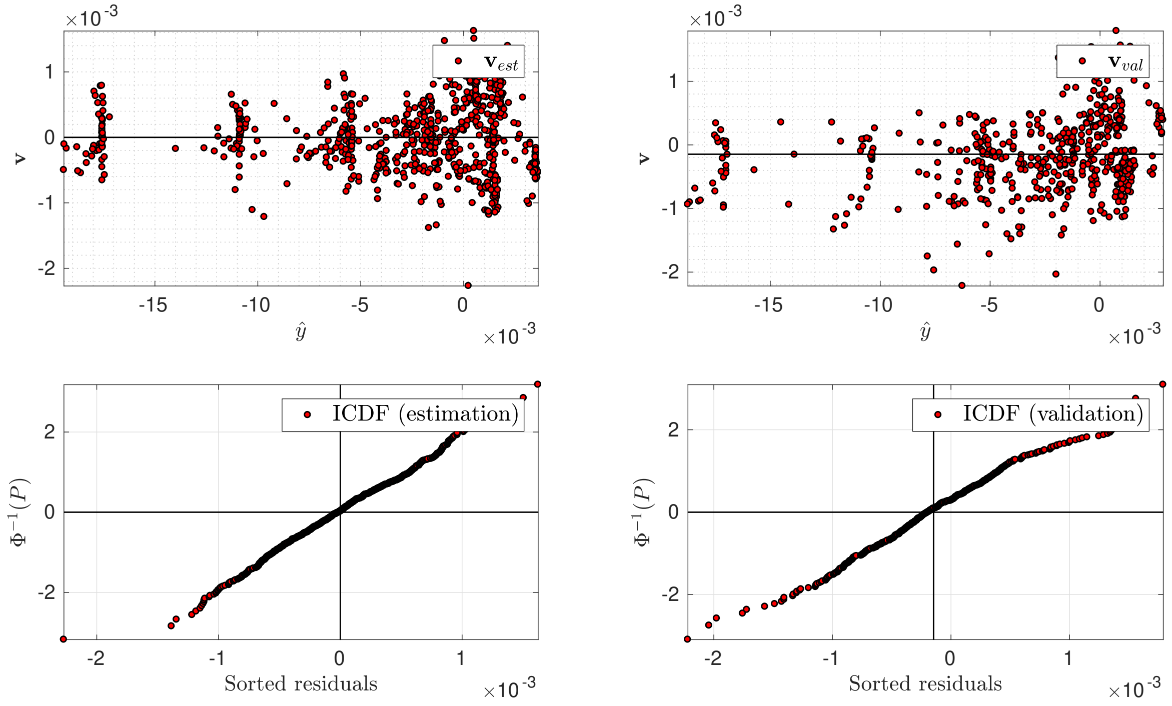

Figure D.14: Residual analysis (C_n polynomial model). Whiteness + normality assumptions.

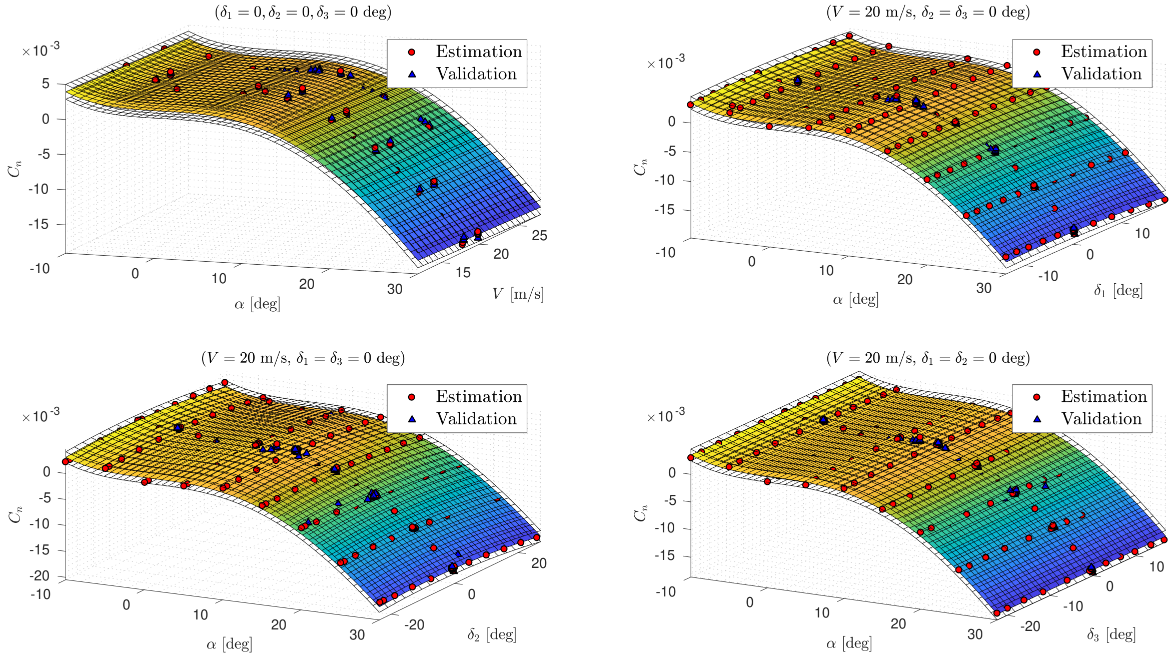

Figure D.15: Model cuts with prediction confidence bounds for $\alpha - V$ and $\alpha - \delta_i$ (C_n polynomial model)

Spline models

Forward force coefficient

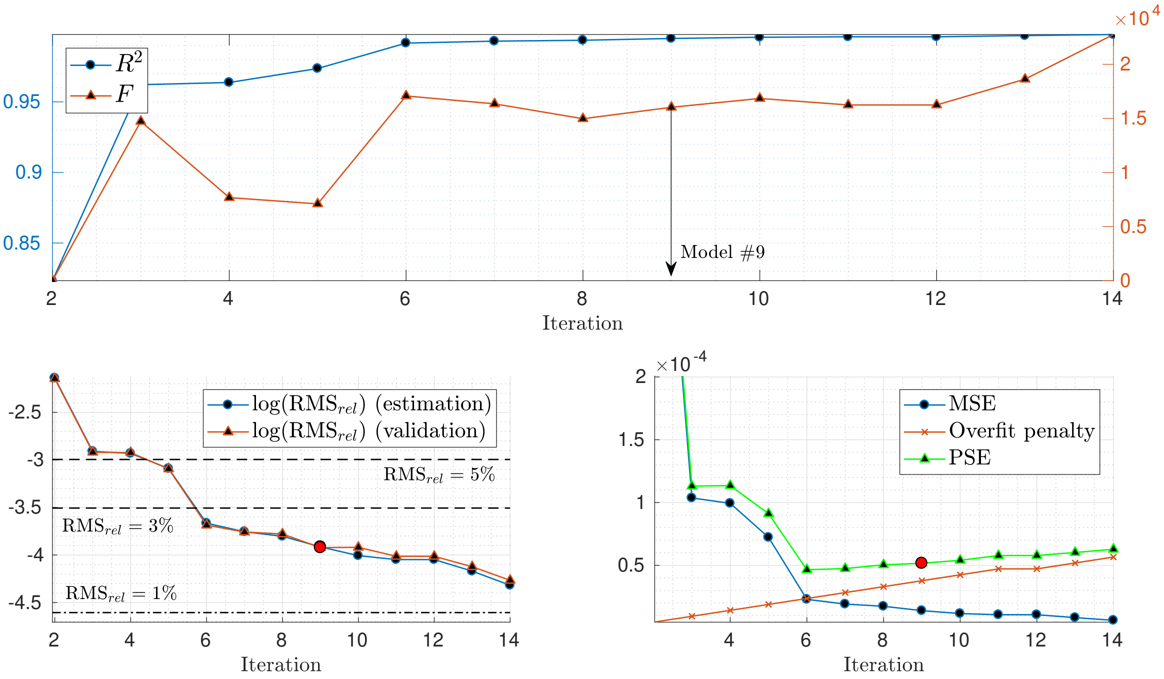

Figure D.16: Stepwise regression results (C_X spline model)

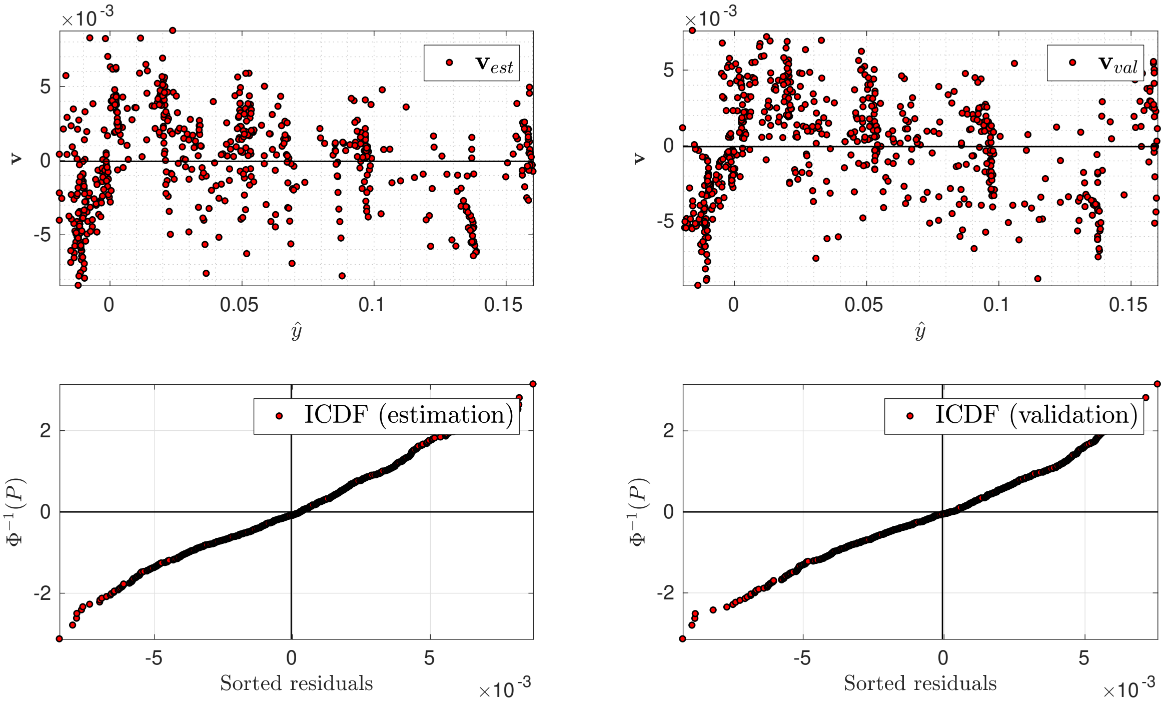

Figure D.17: Residual analysis (C_X spline model). Whiteness + normality assumptions.

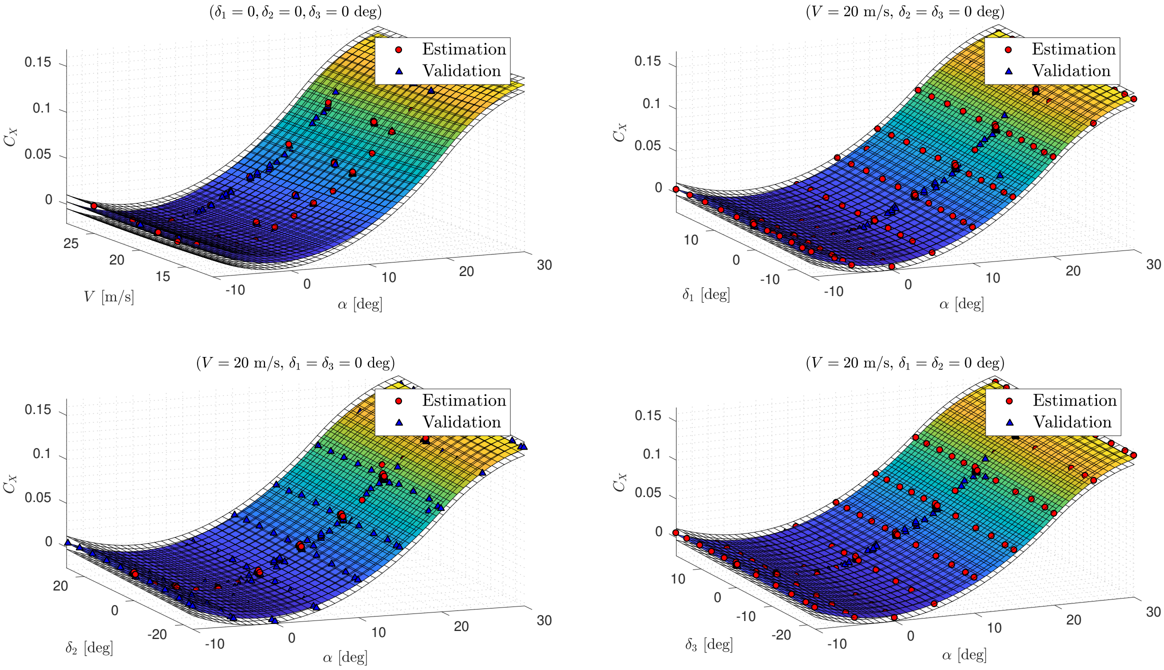

Figure D.18: Model cuts with prediction confidence bounds for $\alpha - V$ and $\alpha - \delta_i$ (C_X spline model)

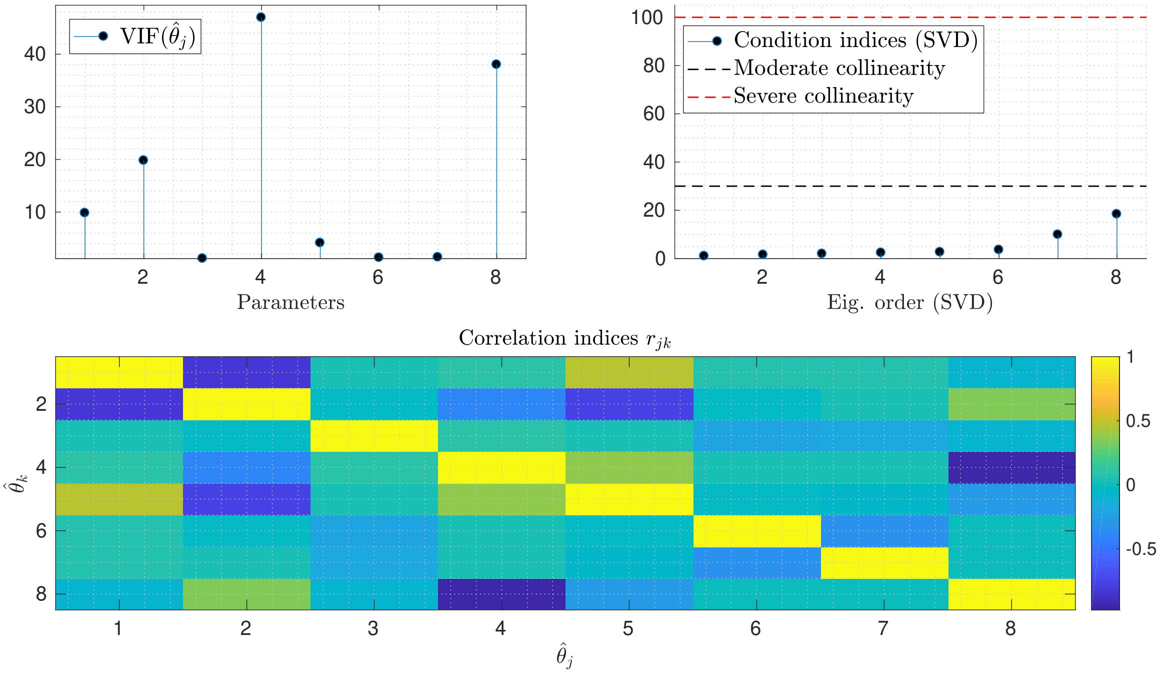

Figure D.19: Collinearity indicators (VIF, SVD decomposition, and correlation indices) (C_X spline model)

Vertical force coefficient

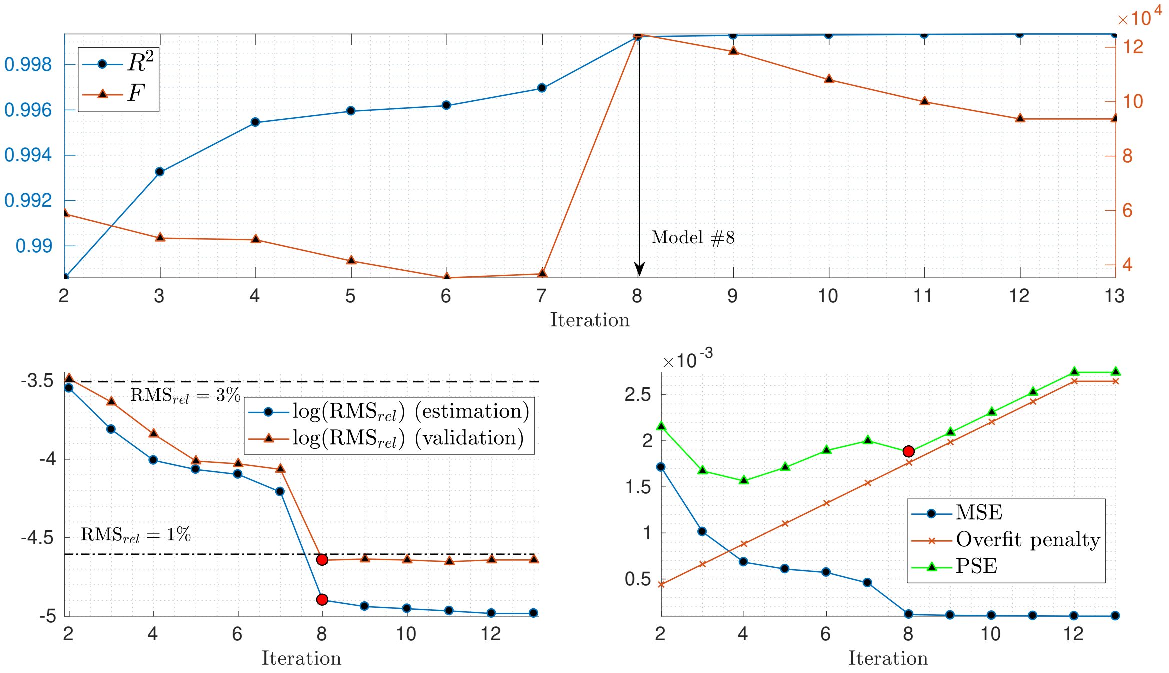

Figure D.20: Stepwise regression results (C_Z spline model)

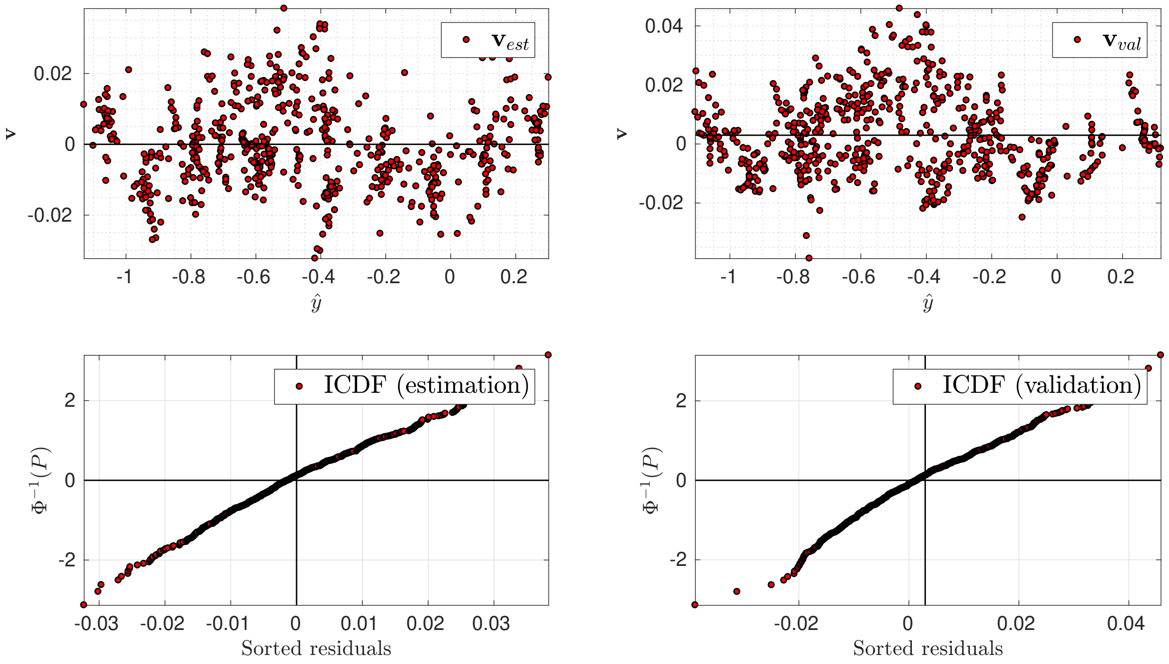

Figure D.21: Residual analysis (C_Z spline model). Whiteness + normality assumptions.

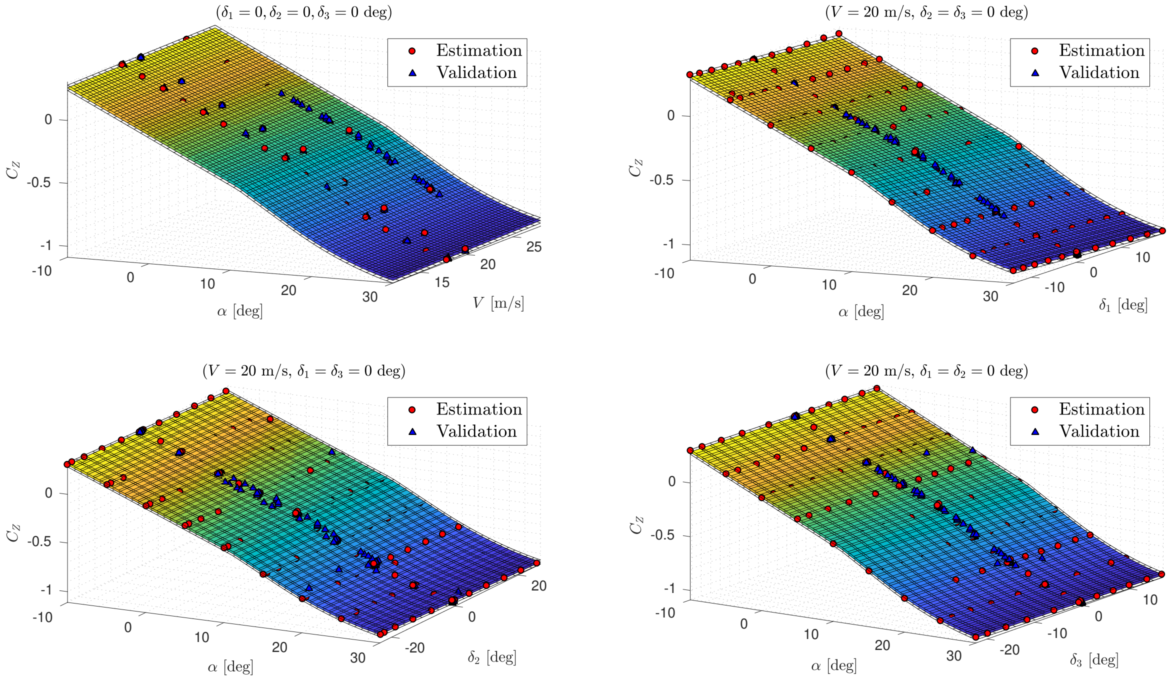

Figure D.22: Model cuts with prediction confidence bounds for $\alpha - V$ and $\alpha - \delta_i$ (C_Z spline model)

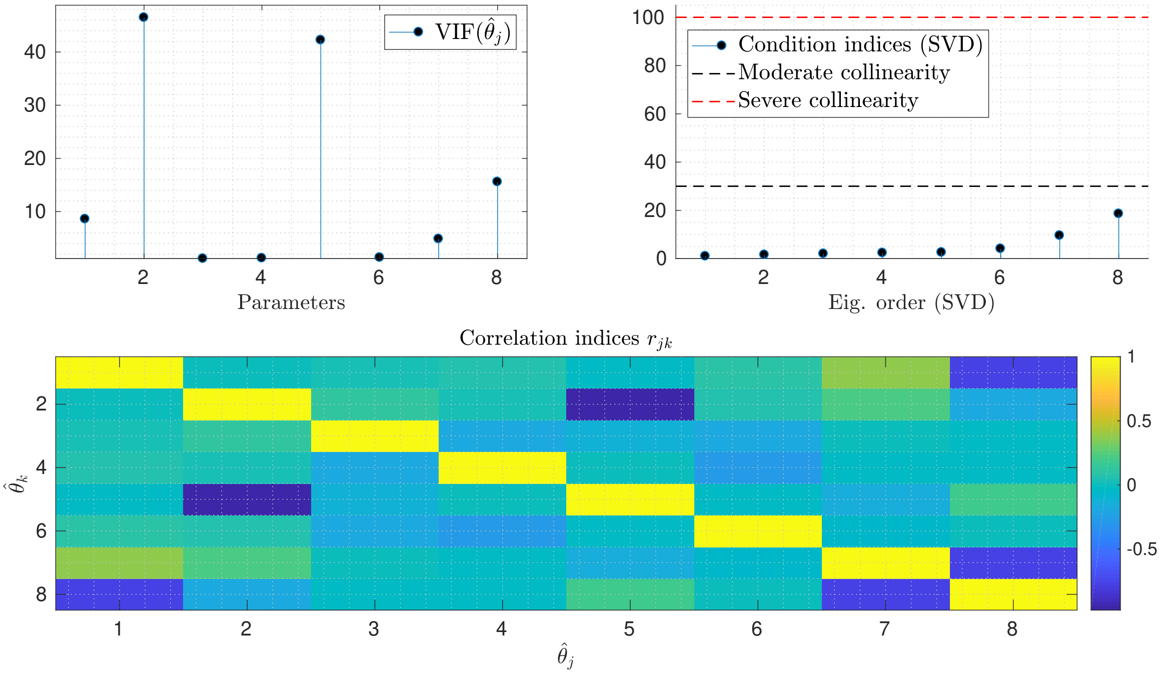

Figure D.23: Collinearity indicators (VIF, SVD decomposition, and correlation indices) (C_Z spline model)

Rolling moment coefficient

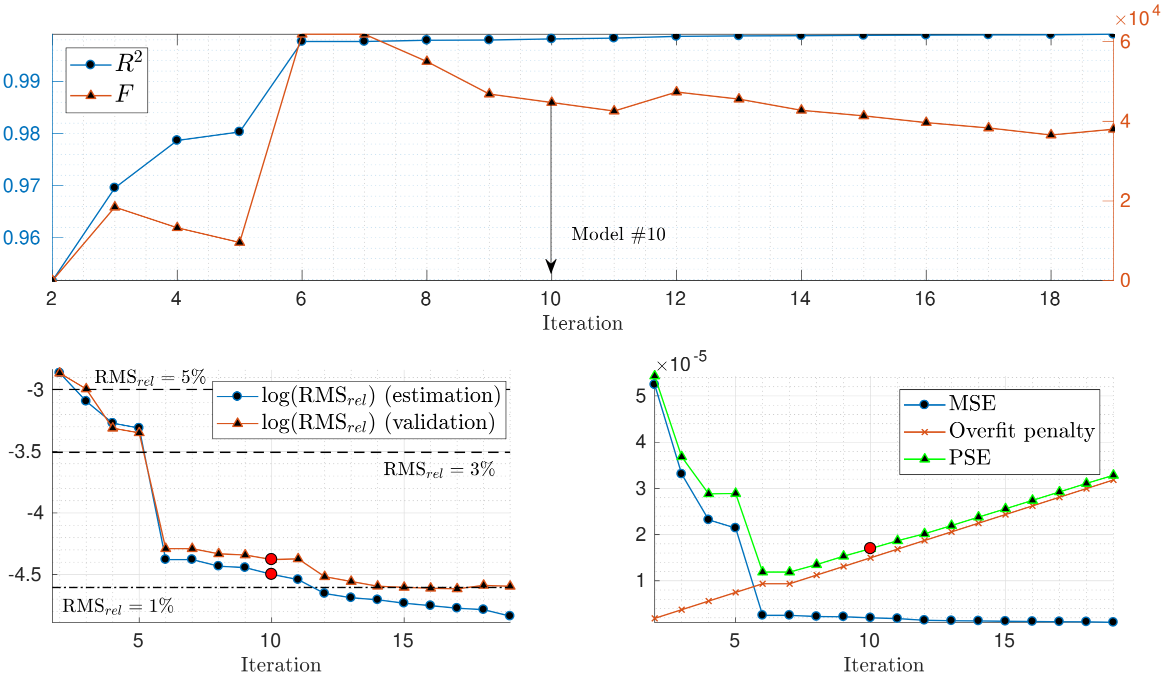

Figure D.24: Stepwise regression results (C_l spline model)

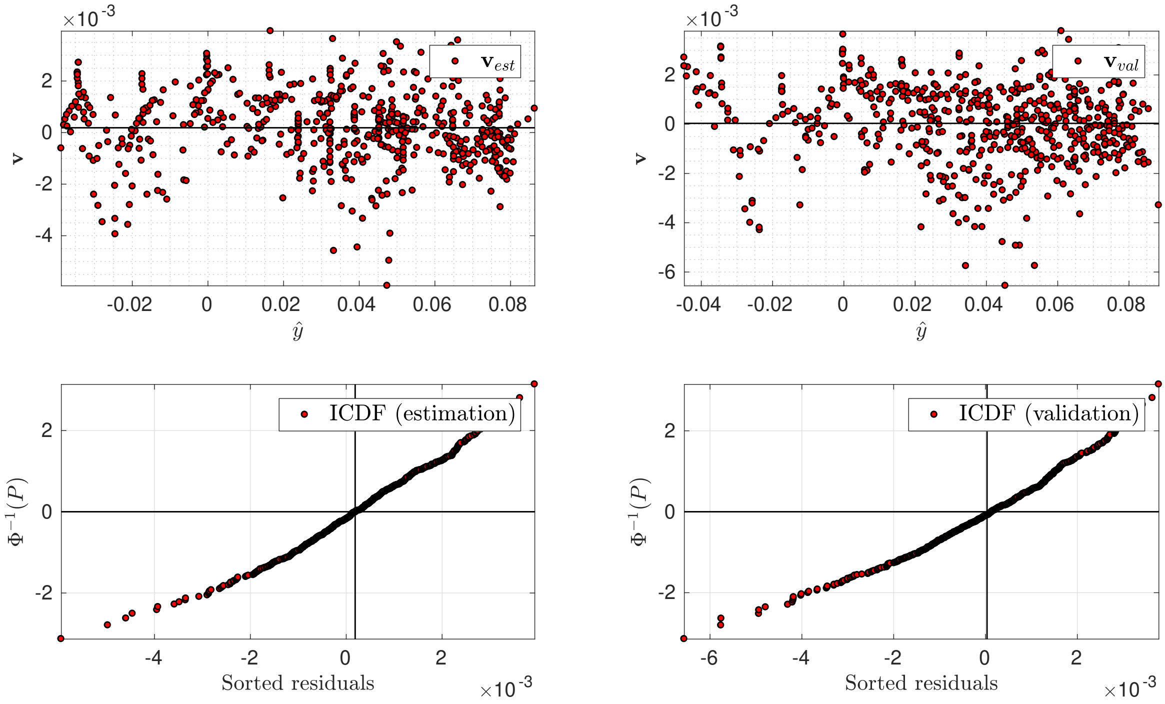

Figure D.25: Residual analysis (C_l spline model). Whiteness + normality assumptions.

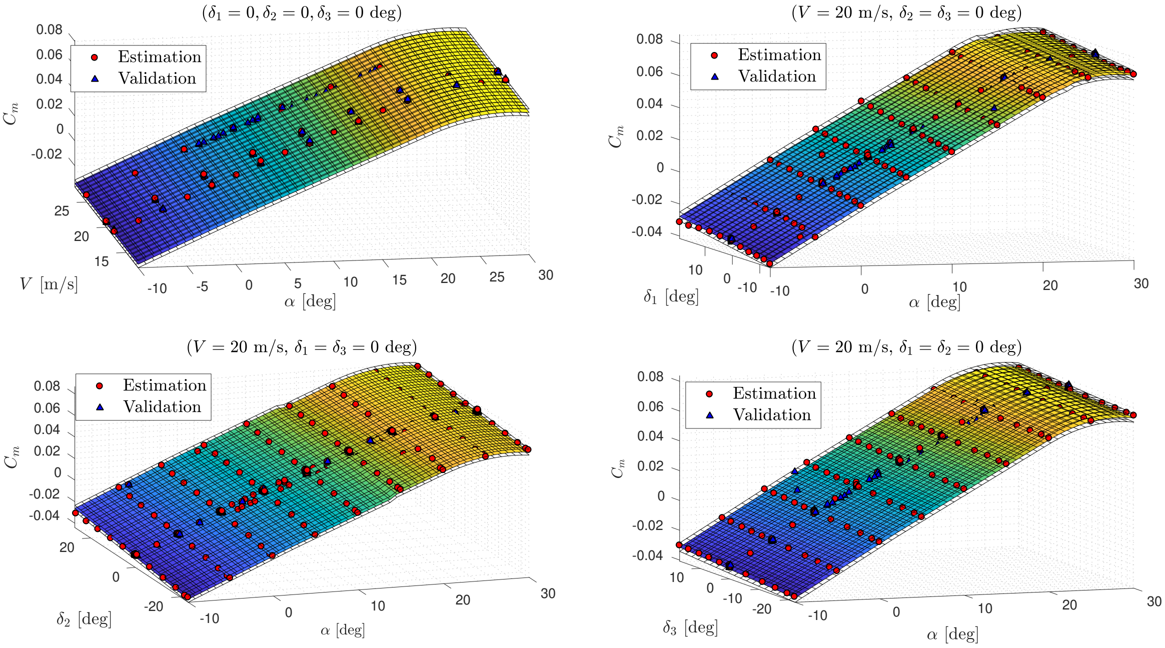

Figure D.26: Model cuts with prediction confidence bounds for $\alpha - V$ and $\alpha - \delta_i$ (C_l spline model)

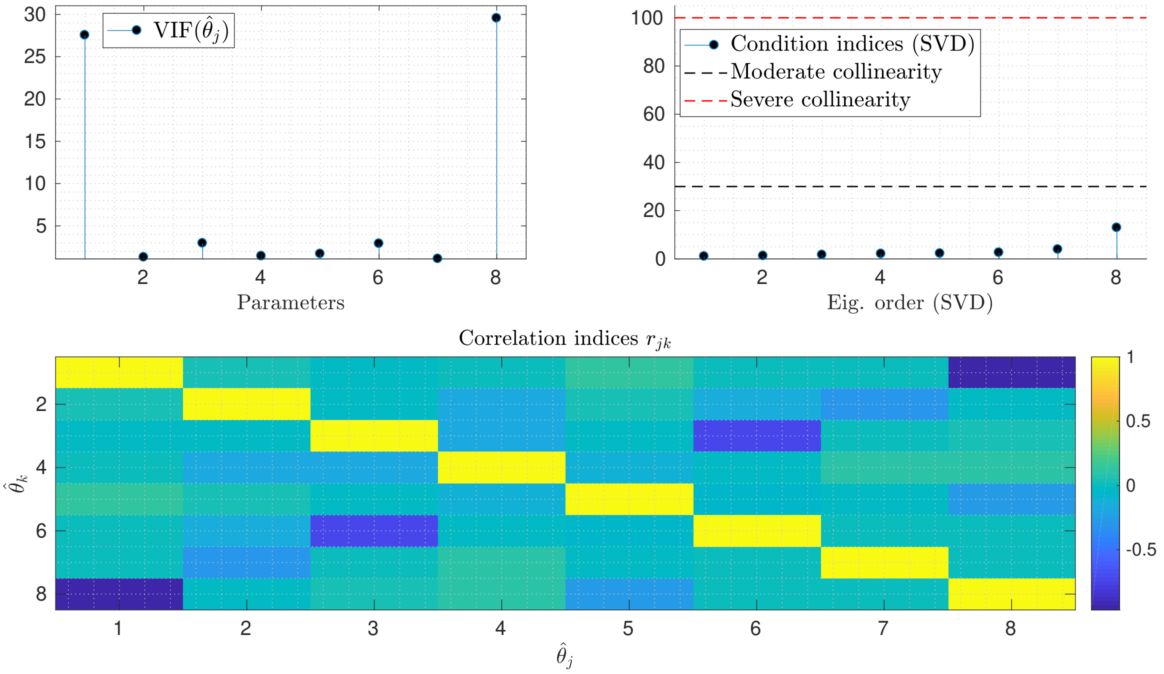

Figure D.27: Collinearity indicators (VIF, SVD decomposition, and correlation indices) (C_l spline model)

Pitching moment coefficient

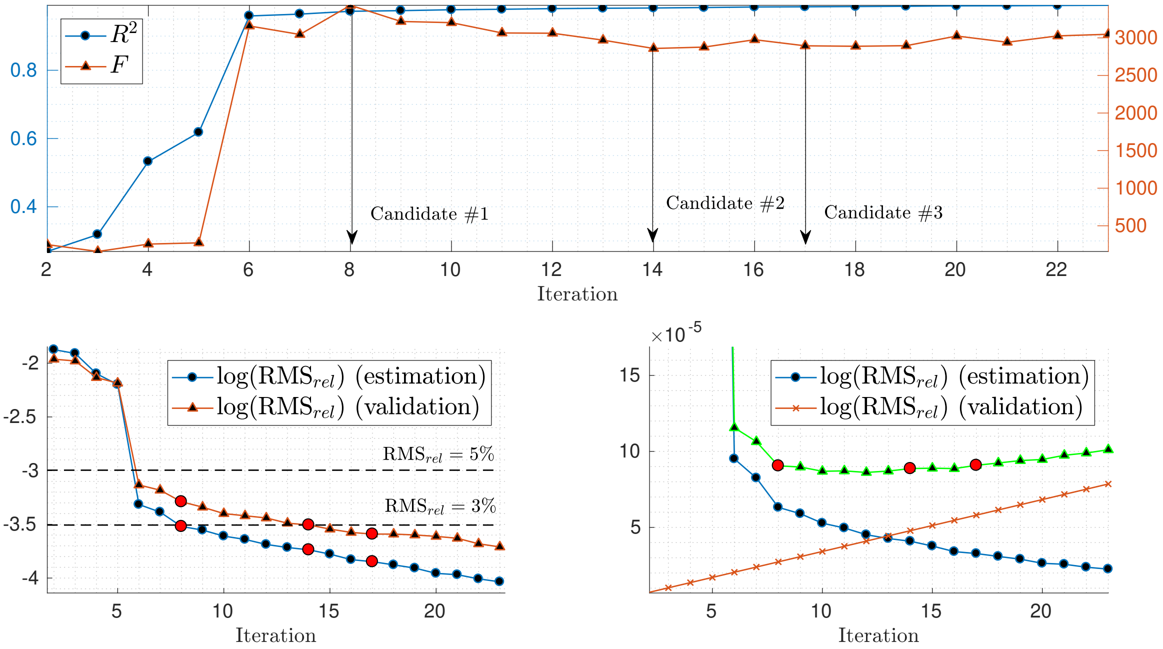

Figure D.28: Stepwise regression results (C_m spline model)

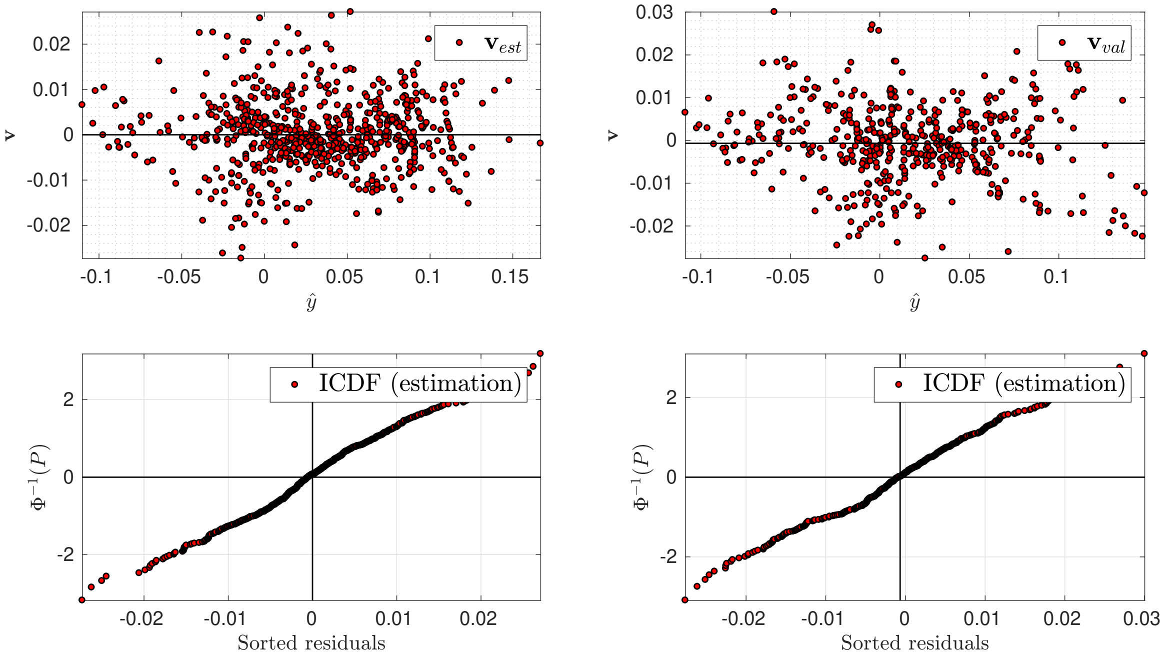

(a) Iteration #8

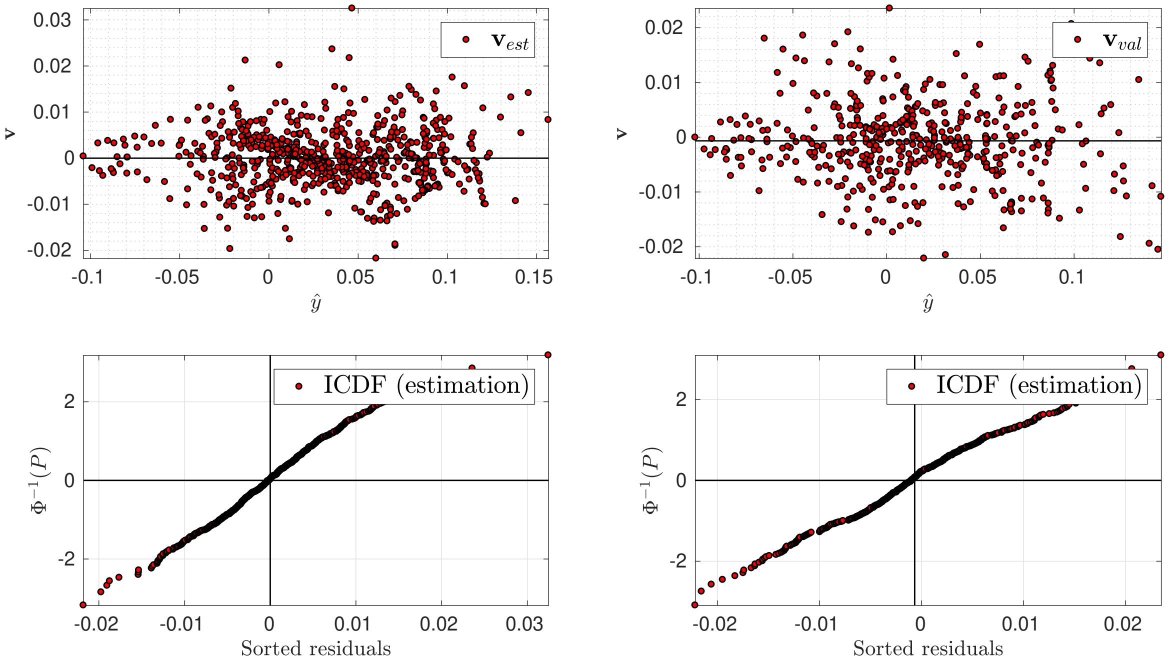

(b) Iteration #14

Figure D.29: Residual analysis at different iterations of the stepwise regression (C_m spline model). Whiteness + normality assumptions.

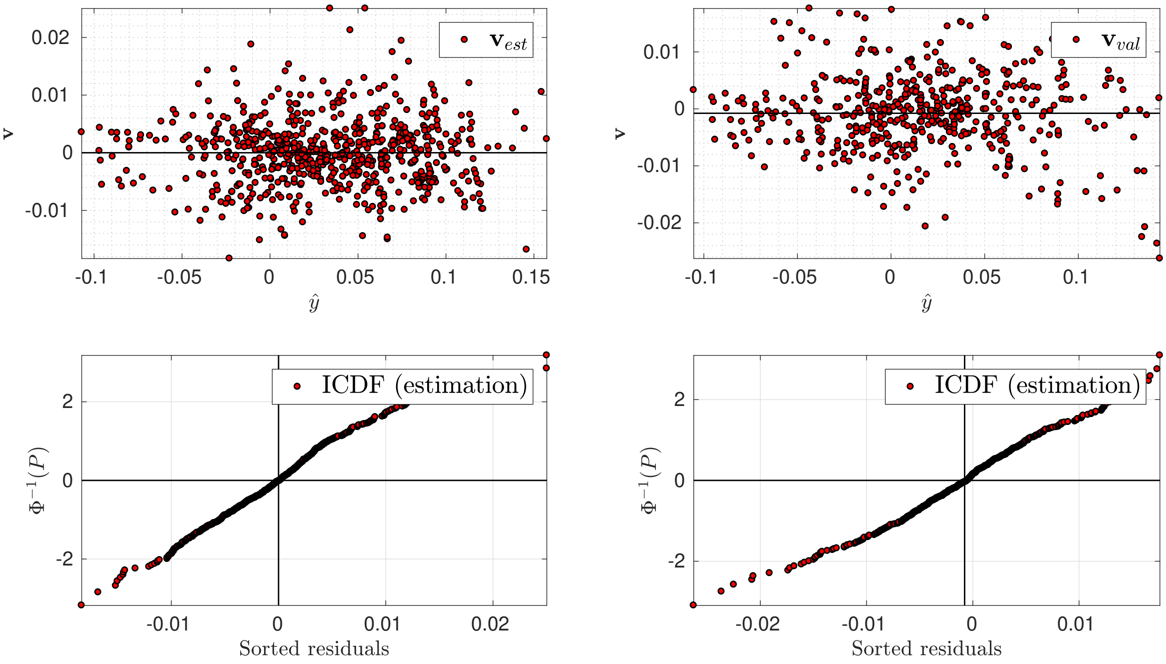

(c) Iteration #17

Figure D.29: Residual analysis at different iterations of the stepwise regression (C_m spline model). Whiteness + normality assumptions.

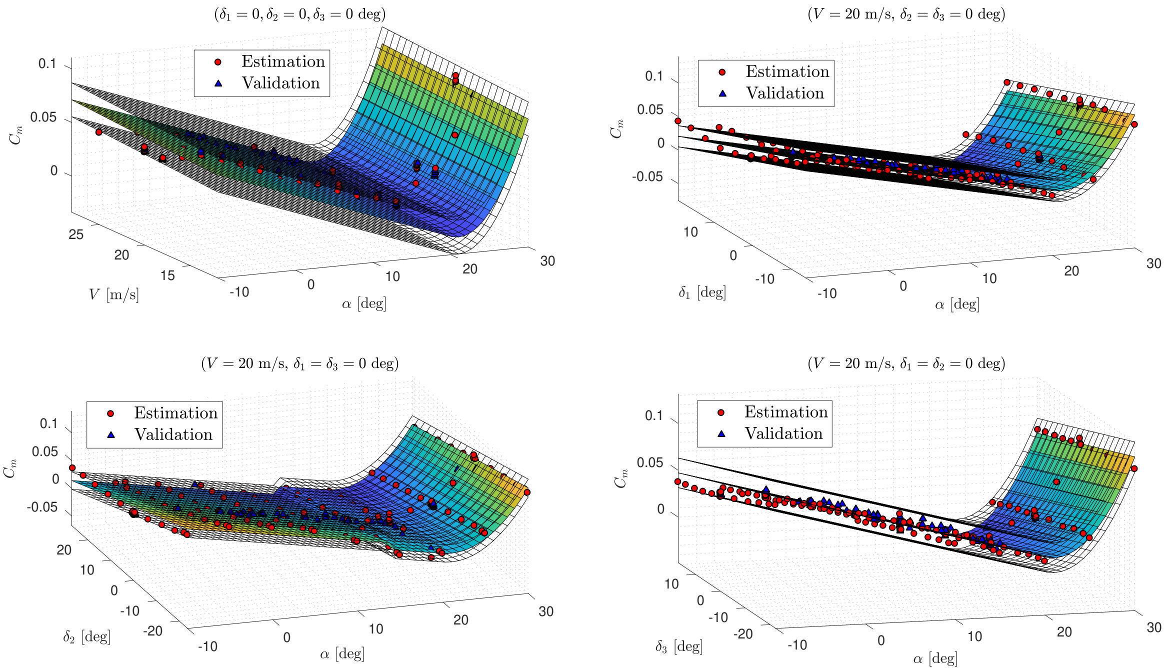

(a) Iteration #8

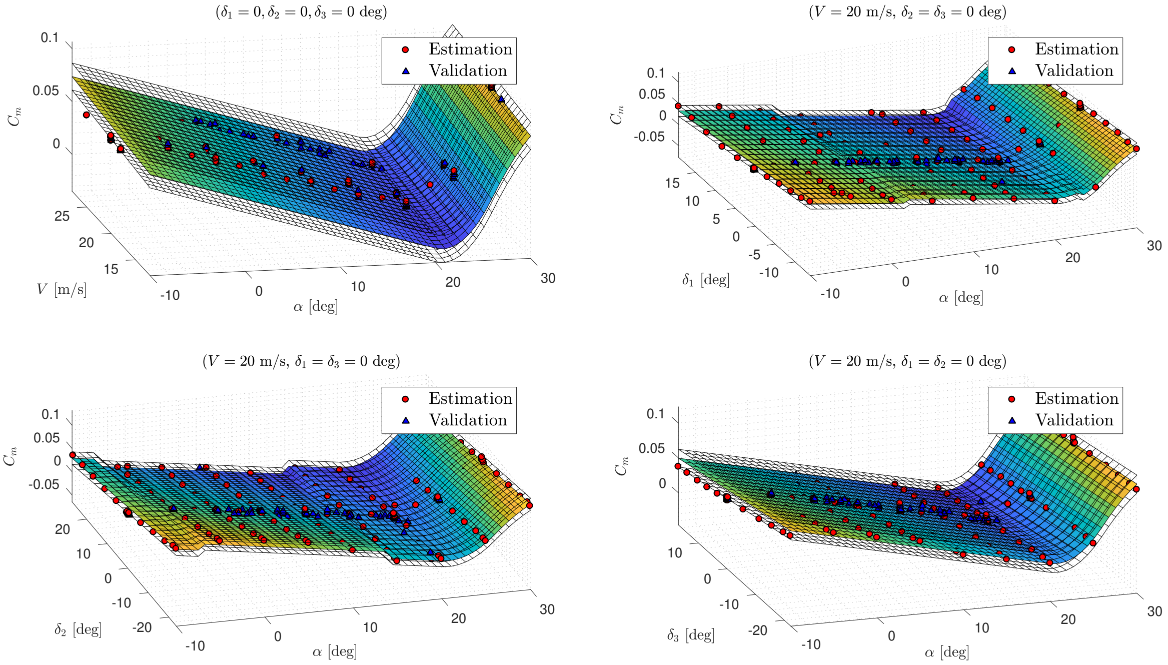

(b) Iteration #14

Figure D.30: Model cuts with prediction confidence bounds for $\alpha - V$ and $\alpha - \delta_i$ at different iterations of the stepwise regression (C_m spline model)

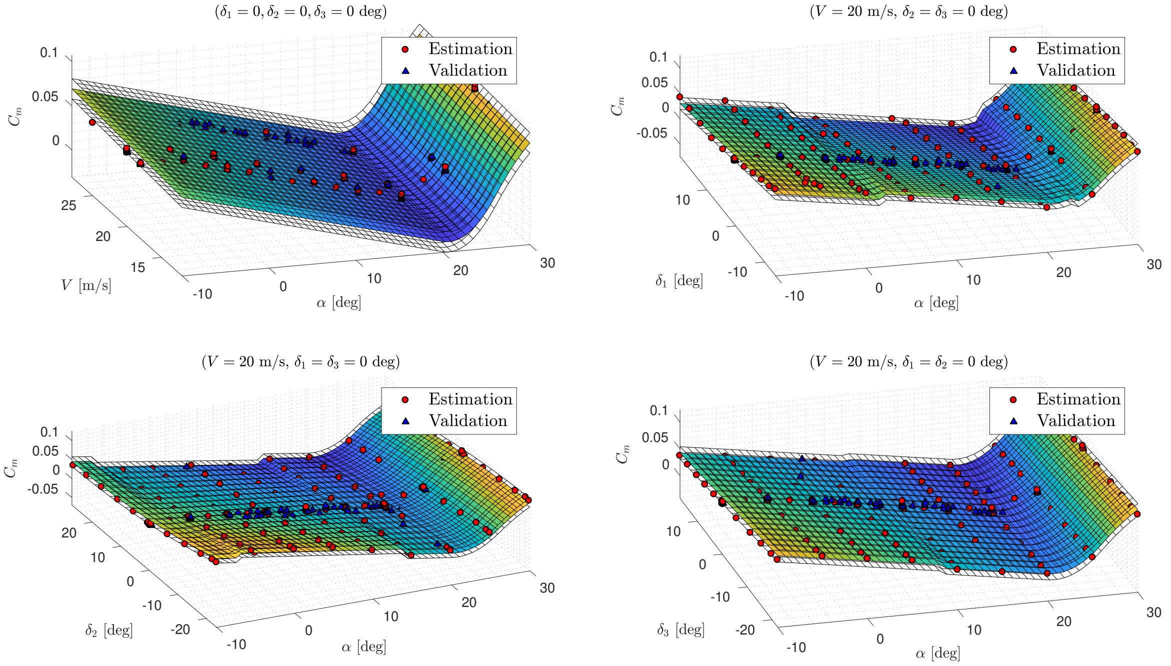

(c) Iteration #17

Figure D.30: Model cuts with prediction confidence bounds for $\alpha - V$ and $\alpha - \delta_i$ at different iterations of the stepwise regression (C_m spline model)

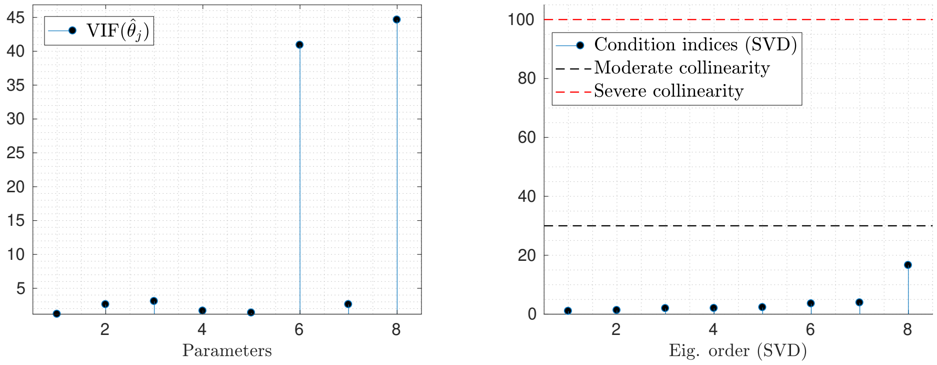

(a) Iteration #8

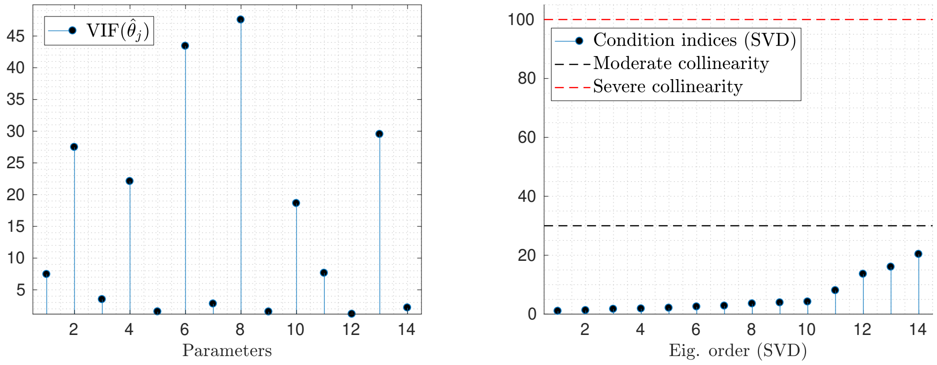

(b) Iteration #14

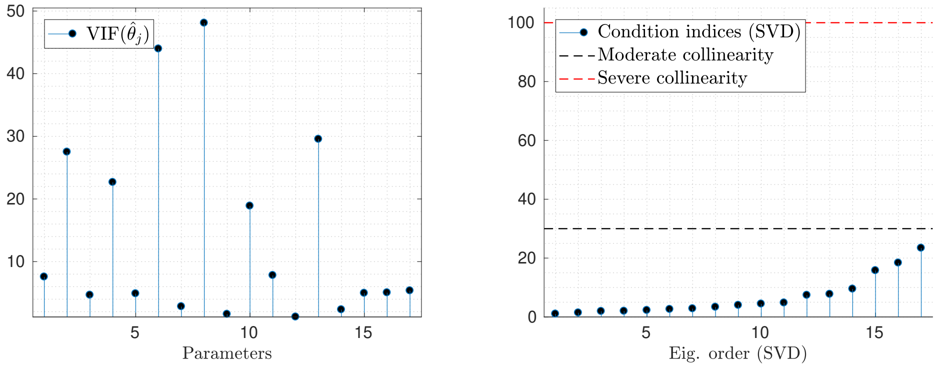

(c) Iteration #17

Figure D.31: Collinearity indicators evolution (VIF + SVD decomposition) at different iterations of the stepwise regression (C_m spline model)

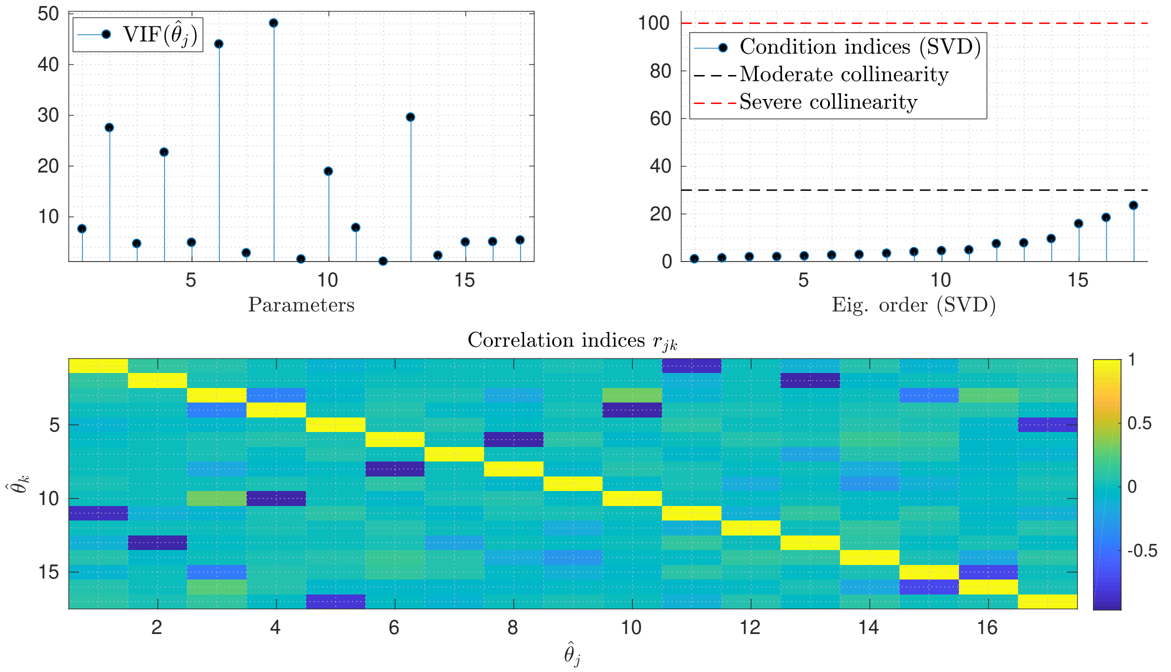

Figure D.32: Collinearity indicators (VIF, SVD decomposition, and correlation indices) (C_m spline model)

Yawing moment coefficient

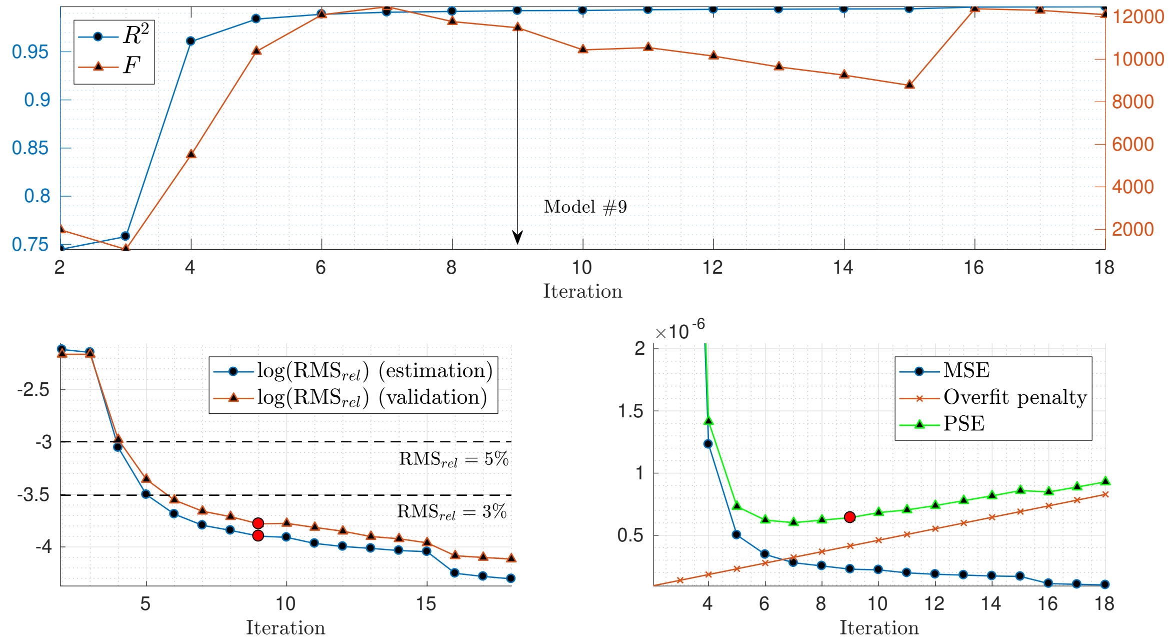

Figure D.33: Stepwise regression results (C_n spline model)

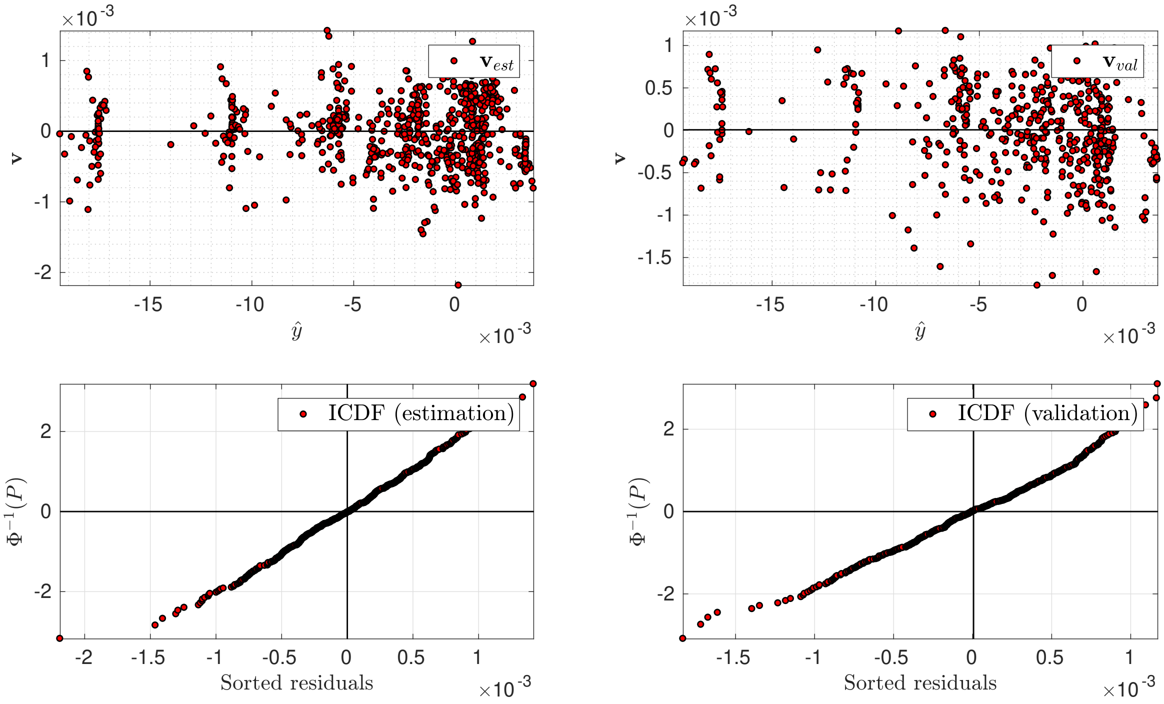

Figure D.34: Residual analysis (C_n spline model). Whiteness + normality assumptions.

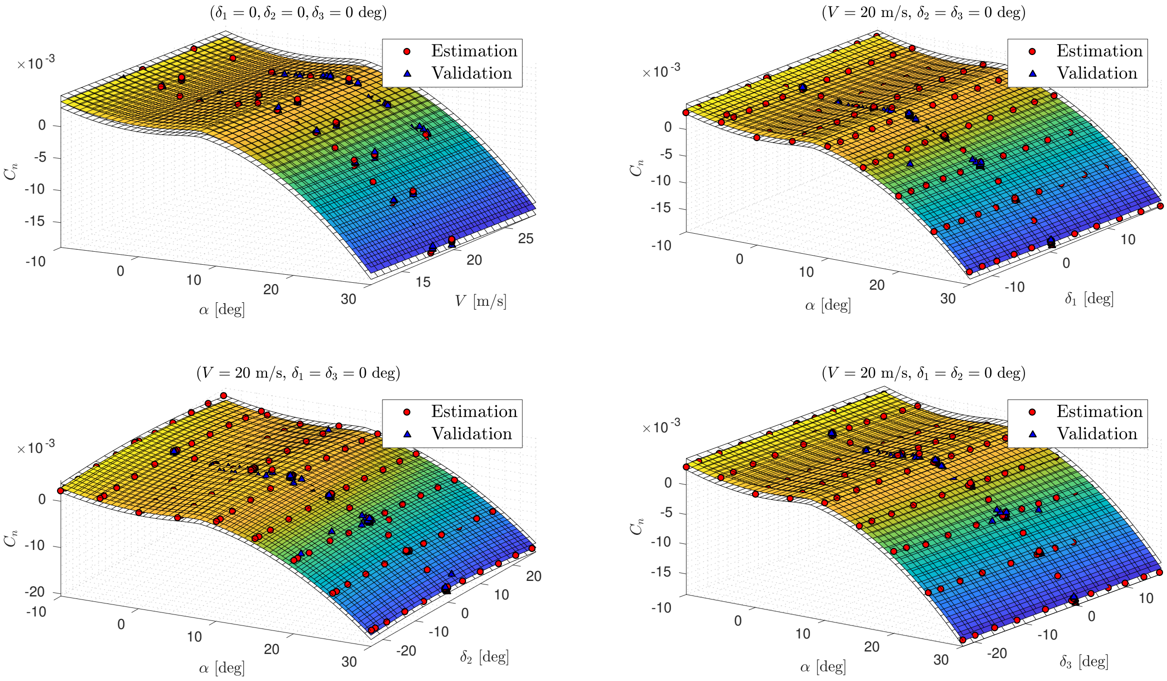

Figure D.35: Model cuts with prediction confidence bounds for $\alpha - V$ and $\alpha - \delta_i$ (C_n spline model)

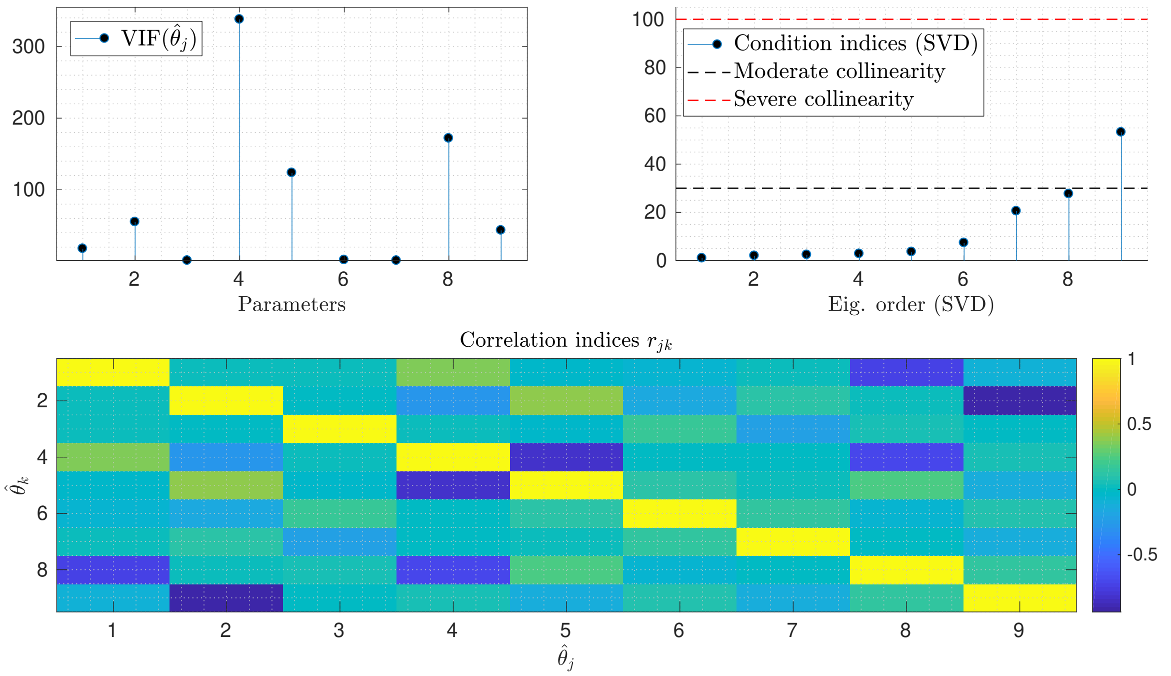

Figure D.36: Collinearity indicators (VIF, SVD decomposition, and correlation indices) (C_n spline model)

Appendix E

Actuators identification results

Models for the actuators response with time were estimated from the measured data, which included a large number of input/output data at different angles of attack, airspeeds, and maximum deflection. The sampling time was set to 10 ms in order to properly capture the transient response of the ramps up and down.

It was found that the angle of attack and the airspeed did not affect the response of the actuator in a significant way: the small differences in delay and time constant from run to run seem to be random and not follow a specific pattern. The maximum deflection, however, affected the estimation in the sense that runs with large deflections generally led to worse models than smaller ones, even though the response of the servo seemed very similar. For this reason, the runs with smaller deflections were preferred to estimate the actuator model.

As it could be expected, since linear regression could only be applied for the step response, its models had a considerably worse performance with respect to ARMAX and nonlinear regression models, which included all input/output data and will be the only results shown here.

An example of the estimation of the actuator for the second control surface (Hitec D89MW) is presented in Figures E.1 (estimation) and E.2 (validation). The estimated output, the input command, and the measured output are plotted against time, showing a good agreement for both the ramp up and ramp down and the steady values for both models, which perform similarly for many of the estimated runs.

The estimated discrete ARMAX model is given by:

$$A(z)y(t) = B(z)u(t) + C(z)e(t) \tag{E.1}$$

$$\begin{aligned} A(z) &= 1 - 1.402z^{-1} + 0.8776z^{-2} - 0.3216z^{-3} + 0.05933z^{-4} \\ B(z) &= 0.07146z^{-2} + 0.09506z^{-3} + 0.02848z^{-4} + 0.01754z^{-5} \\ C(z) &= 1 - 0.3946z^{-1} + 0.3627z^{-2} - 0.0497z^{-3} + 0.0144z^{-4} \end{aligned} \tag{E.2}$$

with $n_k = 2$, which given the sampling time of 10 ms, means the dead time of the actuator is:

$$(t_d)_{ARMAX} \cong 20\text{mS} \tag{E.3}$$

The results of the nonlinear regression for the 1st-order lag model are:

$$\tau \frac{\mathrm{d}y(t)}{\mathrm{d}t} = y(t) + K \cdot u(t - t_d) \tag{E.4}$$

$$\begin{aligned} \tau &= 0.02125 \text{ s}^{-1} \\ K &= 0.9987 \\ t_d &= 0.026 \text{ s} \end{aligned} \tag{E.5}$$

The ARMAX model had a validation residual $(\text{RMS}_{rel})_{val} = 1.4\%$ and a coefficient of determination of $R^2 = 99.88$, whereas for the 1st-order lag, $(\text{RMS}_{rel})_{val} = 1.6\%$, $R^2 = 99.84$. The very similar values between the models characteristics, estimated delay, etc. suggests that the 1st-order lag approximation is very good if it holds, and should be tried first because of its simplicity. Otherwise, ARMAX models of different orders could also be used in order to estimate a more complex dynamic response (for servos, a model order of 4 is proved to be adequate). It can be seen that the dead time agrees in both estimation methods, and is approximately equal to the standard sampling rate of the internal electronics of the servos ($t_{servo} = 20$ ms), which confirms that the software and the aerodynamic forces do not affect drastically the response speed of the servos.

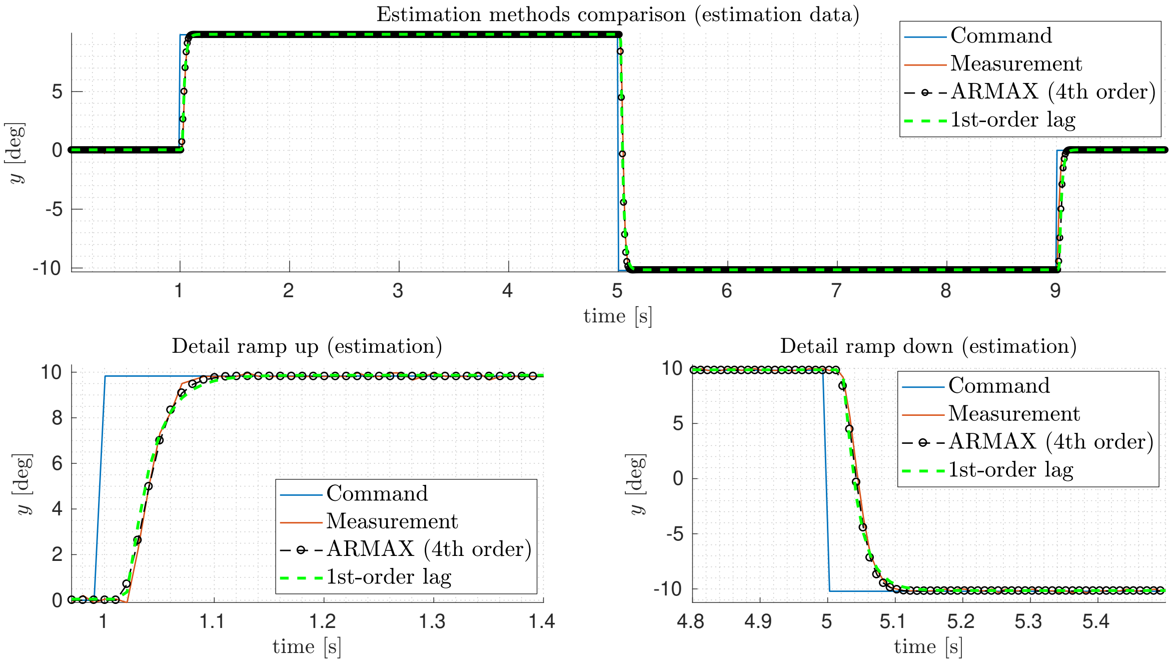

Figure E.1: ARMAX and 1st order lag model for the actuator from CS#2 (estimation)

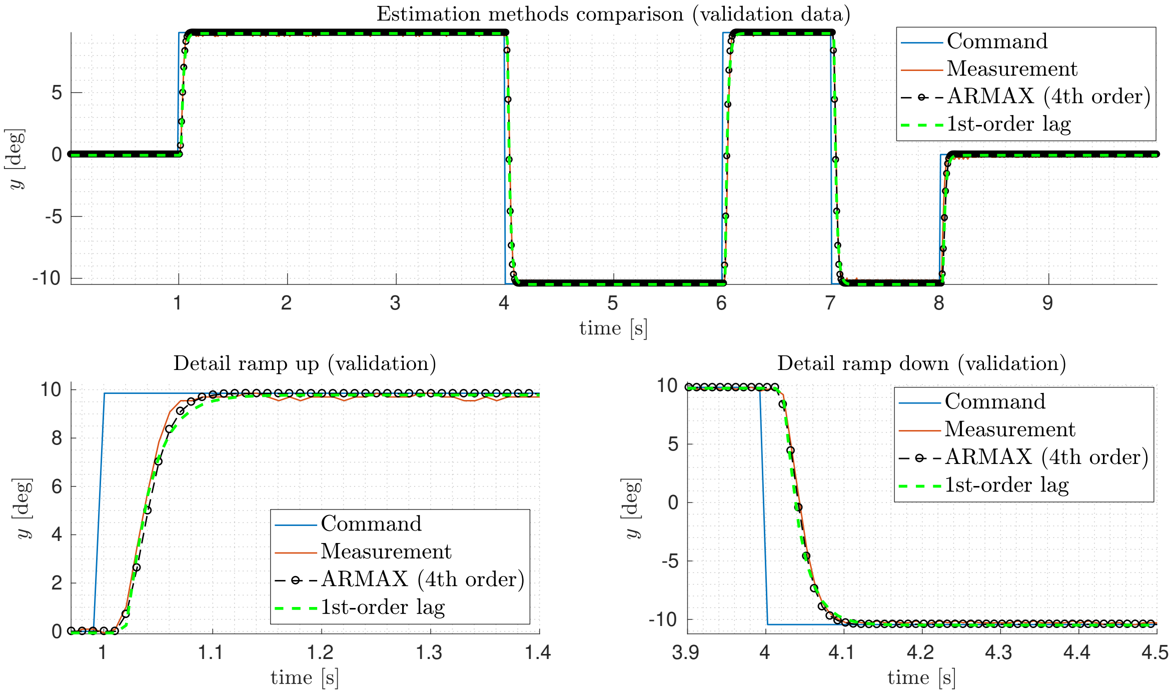

Figure E.2: ARMAX and 1st order lag model for the actuator from CS#2 (validation)